

# GEMS & GEMOLOGY

SPRING 2023  
VOLUME LIX

THE QUARTERLY JOURNAL OF THE GEMOLOGICAL INSTITUTE OF AMERICA



Characterization of Montana Sapphire  
Morphology of Colombian Emerald  
2023 Tucson Report





p. 20



p. 63



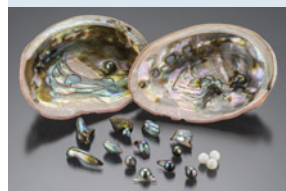
p. 74



p. 89



p. 129



p. 140

## EDITORIAL

- 1 **Sapphire from Montana's Secondary Deposits, Colombian Emerald Morphology, The 2023 Tucson Shows, and More...**

*Duncan Pay*

## FEATURE ARTICLES

- 2 **Gemological Characterization of Montana Sapphire from the Secondary Deposits at Rock Creek, Missouri River, and Dry Cottonwood Creek**

*Aaron C. Palke, Nathan D. Renfro, Jeffrey R. Hapeman, and Richard B. Berg*

Examines the mining history and geological characteristics of the three secondary sapphire deposits in the state of Montana, as well as the properties of these sapphires (unheated and heat-treated).

- 46 **Morphology of Colombian Emerald: Some Less Common Cases and Their Growth and Dissolution History**

*Karl Schmetzer and Gérard Martayan*

Evaluates the growth mechanisms of special morphological features in Colombian emerald, including possible relationships to trapiche emeralds and samples displaying the *gota de aceite* effect.

## REGULAR FEATURES

- 72 **Lab Notes**

Purple anhydrite • Pink pyrope garnet • Libyan Desert glass bangle • Atypical bead cultured pearls • Treated freshwater non-bead cultured pearls with antique appearance • Heart-shaped golden South Sea cultured pearl • Gastropod shell in a shell blister • Ruby with synthetic overgrowth • Exceptionally large synthetic rutile

- 83 **The Dr. Edward J. Gübelin Most Valuable Article Award**

- 84 **G&G Micro-World**

Three-phase inclusion in alexandrite • Apatite in hackmanite • Inclusions in chondrodite • "Flying insect" in diamond • Starry night in diamond • Xenomorphic garnet in diamond • Arrow-patterned negative crystals in sapphire • Solid inclusions in flame-fusion ruby • Quarterly Crystal: Columbite(?) in beryl

- 92 **2023 G&G Challenge**

- 94 **Diamond Reflections**

A look at plastic deformation, one of the most prevalent features in natural diamond.

- 102 **Gem News International**

Tucson 2023 • Enormous cat's-eye aquamarine • Ethiopian orbicular chalcedony • Italian coral • Exceptional gem acquisitions by the Kreises • Double pseudomorph ikaite-calcite-opal • Cultured pearl market update • Edison pearls • Natural nacreous pearls • Rare pearls from ECJA • Petroleum-included quartz from Madagascar • Orange sapphire from Greenland • Sweet Home mine rhodochrosite • New tourmaline find in San Diego County • Vibrant green "Transvaal jade" • Misfit Diamonds • Jewelry designs by Sean Hill, Brenda Smith, and Surbhi • Zeki Karaca luxury pens • Virtu Gem's ethical supply chain practices • Luminescent synthetic garnet-like crystals • Exhibits by the GIA Museum and the GIA Library • Gianmaria Buccellati Foundation Award • Atypical bead cultured pearls from the UAE • Chilean abalone cultured pearls • Microscopic shells in natural pearls • Color study of fancy sapphire from Greenland • Liberian ruby • Forsterite in purple Tanzanian spinel • Grayish blue CVD diamond • Phosphorescence of HPHT-grown diamond • Synthetic color-change wakefieldite • Heated purplish pink sapphire with monazite inclusions • Chromophores in irradiated pink sapphire

## Editorial Staff

**Editor-in-Chief**  
Duncan Pay

**Managing Editor**  
Stuart D. Overlin  
soverlin@gia.edu

**Editor**  
Brooke Goedert

**Editorial Coordinator**  
Erica Zaidman

**Senior Technical Editor**  
Jennifer Stone-Sundberg

**Technical Editor**  
Tao Z. Hsu

**Associate Technical Editor**  
Si Athena Chen

**Editors, Lab Notes**  
Thomas M. Moses  
Shane F. McClure

**Editors, Micro-World**  
Nathan Renfro  
Elise A. Skaltwold  
John I. Koivula

**Editors, Gem News**  
Gagan Choudhary  
Christopher M. Breeding  
Guanghai Shi

**Editors, Colored Stones Unearthed**

Aaron C. Palke  
James E. Shigley

**Editor, Diamond Reflections**  
Evan M. Smith

**Contributing Editors**  
James E. Shigley  
Raquel Alonso-Perez

**Editor-in-Chief Emeritus**  
Alice S. Keller

**Assistant Editor**  
Erin Hogarth

## Production Staff

**Creative Director**  
Faizah Bhatti

**Production and Multimedia Specialist**  
Michael Creighton

**Photo/Video Producer**  
Kevin Schumacher

**Photographer**  
Robert Weldon

**Multimedia Associate**  
Christopher Bonine

**Video Production**  
Albert Salvato

## Editorial Review Board

Ahmadjan Abduriyim  
Tokyo, Japan

Timothy Adams  
San Diego, California

Edward W. Boehm  
Chattanooga, Tennessee

James E. Butler  
Washington, DC

Alan T. Collins  
London, UK

Sally Eaton-Magaña  
Carlsbad, California

John L. Emmett  
Brush Prairie, Washington

Emmanuel Fritsch  
Nantes, France

Eloïse Gaillou  
Paris, France

Al Gilbertson  
Carlsbad, California

Gaston Giuliani  
Nancy, France

Lee A. Groat  
Vancouver, Canada

Yunbin Guan  
Pasadena, California

George Harlow  
New York, New York

Peter Heaney  
University Park, Pennsylvania

Richard W. Hughes  
Bangkok, Thailand

Jaroslav Hyřl  
Prague, Czech Republic

Dorrit Jacob  
Canberra, Australia

A.J.A. (Bram) Janse  
Perth, Australia

Mary L. Johnson  
San Diego, California

Robert E. Kane  
Helena, Montana

Stefanos Karamelas  
Paris, France

Lore Kiefert  
Lucerne, Switzerland

Simon Lawson  
Maidenhead, UK

Ren Lu  
Wuhan, China

Thomas M. Moses  
New York, New York

Laura Otter  
Canberra, Australia

Aaron C. Palke  
Carlsbad, California

Ilene Reinitz  
Chicago, Illinois

Nathan Renfro  
Carlsbad, California

Benjamin Rondeau  
Nantes, France

George R. Rossman  
Pasadena, California

Sudarast Saeseaw  
Bangkok, Thailand

Karl Schmetzer  
Petershausen, Germany

Andy Shen  
Wuhan, China

Guanghai Shi  
Beijing, China

James E. Shigley  
Carlsbad, California

Elisabeth Strack  
Hamburg, Germany

Nicholas Sturman  
Bangkok, Thailand

D. Brian Thompson  
Florence, Alabama

Fanus Viljoen  
Johannesburg, South Africa

Wuyi Wang  
New York, New York

Christopher M. Welbourn  
Reading, UK

Chunhui Zhou  
New York, New York

J.C. (Hanco) Zwaan  
Leiden, The Netherlands

# GEMS & GEMOLOGY®

[gia.edu/gems-gemology](http://gia.edu/gems-gemology)

**Customer Service**  
(760) 603-4200  
[gandg@gia.edu](mailto:gandg@gia.edu)



### Subscriptions

Copies of the current issue may be purchased for \$29.95 plus shipping. Subscriptions are \$79.99 for one year (4 issues) in the U.S. and \$99.99 elsewhere. Canadian subscribers should add GST. Discounts are available for renewals, group subscriptions, GIA alumni, and current GIA students. To purchase print subscriptions, visit [store.gia.edu](http://store.gia.edu) or contact Customer Service. For institutional rates, contact Customer Service.

### Database Coverage

*Gems & Gemology's* impact factor is 2.045, according to the 2021 Journal Citation Reports by Clarivate Analytics (issued June 2022). *G&G* is abstracted in Thomson Reuters products (Current Contents: Physical, Chemical & Earth Sciences and Science Citation Index—Expanded, including the Web of Knowledge) and other databases. For a complete list of sources abstracting *G&G*, go to [gia.edu/gems-gemology](http://gia.edu/gems-gemology), and click on "Publication Information."

### Manuscript Submissions

*Gems & Gemology*, a peer-reviewed journal, welcomes the submission of articles on all aspects of the field. Please see the Author Guidelines at [gia.edu/gems-gemology](http://gia.edu/gems-gemology) or contact the Managing Editor. Letters on articles published in *G&G* are also welcome. Please note that Field Reports, Lab Notes, Gem News International, Micro-World, Colored Stones Unearthed, Diamond Reflections, and Charts are not peer-reviewed sections but do undergo technical and editorial review.

### Copyright and Reprint Permission

Abstracting is permitted with credit to the source. Libraries are permitted to photocopy beyond the limits of U.S. copyright law for private use of patrons. Instructors are permitted to reproduce isolated articles and photographs/images owned by *G&G* for noncommercial classroom use without fee. Use of photographs/images under copyright by external parties is prohibited without the express permission of the photographer or owner of the image, as listed in the credits. For other copying, reprint, or republication permission, please contact the Managing Editor.

*Gems & Gemology* is published quarterly by the Gemological Institute of America, a nonprofit educational organization for the gem and jewelry industry.

Postmaster: Return undeliverable copies of *Gems & Gemology* to GIA, The Robert Mouawad Campus, 5345 Armada Drive, Carlsbad, CA 92008.

Our Canadian goods and service registration number is 126142892RT.

Any opinions expressed in signed articles are understood to be opinions of the authors and not of the publisher.

## About the Cover

*Designed by Zoltan David, this opal and green tourmaline necklace contains Knightsteel links with 99.42 total carats of Ethiopian opal beads. The 10.97 ct tourmaline from Afghanistan, faceted by Clay Zava, is set in a bezel with platinum inlay and 0.22 carats of diamonds. The necklace was one of many stunning pieces David exhibited at the 2023 Tucson shows, which are reported on in this issue. Photo by Robert Weldon; courtesy of Zoltan David.*

Printing is by L+L Printers, Carlsbad, CA.

GIA World Headquarters The Robert Mouawad Campus 5345 Armada Drive Carlsbad, CA 92008 USA  
© 2023 Gemological Institute of America All rights reserved. ISSN 0016-626X



# Sapphire from Montana's Secondary Deposits, Colombian Emerald Morphology, the 2023 Tucson Shows, and More...



Welcome to the Spring 2023 issue of *Gems & Gemology*! A new volume year kicks off with our recap of the Tucson gem shows, where buyers, sellers, and industry professionals from all over the globe converge. And with two major feature articles, our regular sections, and the annual *G&G* Challenge, this issue is sure to captivate readers.

In our lead article, Dr. Aaron Palke and coauthors present their study of the gemological characteristics of sapphire from Montana's secondary deposits. Using Rock Creek, Missouri River, and Dry Cottonwood Creek samples in a variety of colors, the authors provide

*"The article also details the fascinating history of sapphire mining in these three Montana mining districts, which still hold substantial resources."*

typical inclusion scenes and trace element chemistry fingerprints. The article also details the fascinating history of sapphire mining in these three Montana mining districts, which still hold substantial resources.

Next, Dr. Karl Schmetzer and Gérard Martayan investigate the less common morphological and growth phenomena of Colombian emerald samples to understand their growth and post-growth history. Based on their observation of 15 isolated emerald crystals and seven specimens in matrix using optical methods, they offer insight into the different patterns, with a goal of expanding the database of morphological features in Colombian emerald.

Our regular features provide informative snapshots, beginning with *Lab Notes*. Highlights from the section include a rare example of the purple collector gem anhydrite, a heart-shaped golden South Sea cultured pearl displaying natural shape and color, and the largest sample of synthetic rutile examined at GIA to date. Explore the inner landscapes of gemstones in our *Micro-World* section, where you'll see rare cloud inclusions resembling a starry night in diamond, a macroscopic mineral inclusion cluster in a Pakistani aquamarine crystal, a three-phase inclusion in alexandrite, and more. *Diamond Reflections* returns in this issue, this time exploring plastic deformation in diamond. Our *Gem News International* section begins with nearly 30 pages covering the 2023 Tucson gem shows, ranging from the latest trends and market updates to noteworthy designs, followed by an opulent photo gallery packed with finds from the shows. The GNI regular features include various pearl discoveries from around the world and a new source of ruby from Liberia.

Finally, test your gemological knowledge of our 2022 feature articles in the annual *G&G* Challenge, and find out which articles received the Dr. Edward J. Gübelin Most Valuable Article Award.

We hope you enjoy the latest issue of *Gems & Gemology*!

Duncan Pay | Editor-in-Chief | [dpay@gia.edu](mailto:dpay@gia.edu)



# GEMOLOGICAL CHARACTERIZATION OF MONTANA SAPPHIRE FROM THE SECONDARY DEPOSITS AT ROCK CREEK, MISSOURI RIVER, AND DRY COTTONWOOD CREEK

Aaron C. Palke, Nathan D. Renfro, Jeffrey R. Hapeman, and Richard B. Berg

Montana has produced large volumes of sapphire from secondary deposits for more than 150 years. While early production was mostly for industrial use as watch and instrument bearings, modern heat treatment technology has enabled the deposits to be worked profitably as gemstone mines, bringing more of this material to the gem and jewelry trade than ever before. Although pale blue and pale green sapphires make up the bulk of the production, fine Montana sapphire comes in nearly every hue, including yellow, orange, purple, and pink, along with very rare finds of ruby. Secondary Montana sapphire shares some similarities with those from Umba and Songea in Tanzania, but it is generally straightforward to separate them on the basis of inclusion scenes and trace element chemistry fingerprints.

Nearly 160 years ago, gold prospectors in the American West stumbled upon one of North America's most important gemstone deposits, discovering sapphire in several locations in Montana. These were first recovered along the Missouri River near Helena, and additional deposits were later found at Rock Creek and Dry Cottonwood Creek. The sapphires recovered from these secondary deposits generally have overlapping properties and are collectively referred to as "Montana sapphire." [Note that these are distinct in their gemological properties from "Yogo sapphires," which are mined from Montana's only primary deposit, at Yogo Gulch; see Renfro et al. (2017).] Surprisingly, the secondary deposits were not initially mined for fine jewelry-grade sapphire but for gold and for industrial-grade sapphire to use as watch and instrument bearings.

While the deposits produce many stones with exceptional natural color, the majority require (or at least benefit from) carefully controlled high-temperature heat treatment to enhance their color for the jewelry market. Various heating procedures—in both

oxidizing and reducing environments at high temperatures—can be used to either create or intensify a variety of colors (e.g., Emmett and Douthit, 1993). Whether heated or with a natural, untreated color, secondary Montana sapphire occurs in a wide range

## In Brief

- Sapphires have been produced from three secondary deposits in Montana for more than 150 years.
- Most sapphires produced are less than 1 ct and require heat treatment to improve their color. However, large unheated stones of several carats are available in the market.
- Montana sapphires have characteristic inclusion suites and chemical profiles that allow their origin to be confidently identified.

of sizes and colors including blue, green, yellow, orange, purple, and pink (figures 1–5). With the reintroduction of large-scale mining 25–30 years ago and the recent acceleration of mining activities at Missouri River and especially Rock Creek, fine Montana sapphire is available in the gem and jewelry market in quantities never seen before. It is also growing in

See end of article for About the Authors and Acknowledgments.

GEMS & GEMOLOGY, Vol. 59, No. 1, pp. 2–45,  
<http://dx.doi.org/10.5741/GEMS.59.1.2>

© 2023 Gemological Institute of America



Figure 1. Top production from Rock Creek from the 2021 mining season, in rough and cut form. The rough stones range from 10.05 to 67.15 ct and the faceted stones from 3.09 to 12.18 ct. The yellow sapphire at top center was named the Yellowstone sapphire and is part of the Somewhere in the Rainbow collection. For the faceted stones, the blue stone on the left and the two blue stones on the bottom are heated, while the others are unheated. Note that one of the rough stones is missing in the faceted stone layout. Photos by Robert Weldon; courtesy of Potentate Mining, LLC.

popularity with the increasing emphasis on transparency and traceability in supply chains within the

jewelry industry. Demand is also increasing as consumers become more interested in the less saturated

Figure 2. At 17.04 ct, this natural-color (unheated) rough sapphire crystal from Eldorado Bar on the Missouri River is exceptionally large for Montana's secondary deposits. Photo by Orasa Weldon; courtesy of Pala International.



Figure 3. The "Bitterroot Flower" brooch by Paula Crevoshay contains nearly 400 Montana sapphires: 79 pink (6.03 carats total), 116 yellow (7.46 carats total), and 202 additional fancy-color (16.26 carats total). Photo by Robert Weldon; courtesy of Paula Crevoshay.







Figure 4. This “Fiume” ring features a wide range of colors seen in Montana sapphire. The sapphires are all heat treated, with 2.07 total carat weight. Photo courtesy of Raintree Jewelry.

blue and teal and fancy-color sapphires that are common in Montana. Fortunately, these sapphires have unique gemological and chemical characteristics that allow their geographic origin to be confidently determined.

## MATERIALS AND METHODS

**Samples.** The Montana sapphires examined in this study are from a variety of sources. The bulk of the samples were collected in 2015 by GIA gemologists at the Potentate mine at Rock Creek and from Cass Thompson’s mining operation at Eldorado Bar on the Missouri River. Additional samples came from the collections of the authors and were generally sourced directly from current operations at Rock Creek and Missouri River. Sapphires from the South Fork of Dry Cottonwood Creek were donated by Dr. John Emmett, director of Crystal Chemistry in Brush Prairie, Washington, who obtained them from the mining operations of American Gem Corporation in 1994–1995. Observations described in this study come primarily from the more than 800 sapphires in the GIA Colored Stone Reference Collection gathered from the sources described above. Additional sapphires were provided from the collection of John I. Koivula, GIA’s analytical microscopist. The largest sapphire studied was the 67.15 ct Yellow-

stone sapphire, but most were much smaller, from less than a carat to several carats in size. Seventy-three Montana sapphires were included in our laser ablation-inductively coupled plasma-mass spectrometry (LA-ICP-MS) trace element measurements, as well as 19 sapphires from Songea, Tanzania, and 17 from Umba, Tanzania. The Songea and Umba sapphires were either collected directly in the field by GIA field gemologists or donated by Dr. Emmett.

**Ultraviolet/Visible/Near-Infrared (UV-Vis-NIR) Spectroscopy.** Spectra were collected with a PerkinElmer Lambda 950 UV-Vis spectrophotometer (PE 950) in the 200–1000 nm range, with 1 nm spectral resolution. Spectra presented were collected from samples oriented as wafers perpendicular to the optic axis, which allows collection only of the ordinary ray (o-ray) spectrum. Samples used in heat treatment experiments were mounted on aluminum plates with 1 mm apertures during spectroscopy. They were set in place using wax to allow the same region of the sample to be measured before and after heat treatment.

**Fourier-Transform Infrared (FTIR) Spectroscopy.** FTIR spectra were collected using a Thermo Fisher Nicolet 6700 FTIR spectrometer equipped with an XT-KBr beam splitter and a mercury-cadmium-telluride (MCT) detector operating with a 4× beam condenser accessory. The resolution was set at 4 cm<sup>-1</sup> with 1.928 cm<sup>-1</sup> data spacing.

**Raman Spectroscopy.** Inclusions were identified, when possible, using Raman spectroscopy with a Renishaw inVia Raman microscope system. The Raman spectra of the inclusions were excited by a Modu-Laser Stellar-REN Ar-ion laser producing highly polarized light at 514 nm and collected at a nominal resolution of 3 cm<sup>-1</sup> in the 2000–200 cm<sup>-1</sup> range. In many cases, the confocal capabilities of the Raman system allowed inclusions beneath the surface to be analyzed.

**LA-ICP-MS.** Trace element chemistry was collected by LA-ICP-MS using a Thermo Fisher iCAP Qc ICP-MS, coupled to an Elemental Scientific Lasers NWR 213 laser ablation system with a frequency-quintupled Nd:YAG laser (213 nm wavelength with 4 ns pulse width). Ablation was carried out with 55 μm spot sizes, with a fluence of 8–10 J/cm<sup>2</sup> and repetition



*Figure 5. Early gold prospecting led to the discovery of Montana sapphire. This gold nugget from Scratchgravel Hills measures about  $4 \times 7$  cm; courtesy of Bill Larson. The rough sapphires and the necklace containing rough sapphires and a 3.5 ct lavender spinel cut by Larry Woods are courtesy of Diana Widman. Photo by Robert Weldon.*



rates of 20 Hz. The isotope  $^{27}\text{Al}$  was used as an internal standard at 529250 ppmw, and synthetic and natural corundum reference materials were used as external standards (Stone-Sundberg et al., 2017). Detection limits ranged from 0.1–0.3 ppma for magnesium, 0.5–2.0 ppma for titanium, 0.03–0.2 ppma for vanadium, 0.06–1.3 ppma for chromium, 1–5 ppma for iron, and 0.03–0.07 ppma for gallium. Trace element values are reported here in parts per million on an atomic basis rather than the more typical parts per million by weight unit used for trace elements in many geochemical studies. Units of ppma are the standard used in GIA laboratories for corundum, as they allow a simpler analysis of crystal chemical properties and an understanding of the color mechanisms of sapphire and ruby. Conversion factors are determined by a simple formula that can be found in table 1 of Emmett et al. (2003).

**Heat Treatment.** Some heat treatment studies were carried out at the commercial heating facility operated by Dale Siegford of the Sapphire Gallery in Philipsburg, Montana. Treatments were claimed to have been at 1400°C, but other details of this commercial treatment were not disclosed. Additional heat treatment experiments were carried out at GIA's experimental heating facility using a Thermal Technology Model 1000-3560-FP24 muffle tube furnace, similar to the system used in Emmett and Douthit (1993).

**Gemology.** Standard gemological instruments were used to measure refractive index, birefringence, specific gravity, and pleochroism. Microscopic observation was performed using either a Nikon Eclipse LV100 compound microscope or Nikon SMZ1500 binocular microscope outfitted with a Nikon DS-Ri2 camera for recording images. Differential interference contrast (DIC) images were taken on the LV100. Also used were a Nikon SMZ25 stereomicroscope equipped with dual fiber-optic illuminators, darkfield and brightfield illumination, polarizing filters, and a Nikon DS-Ri2 camera.

## HISTORY

Like much of the American West, the history of Montana is told in the story of gold. The original prospectors who discovered the state's sapphire deposits generally had little in the way of mineralogical, much less gemological, knowledge. While these prospectors did stumble upon one of the most important gem deposits in the North American continent,

they were mainly targeting gold, whose value was much more obvious than the shiny dense pebbles of sapphire they sometimes found in their jigs and pans. When the first sapphires were discovered in 1865 at the Missouri River, their range of natural colors did not suit the gem and jewelry industry of that time—that happened 30 years later, when bright blue sapphires were found at Yogo Gulch. However, when sapphires were found in abundance at Rock Creek in 1892, another lucrative market opened up for these stones as watch and instrument bearings (figure 6). In fact, mining efforts until the late 1920s were driven almost entirely by the search for gold and the use of sapphires as watch bearings. The bulk of the sapphires mined in Montana had ended up being used for industrial purposes. The availability and affordability of synthetic ruby and sapphire (grown by the Verneuil process) in the 1920s and 1930s ended the first great heyday of sapphire mining in Montana (Berg, 2014). After some small-scale mining to support the war effort in the 1940s, the major operations in this early period ended shortly after World War II. It was not until the introduction of advanced heat treatment procedures that these deposits became economically viable again.

The following sections will document each of the three secondary sapphire deposits in more detail. Historical information in this section comes primarily from the works of Berg (2007, 2014) and Berg and Landry (2018), which are currently the most comprehensive historical works on sapphire mining in these deposits. These three publications contain original historical research based on archived historical resources and interviews with primary historical figures. When possible, the primary published source of information is cited; however, when no citation is provided, it should be understood that the primary reference is the original historical research in Berg (2007), Berg (2014), or Berg and Landry (2018) for Dry Cottonwood Creek, Rock Creek, and Missouri River, respectively. Additional sources of historical information are Kunz (1890), Pratt (1906), Clabaugh (1952), Emmett and Douthit (1993), Garland (2002), Barron and Boyd (2015), Hsu et al. (2017), and Kane (2020).

**Missouri River.** The first influx of European settlers into the Montana territory began in 1862 with the discovery of rich gold placers in Grasshopper Creek at the town of Bannack. With rumors of gold circulating, prospectors would seek their fortune up and down nearly every creek and river in the territory, no matter how large or small. Gold in abundance would



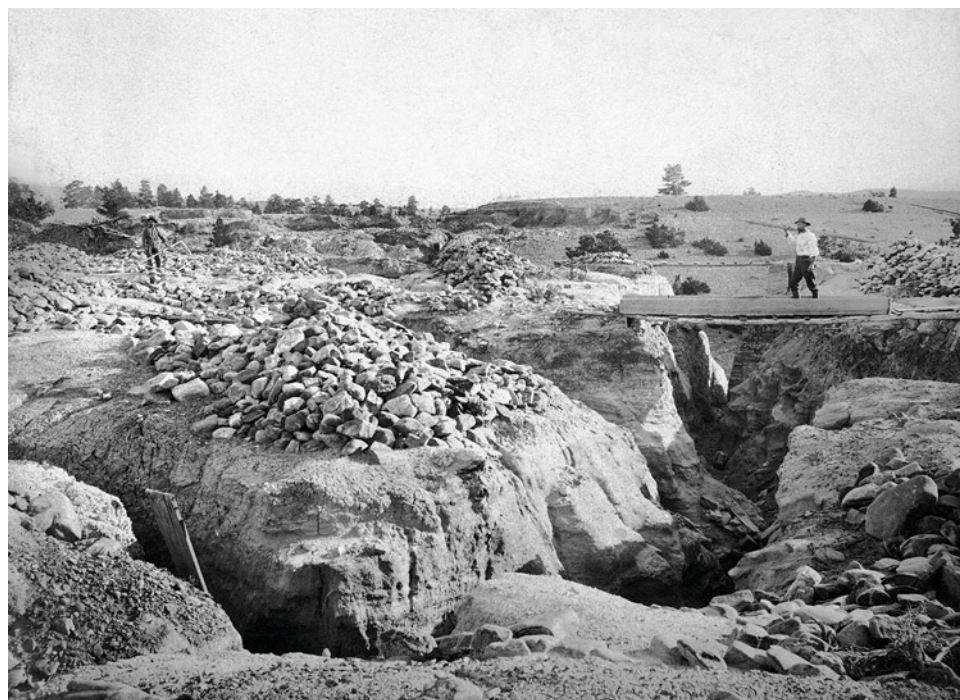
Figure 6. Watch bearings fashioned out of Montana sapphires in various stages of completion. The leftmost pile contains rough sapphires ready for fabrication, and the pile second from the left contains sapphires ground to wafers of standard thickness to be drilled out to produce bearings. The four piles to the right show finished natural sapphire watch bearings. Photo by Robert Weldon; courtesy of the Sapphire Gallery.

be found the next year at Virginia City in Alder Gulch and, importantly, at Last Chance Gulch near Helena.

The first report of sapphire came in 1865, when gold prospector Ed Collins found several while working a gravel deposit along the Missouri River near Helena at what came to be known as Eldorado Bar. The stones were found not in the river itself, but in gravel beds sitting atop bedrock just off the banks of the river, sometimes several hundred meters above water level. Over the years, similar deposits were identified along a roughly 21 km stretch of the Missouri River, with eight major gravel bars eventually worked to some extent. Collins was apparently unsure what to make of the gemmy stones he found, so he sent them east to Tiffany & Co. in New York and other parties overseas ("Eldorado Bar sapphires," 1867). The gems were identified as sapphire, although the discovery generated little attention (Browne, 1868, p. 50). These gravel bars sitting alongside the Missouri River were also rich in gold, so mining activities continued regardless.

The earliest workings on these bars involved horizontal drifts cut through the gravel beds, which allowed miners to avoid the labor of removing the several meters of overburden that typically overlie the sapphire- and gold-bearing gravels (figure 7). Hydraulic mining, which had been used at other gold camps, would have been more efficient. Yet here, as in much of the American West, this advanced mining technique was limited by access to water. Despite their proximity to the Missouri River, the gravel beds were at a higher elevation than the river level, so the water would have to be pumped up to the gravel beds or brought in from elsewhere. The first major mining efforts commenced in 1868, when the Eldorado Ditch Company completed a ditch from Trout Creek, at a higher elevation than the Missouri River, to bring water to the upper terraces of Eldorado Bar (figure 8). This allowed the gravel beds to be worked by hydraulic mining, in which high-pressure jets of water were employed to wash sapphire-bearing gravels into sluice boxes with riffles





*Figure 7. Mining operation at Dana's Bar. The piles of rock are from the trenches below. Photo by Edgar H. Train between 1870 and 1879, Lot 026 B3F15.03 Dana's Bar, Montana Historical Society Photograph Archives.*

set up at intervals to capture sapphire and gold (figure 9). This led to the consolidation of smaller claims on Eldorado Bar, creating larger and more efficient operations. The process of consolidation continued until 1872, when original discoverer Ed Collins joined with seven partners to control a 641 hectare claim encompassing most of the upper terrace of Eldorado Bar.

During a lull in mining in the 1880s, brothers Frank D. and Thomas H. Spratt began buying up and staking new mining claims, especially on Eldorado Bar. In 1887, with the financial backing of a third brother, Augustus N. Spratt, they incorporated the Trout Creek Mining Company and began actively marketing the sapphires on a national and international scale. In 1890, an English syndicate was formed to market Missouri River sapphires. The syndicate ended up purchasing properties on Ruby Bar owned by Frank and Edgar Langdon, as well as properties belonging to the Spratt brothers at French Bar and their Eldorado Bar claims. The English syndicate now controlled most of the profitable workings and was incorporated as the Sapphire and Ruby Company of Montana, Ltd. with initial public stock offerings of 400,000 shares at £1 ("Montana's precious stones," 1891; "Sapphire and Ruby Company prospectus," 1891). Sapphire and gold production commenced swiftly, with drift mining utilized initially and hydraulic mining techniques applied later. The Spratt brothers also incorporated the Spokane Sapphire

Company as a subsidiary of the Sapphire and Ruby Company of Montana, Ltd. to mine Spokane Bar.

Given the worldwide interest being generated about the Missouri River deposit, other mining enterprises came along as well. Notably, Henry Matheson acquired claims on Emerald Bar and brought in water with the use of a steam pump. Matheson soon sold out to a group of investors out of Helena forming the Montana Gold and Gem Company.

Despite the budding success of Missouri River sapphires, which were featured at the 1893 Chicago World's Fair, the economic Panic of 1893 crippled the market for them. This was compounded, in no small part, by the discovery in 1895 of sapphires at Yogo Gulch whose natural cornflower blue color was preferred in the gem market. Shortly thereafter, the Sapphire and Ruby Company of Montana, Ltd. went bankrupt and its properties reverted to Augustus N. Spratt, who reformed his holdings as the Eldorado Gold and Gem Company.

In 1911, the lowest terraces of Eldorado and Spokane Bars were submerged with the completion of the Hauser Dam and the creation of Hauser Lake. While it may seem a pity to flood precious gem-bearing gravels, the advantages of the newly created lake did not go unnoticed. Most notably, in 1938, the Perry-Schroeder Mining Company was formed and purchased a Yuba bucket-line dredge. The Perry-Schroeder Mining Company was one of the few operations allowed to continue mining gold throughout



*Figure 8. The flume taking water from Trout Creek to the sapphire and gold mining operations at the Missouri River. In this view, the flume is crossing Trout Creek itself, with the water taken from further upstream. Photo by W.H. Jackson during the 1869–1871 Hayden Survey. Lot 032 B5F09.03a Trout Creek Flume, Montana Historical Society Photograph Archives.*

World War II despite War Production Board Order L-208, which shut down gold mining operations across the country in order to focus extraction efforts on

strategic materials. The company was only allowed to continue mining gold because it was also producing industrial sapphire, which was in short supply



*Figure 9. Hydraulic mining at French Bar along the Missouri River between 1870 and 1879. PAc 97-32.9, Montana, Montana Historical Society Photograph Archives.*



given that the synthetic sapphire manufacturers were all located in Europe at the time. The Yuba dredge continued mining for gold and sapphires until 1947, marking the end of the historic mining activities on the Missouri River. In the ensuing years, several smaller operations continued to mine for sapphire along the gravel bars of the Missouri River. Their efforts have been fueled by the development of high-temperature heat treatment processes to improve the sapphire colors, making them more desirable in the global gem and jewelry market. Today, the mining is nearly all concentrated on Eldorado Bar, where small-scale miners work some virgin gravels but mostly the tailings left over from the Perry-Schroeder Mining Company in the 1940s. As that dredging operation was also tailored to recover gold, the company's sapphire recovery was fairly low compared to modern operations, and many sapphires were left behind.

Between 1988 and 1993, Sam Speerstra mined six million carats of sapphire from Eldorado Bar (Berg and Landry, 2018). Adjacent to American Gem Corporation's main lease, Gem Resources Management Corporation mined Eldorado Bar from 1988 to 1992. While American Gem Corporation's primary mining activities were focused at Rock Creek (see "Rock Creek" history section below), their press release from September 1994 indicated that consulting geologists and engineers had completed bulk sample testing on 260 of the nearly 1,200 acres (105 of 485 ha) at Eldorado Bar controlled by the company (O'Donoghue, 1995). These tests were conducted to determine occurrence and grades (carats per cubic yard) and indicated considerable sapphire reserves at Eldorado Bar. American Gem Corporation also conducted test sampling across the river channel at Dana's Bar. The company never moved beyond the testing phases, electing instead to concentrate its efforts at Rock Creek and Dry Cottonwood Creek.

Present-day mining includes operations of the Spokane Bar mine and Gold Fever Rock Shop (currently the largest operation), Neal Hurni with Lewis and Clark Sapphires, Blaze Wharton with Blaze-N-Gems, Bruce Scharf and Blue Jewel mine, Don Johnson with Obsessed Over Gems, and Tim Beard along Gruell's Bar. Another notable operation in the recent past is that of Mac Mader, who constructed a suction dredge in use from 1983 to 1986 to recover gold and sapphire from Hauser Lake. In 2012, Mader used a handheld suction dredge operated from a small barge-mounted washing plant on Hauser Lake near French Bar.

**Rock Creek.** The discovery of sapphire in the Rock Creek district is often attributed to one Emil Meyer, a German immigrant who later partnered with Swiss native L.J. Moffat to work the deposit ("Sapphire mined on Rock Creek after 1892 discovery there," 2019). However, some reports attribute the discovery to M.H. Bryan Sr. of Philipsburg, who claimed to have been prospecting for gold on the West Fork of Rock Creek when he noticed several bright stones at the bottom of each pan of dirt. He collected the stones and simply gave the choice gems to his grandchildren to play with. Regardless of who truly discovered the deposit, or whether they found it more or less contemporaneously, the recorded date of discovery is 1892. An article from the September 3, 1892 edition of *The Anaconda Standard* ("New sapphire fields," 1892) indicates that local prospectors were already aware of the rich sapphire diggings and were actively preparing to start working the deposit.

While this deposit is colloquially referred to as "Rock Creek," sapphires have largely been mined from several tributary gulches that cut into the mountain to the north of the West Fork of Rock Creek. The two most important, especially in the early days of mining, were Anaconda Gulch and Sapphire Gulch, but mining has taken place at numerous gulches as well as in placers along the banks of the West Fork of Rock Creek, in an area called the Meadow. Also of particular note for this deposit is the relative lack of gold, especially compared to the Missouri River deposit. What Rock Creek lacks in gold it more than makes up for with an overwhelming abundance of sapphire. Rock Creek has produced more than any other deposit in Montana, including Yogo Gulch, likely eclipsing all of them combined by nearly a factor of 10. All told, at least 70 metric tons of sapphire have been mined from the Rock Creek area (Berg, 2014). However, this estimate does not include the mid-1990s yield of nearly 4 million carats by the American Gem Corporation or significant recent production from Potentate Mining (Kane, 2020). In fact, Rock Creek is the only secondary deposit in Montana to be worked only for its sapphire content (gold is recovered there as well but has never been the primary focus of mining).

The early years saw the deposits worked mostly by smaller operations. Figures of note from the first few years include 400,000 carats of sapphires produced by William Knuth of Helena and William Moffitt of Philipsburg in 1900, of which 25,000 carats were fit for cutting. L.J. Moffat and Emil Meyer were two of the important early miners at Rock Creek. Moffat's Swiss heritage may have helped position



Figure 10. A 1908 map of the mining claims of the American Gem Syndicate at Rock Creek. The various placers are labeled along with water-carrying ditches and streams. Map A-457, Plat of the claims of the American Gem Mining Syndicate, Granite County, 1908, Montana Historical Society Photograph Archives.

these stones in the industrial sapphire market, as most of the production was used by fine watchmakers in Switzerland. Their importance in the early days of mining was recognized with the naming of sapphire-bearing gulches. Meyer Gulch was a productive tributary of Sapphire Gulch, and Moffat has two gulches named in his honor: the Little Moffat and the Big Moffat.

The most important era of overall production at the Rock Creek deposit began in 1901, when articles of incorporation were filed for the American Gem Mining Syndicate, based in St. Louis. The company was incorporated by David Jankower of London and New York; Paul A. Fusz, Moses Rumsey, and Charles D. McLure of St. Louis; L.S. McLure of San Diego; and William Knuth of Helena. The American Gem Mining Syndicate was capitalized with \$300,000, with Jankower holding 299,996 shares and one share each distributed to Fusz, Rumsey, A.B. Ewing, and C. McLure ("Sapphire mined on Rock Creek after 1892 discovery there," 2019). In 1902, the American Gem Mining Syndicate patented claims at the Ruby Placer

in upper Sapphire Gulch, the Star Placer in lower Sapphire Gulch, and the Anaconda Placer in Anaconda Gulch. The company would continue acquiring land and patenting placer claims through 1915 (figure 10).

As with the Missouri River deposit, water has always been the limiting factor in mining operations at Rock Creek. Water flowing through the gulches was insufficient to sustain major mining activity. With the vast capital it raised, the American Gem Mining Syndicate solved this problem at Rock Creek by constructing a series of ditches and flumes. The first was Cralle's Ditch, likely in 1904, which brought water from Stony Lake to the McLure placer at the upper end of Sapphire Gulch, although the water was likely used in Anaconda Gulch as well. In 1912, the Upper Sapphire Ditch was completed, taking water from the North Fork of the West Fork of Rock Creek to the head of North Fork Coal Gulch and the head of Anaconda Gulch. An additional unnamed ditch was also constructed, bringing water from the West Fork of Rock Creek upstream 1,200 m to the west to Sapphire Gulch.



---

The water from these ditches and flumes supported mining activities during the two most productive years of 1906 and 1907, which yielded 6,482.3 kg and 6,639.9 kg of sapphire, respectively. Mining was carried out by either ground sluicing or hydraulic mining. During these years, mining activities were intense and the mine often operated 24 hours a day. From 1903 to 1928, while the American Gem Mining Syndicate was working the deposit, 46.4 metric tons of sapphire were produced (Berg, 2014).

Meanwhile, times were changing with increasing competition from synthetic ruby and sapphire, especially starting in the 1920s. Although Auguste Verneuil grew his first flame-fusion rubies in 1883, the material did not become widely available until the 1910s, when he expanded his enterprise. As more and more flame-fusion ruby and sapphire reached the market, and as the quality of the laboratory-grown material improved, Montana sapphire could not compete. Facing a dire financial situation, the American Gem Mining Syndicate sold most of its claims to Charles Carpp Jr. and J. Walt Kaiser. The two worked the deposit until 1943 and produced about 2.8 metric tons of sapphire, largely through hydraulic mining (Clabaugh, 1952). They apparently intended to sell the sapphires as gemstones but were unsuccessful due to the typically pale colors of the natural rough. Therefore, most of the production still went to the industrial sapphire market.

After Carpp and Kaiser stopped mining in 1943, the Rock Creek properties passed through several hands. Carpp and Kaiser sold to Sally and Bill Eaton, who operated a fee dig for tourists. The Eatons in 1966 sold the Meadow property along the West Fork of Rock Creek to Marc Bielenberg and the gulch properties to Wilfred Chaussee, who formed the Chaussee Sapphire Corporation and continued running the tourist operation. This operation was later passed to Wilfred's daughter and son-in-law, Yvette and Kenneth Clevish. The Clevishes sold in 1980 for \$1 million to Ted Smith, who renamed the operation the Gem Mountain Sapphire Corporation. In the meantime, Marc Bielenberg sold the Meadow property in 1978 to Skalkaho Grazing, Inc., which constructed a floating wash plant in 1982 near the confluence of the Anaconda and Coal gulches with the West Fork of Rock Creek.

Still, mining activities during this period never approached the production by the American Gem Mining Syndicate in the early twentieth century. However, another technological advance on the horizon would change the fate of Rock Creek sapphire.

In the 1970s, the Thai gem trade developed and perfected high-temperature heat treatment procedures to dramatically improve the color and clarity of pale and milky sapphires, creating deep, rich blue sapphires. The original material used was the milky *geuda* sapphire from Sri Lanka, but it was soon realized that the same heat treatment method could be applied to secondary Montana sapphire with outstanding results. In the early 1980s, a Mr. McCarthy of Helena was reportedly the first person in Montana to use this high-temperature heat treatment to improve the color of a Montana sapphire; however, the process was perfected in a technical sense in the 1990s and scrupulously detailed in the work of Emmett and Douthit (1993).

With the ability to transform color through heat treatment, the economics of mining and marketing Montana sapphire changed for the better. In 1994, a new player entered the scene when American Gem Corporation purchased much of the gem-producing areas of the Rock Creek district, including the Dann Placer and Anaconda Bench as well as the holdings of the Gem Mountain Sapphire Corporation. All told, American Gem Corporation reported production of more than four million carats of gem-quality rough sapphire, of which more than two million heat-treated faceted sapphires to date have been sold into the international market (Kane, 2020). While American Gem Corporation, a public company listed on the Toronto Stock Exchange, carried out a high-profile marketing campaign, their efforts never materialized into a steady supply of gems, and the company reorganized as an e-commerce entity in 1999. At this point, Chris Cooney purchased their claims at the Anaconda and North Fork Coal gulches, where he now operates a mining and fee-dig tourism operation called Gem Mountain. At the same time, logging company RY Timber acquired the rest of the patented claims in the Rock Creek deposit.

The next chapter in the Rock Creek story is being written by Potentate Mining. In 2011, Potentate purchased Eureka Gulch on the north side of the mountain and became the largest landholder on Gem Mountain in 2014 after purchasing most of the south side of the mountain from RY Timber. Over the years, Potentate has actively developed its claims and now operates a modern operation utilizing state-of-the-art mining technologies to produce sapphire in an environmentally friendly manner while making efficient use of limited water resources. Among the advances implemented are a new gravel-processing facility with a separate gold circuit to maximize gold

---

recovery, as well as a water clarifier to ensure the return of clean water to the pristine mountain streams. In 2020, Potentate finalized the purchase of the Meadow property and now controls the bulk of the sapphire-bearing areas of the Rock Creek deposit. Potentate is pursuing an aggressive marketing campaign to put Montana sapphire in a prominent place in the world market.

**Dry Cottonwood Creek.** Sapphires were first found by gold prospectors in the South Fork of Dry Cottonwood Creek near the city of Butte in 1889 (Kunz, 1894). Mining commenced shortly thereafter by the Northwest Sapphire Company of Butte, which employed hydraulic mining as well as dredging operations at the South Fork of Dry Cottonwood Creek (Struthers and Fisher, 1903). One of the more significant mining enterprises involved the Variegated Sapphire Company, which in 1905 installed a bucket-line dredge at the Grand Pre Flats, an open area along the South Fork of Dry Cottonwood Creek. The dredge worked an area 24–30 m wide, removing 12 m of gravel per day and recovering both gold and sapphire. In 1907, ownership of the enterprise transferred to Mr. West Dodd of Des Moines, but this operation ended by 1911, only to be briefly revived in 1914 by Nat Simon. However, Simon abandoned it after one season of low gold yield and sapphires that were pale and not marketable. In 1908, the Consolidated Gold and Sapphire Mining Company of Butte installed another dredging operation about 1.5 km from the Grand Pre Flats, downstream from the South Fork of Dry Cottonwood Creek. This effort was short-lived as well due to the low concentration of gold and the difficulty of selling the sapphires in the gem and jewelry industry.

Interest in the Dry Cottonwood Creek deposit revived during World War II due to the shortage of industrial laboratory-grown sapphire coming from Europe, but there was no production in those years. Significant mining did not resume until the 1990s, when American Gem Corporation acquired claims here and at Rock Creek and Missouri River. American Gem Corporation purchased land in 1993 from Scott Wurster, who had in turn acquired it from Marc Bielenberg, who had previously owned claims in the Rock Creek district. The advent of high-temperature heat treatment made Montana sapphire much more attractive to the gem and jewelry industry with the rich vivid blue and fancy-color gems that could be produced. In 1995, American Gem Corporation mined 400,000 carats of sapphire from Dry Cotton-

wood Creek (Kane, 2020). However, the Dry Cottonwood Creek sapphires did not react as well to heat treatment as those from Rock Creek (J.L. Emmett, pers. comm., 2022), and American Gem Corporation abandoned operations there in 1996 to focus on Rock Creek. In the same year, Gem River Corporation began mining sapphires in the Grand Pre Flats, but mining stopped in 1998 and the area was reclaimed for nature. No serious mining efforts have taken place at Dry Cottonwood Creek since then. However, the Dry Cottonwood Creek sapphires do react well to heat treatment in an oxidizing environment to produce variegated yellow and orange colors (R.E. Kane, pers. comm., 2022). With changing market behavior and growing interest in such fancy-color sapphires, Dry Cottonwood Creek has the potential to become a viable mining property.

## CHARACTERISTICS OF THE DEPOSITS

**Geology.** The rugged terrain and landscapes of western Montana are the product of both ancient and modern geological forces at work. The very oldest rocks encountered in the sapphire-producing areas belong to the Proterozoic Belt supergroup, which forms the bedrock underlying much of the Missouri River and Rock Creek deposits and also represents much of the Belt Mountains seen to the east of the Missouri River deposits. The Belt supergroup includes metasedimentary rocks deposited between 1470 to 1370 Ma in a sedimentary basin formed at the margin of the North American Craton and some other unknown ancient landmass. The Belt supergroup, an accumulation of sediments an astonishing 15 km thick at its maximum extent, provides many clues to the ancient movement of the earth's protocontinents. But these primeval geological formations serve as nothing more than the backdrop of the gemological story. At the Missouri River, these ancient formations are simply the bedrock upon which the sapphire-bearing gravels were deposited. The Proterozoic Belt supergroup formation here is in the form of an argillite, a low-grade metamorphosed version of a sedimentary shale or claystone. At Rock Creek, the Belt supergroup rocks include metasedimentary rocks that underlie Cenozoic volcanic formations, which are apparently related to the gem deposits.

The story of sapphire formation begins much later in the earth's history, during the Cenozoic era. While the sapphires occur in secondary deposits, field observations indicate in each case that the original host rock is most likely related to Cenozoic volcanic for-



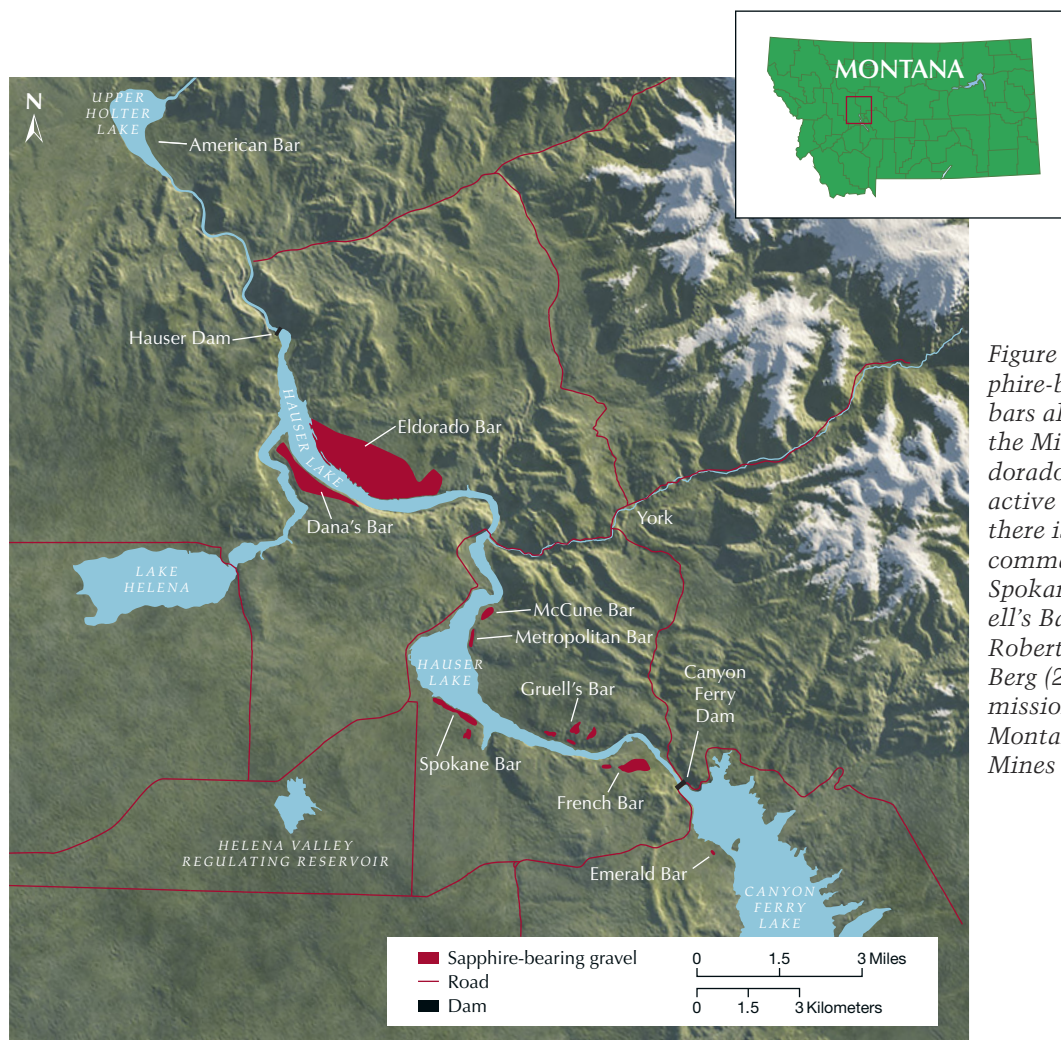


Figure 11. Map of sapphire-bearing gravel bars along the banks of the Missouri River. Eldorado Bar is the main active mining site, but there is also small-scale commercial mining at Spokane Bar and Gruell's Bar. Modified by Robert E. Kane from Berg (2015), with permission; courtesy of the Montana Bureau of Mines and Geology.

mations erupted around 50 Ma. From about 160 to 50 Ma, the entire western seaboard of North America was a convergent margin, with the ancient Farallon plate being subducted beneath the North American continent. Subduction of the Farallon plate led to significant volcanism throughout the western United States, Canada, and Mexico. The volcanic formations in the region of the sapphire deposits are related to the late stages of this period, when a flat-lying Farallon slab started to roll back and eventually detach as it continued its descent into the earth's mantle. As the sapphire-bearing volcanic formations were weathered and broken down, the sapphires were liberated and entrained in the rich gem gravels being mined to this day. The following sections will briefly describe the relevant formations in each deposit.

*Missouri River Geology.* There is very little geological context remaining to explain the deposits at Missouri River, where sapphires are recovered from gravel beds sitting atop bedrock terraces above water level (figure

11). The sapphire-bearing gravel beds are composed predominantly of locally sourced material. This means there are limited options to consider for potential bedrock sources of the sapphire. Further complicating matters is that the Missouri River here has been flooded by the construction of the Hauser Dam and subsequent creation of Hauser Lake, limiting potential exposures of sapphire-bearing lithologies. The Proterozoic Belt supergroup argillites immediately underlying the gravel beds are not suitable lithologies for corundum formation, and the same is true for the Paleozoic and Proterozoic metasedimentary rocks of the nearby Big Belt Mountains and the Paleozoic sedimentary rocks in the Spokane Hills.

What little evidence we have comes from one small sapphire-bearing sill found at French Bar.<sup>1</sup>

<sup>1</sup>Note that while sapphire-bearing sills have been reported at both French Bar and Ruby Bar, Berg and Landry (2018) pointed out that historical analysis proved these two bars are the same, and thus it is likely that only one sapphire-bearing sill has been discovered.

Based on chemical analysis and petrographic observations of thin sections of the volcanic rock, Berg and Palke (2016) described it as a basaltic trachyandesite composed of biotite and augite phenocrysts in a matrix of plagioclase microlites. Rare corundum-bearing xenoliths have been found composed of calcic plagioclase, augite, garnet, margarite, and spinel (Berg and Dahy, 2002).

Importantly, Berg and Palke (2016) used LA-ICP-MS to analyze the chemistry of sapphires found *in situ* in this (sub)volcanic formation, and the results demonstrated that their trace element profiles are consistent with the gem sapphires found in the gravel beds. This indicates that these volcanic formations are viable sources of the Missouri River sapphires. While this single volcanic formation is surely too small and has too low a sapphire concentration to have supplied gems for the entire Missouri River deposit, it suggests a likely geological origin of the sapphires, with the implication that other similar sapphire-bearing (sub)volcanic formations must have been present but were weathered away almost en-

tirely. Additionally, many sapphires from the Missouri River are found with thin encrustations of spinel adhering to their surface. This spinel is inferred to result from a reaction between the corundum and magnesium and iron sourced from mafic magmas that transported the sapphires to the surface. This spinel rim is not found on sapphires from Rock Creek or Dry Cottonwood Creek and is not even found on all Missouri River sapphires.

*Rock Creek Geology.* In the Rock Creek area, sapphires are found in gravel beds in gulches cutting into Gem Mountain (figure 12). The dominant formations in the area are rhyolitic lava flows, dikes, and tuffaceous and volcanoclastic formations that overlie metasedimentary rocks of the Proterozoic Belt supergroup. Given that sapphires are found in the gulches cutting up into the mountain, their source must have been local. The volcanic formations here are relatively silica-rich and rhyolitic in composition. Rhyolite lava flows cap the ridges separating the sapphire-rich gulches, while the more readily eroded



Figure 12. Map of sapphire-bearing gulches and placer deposits at Rock Creek. Modified from Berg (2014).



tuffs and volcanoclastic units are less well preserved. No other volcanic formations have been identified in the immediate area, although it has been postulated that there may be hidden plugs of lamprophyres or other mafic volcanics in the area that have supplied the sapphires (Barron and Boyd, 2015). Notably, Berg (2014) did identify a basaltic dike exposed along a road cut 4 km east of Sapphire Gulch. No sapphires have been found in this dike, but to the authors' knowledge it has never been studied thoroughly. Still, this basaltic dike is likely too small and too far from the deposit to be a viable source of the sapphires. While no sapphires have been found *in situ* in any volcanic rocks here, Berg (2014) did identify some with what was described as a "rhyolitic" encrustation. This encrustation was observed on another sapphire by Belley (2022), with scanning electron microscopy (SEM) images confirming that the adhering crust was composed of quartz, plagioclase, and potassium feldspar. Importantly, Rock Creek sapphires are never found with the spinel encrustation found on some Missouri River sapphires, which is likely formed by interaction with magnesium and iron in the mafic transporting magma at Missouri River. This observation seems to suggest a mafic source is less likely at Rock Creek. With the enormous volume of sapphire produced at Rock Creek, the original source rock must have been extensive, decreasing the likelihood of a hidden source that was weathered away. Given the prevalence of rhyolitic volcanics in the area, the evidence suggests that rhyolitic volcanism is a likely source of the sapphires in this deposit.

*Dry Cottonwood Creek Geology.* Sapphires at Dry Cottonwood Creek are found in gravels and secondary deposits. Bedrock is composed of volcanic formations from the Eocene-age Lowland Creek Volcanics. These overlie Cretaceous granitic rocks of the Boulder Batholith, which contacts the Lowland Creek Volcanics near the western boundary of the Grand Pre Flats on the South Fork of Dry Cottonwood Creek. The Lowland Creek Volcanics are predominantly composed of welded tuffs and lava flows of dacitic composition. No other volcanics or other geological formations exist in the immediate area. While no thorough field studies have been performed to identify the source of the sapphires, the Lowland Creek Volcanics seem to be a likely original bedrock source, given the likely volcanic origin of all Montana sapphire and the paucity of other possible sources.

**Origin of the Secondary Montana Sapphires.** Given the relative lack of hard rock geological evidence in these secondary deposits, one must search elsewhere for clues about the ultimate origin of these sapphires. In fact, while the original sapphire-bearing host rocks have mostly weathered away, remnants of the ancient sapphire-producing geological environments have been preserved within the sapphires as inclusions. Besides hexagonal bands of silk and rutile particles, among the most commonly encountered inclusions are fluid inclusions of an unusual nature. These often have the appearance of typical two-phase fluid inclusions seen in other gems. However, if one were to cut into one of these fluid inclusions, the fluid material would be frozen in place and not leak out of the sapphire as expected. These fluid inclusions represent blebs of magma and indicate that the fluid present during sapphire growth was a molten silicate rock. Upon transport to the surface in volcanic events, the sapphires must have cooled quickly enough to quench these melts into glasses.

The compositions of the melt inclusions are broadly similar across the three deposits, suggesting similar conditions of geological formation. The melts coexisting during sapphire growth were poor in MgO and FeO, moderately enriched in Na<sub>2</sub>O, K<sub>2</sub>O, and CaO, and (surprisingly) relatively rich in SiO<sub>2</sub>. The melts can be classified as dacites or rhyolites according to the total alkali silica (TAS) diagram of Le Bas et al. (1986). Of particular note is that these melts are all quartz-normative, meaning that if cooled in an isolated system, they should have precipitated quartz. This seems counterintuitive at first, as it is well known that corundum and quartz cannot coexist under ordinary geological conditions. However, it is possible for corundum to coexist with a quartz-normative melt in the case of an incongruent (or peritectic) melting reaction. The presence of quartz-normative melts then suggests a genetic model in which the secondary Montana sapphires grew through partial melting of some aluminum-rich rock (e.g., an anorthosite or some similar plagioclase-rich igneous rock). In this model, the magmas that transported the sapphires to the surface in volcanic events might have also been responsible for sapphire formation by initiating partial melting of the proposed aluminum-rich protoliths. In this scenario, the sapphires could still be foreign to the transporting magmas but would not be *accidental* xenocrysts. In fact, based on observations of rhyolitic secondary melt inclusions, Palke et al. (2017) suggested the possibility that some sapphires at Rock Creek may

not be xenocrysts at all if the partial melting event that produced the rhyolites seen at the surface also produced the sapphires entrained in this magma. Of course, proving or disproving this hypothesis would be challenging. At Missouri River, the basaltic trachyandesite magma that likely transported some of the sapphires is significantly different from the melt inclusions seen in those stones, confirming their identity as xenocrysts. The Lowland Creek Volcanics at Dry Cottonwood Creek have not been thoroughly studied, and their relation to the melt inclusions seen in those sapphires is less clear.

The sapphires' origin from some calcium- and aluminum-rich protolith such as an anorthosite is also supported by the prevalence of calcium- and aluminum-rich mineral inclusions such as anorthite-rich feldspar and (clino)zoisite. Other genetic models have been proposed, mostly based on the use of trace element chemistry wherein the low gallium and other trace element patterns were thought to suggest a metasomatic or metamorphic origin for the sapphires (Garland, 1992; Zwaan et al., 2015). Such an origin, however, seems to be contradicted by the pervasiveness of silicate melt inclusions, which indicate that the sapphires grew in the presence of a silicate magma.

## GEMOLOGICAL CHARACTERISTICS OF SECONDARY MONTANA SAPPHIRE

**Physical Properties.** Sapphires from Montana's secondary deposits yield some unique characteristics that make them distinct from other sapphires around the world. While basic physical properties such as refractive index and specific gravity offer no significant differences, the inclusion suite and trace element chemistry can help to distinguish secondary Montana sapphire. However, it should be noted that the characteristics of individual faceted sapphires from Montana's secondary deposits overlap significantly, and these gems cannot currently be reliably separated from each other.

In general, sapphires from Montana's secondary sources naturally occur in a wide range of hues, including blue, green, yellow, orange, pink, and purple (figures 13–19). Most of these colors are somewhat pale, especially when unheated (figures 13 and 14). Vibrant, saturated colors do occasionally occur naturally, but they are more common in heated stones (figures 15–17). Montana sapphire has become increasingly popular in nonstandard cutting styles (figures 18–19). Parti-colored sapphires are frequently

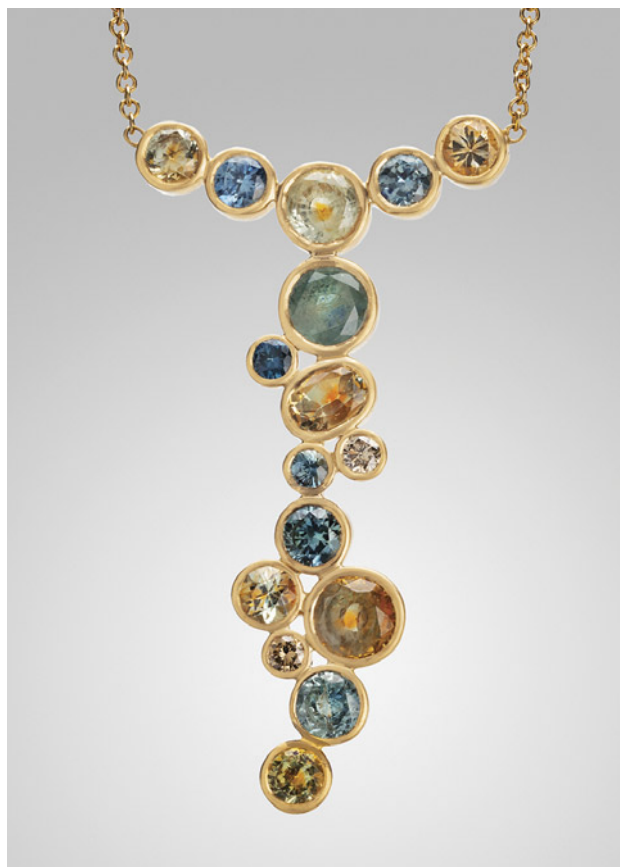


Figure 13. Faceted unheated Montana sapphires set in 18K gold. Photo by Orasa Weldon; courtesy of Diana Widman.

observed, especially for heated stones with a yellow or orange core and a blue, green, pink, or violet rim

Figure 14. This “Twilight” ring showcases some of the common range of colors seen in Montana sapphire. The sapphires are unheated, with 3.80 total carat weight. Photo courtesy of Earth's Treasury.







Figure 15. The “Conchita Sapphire Butterfly,” a collaboration between gem dealer/gemologist Robert Kane and jewelry designer Paula Crevoshay, highlights the variety and color range of heat-treated secondary sapphires from Montana. The 18K yellow gold butterfly is set with 331 round brilliant sapphires and two cabochon-cut sapphires, totaling 27.97 carats. The butterfly was donated by Kane and Crevoshay to the Smithsonian Institution’s National Gem Collection in 2007. Photo by Harold and Erica Van Pelt; courtesy of Robert E. Kane.

(figure 20). Some sapphires exhibit a weak to moderate color change when observed in incandescent to daylight illumination (figure 21). Colors generally change from shades of pink or orange (incandescent) to green or violet (daylight). Rubies are also sometimes found (figure 22). Palke and Hapeman (2019) reported only 29 g of rough ruby crystals recovered from more than 400 kg of mine production at Potentate’s operation at Rock Creek. While truly red gem corundum from Montana’s secondary sapphire deposits are rare, examination of the collection of

Robert Kane (Fine Gems International, Helena) uncovered numerous examples of rubies from color-graded parcels of pink sapphire. While rare, these Montana rubies do exist and may be encountered in the market. Other examples of Montana ruby are known, including one particularly large faceted gem weighing 1.70 ct (Malaquias, 2018).

Sapphire rough from these deposits generally occurs as small crystals measuring a few millimeters in diameter, but larger stones have been found. Notably, the unheated blue sapphire known as the “Big Sky” sap-

Figure 16. A suite of heated Montana sapphires, 0.76–1.04 ct, displaying a range of colors. Courtesy of Rachel Hill, Americut Gems.





Figure 17. Various colors of heated Missouri River sapphire, ranging from 0.16 to 1.65 ct. Photo by Tino Hammid; courtesy of Fine Gems International and American Sapphire Company, © Robert E. Kane.

phire, which sold in 2015 for \$394,000, weighed 12.54 ct (Kane, 2020). Rough crystals as large as 37.78 ct have been reported from Eldorado Bar (Berg and Landry, 2018), while the Rock Creek deposit has produced stones as large as the faceted 12.62 ct heated stone recovered by Potentate Mining known as the “Montana Queen” (@potentateminig, May 27, 2019). Potentate

also recovered a large crystal from Rock Creek in 2018 weighing 64.14 ct, known as the “Ponderosa” sapphire, as well as a 67.15 ct yellow sapphire recovered in 2021 that cut a 12.18 ct stone called the Yellowstone sapphire. This is currently part of the Somewhere in the Rainbow collection (again, see figure 1). Rock Creek also produced a notable 39.14 ct stone in 2008 that was





Figure 18. With their nonstandard colors, Montana sapphires have become popular for cutters experimenting with nontraditional cutting techniques. This 4.17 ct unheated sapphire cut by Nadine Marshall was sourced from the Missouri River. Courtesy of Obsessed Over Gems.

recovered from the Anaconda Bench at Gem Mountain (Berg, 2014). The largest crystal reported from Dry Cottonwood Creek weighed 22 ct but had a flat shape and therefore a low yield when cut into a gem (Berg, 2007). While small stones under a carat are the main production from Rock Creek, figure 1 shows a suite of the

finest and largest sapphires produced by Potentate during the 2021 mining season in their rough and polished states.

*Optical Measurements and Specific Gravity.* Standard gemological testing of Montana sapphire reveals

Figure 19. Montana sapphires in a range of shapes and colors. All are heated, and the faceted stones range from about 0.20 ct for the 3 × 5 mm kite shapes on the left to 2.11 ct for the hexagon on the right. Photo by Dillon Sprague; courtesy of Columbia Gem House.





Figure 20. Parti-colored sapphires are occasionally found in Montana and can combine a wide range of colors. These examples, ranging from 1.62 to 3.20 ct, are all heated. Photo by Jeffrey R. Hapeman.



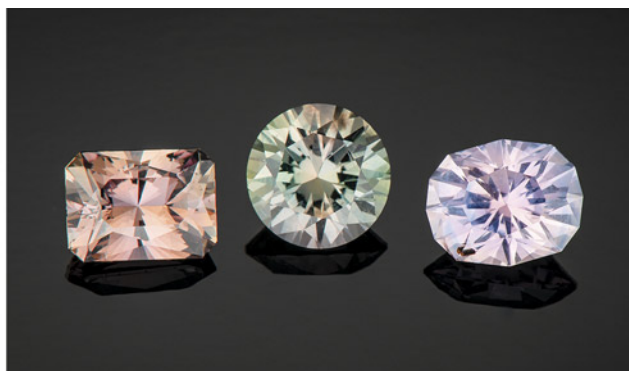
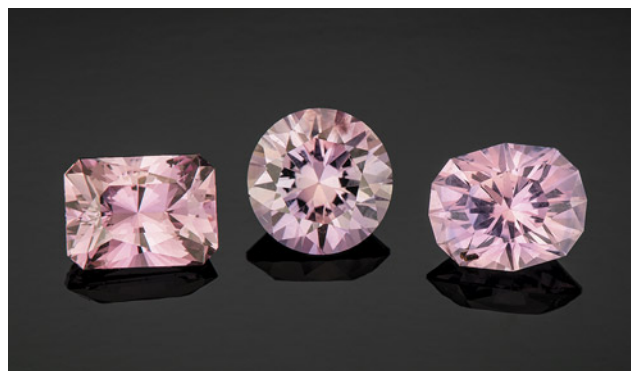
Figure 22. A suite of nine unheated rubies from the Rock Creek deposit ranging from 0.17 to 0.58 ct. Photo by Kevin Schumacher; courtesy of Jeffrey R. Hapeman, Earth's Treasury, Inc.

properties one would expect for corundum. The average refractive index measured is 1.760–1.770, and the birefringence typically ranges from 0.008 to 0.010. The specific gravity ranges from 3.98 to 4.01, also consistent with corundum.

FTIR spectra of Montana sapphire can show a variety of features (figure 23). Commonly seen is a weak single peak at  $3309\text{ cm}^{-1}$ . This peak is believed to be related to hydrogen in the corundum structure associated with titanium substituting for aluminum (Moon and Phillips, 1991). Also common in secondary Montana sapphire is a peak at about  $3220\text{ cm}^{-1}$ . A similar peak is often seen in Yogo sapphire as well (Renfro et al., 2018), but its origin is unknown. Finally, many Montana sapphires show the collection of broad ab-

sorption bands centered around  $3000\text{ cm}^{-1}$  that is often referred to as the “Punsiri peaks” but will be referred to here as the acceptor-dominated  $3000\text{ cm}^{-1}$  series, given that these peaks are related to hydrogen associated with acceptor ions, in this case  $\text{Mg}^{2+}$ , in the corundum (Fukatsu et al., 2003; Sangsawong et al., 2016). The acceptor-dominated  $3000\text{ cm}^{-1}$  series is not an indicator of heat treatment for Montana sapphire, as these peaks sometimes occur naturally. In fact, this series of peaks is very common in unheated Rock Creek sapphire but only occasionally found in Dry Cottonwood Creek sapphire and almost never in Missouri River sapphire. The commercial importance of this finding will be discussed later in the section dealing with heat treatment. The peak at

Figure 21. Some secondary Montana sapphires exhibit a color change between incandescent illumination (left) and daylight (right). These examples are unheated and range from 0.74 to 0.83 ct. Photos by Robert Weldon; courtesy of Jeffrey R. Hapeman, Earth's Treasury, Inc.





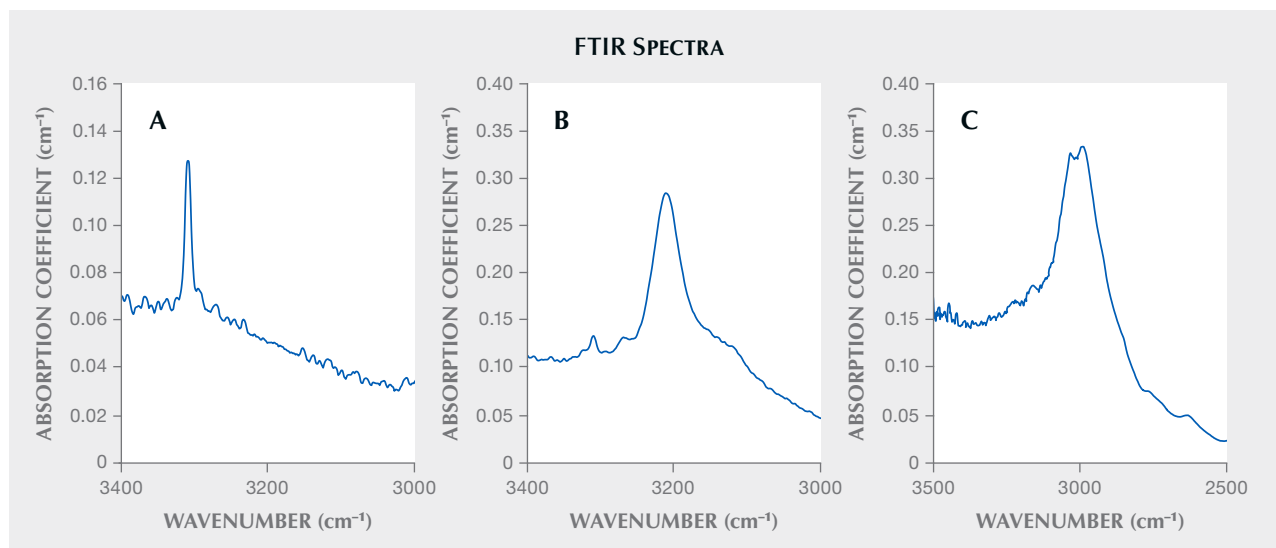


Figure 23. Representative FTIR spectra showing expected features for Montana sapphire, including a single  $3309\text{ cm}^{-1}$  peak (A), a  $3220\text{ cm}^{-1}$  peak (B), and the acceptor-dominated  $3000\text{ cm}^{-1}$  series (known as the “Punsiri peaks,” C).

$3220\text{ cm}^{-1}$  can be used as an indicator of a secondary Montana or primary Yogo origin, but the other FTIR features such as the  $3309\text{ cm}^{-1}$  peak and the acceptor-dominated  $3000\text{ cm}^{-1}$  series of peaks are observed in sapphires from many other origins. Montana sapphire from all the secondary deposits may also show mineral inclusion peaks in their FTIR spectra, especially for kaolinite or gibbsite.

*Shape of Rough Crystals/Morphology.* The sapphire from Montana's secondary deposits is generally tabular or blocky in shape and can also appear somewhat

less commonly as hexagonal prisms. The rough stones also tend to show a rounded appearance, which might cause one to suspect they have been subjected to rounding by abrasion from water transport. However, close examination with a microscope often reveals pronounced geometric patterns on the surface with either the hillocky-type texture seen at Rock Creek or dissolution-type etch features (figures 24–26). In fact, the sapphire morphology from the three deposits generally differs enough to allow identification of the origin of parcels of rough sapphires, even if individual stones cannot be traced back to their source. For in-

Figure 24. SEM image showing the surface of a Rock Creek sapphire. The hillocks on the surface are typical of Rock Creek sapphire. Image by Richard Berg (modified from Berg, 2022).

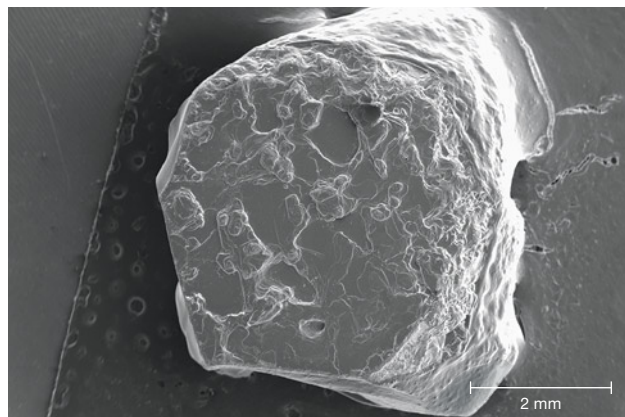
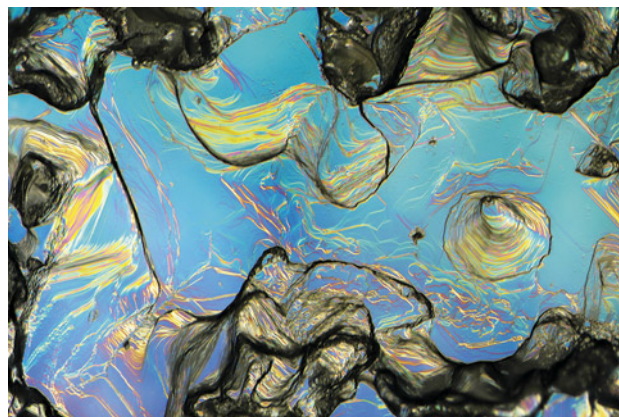


Figure 25. Hillocky structure on the surface of a rough sapphire from Rock Creek shown with differential interference contrast imaging. Photomicrograph by Aaron Palke; field of view 2.88 mm.



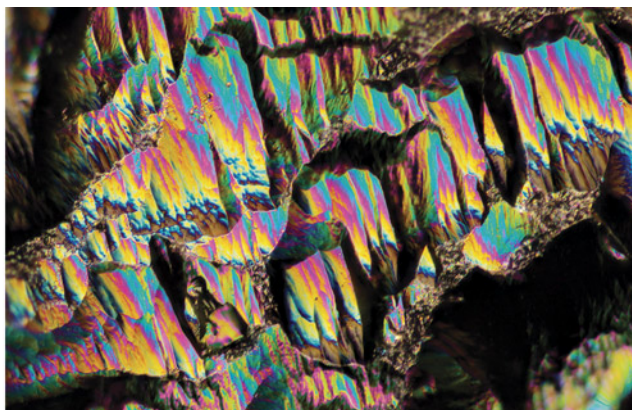
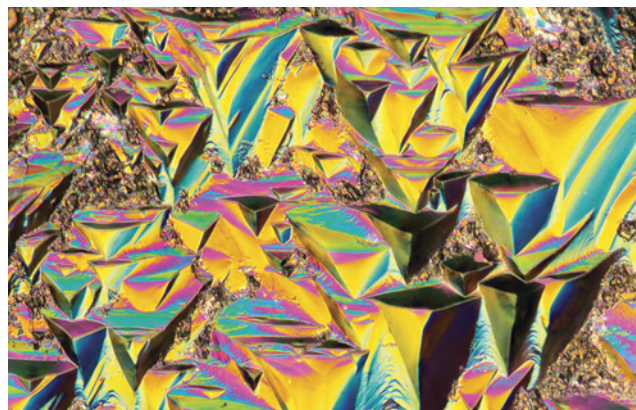


Figure 26. Differential interference contrast imaging of the surface of a rough sapphire from Dry Cottonwood Creek showing etch features on the basal pinacoid surface (left, perpendicular to the c-axis) and on the prismatic crystal face (right, parallel to the c-axis). Photomicrographs by Aaron Palke; field of view 0.72 mm.

stance, some 25% of sapphires from Missouri River have an incomplete or spotty dark green coating of spinel in depressions on the surface, as seen in the SEM image in figure 27. This feature is not seen in sapphire from Rock Creek or Dry Cottonwood Creek. Dry Cottonwood Creek sapphire shows etching along twinning planes as seen in figure 28, which is less common in Rock Creek and Missouri River sapphire. Finally, Rock Creek sapphire often has growth hillocks on the basal surface, some with flat surfaces resembling miniature mesas (figure 24). Examples of rough from each deposit are shown in figure 29.

Figure 27. SEM image of the surface of a sapphire from Missouri River showing the spinel coating sometimes seen in stones from this deposit but never in sapphire from Rock Creek or Dry Cottonwood Creek. Image by Richard Berg.

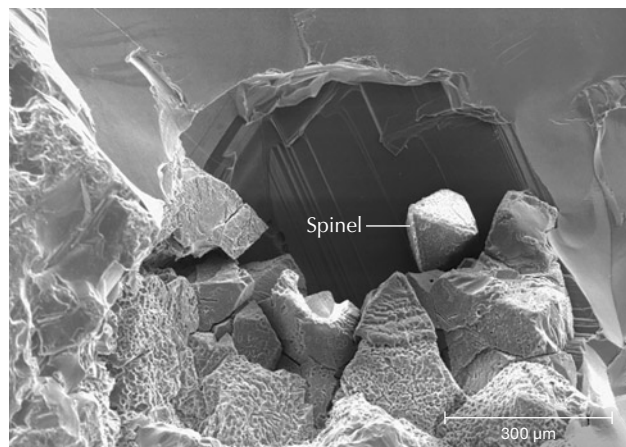
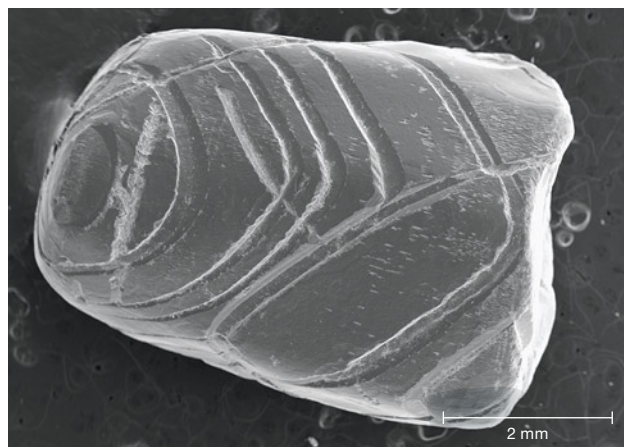


Figure 30 shows typical shapes for the crystals found at all three locations. The two most commonly encountered shapes are hexagonal prismatic crystals with slightly developed rhombohedral faces (figure 30, A and B). Many show development of the hexagonal bipyramidal faces as well (figure 30, A and C). Crystals typically exhibit six-fold or three-fold symmetry on the basal pinacoid; figure 30B shows a classic raised trigonal pyramid on the basal pinacoid. There are slight variations between the three deposits in the prevalence of the various crystal shapes. For example, the majority of the crystals from Dry

Figure 28. As seen in this SEM image, sapphires from Dry Cottonwood Creek are often dissolved or etched along parallel grooves following twin planes. Image by Richard Berg (modified from Berg, 2022).





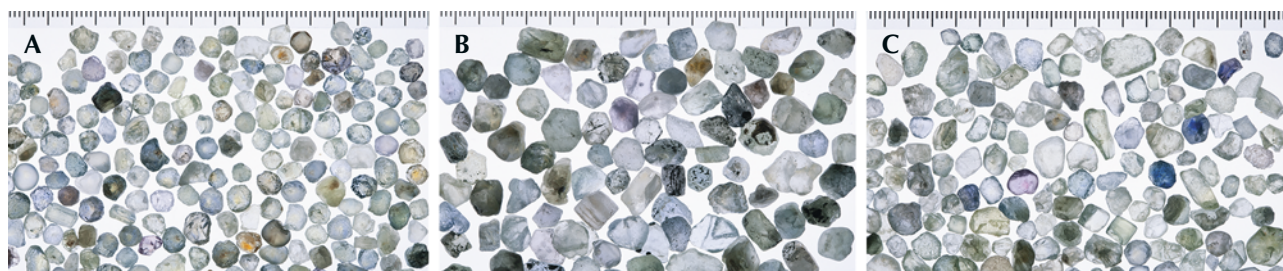


Figure 29. Photos of representative lots of unheated rough from each of Montana's secondary sapphire deposits: Rock Creek (A), Missouri River (B), and Dry Cottonwood Creek (C). The ruler in each photo is in millimeter scale. Photos by John Emmett.

Cottonwood Creek are tabular hexagonal crystals (figure 30C), while elongated hexagonal prisms (figure 30D) are particularly common at Missouri River. At Rock Creek, most of the crystals have been so heavily etched/resorbed that most of their crystal faces are obscured, although color zoning and the patterns of rutile inclusions follow these crystal faces

and can reveal the structure even in heavily etched crystals. Despite this variation at each locality, crystals of all of these shapes can be found at any of the deposits.

**Microscopic Features.** Secondary sapphires from Montana contain a wide array of inclusions, and these are a powerful tool in confirming a Montana origin. In natural, unheated Montana sapphire, the most common features are bands of rutile silk, often arranged in hexagonal patterns, either as dense hexagonal clouds (figure 31, A and B) or in a loosely packed but overall hexagonal pattern (figure 31, C and D). The individual particles making up the clouds may be relatively long,

Figure 30. Typical shapes seen in rough Montana sapphires. Crystal forms include pinacoidal faces (pc), prismatic faces (p), rhombohedral faces (r), and pyramidal faces (py). Most common shapes are prismatic crystals modified by pyramidal and/or rhombohedral faces (A and B); flattened, tabular hexagonal crystals terminated by rhombohedral, pyramidal, and pinacoidal faces (C); and elongate prismatic crystals (D).

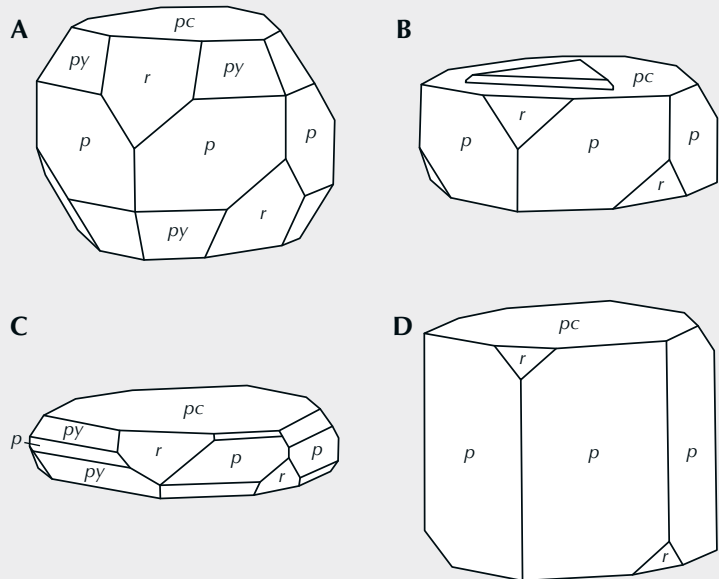
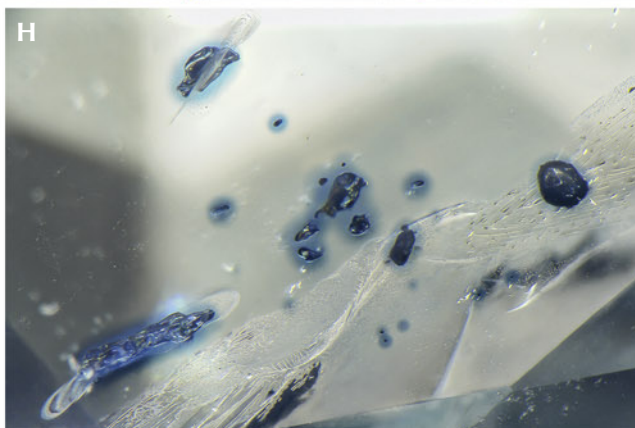
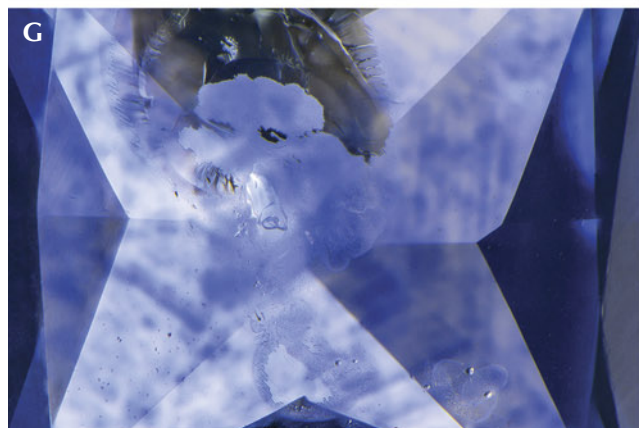
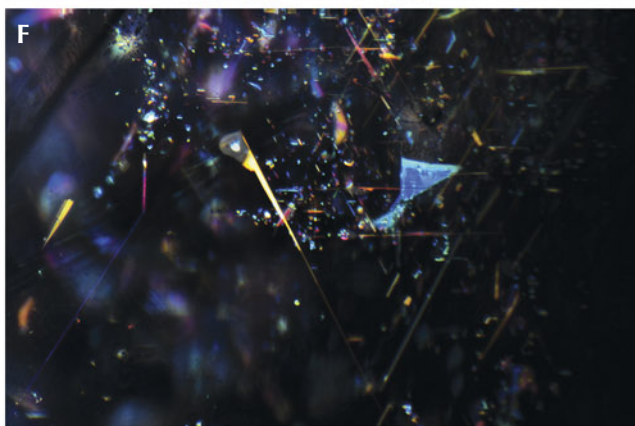
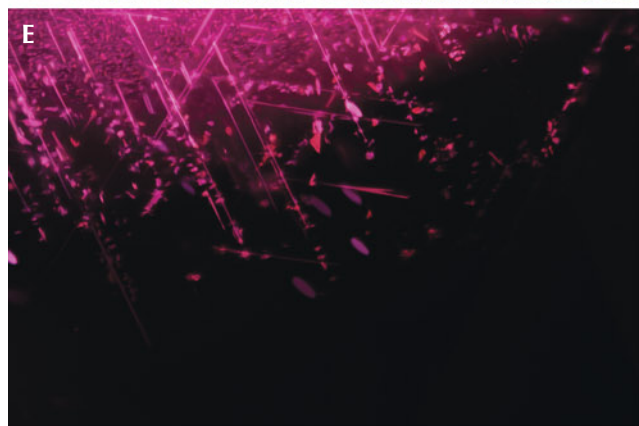
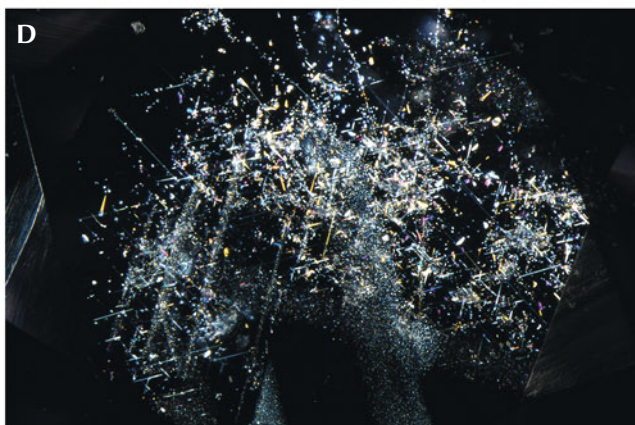
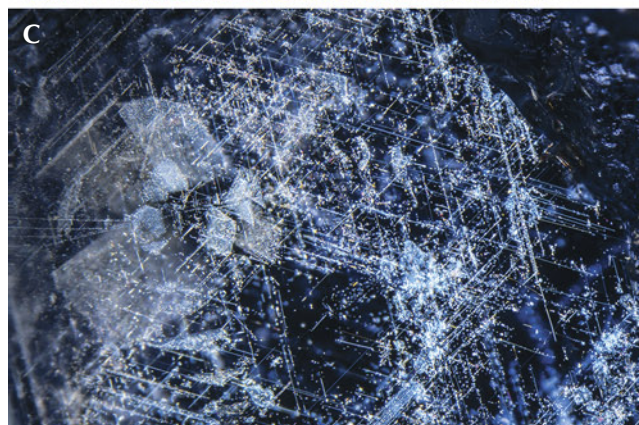
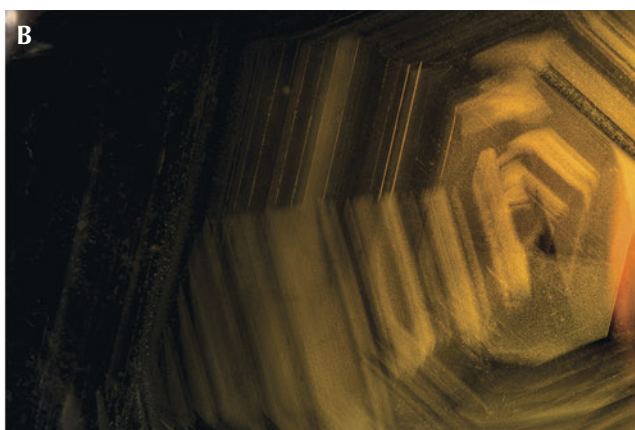
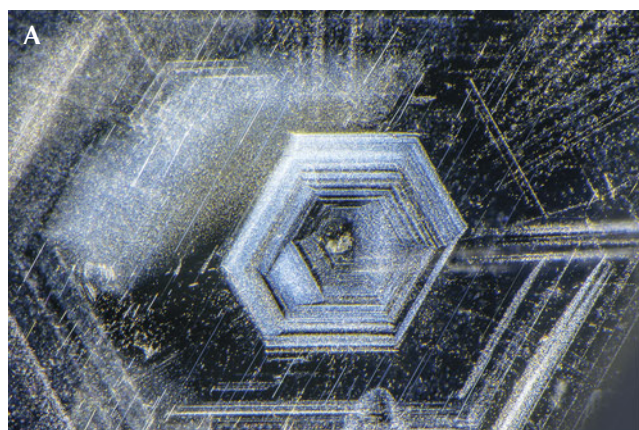


Figure 31 (opposite page). Typical inclusion scenes in unheated (A–F) and heated (G and H) secondary Montana sapphires. A: Dense, hexagonal particulate clouds in a Missouri River sapphire. B: Hexagonal particulate clouds made up of small to medium-sized rutile needles in an unheated orange sapphire from Rock Creek. C: More loosely packed hexagonally arranged silk in an unheated sapphire from Rock Creek. D: Fiber-optic illumination reveals interference colors from flattened silk particles in this Rock Creek sapphire. E: The rare rubies occasionally found in Montana have essentially the same inclusions as the sapphires, such as the flattened rutile silk in this Rock Creek ruby. F: The flattened platelet-like silk in sapphires from Missouri River often has unusual morphology, with an atoll-like inclusion at the head of a platelet particle. G: Blue color zones leaking out of proto-genetic rutile inclusions in a heat-treated sapphire from Rock Creek. H: Patchy blue color zoning in a Dry Cottonwood Creek sapphire, caused by dissolution of bands of rutile silk into the corundum lattice. Photomicrographs by Nathan Renfro (A, G, H) and Aaron Palke (B–F); fields of view 3.31 mm (A), 4.79 mm (B), 4.79 mm (C), 4.57 mm (D), 1.26 mm (E), 1.26 mm (F), 2.19 mm (G), and 3.31 mm (H).





slender needles varying in size all the way to very short, stubby, or dusty particles. In some cases, the particles take on a flattened, platelet-like shape and are highly reflective, often showing iridescent interference colors with the use of an intense fiber-optic light due to a thin-film effect (figure 31, D–F).

Given that the majority of Montana sapphires on the market have been heat treated to enhance their colors, attention must be paid to the inclusions that can help the gemologist confidently identify this treatment. The most obvious effect of heat treatment on Montana sapphire is internal diffusion of blue coloration from rutile inclusions and silk. This can be seen as patchy blue color zones that precisely match the original patterns of the rutile silk. This is most easily observed using diffuse transmitted illumination, but fiber-optic illumination can be useful as well. This will lead to patchy blue color zoning surrounding bands of silk that are partially or nearly completely dissolved into the corundum lattice (figure 31G) as well as dark, inky spots surrounding protogenetic rutile inclusions (figure 31H). More examples will be shown in the section on heat treatment below.

On rare occasions, rutile silk may be dense enough to produce a star sapphire when cut in cabochon form (figure 32A). Yet star sapphires from Montana are exceedingly rare, and the star is usually poorly developed. Many of them show interesting coloration, with yellow or orange zones in the core of the crystal, which is most prominent in heat-treated stones (figure 32B). Twinning with tube-like structures at the intersection of twin planes is fairly common in sapphires from Dry Cottonwood Creek but may occasionally be seen in sapphires from Rock Creek and Missouri River. These features are observed in sapphires from other deposits as well (Hughes, 2017) and have been referred to as “Rose channels” (Notari et al., 2018). (Note that Rose channels have been referred to erroneously in the past as “boehmite needles.”) Large, blocky protogenetic rutile inclusions are common in stones from all the Montana secondary deposits (figure 32C). In this study, garnets were occasionally encountered in sapphires from Dry Cottonwood Creek (figure 32D). Although Zwaan et al. (2015) observed garnet inclusions in sapphire from Rock Creek and Missouri River, the present authors have not; these inclusions are likely rare compared to material from Dry Cottonwood Creek. Garnet inclusions could then be considered a likely indicator of Dry Cottonwood Creek origin. Sapphires from all three deposits are likely to contain inclusions of clinozoisite, which takes on an elongate form (figure 32E), sometimes with multiple

fractures or cleavages perpendicular to the direction of elongation. Sapphires from Dry Cottonwood Creek are also more likely to contain zircon inclusions, especially in clusters and galaxies of crystals resembling rice grains (figure 32F). Zircon inclusions are rare in sapphire from Rock Creek and Missouri River.

Mica inclusions may be seen and range from nearly colorless to pale shades of yellow to occasional dark orange hues (figure 33A). Colorless rounded feldspar inclusions are fairly common as well from all three deposits. Note that a number of other mineral inclusions were documented by Zwaan et al. (2015) and compiled in a table of occurrence. While many of the sapphires they studied appear to have been heated, Zwaan et al. (2015) report a more extensive list of minerals identified in their study and from other literature sources as well.

In some rare sapphires from Missouri River, unusual multiphase inclusions have a negative crystal morphology in which the shape of the inclusion is constrained by the crystal forms of the corundum host and not by the minerals inside the inclusion. These multiphase inclusions are composed of mica, spinel, and some other unidentified phases (figure 33B). These inclusions are interpreted to have been entrapped initially as a melt phase, which recrystallized post-entrapment. In fact, melt inclusions with a negative crystal shape are quite common in secondary Montana sapphire. They often are surrounded by decrepitation halos, which may be partially healed and show iridescent interference colors (figure 33C). In many cases, these inclusions look like standard two-phase fluid inclusions (figure 33, D and E). However, when one of these inclusions is cut into at the surface of a stone, the apparently fluid phase does not flow away but is frozen in place (figure 33F). These inclusions were trapped as a relatively silica-rich melt (Palke et al., 2017) that coexisted with the sapphires as they were growing. After being emplaced at the earth’s surface, the sapphires must have cooled quickly enough to quench the melt phase into a glass. Note that while these inclusions resemble the “melted crystal” inclusions seen in heat-treated sapphires, it is not correct to apply this term to these inclusions. These are properly called “melt inclusions,” as they were included as a melt and do not represent crystalline inclusions melted by artificial heat treatment. Therefore, observation of this type of inclusion is not, in and of itself, evidence of heat treatment in Montana sapphire. Identification of heat treatment is more reliably carried out by observation of the altered crystalline inclusions, the al-



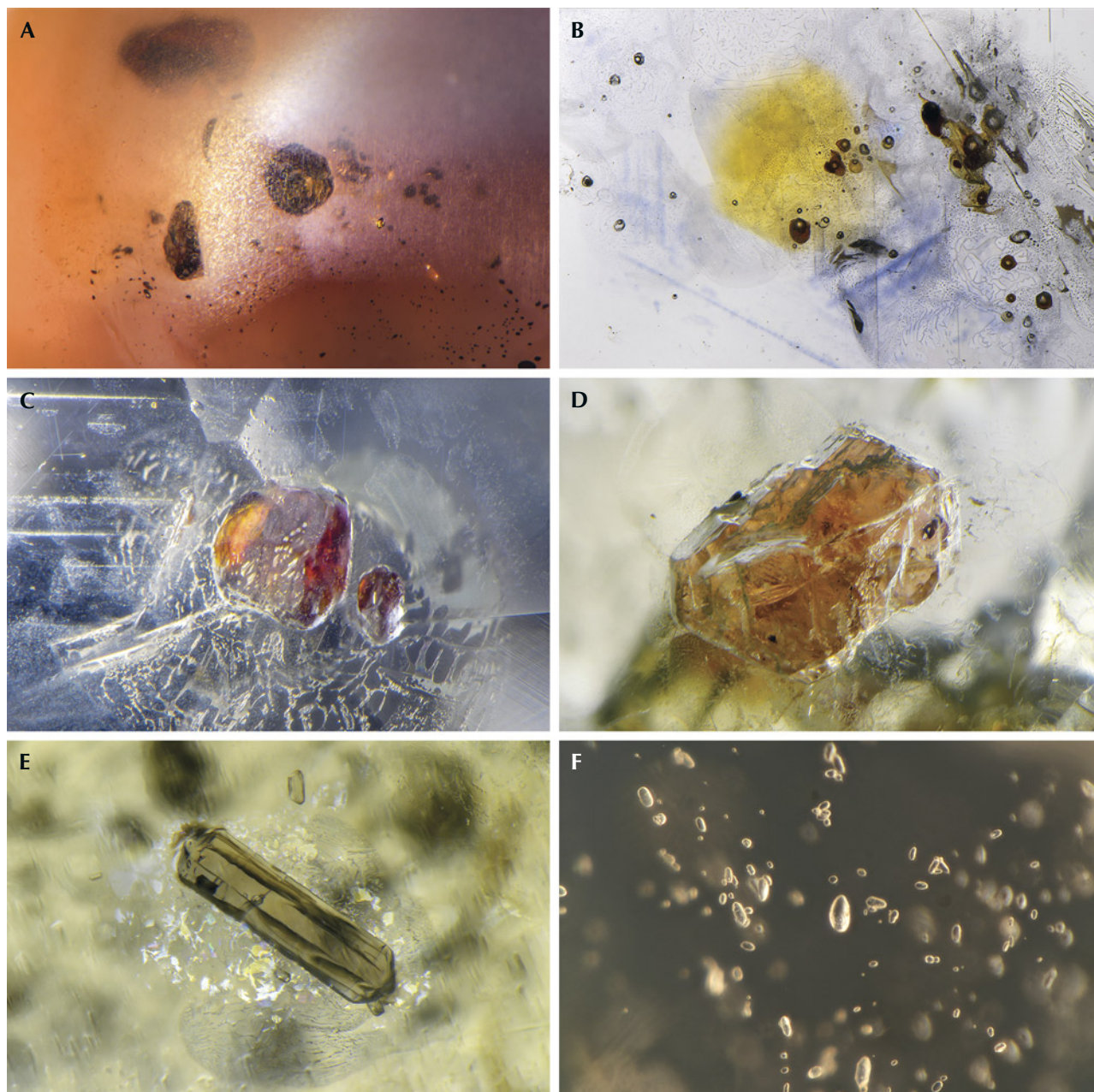


Figure 32. A: Dense rutile silk in a star sapphire from Rock Creek. B: Yellow core in a heated sapphire from Missouri River. C: Progenetic rutile inclusion in a Rock Creek sapphire. D: Garnet inclusion in a sapphire from Dry Cottonwood Creek. E: Clinozoisite inclusion in a Dry Cottonwood Creek sapphire. F: Field of zircon inclusions in a sapphire from Dry Cottonwood Creek. Photomicrographs by Nathan Renfro (A–E) and Aaron Palke (F); fields of view 2.56 mm (A), 6.26 mm (B), 1.30 mm (C), 2.82 mm (D), 2.09 mm (E), and 1.26 mm (F).

tered nature of rutile silk particles, and/or color diffusion around rutile or silk particles.

Also worth mentioning are sulfides assuming a negative crystal shape. These inclusions are dark black in darkfield illumination but may display a

highly lustrous surface with the use of a fiber-optic light (figure 34). They are always accompanied by a decrepitation halo where sulfide material has leaked out into the surrounding corundum host. The negative crystal morphology and observation of a



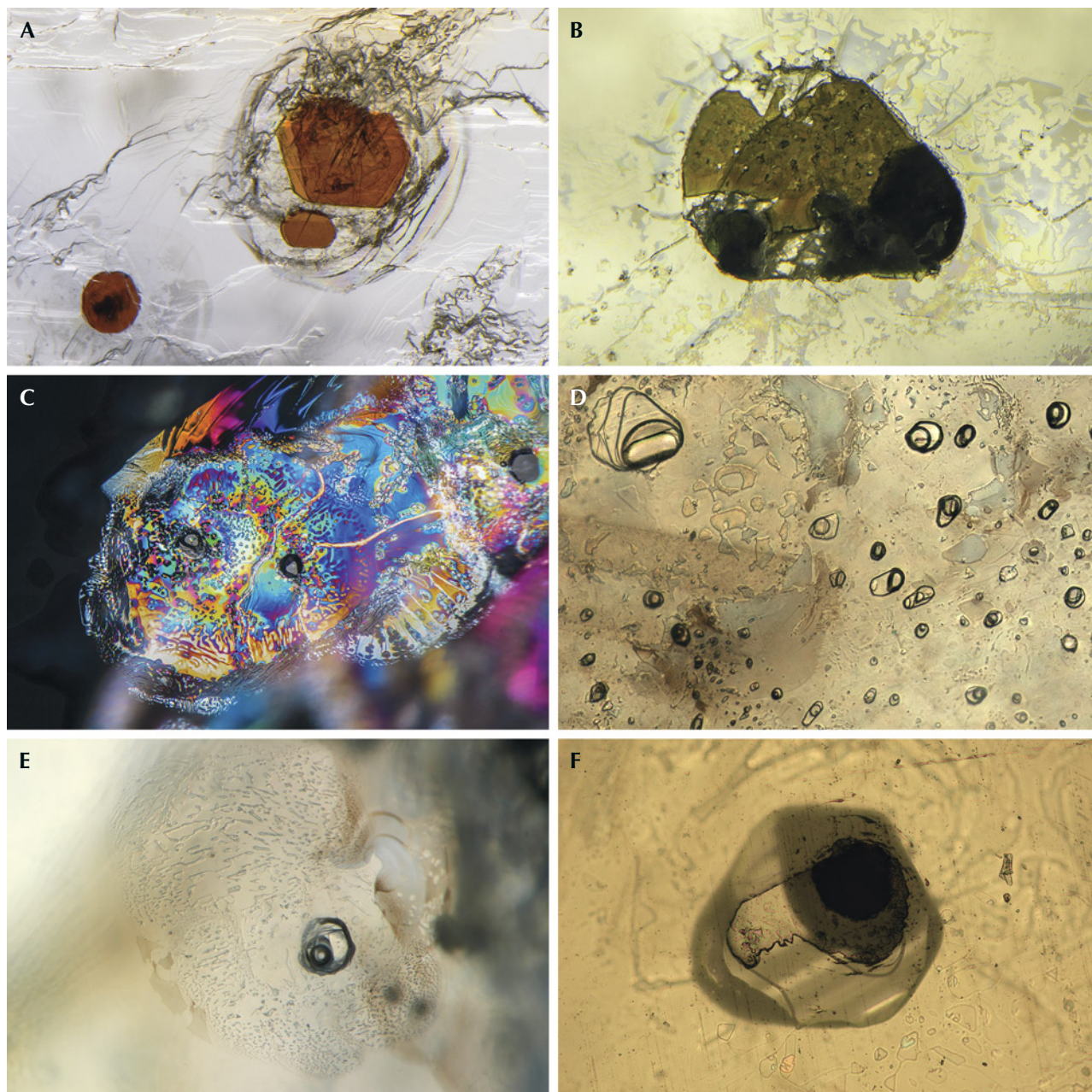


Figure 33. Inclusions in natural-color (unheated) secondary Montana sapphire. A: Mica inclusions in a Rock Creek sapphire. B: Missouri River sapphire with an unusual multiphase inclusion composed of mica, spinel, and other unidentified phases. C: Two negative crystal inclusions with a partially healed decrepitation halo in a Missouri River sapphire. D: Field of glassy melt inclusions in a Rock Creek sapphire. E: Single glassy melt inclusion with a decrepitation halo in a Rock Creek sapphire. F: Glassy melt inclusion breaking the surface of a Missouri River sapphire. Photomicrographs by Nathan Renfro (A and B) and Aaron Palke (C–F); fields of view 2.09 mm (A), 1.31 mm (B), 2.34 mm (C), 0.71 mm (D), 1.26 mm (E), and 0.71 mm (F).

polyphase mineral assemblage by SEM analysis suggests that these are an additional type of melt inclusion. In this case, a sulfide melt must have been

present during sapphire formation in addition to the more silica-rich melts described above. In the authors' experience, these sulfide melt inclusions are

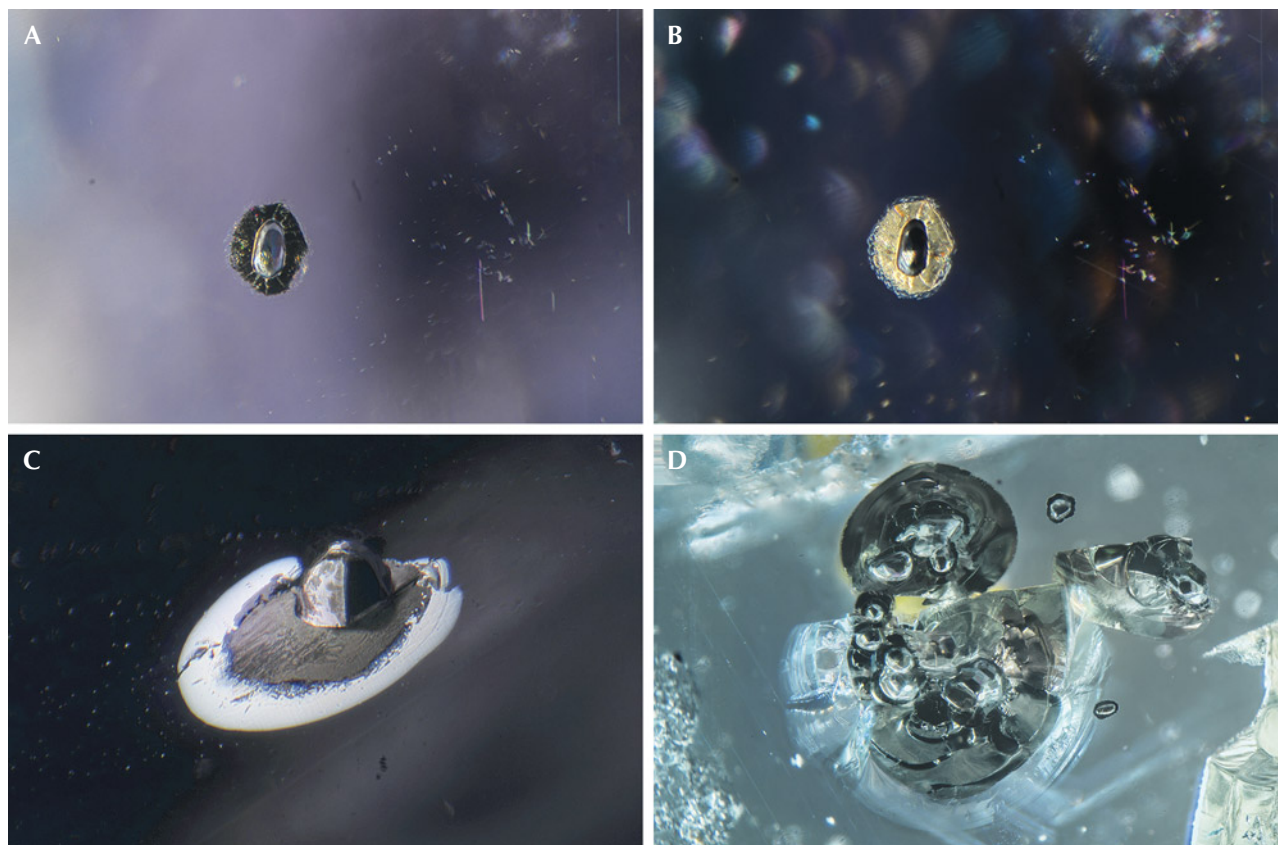


Figure 34. Inclusions in natural-color (unheated) secondary Montana sapphire. A: Sulfide inclusion in a Missouri River sapphire, shown in darkfield illumination. B: The same sulfide inclusion as in A, but with fiber-optic illumination. C: Sulfide inclusion in a Missouri River sapphire with a decrepitation halo where molten sulfide material leaked out into a fracture in the corundum host. D: Field of sulfide inclusions in a Missouri River sapphire. Photomicrographs by Aaron Palke; fields of view 1.26 mm (A–C) and 4.79 mm (D).

seen almost exclusively in sapphires from Missouri River and Dry Cottonwood Creek, though they are not common even then. Although sulfide inclusions have been noted in a few Rock Creek sapphires (J.I. Koivula, pers. comm., 2022), screening of thousands of samples by the authors has not identified this inclusion in Rock Creek sapphire.

*Inclusions/Microscopic Observations of Other Non-Classical Sapphires.* The sapphires most likely to be confused with Montana sapphire are those from Songea in Tanzania. Sapphires from Umba in Tanzania may also show some generally similar characteristics, but the inclusions are generally distinct enough to clearly separate them from secondary Montana sapphires. The first thing one might notice is the overall similar color range among all these deposits, which tends to include light-toned, low- to

medium-saturation pastel hues of blues, greens, yellows, oranges, purples, and pinks. Beyond the initial impression from the bodycolor, one may find evidence to separate these sapphires down the ocular barrel of a microscope. Umba sapphires especially tend to have distinct inclusion features, the most common of which is heavy, repeated twinning. Under cross-polarized light, the variously twinned sectors may create a unique mosaic of colors (figure 35A). The boundaries between twinned sectors are often prominent and may be filled in with some secondary aluminum oxy-hydroxide minerals (figure 35B). Fields of clustered and single zircon inclusions are quite common in Umba sapphires (figure 35C). Dense aggregations of silk are not as common as in Montana sapphires; however, the silk that can be seen often takes on a platy but very angular appearance (figure 35, D–F).



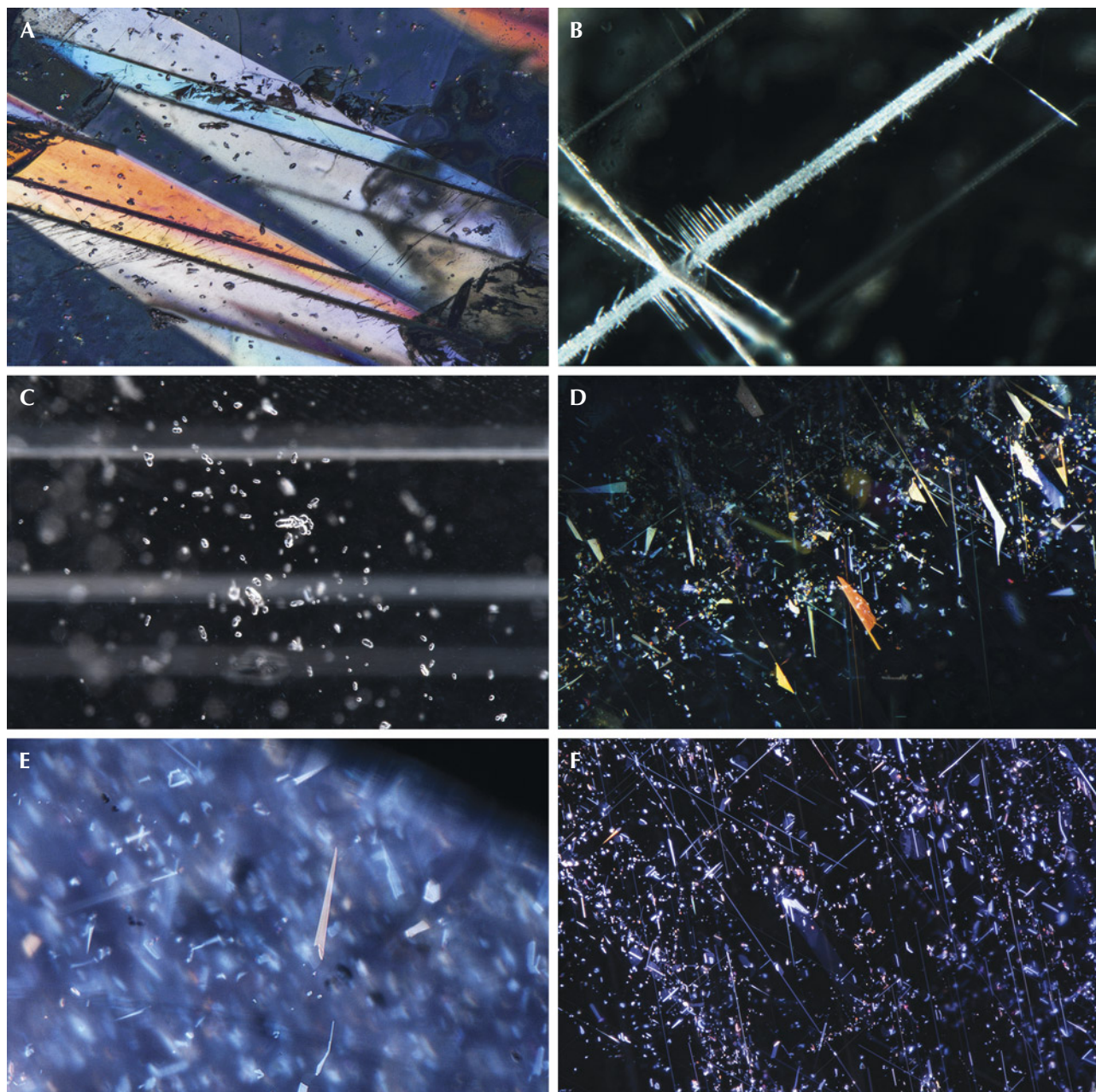


Figure 35. Typical inclusions in Umba sapphires. A: Multiple twinned sectors in cross-polarized light. B: Secondary aluminum oxy-hydroxide minerals formed in the intersection of twins. C: Clusters of zircon inclusions. D: Platelet-like reflective particles with iridescent thin-film interference colors using fiber-optic illumination. E: Platelet inclusions. F: Silk in an Umba sapphire, from elongate needles to platelet-like inclusions. Photomicrographs by Aaron Palke (A, B, D, and F), Charuwan Khowpong (C), and Ungkhana Atikarnsakul (E); fields of view 3.57 mm (A), 1.42 mm (B), 2.90 mm (C), 2.34 mm (D), 4.64 mm (E), and 2.90 mm (F).

Songea sapphires may have inclusion features that could look somewhat similar to secondary Montana sapphire inclusion features. Often seen are

blocky to angular or needle-like protogenetic rutile inclusions (figure 36, A and B). The silk in some Songea sapphire can somewhat resemble the silk in



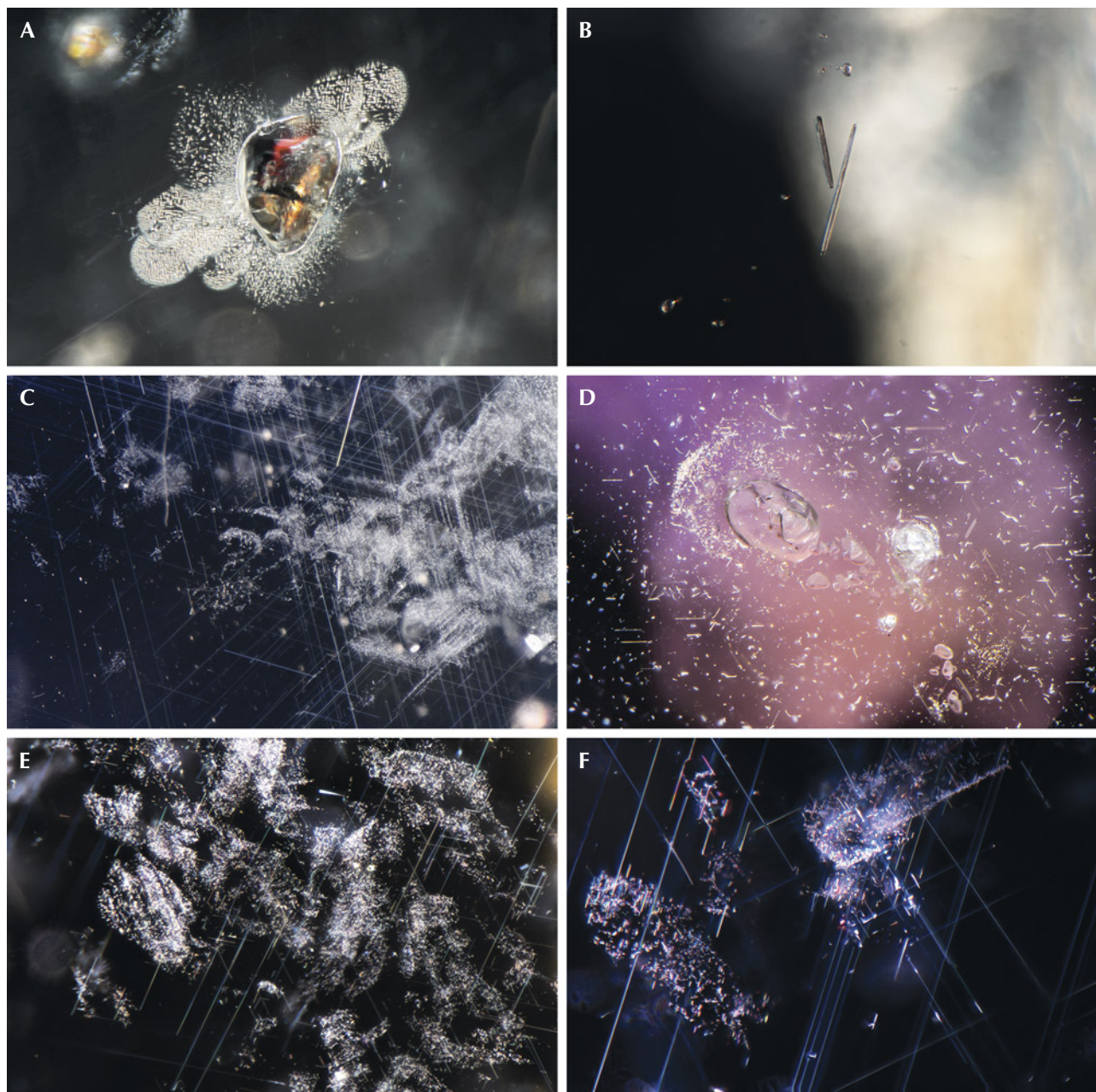


Figure 36. Representative inclusions in Songea sapphires. A: Protogenetic rutile inclusions with lobe-shaped fringes. B: Two slender rutile inclusions. C: Typical pattern of rutile silk in a Songea sapphire, including sparsely distributed medium to long silk and billowy clouds of particles. D: Small rutile dust and needles alongside unidentified colorless crystals. E: Reflective silk and platelet particles. F: Reflective, scattered silk and particles. Photomicrographs by Aaron Palke (A–C, E, and F) and Nathan Renfro (D); fields of view 1.26 mm (A and B), 2.34 mm (C), 1.79 mm (D), 1.76 mm (E), and 2.34 mm (F).

Montana sapphire. However, it is generally much more sparsely distributed and may appear in somewhat randomly placed patches and as flecks of silk

(figure 36, C–F). Songea sapphire generally does not have the well-formed hexagonal bands of silk seen in the Montana sapphire.



**TABLE 1.** Comparison of trace element compositions (in ppma) of sapphires from Montana's secondary sources and other deposits.<sup>a</sup>

	Number of samples	Mg	Ti	V	Cr	Fe	Ga
Secondary Montana (blue, green, yellow, colorless)	51	31 (8–111)	29 (3–109)	3 (1–9)	6 (bdl–43)	1600 (610–2750)	13 (7–18)
Secondary Montana (pink sapphire and ruby)	22	25 (11–49)	29 (9–81)	6 (1–27)	742 (32–2400)	1900 (620–2960)	15 (11–20)
Songea, Tanzania (various colors)	19	17 (9–33)	20 (12–33)	11 (3–21)	106 (37–218)	2580 (2130–3650)	14 (13–20)
Umba, Tanzania (various colors)	17	23 (bdl <sup>b</sup> –45)	25 (1–83)	10 (1–23)	19 (bdl–95)	1330 (430–2640)	16 (7–30)
Myanmar (various colors)	219	41 (bdl–1510)	53 (6–1018)	6 (bdl–73)	31 (bdl–1260)	928 (172–3041)	24 (5–82)
Madagascar (various colors)	263	30 (bdl–167)	128 (bdl–1942)	6 (bdl–43)	7 (bdl–276)	598 (46–2717)	20 (4–51)
Sri Lanka (various colors)	124	42 (bdl–390)	133 (4–1410)	8 (bdl–49)	4 (bdl–74)	330 (bdl–1070)	24 (3–92)
Detection limits (ppma)		0.1–0.3	0.5–2.0	0.03–0.2	0.06–1.3	1–5	0.03–0.07

<sup>a</sup>Averages are shown first, with the full range given in parentheses.  
<sup>b</sup>bdl = below detection limit

**Trace Element Chemistry.** Sapphires from the secondary Montana deposits are classified by gemologists as “non-classical” sapphires. In essence, this means they are distinct from both the typical metamorphic sapphires (from Myanmar, Sri Lanka, Madagascar, and Kashmir) and the typical magmatic, basalt-related sapphires (from Australia, Thailand, Cambodia, Nigeria, and Ethiopia). Their inability to fit into the standard metamorphic/magmatic dichotomy is also seen in their trace element chemistry. As is typical for non-classical sapphires, the secondary Montana sapphires have relatively high iron contents, suggesting a magmatic origin, while the relatively low-gallium, higher-magnesium contents and low-gallium/magnesium ratios suggests a metamorphic origin. This discrepancy was pointed out in Palke et al. (2017), which showed that the Montana sapphires plot in both the metamorphic and magmatic domains in the Fe vs. Ga/Mg and Fe-Mg×100-Ti×10 discriminant diagrams of Peucat et al.

(2007) as well as the Cr/Ga vs. Fe/Ti diagram of Sutherland et al. (1998).

The general trace element characteristics of the secondary Montana sapphire deposits are summarized in table 1, where they are broadly compared with sapphires from other deposits. Note that the trace element chemistry of Montana's three secondary deposits broadly overlaps except for a few very high-titanium Rock Creek sapphires, so they will be considered together here as a single group. There is some degree of overlap between the Montana sapphires and a small subset of higher-iron sapphires from the classical metamorphic deposits of Madagascar and Myanmar (figure 37); however, sapphires from these deposits can generally be distinguished by careful observation of their inclusion characteristics (Palke et al., 2019). The sapphires that are more likely to be confused with the secondary Montana sapphires are those from Umba and Songea in Tanzania. There is broad overlap in

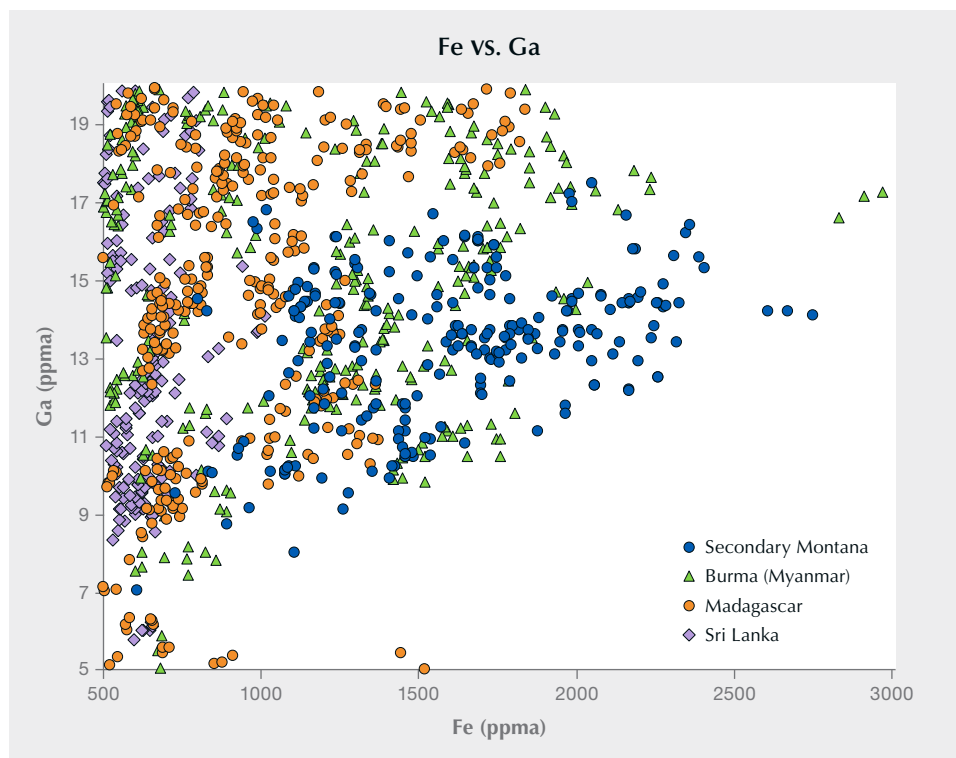


Figure 37. Plot of Fe vs. Ga (in ppma) of the secondary Montana sapphire compared to typical metamorphic blue sapphires. There is overlap in the chemistry with some Burmese and Madagascar sapphires and some minor overlap with Sri Lanka.

most trace elements for these deposits (figure 38). Iron contents are higher on average for Songea, and gallium contents of some Umba sapphires are much higher, but overall these elements cannot

consistently be used for separating the Montana sapphires. But for Montana sapphires occurring in colorless, green, blue, and yellow ranges, the trace element vanadium is a useful identifier. In partic-

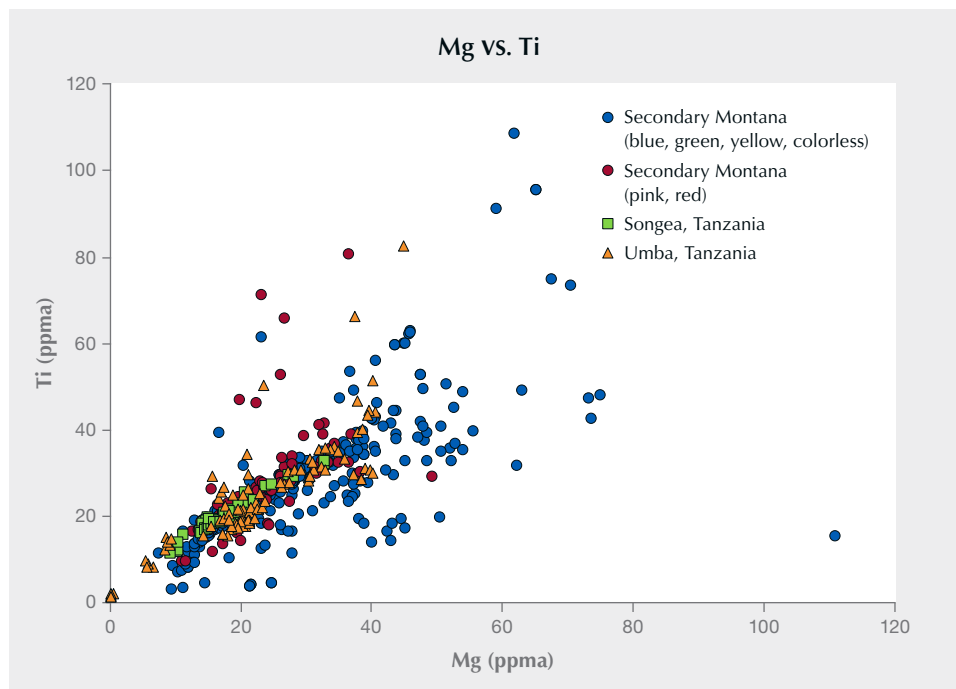


Figure 38. Plot of Mg vs. Ti (in ppma) of the secondary Montana sapphire compared to other deposits whose stones may have generally similar gemological properties.



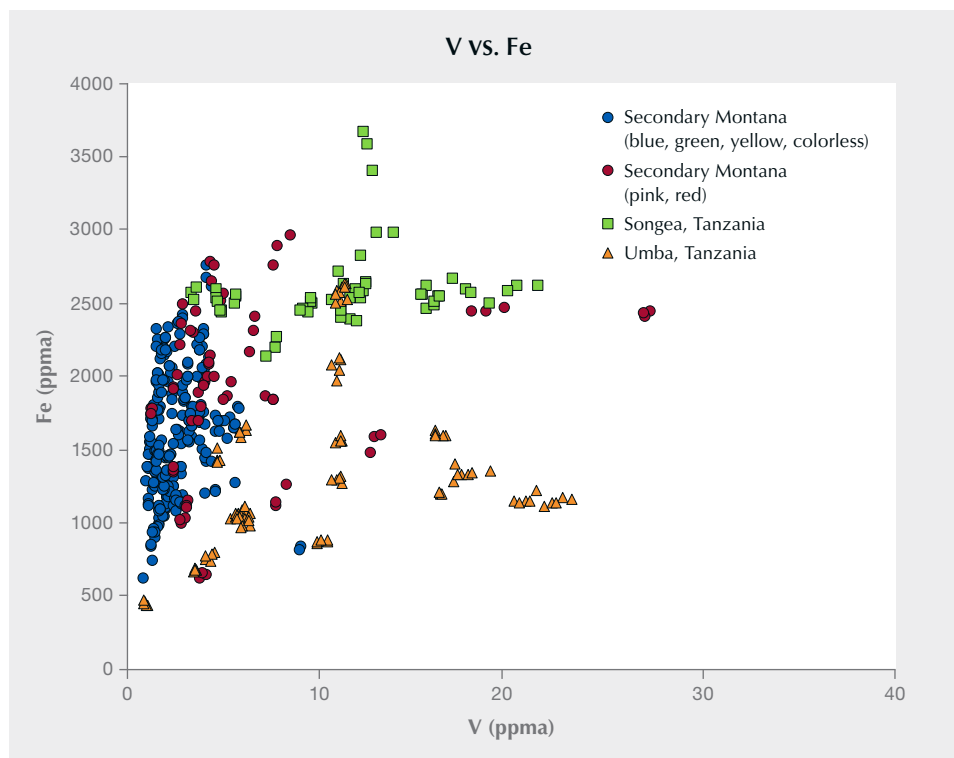


Figure 39. Plot of V vs. Fe (in ppma) of the secondary Montana sapphire compared to other deposits whose stones may have generally similar gemological properties. The secondary Montana sapphires generally have lower vanadium contents than those from Umba and Songea in Tanzania.

ular, the vanadium vs. iron plot can separate most Montana sapphires from Umba and Songea sapphire (figure 39). The caveat is that this does not apply to pink sapphire and ruby from Montana, which have higher vanadium concentrations that overlap with sapphire from Songea and Umba.

**Heat Treatment of Montana Sapphires.** The previous section outlined various internal characteristics with an eye toward establishing the provenance of unheated Montana sapphire from the Rock Creek, Missouri River, and Dry Cottonwood Creek deposits. However, the majority of these sapphires entering the market have been heat treated at high temperatures to improve their color, making them more desirable for use in jewelry. This treatment fundamentally alters the sapphires' internal characteristics as well as their spectroscopic properties.

It is important to note that, due to their unique chemistry, Montana sapphires require specialized and carefully controlled heating environments that can typically be obtained only in modern resistance-style furnaces. The specific technical requirements for the heat treatment of Montana sapphire were realized in the pioneering scientific work of Emmett and Douthit (1993). These involve careful control of not only heating temperatures and duration but also oxidation environments using gas-mixing furnaces.

Emmett and Douthit's technology was used to heat the production of the American Gem Corporation in the 1990s and is currently employed by a small handful of heat treatment facilities in the United States.

This section chronicles the journey of several sapphire wafers through the heat treatment process with careful documentation of their inclusions and spectroscopy before and after heating. Additionally, the samples were cut as oriented wafers with the c-axis (or the optic axis) perpendicular to the plane of the wafer. This allows for only the o-ray spectrum to be collected, while the extraordinary ray (e-ray) spectrum cannot be observed. Note that this section is not meant to be an exhaustive review of the heat treatment process for Montana sapphires, but is intended to give readers an overview of key features that can identify heat-treated Montana sapphires and to demonstrate the effects of heat treatment on stones that are commercially available. More technical details about the heat treatment process can be found in Emmett and Douthit (1993). The first three examples were heated by Dale Siegford of the Sapphire Gallery in Philipsburg, Montana, and conditions of heating were not disclosed. The fourth and fifth examples were heated at GIA's experimental heat treatment facility with carefully controlled conditions described below.

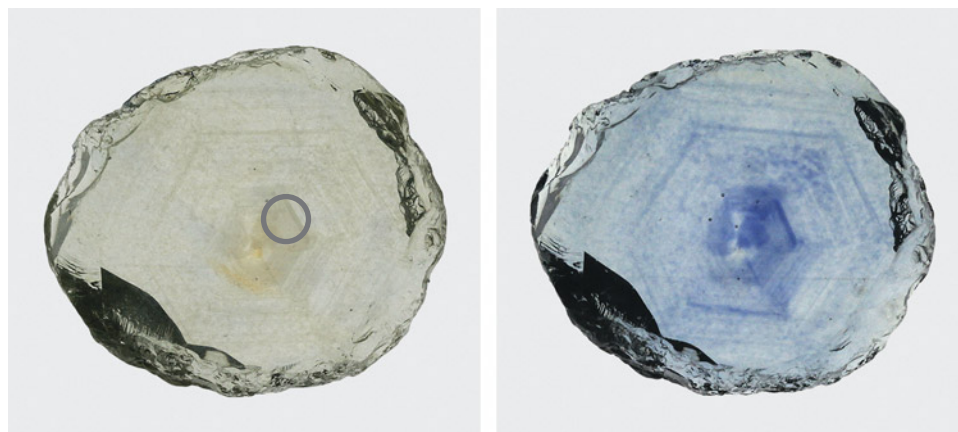


Figure 40. The Rock Creek sapphire in example 1, measuring  $9.5 \times 8.2$  mm, before (left) and after (right) heat treatment shows the blue coloration introduced during treatment. The gray circle on the left shows the position of the UV-Vis spectroscopic measurement. Photos by Aaron Palke.

*Example 1: Colorless and Cloudy to Blue.* The first example illustrates the most advantageous outcome for heat treatment of Montana sapphires. The stone was initially colorless but quite cloudy and included (figure 40, left). The transmitted light photo of the unheated stone shows dense, hexagonal bands of rutile silk that scatter light, creating brown to yellowish patches. While some unheated Montana sapphire can be cut into exceptional colorless or slightly grayish gems, this stone's cloudiness makes it undesirable for faceting. However, heat treatment causes a dramatic change in the sapphire's appearance, creating a rich blue coloration where there were once patches of cloudy silk (figure 40, right).

The change in color is also seen in the UV-Vis spectra of this sapphire before and after heating (figure 41). The unheated sapphire showed narrow absorption

bands at 377, 388, and 450 nm related to  $\text{Fe}^{3+}$  and a gradual upward slope from the near-infrared to the ultraviolet region, caused by scattering of light from the rutile silk. The most obvious change caused by heating is the creation of broad, intense absorption bands at 580 and 880 nm. The 580 nm band is responsible for the stone's blue coloration, as it absorbs most of the red light passing through by way of the excitation of an intervalence charge transfer (IVCT) between  $\text{Fe}^{2+}$  and  $\text{Ti}^{4+}$  (Dubinsky et al., 2020). This band increases in intensity as rutile silk is dissolved into the corundum structure, where the titanium ions introduced can pair locally with iron ions in a charge-balancing substitution of  $\text{Fe}^{2+} + \text{Ti}^{4+}$  for two ions of  $\text{Al}^{3+}$ . The origin of the 880 nm band is not well understood but may be related to clusters of  $\text{Fe}^{2+}$ ,  $\text{Fe}^{3+}$ , and/or  $\text{Ti}^{4+}$  cations in the corundum structure

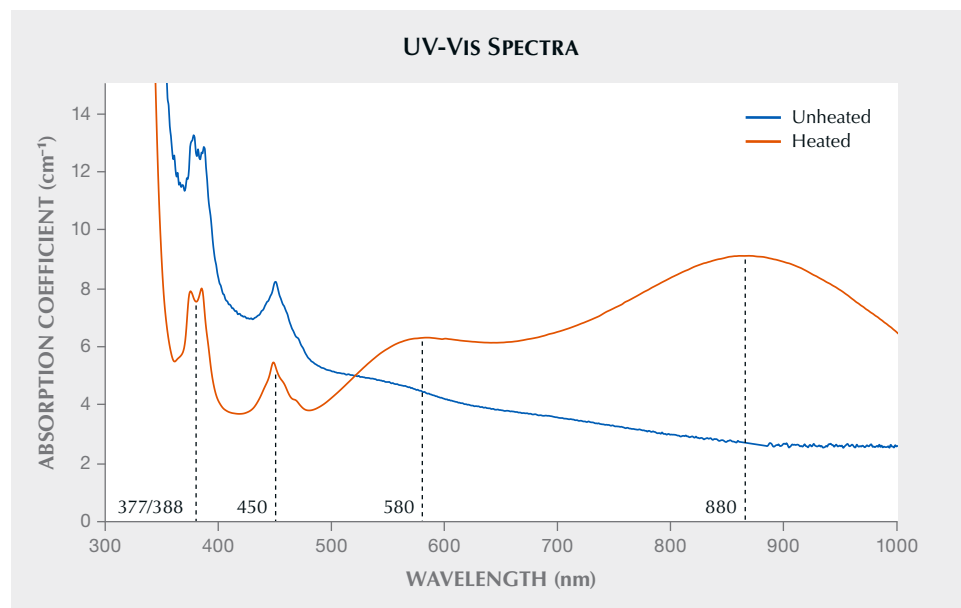


Figure 41. The o-ray UV-Vis spectra of example 1 in its unheated and heated states demonstrating how blue coloration is introduced by heat treatment.



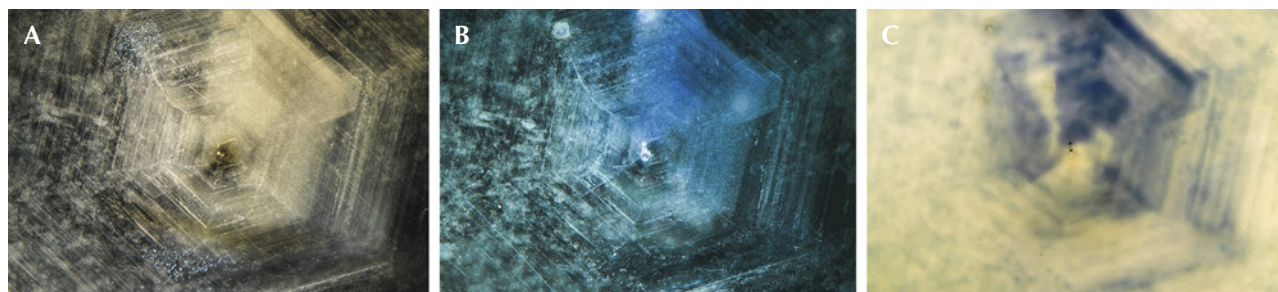


Figure 42. Example 1 before heat treatment under fiber-optic illumination (A), after heat treatment under fiber-optic illumination (B), and after heat treatment under diffuse transmitted illumination (C). Photomicrographs by Aaron Palke; field of view 4.08 mm.

(Hughes et al., 2017). Of particular note is that while unheated blue Montana sapphires have a UV-Vis spectrum reminiscent of a typical metamorphic blue sapphire, with an 880 nm band that is less intense than the 580 nm band (Palke et al., 2019), this heated blue Montana sapphire has a UV-Vis spectrum that resembles a magmatic, basalt-related blue sapphire, with an 880 nm band that is more intense than the 580 nm band. This “reversal” of the UV-Vis spectrum in heated sapphire has been documented by both Emmett and Douthit (1993) and Hughes and Perkins (2019), and it should provide the basis for careful application of this classification scheme for heated blue sapphires. The other notable difference for the heated sapphire is the decrease in absorption in the near-UV and blue/green region of the spectrum from about 350 to 500 nm. This is caused by the dissolution of rutile particles into the corundum structure and the consequent reduction in light scattering, which enhances the blue coloration caused by the  $\text{Fe}^{2+}/\text{Ti}^{4+}$  IVCT.

Finally, evidence of heat treatment can be found through careful microscopic observation. The pristine, unaltered silk in the unheated stone is a mix-

ture of long needles as well as clouds of smaller particles either aligned with the hexagonal growth patterns of the corundum or forming less-regular patterns not ostensibly constrained by the corundum lattice (figure 42A). Also seen are some reflective platelet inclusions at the top left and bottom center of figure 42A. The heated stone still shows significant scattering of light from these rutile particles using fiber-optic illumination, indicating that the particles have not fully dissolved into the corundum structure. The long rutile needles have been completely destroyed by heat treatment, but the overall pattern and distribution of smaller, cloudy rutile particles has not changed dramatically (figure 42B). More conclusive evidence of heat treatment comes from observing the distribution of blue coloration seen using diffuse transmitted illumination (figure 42C) and comparing it to the distribution of incompletely dissolved rutile inclusions (figure 42B). The blue coloration in this sapphire shows a nearly exact correlation with the incompletely dissolved rutile clouds, providing conclusive evidence of high-temperature heat treatment. Also notable is that with the use of intense fiber-optic illumination, the blue

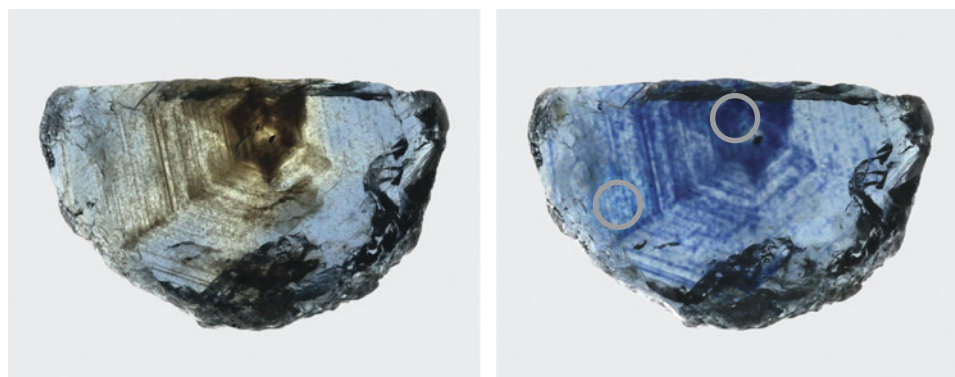


Figure 43. The Rock Creek sapphire in example 2, measuring  $11.7 \times 7.2$  mm, before (left) and after (right) heat treatment shows the blue color introduced by heat treatment. The gray circles on the right show the positions of the UV-Vis spectroscopic measurements. Photos by Aaron Palke.

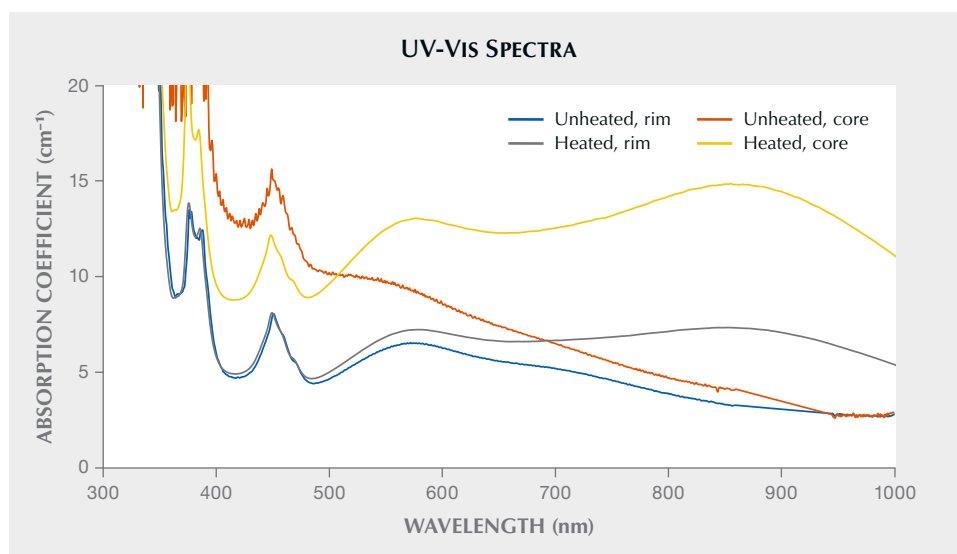


Figure 44. UV-Vis spectra of example 2 in its unheated and heated state. Two spectra were collected in both states in the core and rim of the crystal demonstrating the creation of blue coloration after heat treatment.

coloration does seem to emanate from the especially dense cloudy regions such as the sector seen in the top center of the photomicrograph in figure 42B.

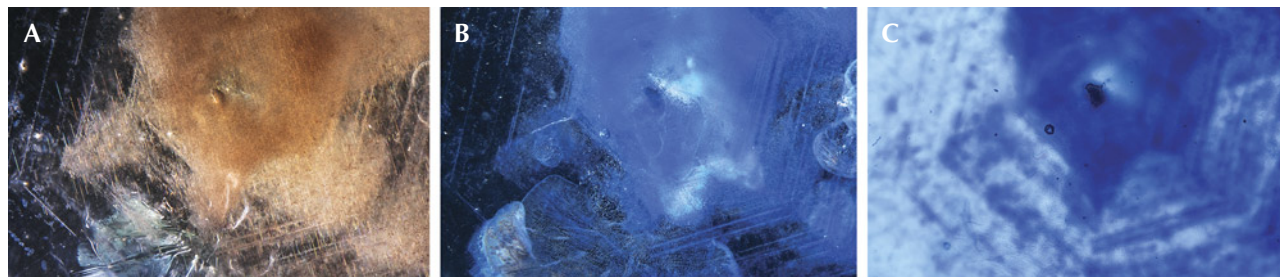
*Example 2: Brownish Blue to Blue.* Our second example involves a sapphire with a fairly well-developed blue coloration in its unheated state. However, the extremely dense, cloudy nature of this stone, especially in its core, would have made it unsuitable for faceting. In this stone, the silk lends a brown coloration. As shown in the before/after photos taken with diffuse transmitted light (figure 43), these brownish cloudy regions take on an intensely saturated blue color after heat treatment.

This intensification of blue color can also be seen in the UV-Vis spectra collected in two spots in the core and rim of the sample before and after heating. In the unheated state, both the core and rim have a noticeable broad absorption band at 580 nm related to  $\text{Fe}^{2+}/\text{Ti}^{4+}$  IVCT as well as narrow  $\text{Fe}^{3+}$ -related absorption bands at 377, 388, and 450 nm (figure 44). The un-

heated core also has a pronounced rise in absorption, and its decrease in wavelength from the near-IR to the near-UV is caused by scattering from the densely concentrated rutile silk particles. After heating, the 580 nm band increases dramatically in the core and slightly in the rim. Increased clarity (and decreased scattering) is also important for improving the blue color in the core, as there is also a significant decrease in absorption in the ~350–500 nm region caused by dissolution of light-scattering silk. Similar to example 1 above, the heated stone has what would appear to be a magmatic, basalt-related blue sapphire absorption spectrum, with the 880 nm band more intense than the 580 nm band. This is in contrast to the ostensibly metamorphic blue sapphire spectrum in the unheated stone.

Finally, microscopic observations are useful for identifying the high-temperature heat treatment of this sapphire. The unheated sapphire shows an extremely dense concentration of silk, largely composed of medium to long needles, especially in the core (figure 45A). The long needles have become par-

Figure 45. Example 2 before heat treatment with fiber-optic illumination (A), after heat treatment with fiber-optic illumination (B), and after heat treatment with diffuse transmitted illumination (C). Photomicrographs by Aaron Palke; field of view 4.79 mm.





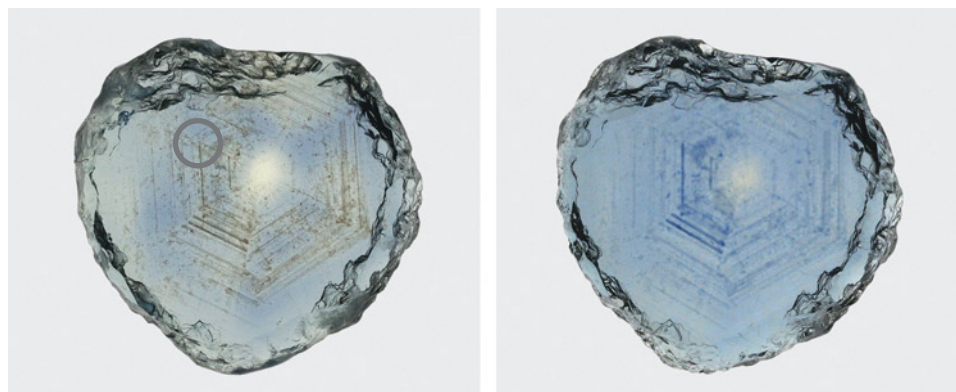


Figure 46. The Rock Creek sapphire in example 3, measuring  $9.5 \times 9.2$  mm, before (left) and after (right) heat treatment shows creation of blue color by heat treatment. The gray circle on the left shows the position of the UV-Vis spectroscopic measurement. Photos by Aaron Palke.

tially dissolved into the corundum in the heated sapphire (figure 45B). The use of fiber-optic illumination reveals that the silk has not completely dissolved and can still scatter light quite intensely. Importantly, in the heated stone, the light scattering off the remnant clouds has a distinct blue color as a result of the leaching of  $\text{Ti}^{4+}$  ions locally into the corundum. The correlation between dense blue coloration and the remnant rutile clouds can be seen more clearly with the use of diffuse transmitted illumination (figure 45C), clearly demonstrating heat treatment.

**Example 3: Light Blue to Deeper Blue.** The next example involves a light blue sapphire with sparse silk arranged in a hexagonal pattern, which is made obvious in diffuse transmitted light by the brownish coloration of the silk. Heat treatment increased the blue coloration by dissolving some of this silk into the corundum structure (figure 46). The change in

color is, perhaps, less obvious from the UV-Vis spectra (figure 47). The absolute intensity of absorption at 580 nm is not significantly different before and after treatment. The main difference is the decreased absorption between  $\sim 350$ – $500$  nm caused by reduction in scattering when the fine rutile silk is dissolved into the corundum, allowing more blue light to be transmitted. While not as obvious, the 580 nm band likely becomes more intense as well, although its increased intensity may be masked by the decrease in absorption related to scattering. Note that while the 880 nm band does increase after heating, this change is not significant enough to make it more intense than the band at 580 nm.

Microscopic observation reveals significant alteration of the rutile silk upon heating. Before heating, the silk was composed of a mixture of long, medium, and short needles and particles arranged in a hexagonal pattern (figure 48A). After heating, the long and

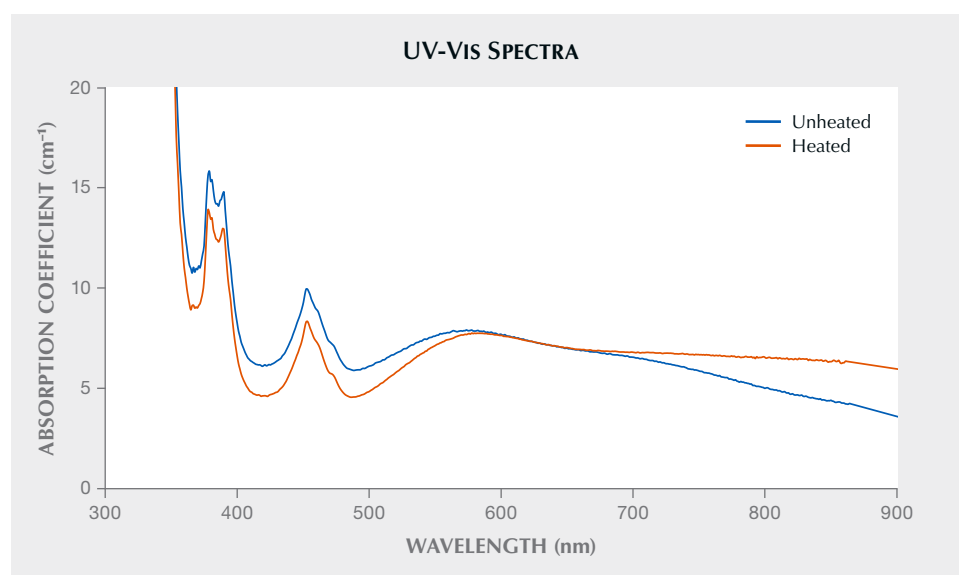


Figure 47. UV-Vis spectra of example 3 in its unheated and heated state demonstrating the deepening of blue coloration by heat treatment.

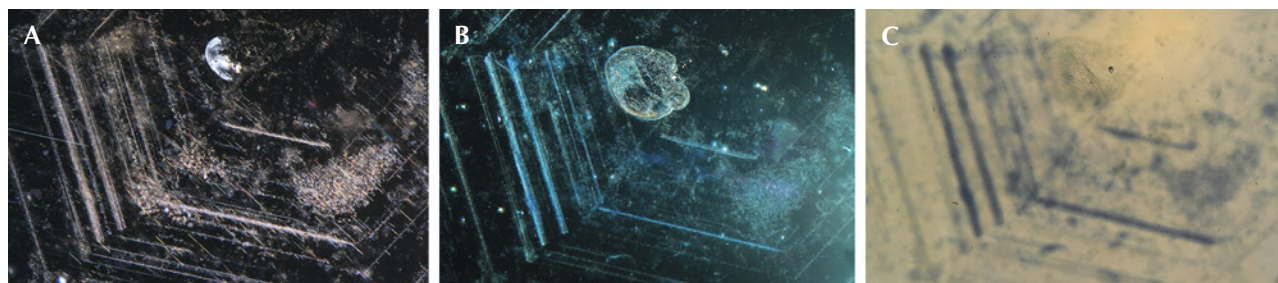


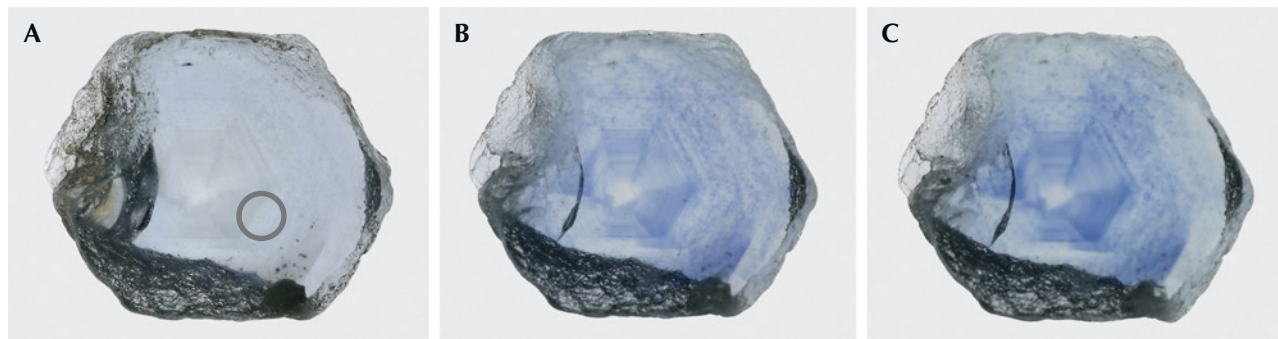
Figure 48. Example 3 before heat treatment with fiber-optic illumination (A), after heat treatment with fiber-optic illumination (B), and after heat treatment with diffuse transmitted illumination (C). Photomicrographs by Aaron Palke; field of view 2.34 mm.

medium silk are completely decomposed and the hexagonal clouds of particles are made up of very fine, dusty particles (figure 48B). Also notable is the small inclusion in the core with the concentrically aligned decrepitation halo (figure 48A, top center). After heating, the decrepitation halo has become filled with some residual material, likely from the melting or alteration of the originally intact central inclusion. Finally, the most conclusive evidence of heat treatment comes from comparing the distribution of partially dissolved silk using a fiber-optic light and blue patches of coloration using diffuse transmitted light (figure 48C). The correlation between the remnant silk clouds and the blue zones of color allows for easy identification of heat treatment in this case.

*Example 4: Effect of Cooling Rate.* While the precise heating conditions for the above experiments are not known, additional tests have been carried out at GIA's experimental heat treatment facility. In the first experiment, a cloudy, pale blue stone with sig-

nificant rutile particles and silk was heated at 1700°C for 12 hours in a reducing atmosphere composed of 0.33 atm partial pressure of H<sub>2</sub> and 0.67 atm partial pressure of CO<sub>2</sub>. The sapphire was cooled slowly at a rate of 4°C/minute. This was done twice to ensure the sapphire reached a steady state at these conditions. The same sapphire was heated again at the same conditions but quenched rapidly by placing it in a crucible affixed to an alumina rod that can be retracted from the bottom of the muffle tube. In this way, the sapphire is cooled from 1700°C to about 1000°C in 1–2 minutes and then further cooled to room temperature in roughly 15 minutes. The spectra and photos of the sapphire after various stages of heat treatment demonstrate the deeper blue color of the rapidly cooled sapphire compared to the slowly cooled heating (figures 49 and 50). When the sapphire is slowly cooled, the titanium dissolved into the corundum can start to exsolve as rutile (TiO<sub>2</sub>) as the solubility of titanium in corundum decreases with decreasing temperature. As the rutile particles pre-

Figure 49. The sapphire in example 4, measuring 8.1 × 6.5 mm: unheated (A), heated to 1700°C and slowly cooled (B), and heated to 1700°C and rapidly cooled (C), showing a deeper blue color with rapid cooling. The gray circle shows the area of analysis. Photos by Aaron Palke.





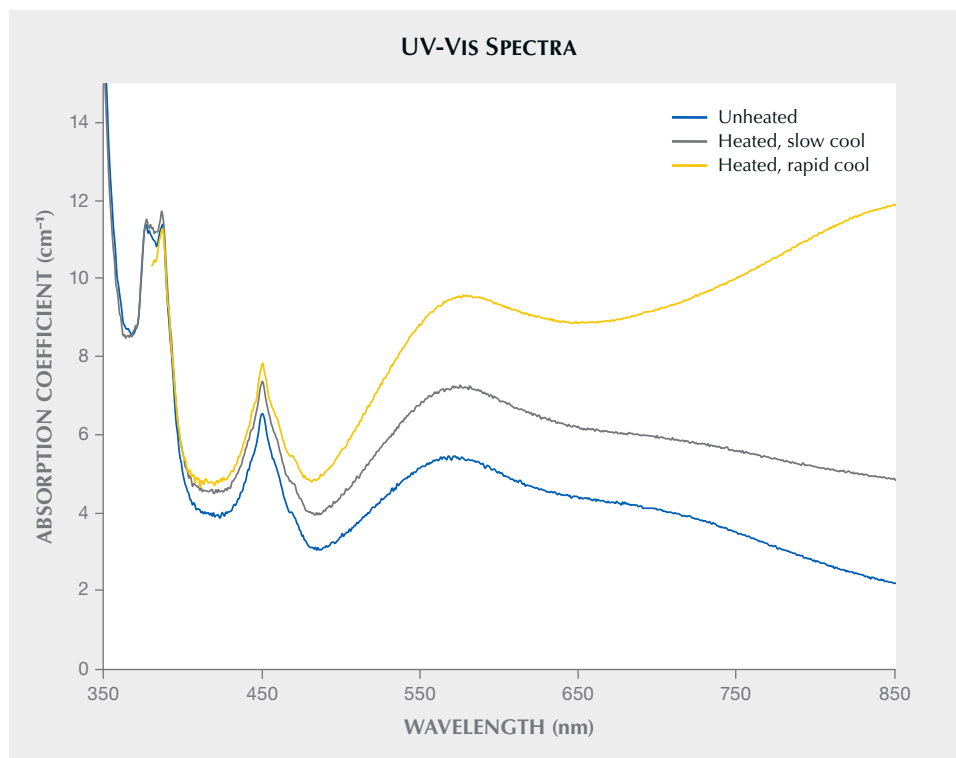


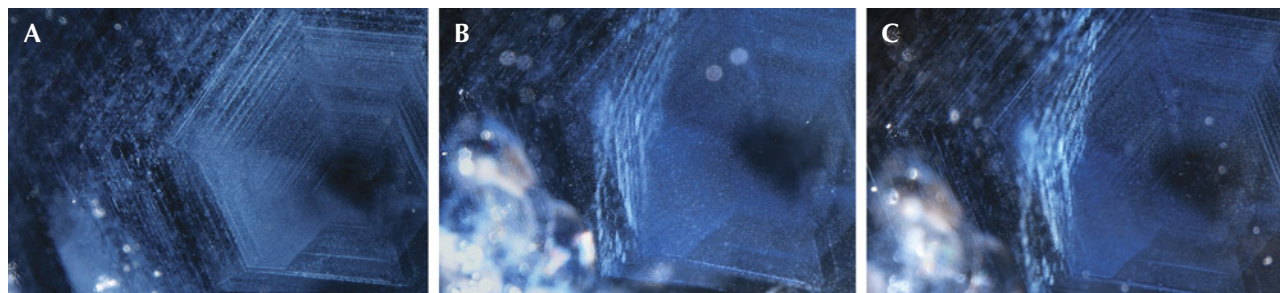
Figure 50. UV-Vis spectra of example 4 in its unheated, heated (slowly cooled), and heated (rapidly cooled) states demonstrating the increased  $\text{Fe}^{2+}\text{-Ti}^{4+}$  IVCT band at 580 nm, with rapid cooling leading to deeper blue color.

precipitate and grow during cooling, the titanium exits the corundum lattice, causing a reduction in the  $\text{Fe}^{2+}\text{-Ti}^{4+}$  intervalence charge transfer band and a reduction in the blue coloration. Rapid cooling quenches in the high-temperature solubility of titanium in the corundum lattice and retards exsolution of rutile upon cooling. Note, however, that rapid cooling does not lead to complete dissolution of rutile silk and particles in the sapphire, as seen in the photomicrographs in figure 51. The use of intense fiber-optic lighting shows that even the rapidly cooled sapphire has an abundance of light-scattering rutile particles. The presence of these rutile particles

suggests either that rutile was never fully dissolved into the corundum lattice at 1700°C or that even with rapid cooling there was still some very rapid exsolution of rutile.

*Example 5: Creation of Trapped-Hole Coloration.* For one final example, we consider two sapphires with entirely different responses to heat treatment. Many Montana sapphires are heated to create or intensify yellow or orange color by creating what is referred to as a “trapped hole.” This trapped-hole chromophore involves a  $\text{Mg}^{2+}$  atom substituting for  $\text{Al}^{3+}$  with a missing electron on a nearby oxygen

Figure 51. Rutile silk and particles in example 4 in the unheated (A), heated (slowly cooled, B), and heated (rapidly cooled, C) states showing the existence of rutile particles even in the heated and rapidly cooled sapphire. Photomicrographs by Aaron Palke; field of view 3.57 mm.



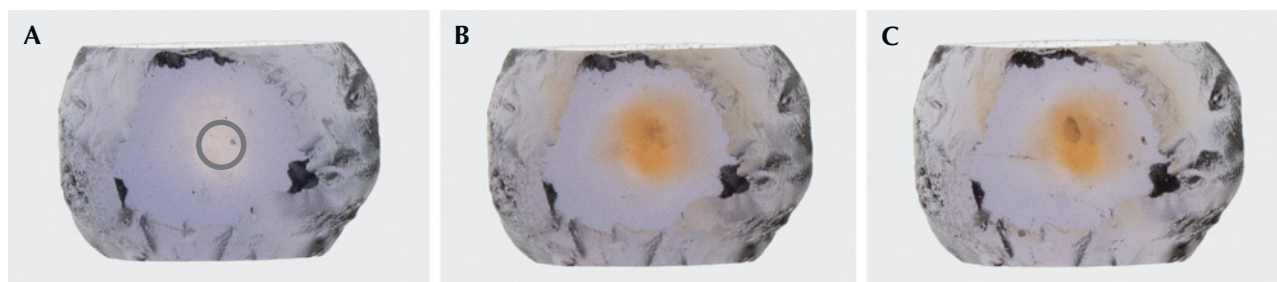


Figure 52. The Rock Creek sapphire in example 5, measuring  $0.8 \times 0.5$  mm: unheated (A), heated to  $1200^{\circ}\text{C}$  in pure  $\text{O}_2$  (B), and heated to  $1700^{\circ}\text{C}$  in pure  $\text{O}_2$  (C). The gray circle shows area of analysis. Photos by Aaron Palke.

anion for charge balance (a trapped hole). This leaves the oxygen anion with a charge of  $-1$  and causes it to absorb light at  $450$  nm, creating intense yellow or orange color (see Dubinsky et al., 2020). Some heaters who specialize in treating Montana sapphire will carry out what is referred to as a “fancy burn” in an oxidizing atmosphere to bring out yellow and orange hues. The creation of trapped-hole absorption centers by heating Montana sapphires in an oxidizing environment was carefully documented by Emmett and Douthit (1993).

Many heated fancy-color sapphires will display an intense yellow or orange core where the trapped-hole chromophore is developed. This heating needs to be carried out in an oxidizing environment in order to create a trapped hole. Heating in reducing environments can facilitate the charge balance of  $\text{Mg}^{2+}$  by

oxygen vacancies instead of the trapped hole on the  $\text{O}^-$  anion.

Figures 52–55 show the results of an oxidizing heat treatment run on two sapphires, one from Rock Creek (figures 52 and 53) and one from Dry Cottonwood Creek (figures 54 and 55). Both were heated once at  $1200^{\circ}\text{C}$  in a pure  $\text{O}_2$  atmosphere for 12 hours, then heated again at  $1700^{\circ}\text{C}$  in a pure  $\text{O}_2$  atmosphere for 12 hours.

The sapphire from Rock Creek developed an orange core after heating in  $\text{O}_2$  at  $1200^{\circ}\text{C}$  (figure 52). The UV-Vis spectrum shows this change, with an increase in absorption in the region from  $350$  to  $500$  nm (figure 53). The difference between the heated and unheated spectra shows the creation of the trapped-hole absorption band centered at around  $480$  nm. The negative dip in the difference spectrum centered at about

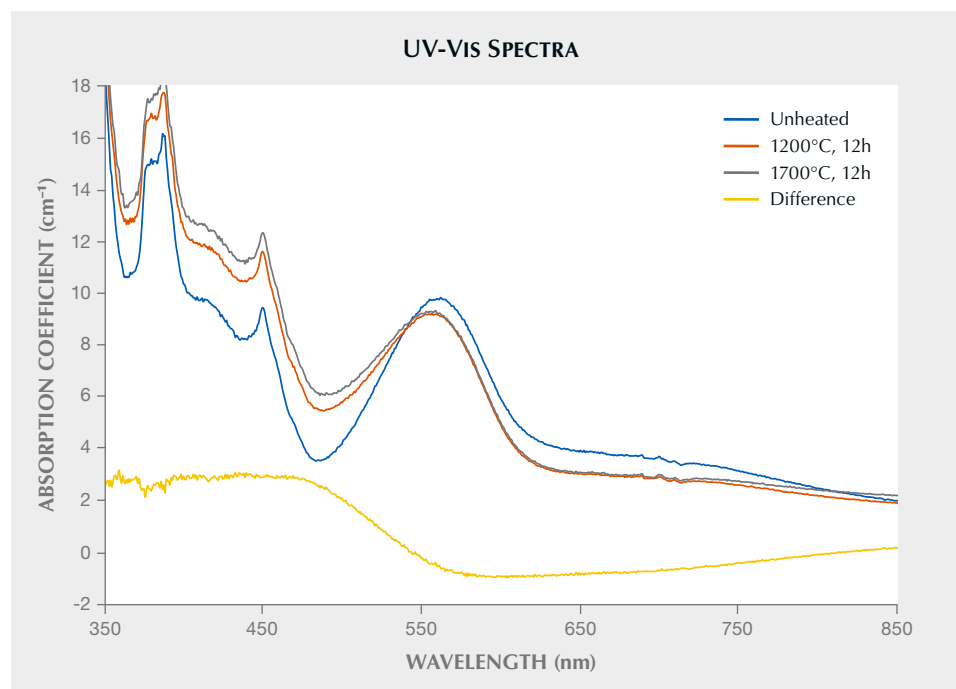


Figure 53. UV-Vis spectra of example 5 from Rock Creek: unheated, heated to  $1200^{\circ}\text{C}$  for 12 hours in pure  $\text{O}_2$ , and heated to  $1700^{\circ}\text{C}$  in pure  $\text{O}_2$ .



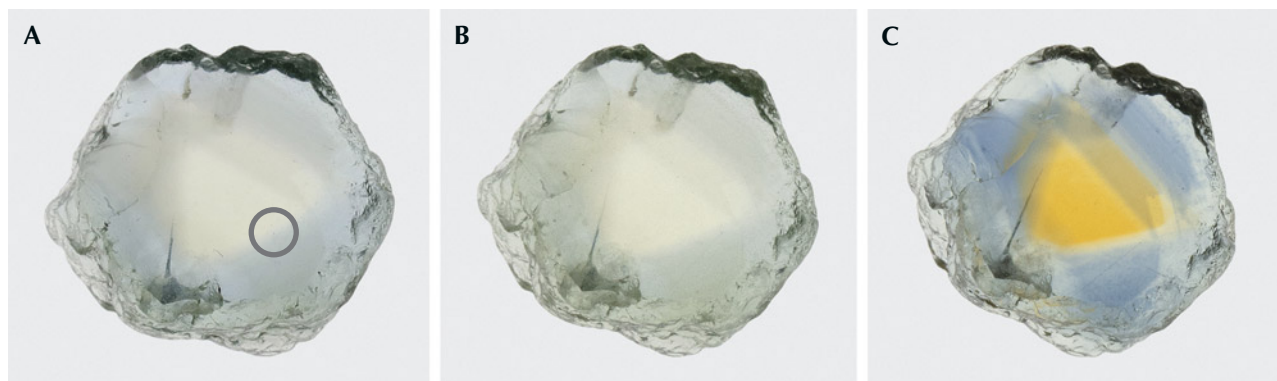


Figure 54. The Dry Cottonwood Creek sapphire in example 5, measuring  $7.2 \times 6.7$  mm: unheated (A), heated to  $1200^{\circ}\text{C}$  in pure  $\text{O}_2$  (B), and heated to  $1700^{\circ}\text{C}$  in pure  $\text{O}_2$  (C). The gray circle shows area of analysis. Photos by Aaron Palke.

580 nm indicates that heating also reduced the  $\text{Fe}^{2+}$ - $\text{Ti}^{4+}$  intervalence charge transfer absorption. Heating at  $1700^{\circ}\text{C}$  resulted in a negligible change in color, possibly with a slight increase in the trapped-hole absorption band in the UV-Vis spectrum.

The sapphire from Dry Cottonwood Creek did not develop the trapped-hole chromophore after heating at  $1200^{\circ}\text{C}$  (figure 54). The only change at this lower temperature was a lightening of the blue color due to a reduction in the  $\text{Fe}^{2+}$ - $\text{Ti}^{4+}$  IVCT absorption (figure 55). The trapped-hole chromophore is only developed

in this sample by heating at the higher temperature of  $1700^{\circ}\text{C}$  in pure  $\text{O}_2$  (figure 55). This sapphire also developed blue color in its rim during heating due to dissolution of rutile particles and introduction of  $\text{Ti}^{4+}$  cations into the corundum structure, leading to creation of  $\text{Fe}^{2+}$ - $\text{Ti}^{4+}$  IVCT chromophores.

The fundamental difference in the behavior during the oxidizing heat treatment is in the way excess  $\text{Mg}^{2+}$  cations are charge-balanced in the original unheated sapphire. The FTIR spectrum of the Rock Creek sapphire here contained the acceptor-domi-

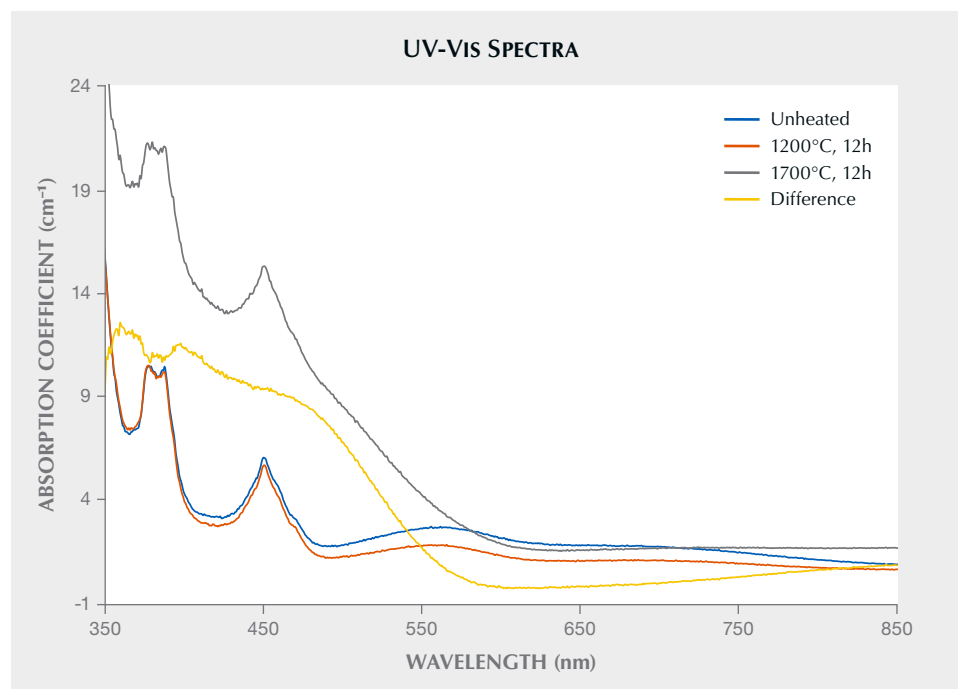


Figure 55. UV-Vis spectra of example 5 from Dry Cottonwood Creek: unheated, heated to  $1200^{\circ}\text{C}$  for 12 hours in pure  $\text{O}_2$ , and heated to  $1700^{\circ}\text{C}$  in pure  $\text{O}_2$ .



Figure 56. Heat-treated Rock Creek sapphires; the largest rough stone weighs 4.62 ct. Photo by Jeff Scovil; courtesy of Potentate Mining.

nated  $3000\text{ cm}^{-1}$  series (the “Punsiri band”), which is caused by  $\text{H}^+$  cations charge-balancing excess  $\text{Mg}^{2+}$  cations. This hydrogen is easily burned away at relatively low temperatures (i.e.,  $1200^\circ\text{C}$ ), leaving the  $\text{Mg}^{2+}$  to be charge-balanced by a trapped hole when heated in an oxidizing environment (J.L. Emmett, pers. comm., 2022). The Dry Cottonwood Creek sapphire did not have the acceptor-dominated  $3000\text{ cm}^{-1}$  series in its FTIR spectrum, indicating that any excess  $\text{Mg}^{2+}$  would have been charge-balanced by oxygen vacancies. Trapped holes in this case can only be created by diffusion of aluminum vacancies into the sapphire to annihilate oxygen vacancies, thereby allowing  $\text{Mg}^{2+}$  to be charge-balanced by trapped holes instead of the oxygen vacancy (J.L. Emmett, pers. comm., 2022). But diffusion of aluminum vacancies requires extreme temperatures and long heating times, which is why this is only seen in the sapphire heated at  $1700^\circ\text{C}$  for 12 hours and not when heated at the lower temperature of  $1200^\circ\text{C}$ . Only a small number of Montana sapphires have been heated this way at GIA’s experimental heat treatment facility so far. However, in many years of heat

treating Montana sapphires from all three secondary deposits, Dr. Emmett has observed significant differences in the way sapphires from these deposits react to oxidizing heat treatment. Missouri River sapphires do not have the acceptor-dominated  $3000\text{ cm}^{-1}$  series in the infrared and therefore require high temperatures in oxidizing conditions to develop trapped-hole coloration. On the other hand, Rock Creek sapphires often have the acceptor-dominated infrared features at  $3000\text{ cm}^{-1}$  (see figure 23) and frequently react well to an oxidizing fancy burn at temperatures as low as  $1200^\circ\text{C}$ . According to Dr. Emmett, a small proportion of Dry Cottonwood Creek sapphires have the acceptor-dominated  $3000\text{ cm}^{-1}$  features and will develop yellow or orange color at  $1200^\circ\text{C}$ , but more frequently these require higher temperatures around  $1700\text{--}1800^\circ\text{C}$ .

## CONCLUSIONS

With large volumes of Montana sapphire being produced in consistent and reliable quantities (figure 56), the secondary Montana sapphire deposits are some of the most important American gem mines in mod-





Figure 57. A 2.02 ct unheated Montana sapphire featuring concave faceting. Courtesy of Derek Katzenbach.

ern times. The material fits a wide variety of market demands, from heated goods under 1 carat size to rare, fine, unheated sapphires up to several carats. Aggressive marketing by Potentate Mining and its affiliates as well as by independent artisanal miners, especially through social media, has driven up interest in these gemstones both domestically and in the international gem and jewelry market. Identifying the origin and treatments for Montana sapphires can be relatively straightforward based on inclusions and

trace element chemistry, allowing the provenance of these stones to be preserved and traced once the stones enter the gem and jewelry market. With the wide range of colors produced, Montana sapphire is an exceptionally versatile gem, finding a home in nearly any style of jewelry (figure 57). With large reserves remaining at Rock Creek, Missouri River, and Dry Cottonwood Creek and their growing popularity with consumers, Montana sapphire is likely to play an increasingly important role in the market.

#### ABOUT THE AUTHORS

Dr. Aaron Palke is senior manager of colored stone research, and Nathan Renfro is senior manager of colored stone identification, at GIA in Carlsbad. Jeffrey R. Hapeman is president of Earth's Treasury (Westtown, Pennsylvania). Dr. Richard Berg is a research geologist emeritus at the Montana Bureau of Mines and Geology at Montana Tech of the University of Montana in Butte.

#### ACKNOWLEDGMENTS

Many samples containing prominent inclusions were sourced from the inclusion collection of John I. Koivula. Samples from GIA's Colored Stone Reference Collection were collected in the

field at Eldorado Bar at Cass Thompson's operation (Eldorado Sapphire mine) and from Potentate's operations at Rock Creek. Some Dry Cottonwood Creek samples were donated by Dr. John Emmett, who obtained them from the mining operations of American Gem Corporation in 1994–1995. Dale Siegford provided samples for analysis and heat treatment services for some of the samples here. Many thanks are owed to Dr. Keith Barron and Warren Boyd of Potentate Mining for providing samples, information, and advice for this manuscript. The authors are grateful for thorough reviews by Dr. Emmett as well as two anonymous reviewers.

#### REFERENCES

- Barron K.M., Boyd W.F. (2015) The Rock Creek sapphire mine of Montana – A new era. *InColor*, No. 28, pp. 2–12.
- Belley P.M. (2023) A method for detrital corundum characterization in sediments: Case study of the Gem Mountain Mine placer sapphire deposit (Rock Creek, Montana, USA). *Canadian Journal of Mineralogy and Petrology*, Vol. 61, pp. 61–85, <http://dx.doi.org/10.3749/canmin.2200033>
- Berg R.B. (2007) Sapphires in the Butte-Deer Lodge area, Montana. *Montana Bureau of Mines and Geology Bulletin*, Vol. 134.
- (2014) Sapphires in the southwestern part of the Rock

- Creek Sapphire District, Granite County, Montana. *Montana Bureau of Mines and Geology Bulletin*, Vol. 135.
- (2015) Compilation of reported sapphire occurrences in Montana. *Montana Bureau of Mines and Geology Report of Investigation* 23, 84 pp.
- (2022) Morphology of sapphires from secondary deposits, southwestern Montana. *Montana Bureau of Mines and Geology Report of Investigation*, Vol. 34.
- Berg R.B., Dahy J.P. (2002) Montana sapphires and speculation on their origin. In P.W. Scott and C.M. Bristow, Eds., *Industrial Minerals and Extractive Industry Geology*. Geological Society, London, pp. 199–204.
- Berg R.B., Landry M.T. (2018) Sapphire deposits along the Missouri River near Helena, Montana. *Montana Bureau of Mines and Geology Bulletin*, Vol. 136.
- Berg R.B., Palke A.C. (2016) Sapphires from an Eocene sill near Helena, Montana. *Proceedings of the GSA Annual Meeting*, Denver, p. 48, <http://dx.doi.org/10.1130/abs/2016AM-278371>
- Berger A.L., Berg R.B. (2006) The Silver Bow sapphire occurrence, Montana: Evidence for a volcanic bedrock source for Montana's alluvial sapphire deposits. *Economic Geology*, Vol. 101, No. 3, pp. 679–684, <http://dx.doi.org/10.2113/gsecongeo.101.3.679>
- Clabaugh S.E. (1952) *Corundum Deposits of Montana*. U.S. Geological Survey Bulletin 983, Washington, DC.
- Dubinsky E.V., Stone-Sundberg J., Emmett J.L. (2020) A quantitative description of the causes of color in corundum. *G&G*, Vol. 56, No. 1, pp. 2–28, <http://dx.doi.org/10.5741/GEMS.56.1.2>
- Eldorado Bar sapphires (1867) *Tri-Weekly Post* (Virginia City, Montana), August 27, p. 3, c. 2.
- Emmett J.L., Douthit R. (1993) Heat treating the sapphires of Rock Creek, Montana. *G&G*, Vol. 29, No. 4, pp. 250–272, <http://dx.doi.org/10.5741/GEMS.29.4.250>
- Emmett J.L., Scarratt K., McClure S.F., Moses T., Douthit T.R., Hughes R., Novak S., Shigley J.E., Wang W., Bordelon O., Kane R.E. (2003) Beryllium diffusion of ruby and sapphire. *G&G*, Vol. 39, No. 2, pp. 84–135, <http://dx.doi.org/10.5741/GEMS.39.2.84>
- Fukatsu N., Kurita N., Oka Y., Yamamoto S. (2003) Incorporation of hydrogen into magnesium-doped  $\alpha$ -alumina. *Solid State Ionics*, Vol. 162–163, pp. 147–159, [http://dx.doi.org/10.1016/S0167-2738\(03\)00218-2](http://dx.doi.org/10.1016/S0167-2738(03)00218-2)
- Garland M.I. (2002) The alluvial sapphire deposits of western Montana. Ph.D. thesis, University of Toronto.
- Hsu T., Lucas A., McClure S., Schumacher K. (2016) Montana's Gem Mountain sapphire mine: Sharing the excitement of mining with the public. GIA Field Report, June 3, <https://www.gia.edu/gia-news-research/montana-gem-mountain-sapphire-mine>
- Hsu T., Lucas A., Kane R.E., McClure S.F., Renfro N.D. (2017) Big Sky Country sapphire: Visiting Montana's alluvial deposits. *G&G*, Vol. 53, No. 2, pp. 215–227, <http://dx.doi.org/10.5741/GEMS.53.2.215>
- Hughes E.B., Perkins R. (2019) Madagascar sapphire: Low-temperature heat treatment experiments. *G&G*, Vol. 55, No. 2, pp. 184–197, <http://dx.doi.org/10.5741/GEMS.55.2.184>
- Kane R.E. (2020) America's royal gem: Montana and Yogo sapphires. *InColor*, Vol. 45, pp. 30–39.
- Kunz G.F. (1885) Precious stones. In *U.S. Geological Survey, Mineral Resources of the U.S. for 1883–1884*, Washington, DC, pp. 723–782.
- (1890) *Gems and Precious Stones of North America*. Scientific Publishing Company, New York.
- Le Bas M.J., Maitre R.L., Streckeisen A.L., Zanettin B.A. (1986) A chemical classification of volcanic rocks based on the total alkali-silica diagram. *Journal of Petrology*, Vol. 27, No. 3, pp. 745–750, <http://dx.doi.org/10.1093/petrology/27.3.745>
- Malaquias C. (2018) Lab Notes: A rare ruby from Montana. *G&G*, Vol. 54, No. 4, pp. 434–435.
- Montana's precious stones (1891) *Dalles Daily Chronicle*, Dalles, Oregon, October 13.
- Moon A.R., Phillips M.R. (1991) Titanite precipitation in sapphire containing iron and titanium. *Physics and Chemistry of Minerals*, Vol. 18, No. 4, pp. 251–258, <http://dx.doi.org/10.1007/BF00202577>
- New sapphire fields (1892) *Anaconda Standard*, Anaconda, Montana, September 3, p. 8.
- Notari F., Fritsch E., Caplan C., Hainschwang T. (2018) “Boehmite needles” in corundum are Rose channels. *G&G*, Vol. 54, No. 3, p. 257.
- O'Donoghue M. (1995) *Montana Sapphires*. Unpublished manuscript, Sevenoaks, England.
- Palke A.C., Hapeman J.R. (2019) Gem News International: Rubies from Rock Creek, Montana. *G&G*, Vol. 55, No. 2, pp. 286–288.
- Palke A.C., Renfro N.D., Berg R.B. (2017) Melt inclusions in alluvial sapphires from Montana, USA: Formation of sapphires as a restitic component of lower crustal melting? *Lithos*, Vol. 278, pp. 43–53, <http://dx.doi.org/10.1016/j.lithos.2017.01.026>
- Palke A.C., Saeseaw S., Renfro N.D., Sun Z., McClure S.F. (2019) Geographic origin determination of blue sapphire. *G&G*, Vol. 55, No. 4, pp. 536–579, <http://dx.doi.org/10.5741/GEMS.55.4.536>
- Peucat J.J., Ruffault P., Fritsch E., Bouhnik-Le Coz M., Simonet C., Lasnier B. (2007) Ga/Mg ratio as a new geochemical tool to differentiate magmatic from metamorphic blue sapphires. *Lithos*, Vol. 98, No. 1–4, pp. 261–274, <http://dx.doi.org/10.1016/j.lithos.2007.05.001>
- Pratt J.H. (1906) *Corundum and Its Occurrence and Distribution in the United States*. U.S. Geological Survey Bulletin 180, Washington, DC.
- Renfro N.D., Palke A.C., Berg R.B. (2018) Gemological characterization of sapphires from Yogo Gulch, Montana. *G&G*, Vol. 54, No. 2, pp. 184–201, <http://dx.doi.org/10.5741/GEMS.54.2.184>
- Sangsawong S., Pardieu V., Raynaud V., Engniwat S. (2016) Gem News International: “Punsiri”-type FTIR spectral features in natural yellow sapphires. *G&G*, Vol. 52, No. 3, pp. 325–327.
- Sapphire mined on Rock Creek after 1892 discovery there (2019) *Philipsburg Mail*, Philipsburg, Montana, March 7, p. 6.
- Sapphire and Ruby Company prospectus (1891) *St. James Gazette*, London, October 29, p. 16.
- Stone-Sundberg J., Thomas T., Sun Z., Guan Y., Cole Z., Equall R., Emmett J.L. (2017) Accurate reporting of key trace elements in ruby and sapphire using matrix-matched standards. *G&G*, Vol. 53, No. 4, pp. 438–451, <http://dx.doi.org/10.5741/GEMS.53.4.438>
- Struthers J., Fisher H. (1903) Gems and precious stones. In J. Struthers, Ed., *The Mineral Industry: Its Statistics, Technology, and Trade in the United States and Other Countries to the End of 1902*, Vol. 6, New York, The Engineering and Mining Journal, New York and London, pp. 244–251.
- Sutherland F.L., Schwarz D., Jobbins E.A., Coenraads R.R., Webb G. (1998) Distinctive gem corundum suites from discrete basalt fields: A comparative study of Barrington, Australia, and West Pailin, Cambodia, gemfields. *Journal of Gemmology*, Vol. 26, No. 2, pp. 65–85.
- Zwaan J.C., Buter E., Mertz-Kraus R., Kane R.E. (2015) Alluvial sapphires from Montana: Inclusions, geochemistry, and indications of a metasomatic origin. *G&G*, Vol. 51, No. 4, pp. 370–391, <http://dx.doi.org/10.5741/GEMS.51.4.370>



# MORPHOLOGY OF COLOMBIAN EMERALD: SOME LESS COMMON CASES AND THEIR GROWTH AND DISSOLUTION HISTORY

Karl Schmetzer and Gérard Martayan

The morphology of Colombian emerald, including growth and dissolution features of their faces, gives insight into growth and post-growth history of individual crystals. A collection of 15 isolated crystals and seven emeralds in matrix was studied by optical methods. The authors observed layered growth of prismatic, dipyrarnidal, and basal sectors that leads to crystals with prismatic to columnar or rarely pyramidal habit. In the latter case, prismatic growth sectors were not developed. The visual appearance of the crystal faces at the surface was influenced by etch patterns with the formation of cavities, pits, pointed hillocks, and stepped grooves, followed occasionally by layered overgrowth. Skeletal growth led to the formation of cavities in crystals, some of them resembling empty cups with planar bottoms. In these crystals, the basal faces showed indentations or deep cavities, surrounded by shells or rims of emerald, bound on both vertical surfaces by prism or dipyrarnidal faces. Emeralds in the form of slightly conical empty tubes also belong to the latter group. Possible relationships to trapiche emeralds and samples exhibiting the *gota de aceite* effect are discussed.

In general, the morphology of Colombian emerald originating from different mines is rather simple and formed by a small number of external crystal faces. We observe two dominant planes, the basal pinacoid and the first-order hexagonal prism, occasionally in combination with small second-order hexagonal prism faces and first- and/or second-order hexagonal dipyrarnids (Goldschmidt, 1913; Schwarz and Giuliani, 2002; Moore and Wilson, 2016). The internal growth pattern of such samples, which normally show prismatic habit, consists of growth planes parallel to the external crystal faces (Kiefert and Schmetzer, 1991).

Occasionally, natural emerald and beryl crystals show etching and dissolution features (an overview of the pertinent literature is given in box A). Other growth features are due to skeletal and polygonal growth of beryl crystals (see box B). Both growth features are related to the observations made in this article for Colombian emerald crystals.

Rarely mentioned are emerald crystals with conical habit (Johnson, 1961a,b)—or *vasos* in the form of

slightly conical empty tubes (Klein, 1941)—or emeralds in the form of prismatic, empty “cups” with planar bottoms (Weldon et al., 2016). In most references,

## In Brief

- The surface texture of Colombian emerald crystals reveals details about growth and post-growth history.
- Several crystals show indications of natural etching in aggressive fluids, and some samples have undergone several subsequent growth and corrosion steps.
- In crystals with a conical shape, only basal and dipyrarnidal growth sectors were developed.
- Skeletal growth is observed in emeralds showing the form of empty cups or emeralds with indentations on the basal face.
- Within the empty cups, polygonal growth of small emerald columns is observed.

such emeralds with conical habit (figure 1) or emerald *vasos* or cups (figure 2) have been briefly mentioned or have only been pictured without considering a possible growth mechanism. In the following discussion, we will use only the term “cups” for both slightly different variants.

See end of article for About the Authors and Acknowledgments.

GEMS & GEMOLOGY, Vol. 59, No. 1, pp. 46–71,  
<http://dx.doi.org/10.5741/GEMS.59.1.46>

© 2023 Gemological Institute of America



*Figure 1. This Colombian emerald (sample 10, 25.0 mm in length) shows conical habit in the upper part and prismatic habit in the lower part; the base is covered with numerous pointed hillocks. Photo by G. Martayan.*

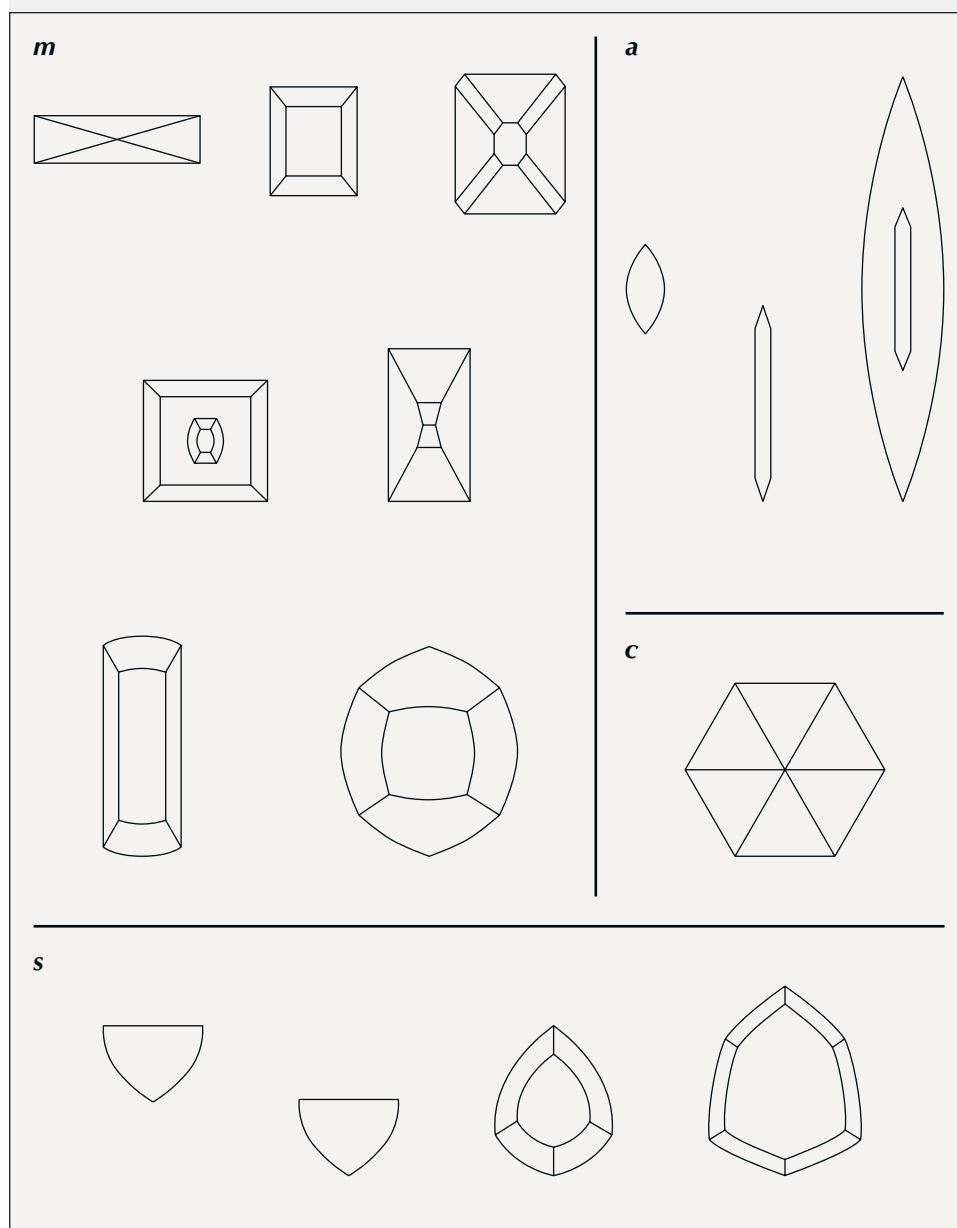


## BOX A: LITERATURE ON DISSOLUTION FEATURES OF BERYL AND EMERALD CRYSTALS

Etch pits on basal, prismatic, and pyramidal faces of Colombian emerald have been described or depicted by a few authors (e.g., Honess, 1917, 1929; Medina et al., 1983; Moore and Wilson, 2016). Considering the mineral beryl in general, various forms of tiny cavities or pits have been observed with different shapes reflecting the symmetry of the individual basal, prismatic, or dipyramidal crystal faces (figure A-1). In addition, the shape of etch patterns varies between samples from different localities (Kurumathoor and Franz, 2018). It has also been mentioned that while some faces of crystals

might show etch pits, other faces of the same crystal are completely free of such textures (Petersson, 1889; Arzruni, 1894; Vrba, 1895; Tschermak, 1897; Kohlmann, 1908; Sinkankas, 1981).

These generally observed features of etch patterns in beryls from numerous localities are consistent with the results of etching experiments performed in the laboratory (Taube, 1895/1896; Feklichev, 1963). Such experimental processes were done in various acidic or basic solutions, but normally only for periods of seconds to minutes.

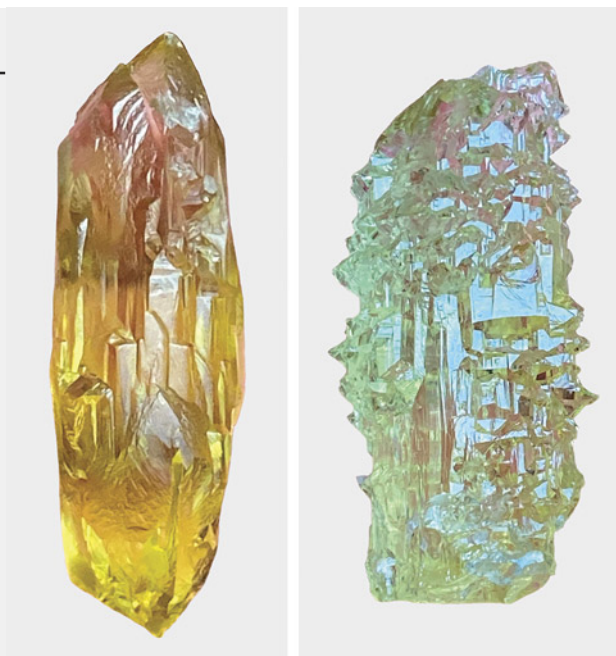


*Figure A-1. Shape of etch pits observed optically on prismatic m and a faces, on the basal pinacoid c and on dipyramidal s faces of numerous beryl crystals from Brazil. After Kohlmann (1908).*

Examination at high magnification by optical and electron microscopy reveals that the patterns of variously shaped cavities developed by natural or artificial etching show stepped surfaces of various forms (Scandale et al., 1990; Sunagawa and Urano, 1999; Sunagawa, 2003; Demianets et al., 2006; Dem'yanets and Ivanov-Schitz, 2009; Kurumathoor and Franz, 2018).

All these observations, however, are different from the effects of heavy dissolution, in which the crystals' original surfaces are completely or partially dissolved, forming more or less deep cavities or grooves (Ford, 1906; Zedlitz, 1941; Bartoshinsky et al., 1969; Koivula, 1981; Lyckberg et al., 2009; Tempesta et al., 2011). Such heavy resorption has been mentioned for beryl from specific localities—e.g., California, Brazil, or Ukraine (figure A-2)—and it has also been shown for emerald from Colombia (figure A-3, left).

Furthermore, it should be mentioned that heavy etching can produce pointed forms consisting of single or multiple tapering tips representing the residue of the former as-grown basal plane (figure A-3, right; see Penfield and Sperry, 1888; Penfield, 1890; Lacroix, 1896; Sunagawa, 2005; Moore and Wilson, 2016). This feature is also seen in the heavily etched Colombian emerald shown in figure A-3, left.



*Figure A-2. Yellow and greenish yellow beryl crystals from the Volodarsk mining area in Ukraine showing heavily dissolved surface patterns due to natural etching and dissolution subsequent to the crystal growth process. Crystal length: 61 mm (left) and 43 mm (right). Photos by Peter Lyckberg.*

*Figure A-3. Left: A heavily etched Colombian emerald crystal from Muzo measuring 27 mm in length. The basal pinacoid is completely dissolved, leading to numerous pointed hillocks; the growth sectors related to the a prism faces are optically reflective. Photo by Jeff Scovil. Right: Etched beryl crystal from Pont de Barost, Haute-Vienne, France, showing a completely dissolved basal face with numerous pointed hillocks. From Lacroix (1896).*





## BOX B: LITERATURE ON SKELETAL AND POLYGONAL GROWTH OF BERYL CRYSTALS

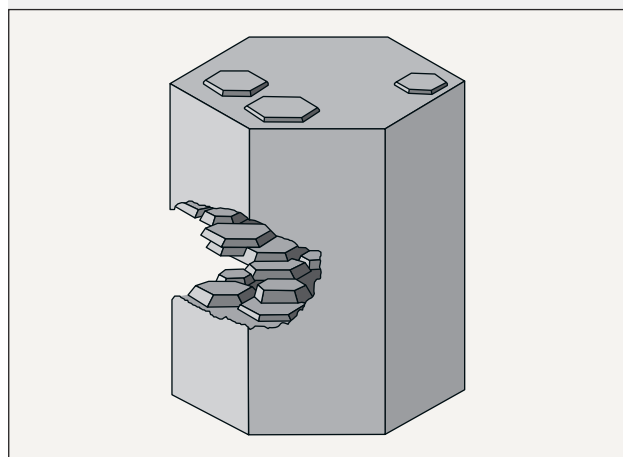
From the literature, beryls with hexagonally outlined rims or walls are known from different pegmatites. Within these main walls, highly variable, irregularly shaped to hexagonally outlined areas of beryl are found, with other pegmatite minerals filling the remaining space (figure B-1). These beryls, designated as “skeletal” or “shell” crystals, mostly consist of a rim or shell enclosing additional beryl shells or rims and other pegmatite minerals (Hunt, 1892; Shaub, 1937; Johnston, 1945; Norton et al., 1962; Beus, 1966; Sinkankas, 1981). It is not mentioned in the works cited whether the beryl inside the dominant surrounding wall represents parts of a single crystal, connected to the main wall or rim, or independent individual crystals.

From the viewpoint of crystal growth, in skeletal crystals with incomplete planes, crystal edges grow in favor of plane faces (Sunagawa, 1981, 1999). This is of course dependent on the growth environment. In the flux synthesis of emerald, for example, it is possible to grow skeletal crystals with depressions of the *m* prism face (Oishi et al., 1994).

On the other hand, the polygonal growth of small beryl columns on a basal plane of a larger crystal and the subsequent overgrowth of this structure by later generations of beryl was described by Sahama (1966) and is shown in figure B-2.

Visually, a beryl crystal depicted by Hills (1890) and shown in figure B-3, seems to show both growth features: skeletal and polygonal growth. In this sample, we observe a rim surrounding a larger cavity. Within this cavity, we observe irregular walls or columns, which end at different heights in the cavity with small crystal faces.

*Figure B-2. Sketch of a beryl crystal showing polygonal growth of small individual pyramidal beryl crystals ending in basal faces; this morphological structure is seen on the surface and within the crystal. In the latter case, this area was overgrown in subsequent growth steps. From Sahama (1966).*



*Figure B-1. Slices of three beryl crystals from Alto Cruzeiro, Paraíba, Brazil, with skeletal growth structure. Three slices were cut from each sample oriented perpendicular to the *c*-axis. Within an outer skeletal rim or shell of beryl, further beryl crystals and other pegmatite minerals were observed. From Johnston (1945).*

*Figure B-3. Surface structure in a beryl from Mount Antero, Colorado, with a rim surrounding a larger cavity with irregular walls or columns developed within the cavity. From Hills (1890).*

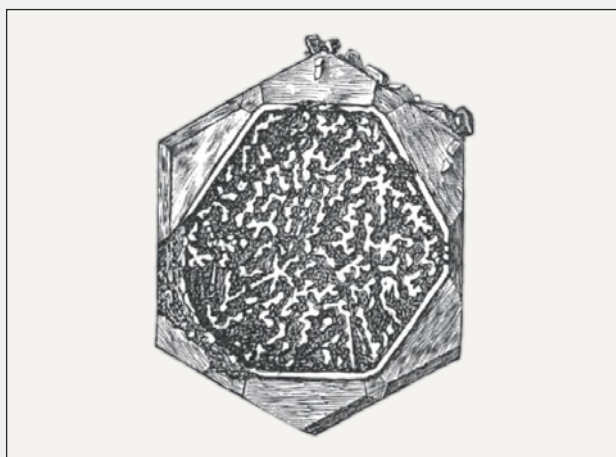




Figure 2. In sample 17 (26 mm in length), a base of black shale (not visible) is covered with numerous albite, calcite, and pyrite crystals. In this matrix, five emerald crystals are embedded, two of them developed in the form of empty cups. The emerald cup on the right is 5.5 mm long. Photo by G. Martayan.

Of commercial interest, in addition to facetable material without special structural properties, are samples with a fixed six-rayed pattern with or without a central core—designated “trapiche” emerald (Bernauer, 1926; Nassau and Jackson, 1970; Pignatelli et al., 2015; Schmetzer, 2019; Smith, 2021) or samples with an internal growth pattern named *gota de aceite* (Spanish for “drop of oil”) (Gübelin, 1944; Bosshart, 1991; Ringsrud, 2008; Hainschwang, 2008; Schmetzer, 2009; Gao et al., 2017).

Some of the morphological features mentioned above, such as the various forms of the trapiche pattern, have been studied in detail to evaluate the growth mechanism. The *gota de aceite* effect has also been properly described, but its formation, either by dissolution (etching) or polygonal growth and, in both models, by subsequent overgrowth of the surfaces of the small hillocks or columnar crystals formed in the first step, is still a matter of discussion (Bosshart, 1991).

In a recent publication, Pignatelli et al. (2022) described several Colombian emeralds with unusual habits. According to their results, the growth mechanism of two emerald cups, one spongy emerald crystal, and one spear-shaped sample is mainly due to etching (post-growth dissolution), and the morphology of an

emerald crystal with a horseshoe-shaped appearance is related to incomplete, nonuniform growth caused by mineral inclusions acting as growth obstacles.

The present paper tries to contribute to the understanding of these less common morphological and growth phenomena of Colombian emerald and offer descriptions and understanding of different patterns mentioned, especially by enlarging the database for such rare samples with remarkable morphological features. These samples provide a unique opportunity for investigation, but their rarity limits the investigation to nondestructive methods. In this way, the paper would further contribute to our understanding of the growth and post-growth history of Colombian emerald.

## MATERIALS AND METHODS

The present study is based on examination of 15 isolated emerald crystals and seven specimens with emerald crystals in mineral assemblages with albite, calcite, dolomite, and pyrite on gray or black shales (table 1). All samples are from a private collection and were purchased within the last 20 years in Bogotá or near emerald mines in Colombia. This does not necessarily indicate that all samples were un-

**TABLE 1.** Properties of the examined emerald crystals.

Sample no. and locality	Matrix specimen dimensions (mm)	Emerald crystal dimensions (mm) <sup>a</sup>	Weight <sup>b</sup>	Crystal faces <sup>c</sup> and habit	Surface features of emerald crystals	Remarks	Figures
1: Chivor	Crystal on gray shale, 40 × 28	L 11.8, D 3.5	22.7 g	<i>c, m</i> ; columnar	Growth steps on <i>m</i>	Associated minerals: dolomite, pyrite	4
2: La Pita	—	L 18.0, D 11.1–12.0	18.61 ct	<i>c, m, s</i> ; columnar	Irregular openings in <i>c</i> , etch pits and grooves on <i>m</i>	Cavities below <i>c</i> , larger than the different openings	5
3: Chivor	Crystal on black shale, 41 × 30	L 23.6, D 5.1–15.5	21.4 g	<i>c, m, a, p, s</i> ; elongated tabular	Irregular openings in <i>c</i> , partly deeply etched <i>m</i> growth sectors	Associated minerals: albite, pyrite, calcite	6
4: Coscuez	—	L 31.1, D 7.1–7.6	11.42 ct	<i>c, m, a</i> ; columnar	Partly deeply etched <i>m</i> growth sectors; in other parts, growth steps on <i>m</i>	—	7
5: La Pita or Muzo	—	L 10.0, D 4.0	0.67 ct	<i>c</i> ; conical	Growth striations on the sides of the pyramid	—	8, A and B
6: La Pita	—	L 8.8, D 2.0–2.1	0.33 ct	<i>c</i> ; conical and prismatic part	Growth striations on both parts	—	8A
7: La Pita	—	L 8.8, D 2.5–2.8	0.46 ct	<i>c</i> ; conical and prismatic part	Growth striations on both parts	—	8, A and C
8: Chivor	—	L 9.8, D 4.8–5.1	1.61 ct	<i>c, m, a, s, p</i> ; partly conical with tabular part	Growth steps on conical surface and on <i>m</i> faces of the tabular part	Groth tubes along the <i>c</i> -axis in tabular part	9
9: Muzo (?)	—	L 20.8, D 10.8–12.1	10.76 ct	<i>c, m, a, s, p</i> ; conical	Growth steps on <i>m</i> , finer structures on the conical part	Residual dark gray (carbonaceous) material in cavities	10
10: La Pita	—	L 25.0, D (top) 15.0–16.6, D (bottom) 9.5–13.0	35.87 ct	<i>m, a</i> ; partly conical with columnar part	Growth steps, mainly parallel to <i>c, p</i> on conical surface; growth steps on <i>m</i> of the columnar part; hillocks on <i>c</i>	Extensions of growth sectors confined to the <i>a</i> prism	1 and 11
11: Chivor	Crystal on gray shale, 56 × 37	L 15.5, D 3.5–4.1	43.2 g	<i>c, m, a, u, p, s</i> ; columnar	Indentations on <i>c</i> , growth steps on prismatic faces	Associated minerals: calcite, pyrite	12A
12: Chivor	Crystals on dark gray shale, 51 × 37	aggregate of 11 parallel crystals; largest L 12.5, D 5.0–6.5	50.0 g	<i>c, m, a</i> ; columnar	Indentations on <i>c</i> of all crystals, growth steps on prismatic faces	Associated minerals: pyrite, dolomite, albite	12B and 13, A and D

earthed within this period or in the last few years—some of them might originate from Colombian collections, with samples being kept there for several years or even decades before they were offered for sale.

According to the general knowledge of emerald formation in the various Colombian deposits, all of the emeralds grew in cavities and were removed by the miners, either as isolated crystals or in matrix.



**TABLE 1 (continued).** Properties of the examined emerald crystals.

Sample no. and locality	Matrix specimen dimensions (mm)	Emerald crystal dimensions (mm) <sup>a</sup>	Weight <sup>b</sup>	Crystal faces <sup>c</sup> and habit	Surface features of emerald crystals	Remarks	Figures
13: Chivor	Crystals on gray shale, 44 × 29	Three aggregates of nine, eight, or three parallel crystals; largest L 16.5, D 6.5–7.5	31.1 g	<i>c, m, a</i> ; columnar	Indentations on <i>c</i> of all crystals, growth steps on prismatic faces	Associated minerals: calcite, dolomite, albite, pyrite	12C and 13, B and C
14: Chivor	Crystal on black shale, 49 × 22	L 6.3, D 3.8–6.0	14.6 g	<i>c, m, a</i> ; columnar	Deep indentations on <i>c</i> , growth steps on prismatic faces	Associated minerals: calcite, albite, pyrite	14
15: Chivor	—	L 37.4, D 6.6–7.1	17.24 ct	<i>c, m, a, i, f, k</i> ; columnar	Deep indentations on <i>c</i> , growth steps on prismatic faces	Color zoning	15
16: Chivor	—	L 10.8, D 7.3–8.7	6.37 ct	<i>c, m, a, s, p</i> ; columnar	Open cup, growth steps on prismatic faces	Irregularly shaped hillocks and columns in cup	16
17: Chivor	Five crystals on black shale; 26 long, 11–20 wide	cup 1: L 5.5, D 2.5–3.0 cup 2: D 3.0 crystal 1: L 12.0, D 2.0 crystals 2 and 3 are smaller crystal 3: L 3.8	4.5 g	<i>c, m</i> ; columnar	Open cups, growth steps on <i>m</i>	Associated minerals: albite, calcite, pyrite; irregularly shaped hillocks and columns in both cups	2 and 17
18: Chivor	—	L 19.6, D 9.2–10.0	13.58 ct	<i>c, m, a, u, p, s</i> ; columnar	Open cup, openings also in <i>p</i> , growth steps on prismatic faces	Irregularly shaped framework of walls in cup	18
19: Chivor	—	L 3.0 and 7.8, D 7.3–7.5	2.68 ct	<i>c, m, a, i, u, p, s, f, k</i> ; columnar	Half cup	Internal channels filled with fine-grained beryl	19
20: Chivor	—	L 13.0, D 3.5–4.5	1.96 ct	<i>c, m, p</i>	Partial cup	Pyrite at the bottom of the cavity, internal channels	20, left
21: Chivor	—	L 9.0, D 4.0–5.5	1.41 ct	<i>c, m, a</i>	Partial cup	Pyrite at the bottom of the cavity	20, right
22: Chivor	—	L 14.4, D 3.4–4.4	1.63 ct	<i>c, m, a</i> ; elongated columnar, slightly conical	Etch pits and grooves on prismatic faces	Slightly conical tube along the <i>c</i> -axis through the complete crystal	21 and 22

<sup>a</sup>L represents the length of the emerald crystal, D represents measurements of diameters between two *m* prismatic faces.

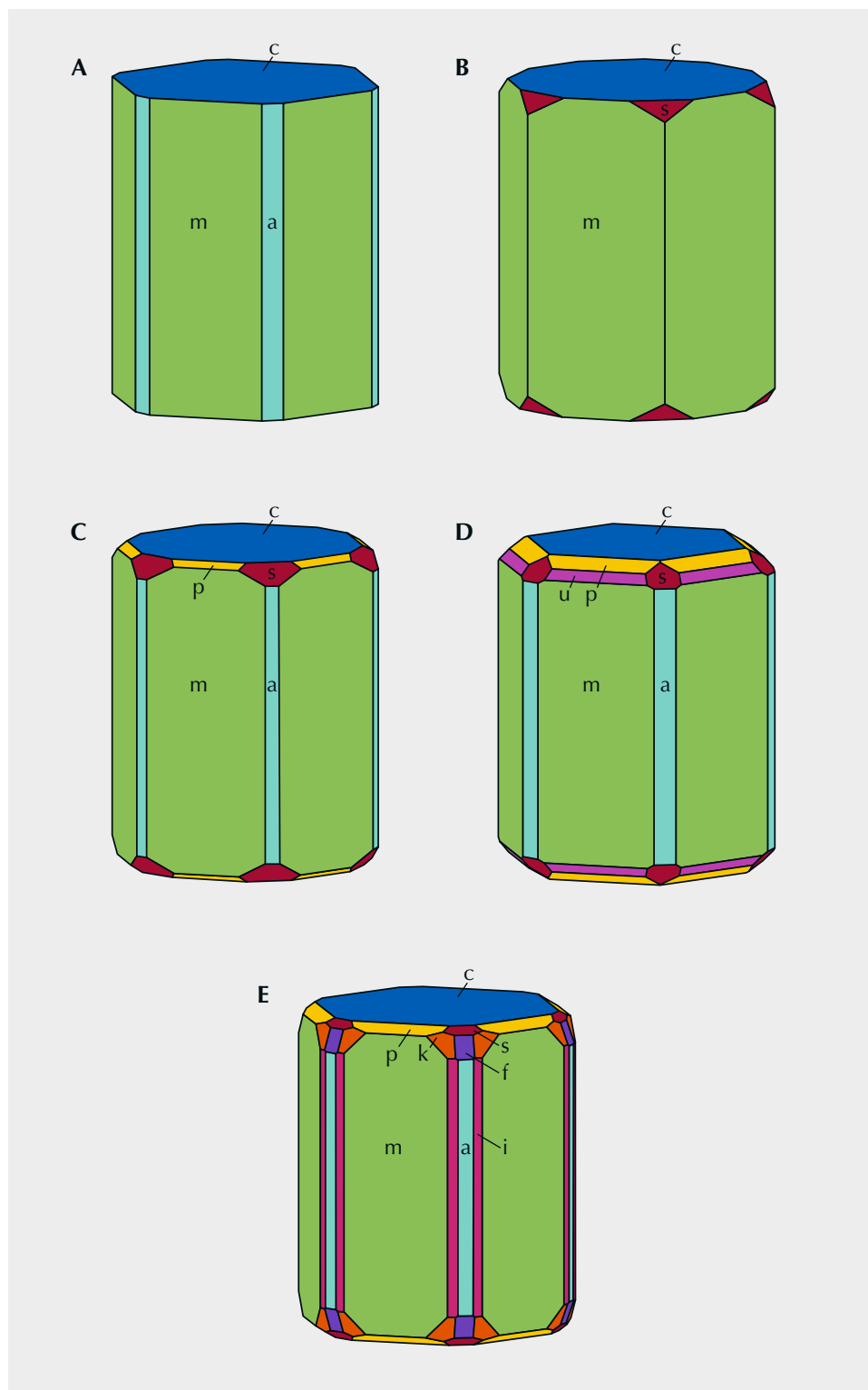
<sup>b</sup>Weights of samples with emerald crystals in matrix are given in grams; weights of isolated emerald crystals are given in carats.

<sup>c</sup>Based on a cell with a:c ratio of 1:0.996; basal pinacoid *c* {0001}, first-order hexagonal prism *m* {10 $\bar{1}$ 0}, second-order hexagonal prism *a* {11 $\bar{2}$ 0}, dihexagonal prism *i* {21 $\bar{3}$ 0}, first-order hexagonal dipyrramids *p* {10 $\bar{1}$ 2} and *u* {10 $\bar{1}$ 1}, second-order hexagonal dipyrramids *s* {11 $\bar{2}$ 2} and *f* {33 $\bar{6}$ 2}, and dihexagonal dipyrramid *k* {21 $\bar{3}$ 1}.

For the evaluation of growth history, it is important to look at all morphological features of a sample as a summary and not only at isolated crystal faces. The morphology of the samples was examined visu-

ally, and crystal faces were determined by goniometric measurements and/or by the measurement of angles between crystal faces in the microscope.

The samples were studied exclusively by nonde-



*Figure 3. Morphology of Colombian emeralds observed in the present study. A–D: Most samples show dominant m prism and basal c faces; occasionally we also observed smaller a prism faces in combination with s, p, and u hexagonal dipyramids. E: Furthermore, two of the crystals showed additional small i prism faces in combination with f and k dipyramids. Drawings by K. Schmetzer.*

structive methods, especially by optical microscopy at low magnification (up to 80×). A few transparent samples of appropriate size were also examined in immersion using benzyl benzoate as the immersion

liquid. For such rare materials (isolated emerald crystals or matrix specimens), no destructive techniques (e.g., slicing or polishing of the crystals) could be applied nor any coating of the samples for an investiga-

tion at higher magnification in the scanning electron microscope.

In one sample, the identity of the substances filling the growth tubes was determined by a combination of X-ray diffraction (using a Bruker D8 Advance Eco X-ray diffractometer), energy-dispersive X-ray fluorescence (EDXRF, using a portable Bruker Tracer III-SD EDXRF analyzer), and Raman spectroscopy (using an Ahura First Defender portable Raman device). Part of the filling could be removed easily with a needle and was made available in that way for examination.

## RESULTS AND DISCUSSION

**General Aspects.** Some general aspects of crystal morphology will be described first, which can help to characterize the individual samples.

**Morphology.** Most isolated emerald crystals were slightly distorted (e.g., with different diameters measured between opposite prisms) but with clearly defined faces. Nine of these crystals were columnar to prismatic, and six were conical, some of them with prismatically developed areas. The emeralds on six of the seven matrix samples showed columnar to prismatic habit, and only one crystal on matrix was tabular with significant differences of thickness between prism faces in different directions.

Idealized crystal drawings are presented in figure 3. Considering the columnar to prismatic crystals and the tabular crystals in our sample set, dominant crystal faces were the first-order hexagonal prism  $m$   $\{10\bar{1}0\}$  and the basal pinacoid  $c$   $\{0001\}$ . These were frequently in combination with a smaller second-order hexagonal prism  $a$   $\{11\bar{2}0\}$ , and/or first-order hexagonal dipyramids  $p$   $\{10\bar{1}2\}$  and  $u$   $\{10\bar{1}1\}$ , and/or a second-order hexagonal dipyramid  $s$   $\{11\bar{2}2\}$ . In addition, two

crystals showed small dihexagonal prism faces  $i$   $\{21\bar{3}0\}$ , in combination with the second-order hexagonal dipyramid  $f$   $\{3362\}$  and the dihexagonal dipyramid  $k$   $\{21\bar{3}1\}$ . The faces determined on conical or at least partly conical crystals were identical to those observed on all other emeralds.

So far, the morphology is consistent with the published literature data above and information determined from photos of Colombian emerald crystals in numerous publications. The two dipyramids  $f$  and  $k$  are rarely found in Colombian samples, as previously mentioned by Vrba (1881).

**Growth Features on Crystal Faces.** Numerous Colombian emerald crystals from the present study showed growth features on crystal faces, especially elongated stepped surface structures on  $m$  prism faces (figure 4, A and B). These as-grown surface features represent layered growth in subsequent growth steps and resemble contour lines in topographic maps. In sample 1 shown in figure 4, different layers are already seen with the unaided eye, but normally the steps between subsequent layers are smaller and need examination by optical microscopy. To best observe the layered surface structures with optical microscopy, reflected light is ideal (figure 4C). Similar growth layers on the basal pinacoid of the majority of Colombian emeralds, if present, are less pronounced and often not observable at the magnification applied in this study.

These observations are consistent with the existing literature about growth mechanisms of beryl crystals. Similar stepped growth layers of surfaces of beryl crystal faces have been described by various authors (von Kokscharow, 1881; Himmel and Schmidt-Zittel, 1927; Griffin, 1951a,b; Seager, 1953; Grigor'ev, 1965;

Figure 4. A and B: In sample 1 (11.8 mm in length), stepped surface structures on different prismatic  $m$  faces of a Colombian emerald crystal represent layered growth in subsequent growth steps. C: Best observation of such layered stepped growth structures is achieved in reflected light. Photos by G. Martayan (A and B) and K. Schmetzer (C; field of view 6.0 mm).





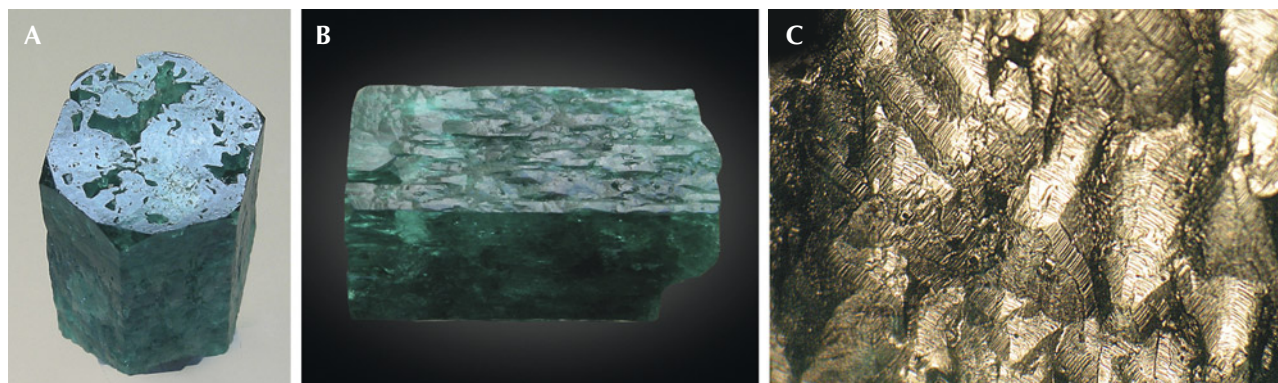


Figure 5. Sample 2 (18.0 mm in length), a columnar emerald that has been heavily corroded by natural etching. A: The basal plane shows irregularly shaped openings to larger cavities below this face. B: The *m* prism planes show etch structures, especially irregularly oriented grooves between hillocks. C: Details of the etch structures with grooves and hillocks, seen on the *m* prism face in image B, which are covered by micro-steps as seen in reflected light. Photos by K. Schmetzer; field of view 3.5 mm (C).

Sinkankas, 1981; Sunagawa and Urano, 1999; Sunagawa, 2003; Demianets et al., 2006).

#### Characteristics of Individual Groups of Samples with Respect to Growth or Post-Growth Surface Patterns.

*Emeralds with Dissolution Features.* A group of three samples with “common” habit (samples 2, 3, and 4) showed pronounced dissolution features with partially dissolved (corroded) crystal surfaces. In the groups describing samples with extraordinary and rare habits in the following sections, some emeralds that have undergone dissolution are also mentioned. To understand the various observations, one general aspect should be mentioned at the beginning of this section: Some of the crystals examined in this study show strong etching and dissolution features only at part of the surface. This indicates that only these parts of the emerald crystals were exposed to the aggressive dissolution fluid and the other parts of the crystals were shielded from the fluid. It can be assumed that such shielding processes were caused by different minerals of the assemblage found in Colombian emerald deposits, which were in close contact with the emeralds’ as-grown surfaces (crystal faces). In the present state, these minerals are at least partially dissolved or broken away, now exposing the crystal faces of the emeralds for visual examination.

Sample 2 (figure 5A) with columnar habit (see figure 3B) shows distinct corrosion features. The basal face reveals several irregularly shaped openings to a cavity below this plane, which is larger than the openings, extending widely into the crystal. Prism faces are completely covered by etch structures (figure 5B).

Between the deep irregular grooves, small hillocks are observed that show micro-steps on the surface (figure 5C). These micro-steps resemble the pattern produced as fine structure in etch pits by artificial dissolution of beryl crystals (see box A). It is unknown and must be examined in additional samples, which are not available at the moment, whether this pattern and the form of the irregularly shaped grooves are related to the common inclusion features of Colombian emerald (e.g., feathers and healed fractures).

Sample 3 with tabular habit shows a completely and irregularly dissolved surface of the *m* prism, but the smaller *a* prism is not corroded (figure 6A). Only small parts of the original surface of the *m* prism are still present, reflecting under appropriate illumination (figure 6B). In this case, we can speak of a preferred dissolution of the *m* prism compared to the *a* prism face. The basal face shows irregularly terminated openings to deep cavities, but part of this face contains no dissolution features (figure 6C), and therefore it might be concluded that this face was shielded by minerals from the dissolution fluid.

Sample 4 shows long prismatic habit with first- and second-order *m* and *a* prism faces (figure 3A). Toward one end of the crystal, the prism faces show growth steps of an almost undistorted surface (figure 7A). This part represents about one-third of the length of the crystal. The remaining part is extensively etched, deeply corroded on *m* faces and to a much lesser extent on *a* prism faces (figure 7, A and B). In some areas, the *m* prism faces are completely dissolved to an area with numerous grooves and hillocks. In contrast, we observe highly reflective

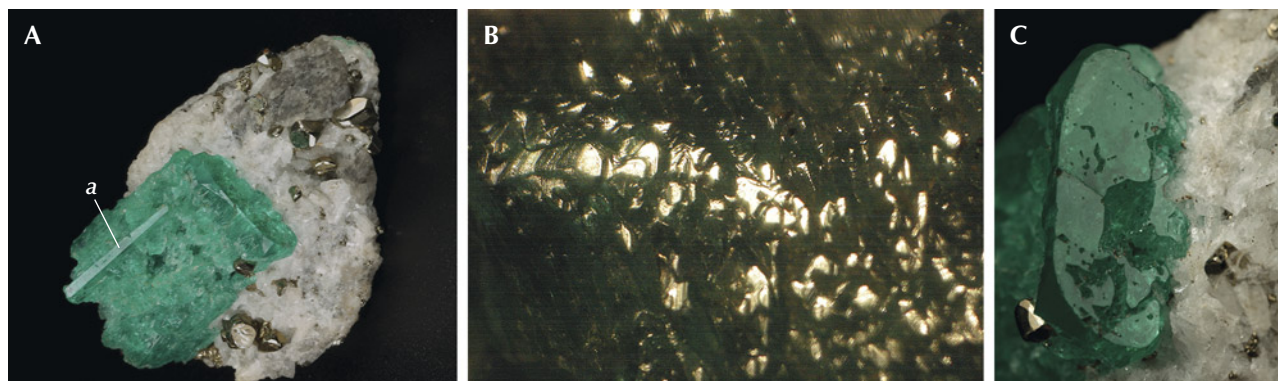


Figure 6. A: Sample 3 (23.6 mm in length), a heavily corroded emerald crystal with a completely dissolved surface related to the *m* prism face, but with a small protruding area related to the *a* prism that is almost free of corrosion. B: Only small areas of the original surface of the *m* prism are still reflective. C: The *c* basal pinacoid reveals irregularly shaped holes leading to cavities below this face. Photos by G. Martayan (A and C), and K. Schmetzer (B); field of view 7.6 mm (B).

ledges of the *a* prism protruding from the dissolved *m* growth sectors (figure 7B). This indicates that, as also observed in sample 3, the *a* prism sectors were less intensely corroded. At the end, one basal pinacoid is only influenced slightly or not at all by corrosion, while the other basal plane on the other end of the crystal is heavily dissolved (figure 7, C and D).

**Evaluation.** Comparing these observations with descriptions from the known literature (box A), it is

concluded that samples 2–4 have undergone a heavy natural dissolution process in which the original surfaces of the crystal faces were partially or completely dissolved by natural etching. In other words, the patterns observed in our Colombian samples are related to intense natural etching processes causing at least a partial dissolution of the as-grown crystal faces and creating deep cavities and irregular grooves between hillocks with stepped surfaces. All three crystals show

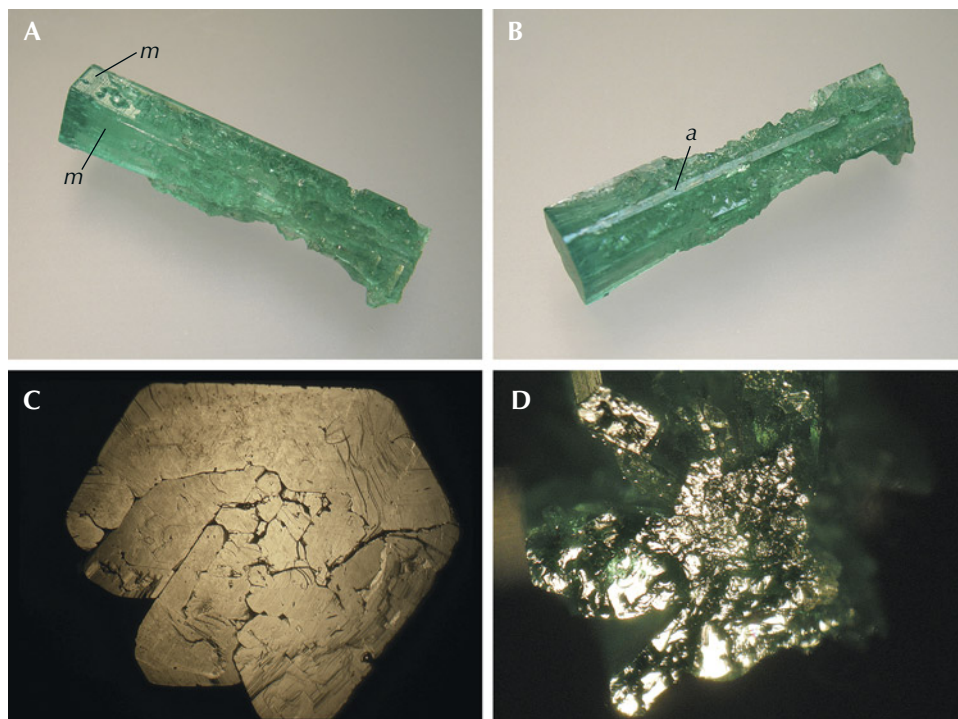


Figure 7. Sample 4 (31.1 mm in length), a columnar emerald that has been heavily corroded by natural etching. One end of the crystal (A, upper left) still shows natural crystal faces, while the rest of the sample shows completely dissolved *m* prism faces (A and B) and highly reflective but still undissolved smaller *a* prisms (B). At one end, the basal face is only slightly corroded (C), while the basal face at the other end of the crystal is heavily corroded (D). Photos by K. Schmetzer; field of view 9.5 mm (C and D).



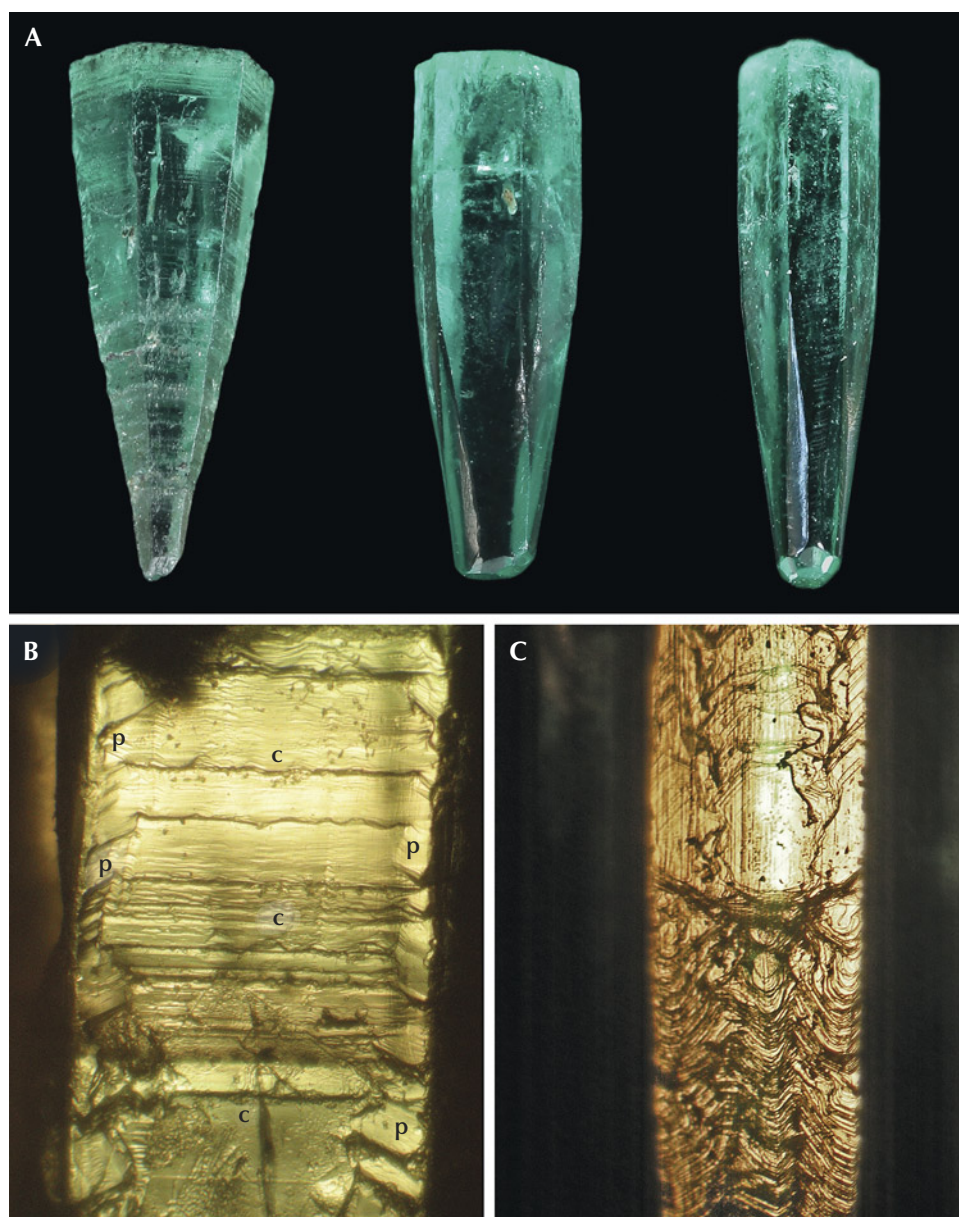


Figure 8. A: Emerald crystals with pyramidal or partly pyramidal habit: sample 5 (left, 10.0 mm in length), sample 7 (center, 8.8 mm in length), and sample 6 (right, 8.8 mm in length). B: Surface texture of the pyramidal emerald crystal (sample 5) showing growth lines related to the basal pinacoid c (center) and pyramidal faces p (left and right). C: Complex surface texture of a partly pyramidal, partly prismatic crystal (sample 7) showing a complex pattern related to pyramidal faces (lower part) and to basal, pyramidal, and prism faces (upper part). The growth direction of the crystals shown in A–C is always from the bottom to the top. Photos by G. Martayan (A) and K. Schmetzer (B and C); fields of view 2.4 mm (B) and 2.4 mm (C).

various dissolution features on different surfaces. Sample 4, for example, shows heavy dissolution from one end with a dissolved basal *c* face to almost two-thirds of its length, while the other end with basal *c* face to about one-third of its length is barely affected. In samples 2 and 3, it seems that the basal *c* faces were partially shielded from the dissolution fluid.

An emerald with pointed forms (sample 10) caused by natural etching will be described in the next section.

*Emerald Crystals with Conical Habit or Conical Zones.* Several samples showed, at least partly, a conical habit, comparable to six-sided pyramids.

Referring to the observations made in this study for samples 5–10, the authors must underscore that with the optical methods applied, we only can describe the features representing the last stage of growth and/or dissolution.

Three relatively small emerald crystals, designated samples 5, 6, and 7, show the habit of a six-sided pyramid or the habit of a six-sided pyramid combined with a six-sided prism (figure 8A). The surface texture of the pyramidal sample 5 shows growth steps related to basal and pyramidal growth layers (figure 8B). The basal growth layers are visible as striations perpendicular to the *c*-axis, which indicate alternating basal and dipyramidal faces. The surface



texture of samples 6 and 7 is more complex. In the pyramidal parts, growth steps related to basal and pyramidal layers are seen; in the prismatic parts, the crystals show textures related to basal, dipyrarnidal, and prism faces (figure 8C). These observations were confirmed in immersion with transmitted light (not shown). In the conical parts of all three samples, no growth layers related to prism faces were developed. In contrast, the prismatic parts of samples 6 and 7 are quite “normal,” with growth zones related to basal, pyramidal, and prismatic faces.

Sample 8 consists of a conical and a tabular part (figure 9). At the upper (conical) end of the crystal, we observe a perfect basal face in combination with part of

the *m* prism faces and *s* and *p* dipyrarnids (see figure 3C). Next to this end of the crystal, we observe a conical part, followed by a tabular area. The diameter of this tabular area is slightly larger than the crystal's diameter at the upper end. Growth steps are found on the surfaces of the conical area (figure 9C) and on the tabular part. Only the outer area of the tabular part contains growth channels (hollow tubes) parallel to the *c*-axis. In transparent areas of the conical part, internal growth planes parallel to the basal pinacoid *c* and parallel to two hexagonal dipyrarnids *p* and *u* are observed in immersion (figure 9D). These features indicate growth in subsequent layers, but without development of prismatic growth sectors in this area of the crystal.

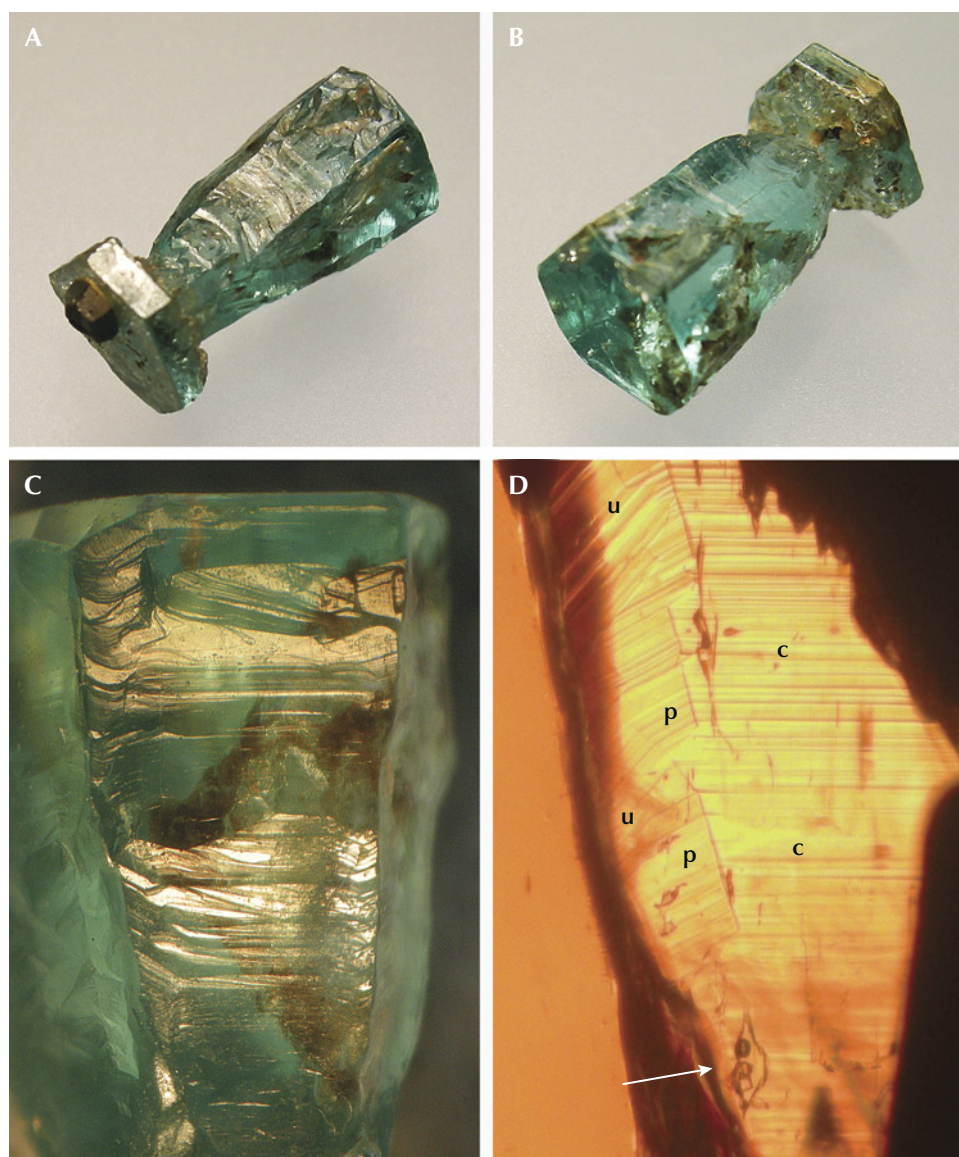


Figure 9. A and B: Sample 8 (9.8 mm in length), an emerald crystal with conical shape and a tabular part, with a pyrite crystal attached to the tabular part. C: Growth steps on the surface of the conical part of the crystal. D: Viewed in immersion, internal growth planes parallel to the basal face *c* and parallel to the hexagonal dipyrarnids *p* and *u*, as well as a three-phase inclusion with two salt cubes and one gas bubble in a liquid-filled cavity (arrow); the *c*-axis runs vertically. Photos by K. Schmetzer; fields of view 5.7 mm (C) and 2.2 mm (D).

Sample 9 is of conical shape. At the upper (wide) end of the crystal, we observe a perfect basal face in combination with part of the *m* prism faces and *s* and *p* dipyrramids (figures 3C and 10A). The *m* prism faces reveal growth steps (figure 10B), while the conical part is covered with finer surface structures. We observe irregularly shaped grooves, hillocks covered by micro-steps, and openings of deep cavities or indentations (figure 10C). Comparing these surface textures with those of corroded emerald samples 2, 3, and 4, these parts of sample 9 were exposed to an aggressive fluid causing dissolution. Within some of the indentations mentioned, residual dark gray carbonaceous material is captured (figure 10D).

Sample 10 shows an even more complex morphology. The crystal consists of a conical part that is followed by a prismatic part at the lower end of the crystal (figures 1 and 11A). The prismatic part is narrower than the conical part at its upper end. The surfaces on both parts show growth steps (figure 11, B and C). Protruding from both parts are two areas with extensions of growth sectors confined by the second-order hexagonal prism *a*, which are as thick as the upper end of the conical part (figure 11A). The basal pinacoid is covered by tiny pointed hillocks (figures 1 and 11D). By varying the crystal's orientation with respect to the light source, positions can be found

where multiple small crystal faces covering different hillocks reflect light simultaneously (figure 11D).

**Evaluation.** The growth history of natural beryl crystals frequently shows multiple subsequent growth steps that might be separated by partial dissolution from natural corrosion and etching. The different steps of growth history of such samples have been characterized by a combination of optical and X-ray topography methods, especially for oriented slices of the original crystals (Scandale et al., 1990; Sunagawa and Urano, 1999; Sunagawa, 2003).

In our study, all samples of this group show one common morphological feature: a tapered appearance, at least in parts of the crystal. This feature is caused by a growth process in which no prismatic growth sectors were developed during crystal growth. This indicates that the conical appearance is caused by basal and pyramidal sectors growing together, which are seen on the surface of the crystals in reflected light or in immersion in transmitted light. In the conically developed sample 5, we observe only such basal and pyramidal growth layers. Samples 6 and 7, in addition to a conical part, developed prismatic parts in later growth stages (see again figure 8).

Samples 8, 9, and 10 are emerald crystals with an even more complex growth history. In all three samples we observe growth stages in which basal and

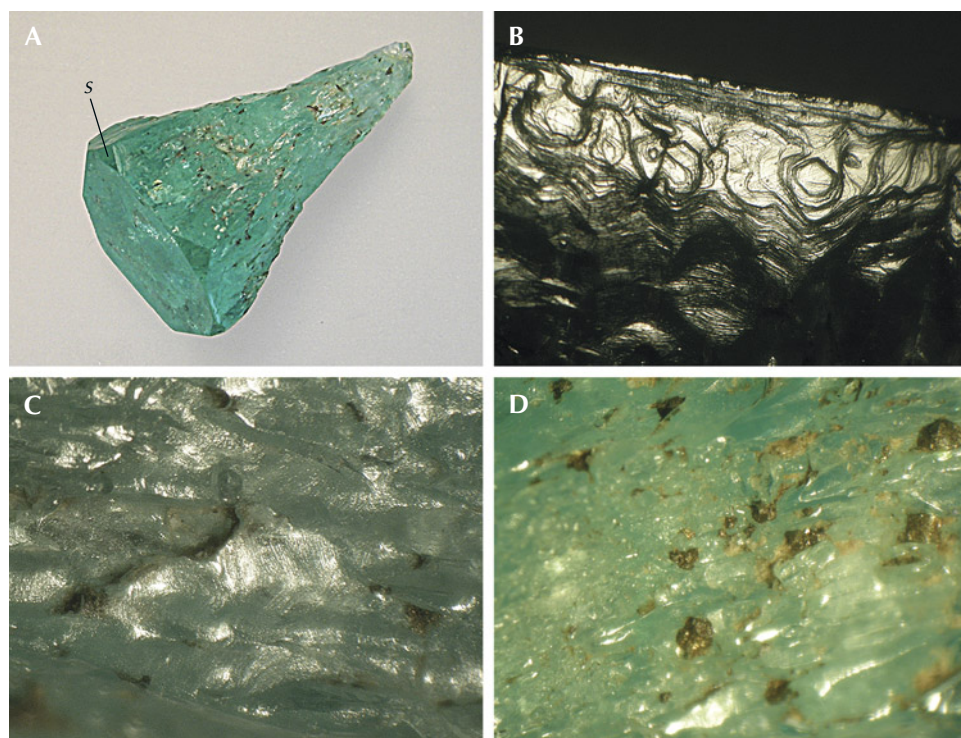


Figure 10. A: Sample 9 (20.8 mm in length), an emerald crystal with conical shape, with basal pinacoid *c*, small *m* prism faces, and hexagonal *s* dipyrramids. B: Growth steps on the surface of one of the *m* prism faces, viewed almost perpendicular to the *c*-axis. C: Hillocks with fine micro-steps between irregularly shaped grooves on the surface of the conical part. D: Residual dark gray carbonaceous material captured in indentations on the surface of the conical part. Photos by K. Schmetzer; fields of view 4.5 mm (B), 3.5 mm (C), and 7.6 mm (D).



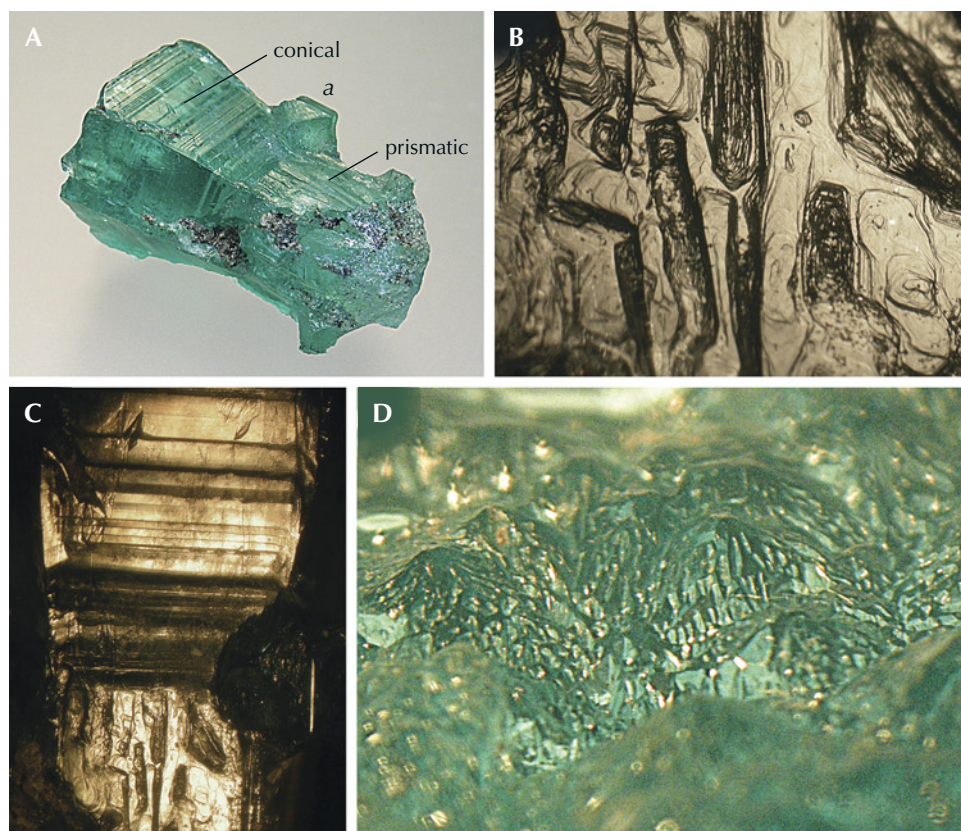


Figure 11. A: Sample 10 (25.0 mm in length), an emerald with conical habit in the upper left and prismatic habit in the lower right; the base is covered with numerous hillocks; a protrusion at the conical part represents a growth sector confined to the prism *a*. B: Stepped surface texture of the prismatic part. C: Growth steps at the prismatic part (bottom) and the conical part (top), and the *c*-axis runs vertically. D: On the basal face, the surfaces of the hillocks consist of numerous small faces that reflect light; viewed oblique to the *c*-axis. Photos by K. Schmetzer; fields of view 5.7 mm (B), 9.5 mm (C), and 5.0 mm (D).

dipyramidal growth sectors were developed, but without development of related prismatic growth layers. These growth stages without formation of prismatic growth layers apply at least to part of the crystal's growth history.

In the tabular area of sample 8, we observe growth channels parallel to the *c*-axis, which were not seen in the tapered part of the crystal. The diameter of the tabular area is larger than the diameter of the conical part at its upper end. This might indicate a later partial overgrowth of a crystal with conical habit and, in this later growth period, the development of a tabular area, on top of the tapered part of the crystal (see again figure 9).

Sample 9, at its wider end, has a short prismatic area and a long, tapered cone. This cone shows dissolution features on its surface. These features indicate an etching process of the conical part after crystal growth and a subsequent growth step with the formation of prismatic layers at the end of the crystal (see again figure 10).

Sample 10 has likely undergone several growth and corrosion processes. The residual parts of prismatic *a* growth zones and the small pyramids or hillocks forming the end of the conical part of the crystal indicate strong corrosion after an initial

growth step (see references cited above). Skeletal growth (see box B and examples below) with pointed pyramids and sharp hillocks has never been mentioned in any beryl and is therefore considered very unlikely for this morphological structure.

After corrosion, we observe several subsequent growth steps, in which an area with prismatic growth layers and the conical zone with basal striations were developed. Obviously, in one of these growth steps, only basal growth layers without prismatic areas were formed. It is not completely understood whether the prismatic *m* growth sectors in the lower part of the crystal were grown before or after the conical zone with tapered surface of the crystal (see again figure 11).

*Emeralds with Incomplete Growth of the Basal Face.* Several variants of incomplete growth of the basal pinacoid were observed.

Samples 11, 12, and 13 show incomplete growth of the basal face *c*, a pattern that could be described as resembling surface indentations. Sample 11 (figure 12A) is a single emerald crystal on matrix and reveals well-developed prism and pyramidal faces. Sample 12 (figure 12B) is an aggregate of approximately 11 crystals, grown parallel to each other with somewhat different lengths. All crystals of this aggregate show



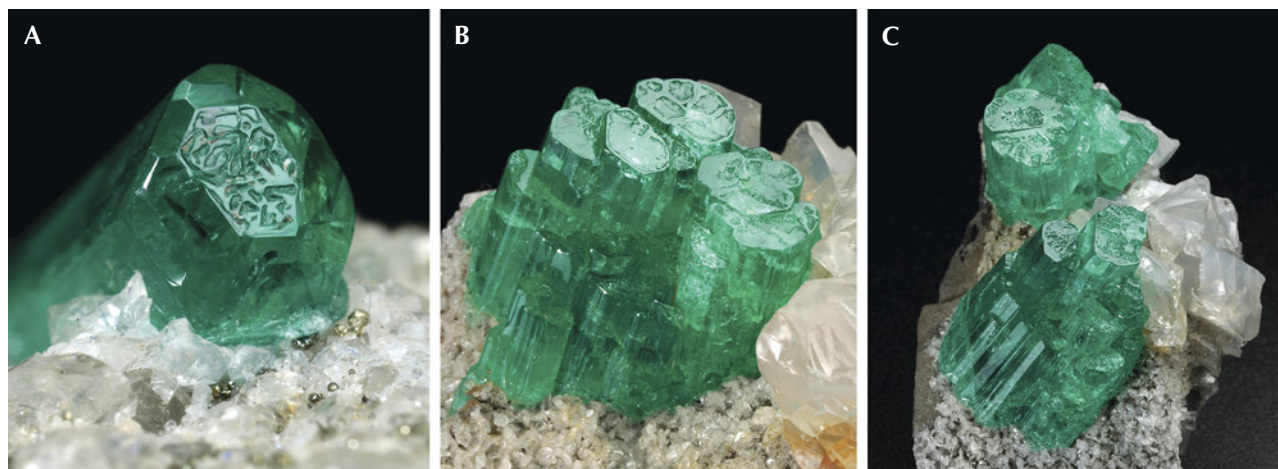


Figure 12. Emeralds with surface indentations on the basal face, developed as either a single crystal (A: sample 11, 4.1 mm in largest diameter) or as aggregates of parallel emerald crystals (B and C: samples 12 and 13 with crystal length up to 12.5 mm and 16.5 mm, respectively). Photos by G. Martayan.

incompletely developed *c* faces. Sample 13 (figure 12C) is similar to sample 12, but with three such aggregates consisting of approximately nine, eight, and three emerald crystals. All basal faces have a stepped micro-texture consisting of numerous layers stacked parallel to the *c*-axis of the emerald crystal (figure 13, A–C). These structures occasionally end at the level of the horizontal surface of the rim, but some columns

or other structures have different heights within the rim. In addition, all three samples have a step-like texture on prism faces and no etch features. A representative example of that pattern is shown in figure 13D.

Samples 14 and 15 show somewhat deeper indentations on the basal faces. Sample 14 has an almost continuous rim parallel to the basal face and inside several hillocks within the indentation zone (figure

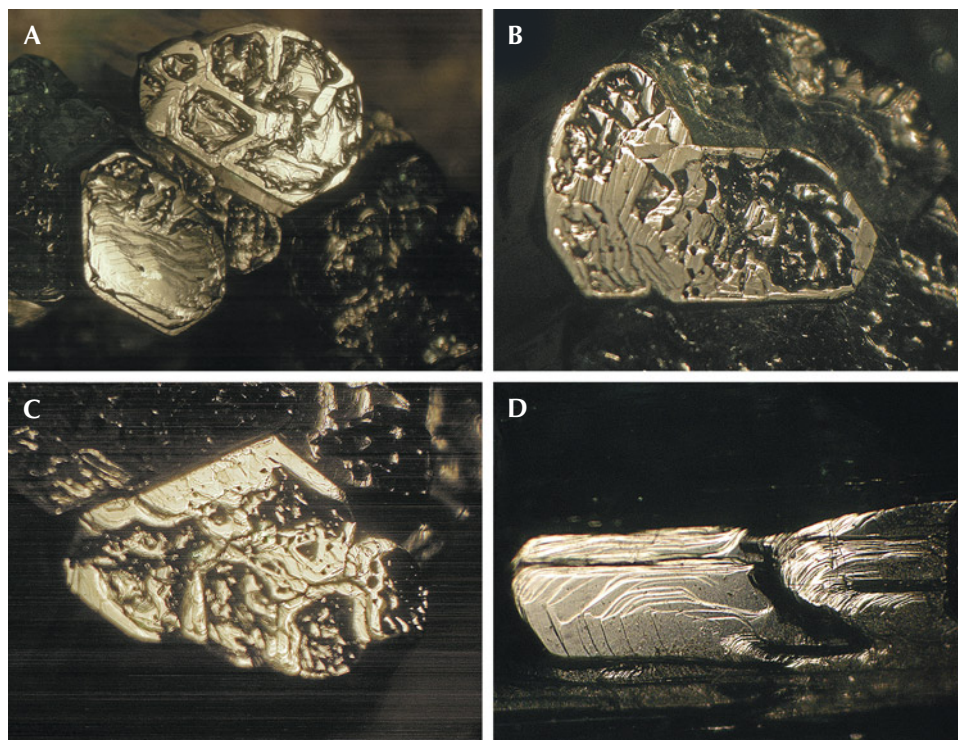


Figure 13. A–C: The stepped micro-texture of emeralds with incompletely developed basal planes shows stacked layers parallel to the *c*-axis. D: Growth steps on the prism face of one of the crystals in figure 12B. Shown here are sample 12 (A and D) and sample 13 (B and C). Photos by K. Schmetzer; fields of view 11.5 mm (A), 7.6 mm (B and C), and 4.6 mm (D).

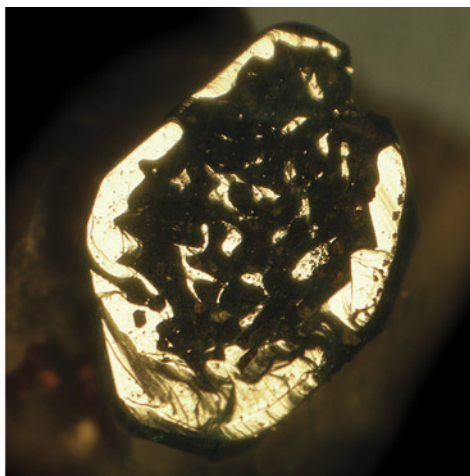


Figure 14. Left: Sample 14 (6.0 mm in largest diameter), a crystal with an almost continuous rim surrounding growth areas ending in small basal faces, but at a different height along the *c*-axis compared to the horizontal surface of the rim. Right: Reflective areas of the rim and the small columns inside this rim ending in tiny crystal faces parallel to the basal pinacoid. Photos by G. Martayan (left) and K. Schmetzer (right).

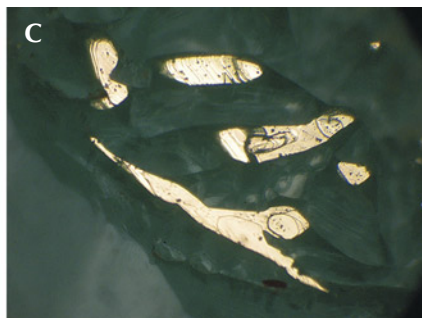
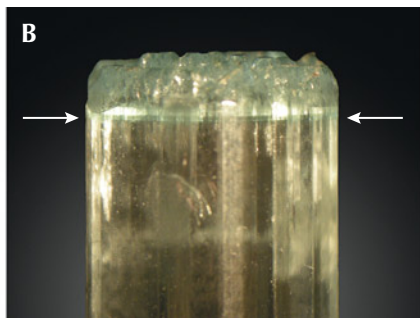
14, left). Part of these hillocks in the form of tiny columns end with faces parallel to the base (figure 14, right), but lower than the horizontal surface of the rim, which is formed by the incomplete basal face of the crystal. Sample 15, with similar appearance, shows an almost colorless region that ends in a basal face with indentations (figure 15A). The end of the crystal with these indentations is separated from the main part by a small zone with intense green coloration (figure 15B). This demonstrates that at the beginning of the growth of this zone with a length of about 1.5 mm along the *c*-axis, growth conditions were different compared to the earlier growth stages. Hollow channels parallel to the *c*-axis are found in all parts of the crystal. The areas parallel to the basal face show growth steps (figure 15C).

Several crystals were formed as “emerald cups.” Sample 16 is a crystal with columnar habit in the form of an open cup. The morphology consists of

first- and second-order prism faces in combination with first- and second-order hexagonal dipyrramids (figure 3C and figure 16, A and B). The *m* prism faces are planar; no growth steps or etch features were visible in the optical microscope with the magnification applied. The wall thickness of the cup varies between 0.8 and 1.4 mm. Irregularly shaped hillocks or columns cover the bottom of the cup, which forms a clear boundary with the other part of the crystal (figure 16C). In a view parallel to the *c*-axis, a microstructure is observed forming a three-dimensional framework of walls, columns, and hillocks at the bottom of the cavity (figure 16D). Part of the columns or irregular walls end in planar faces parallel to the basal pinacoid (figure 16, A and B).

Sample 17 is a piece of black shale covered by albite, calcite, and pyrite crystals. Embedded in this matrix are five emerald crystals (figures 2 and 17A). Two of these are columnar and hollow, forming deep

Figure 15. A: Sample 15 (37.4 mm in length), an emerald crystal with color zoning; at one end, the sample reveals a continuous rim surrounding growth areas ending in small basal faces. B: Growth and color zoning (arrows) of the crystal along the *c*-axis. C: Areas of the rim and small columns inside the rim with planes parallel to the basal pinacoid appear bright in reflected light, viewed parallel to the *c*-axis. Photos by K. Schmetzer; field of view 3.6 mm (C).





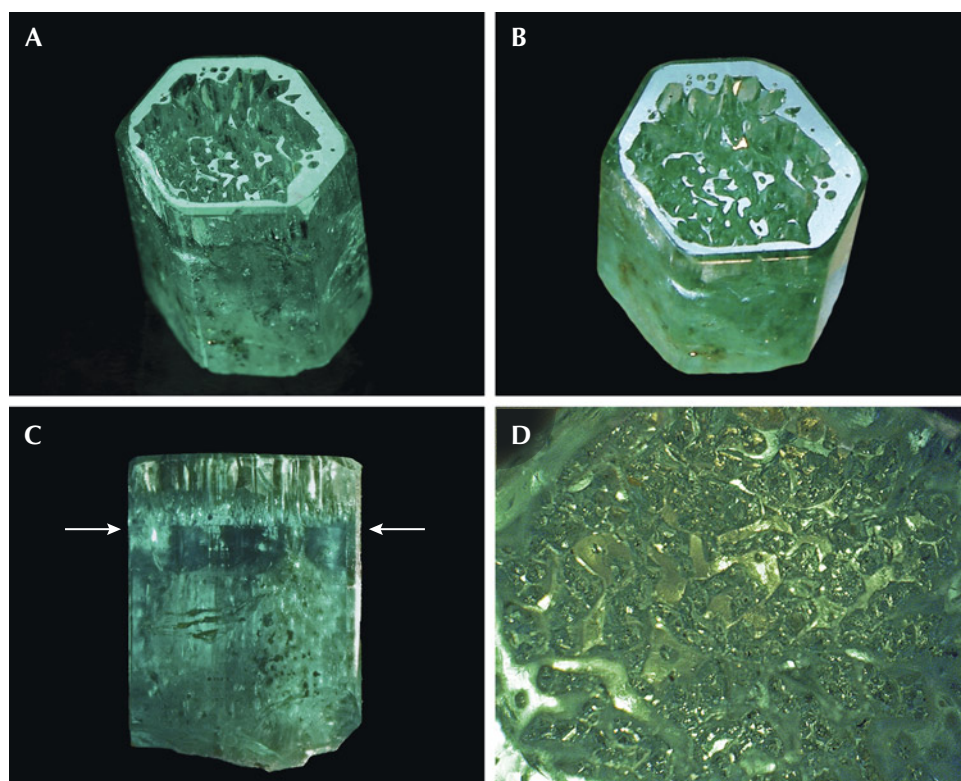


Figure 16. A: Sample 16 (10.8 mm in length), an emerald crystal developed in the form of a cup. B: The basal plane of the cup reflects together with the basal faces of small hillocks or columns in the cup. C: The bottom of the cup is located in the upper half of the crystal, as indicated by arrows. D: Framework of irregular hillocks, columns, and walls on the bottom of the cup in a view parallel to the c-axis. Photos by G. Martayan (A) and K. Schmetzer (B–D); field of view 4.6 mm (D).

cups with one open end (figure 17B). The cups have a wall thickness of approximately 0.5 mm. The bottom of each cup is covered with emerald hillocks or columns, which frequently end within the hollow

space of the cups with irregularly shaped planes. Other planes at the ends of the tiny crystals in the hollow cups reflect together with the residual basal face of the rims (figure 17C), indicating that some of

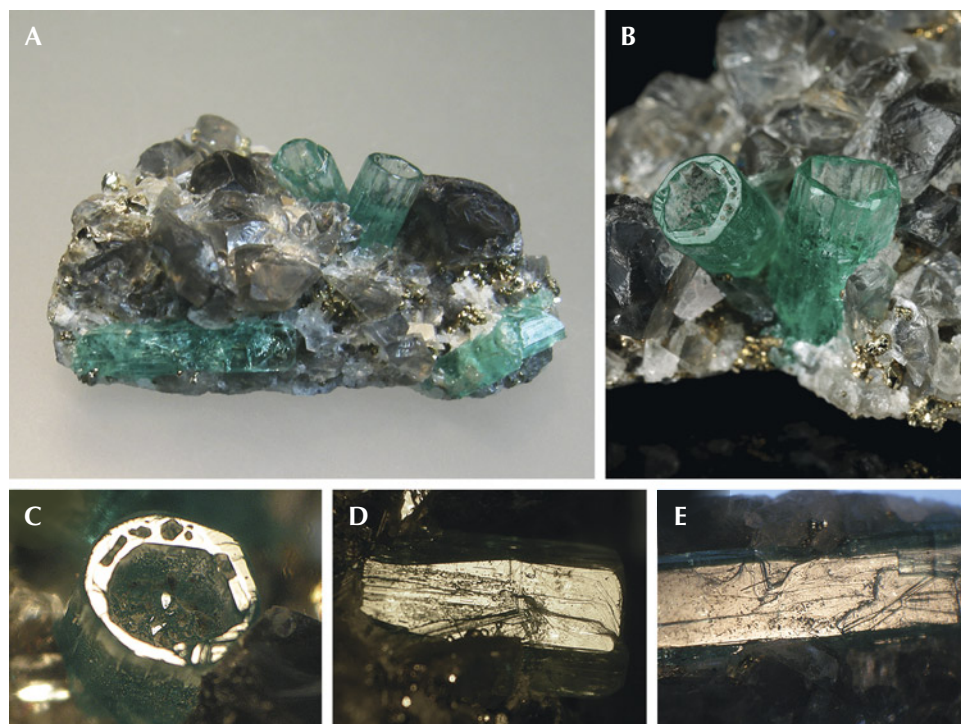


Figure 17. A: In sample 17 (26 mm long), a base of black shale (not visible) is covered with albite, calcite, and pyrite crystals. In this matrix, five emerald crystals are embedded, two of them as deep cups (center) and three as “normal” emeralds (lower right and left). B: Details of the two emerald cups (5.5 mm long on the right). C: In reflected light, the basal plane of one cup appears bright together with the basal faces of small hillocks or columns in the cup. D: Growth steps on the surface of one m prism face of a cup. E: Growth steps on the surface of the m prism face of a “normal” emerald crystal. Photos by K. Schmetzer (A, C–E) and G. Martayan (B); field of view 7.6 mm (C–E).



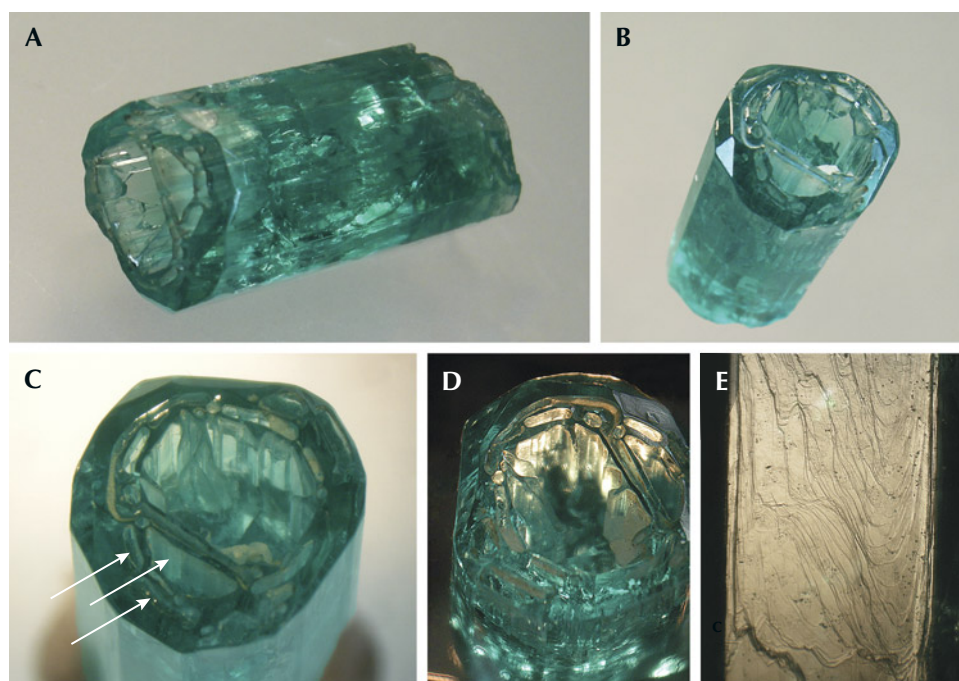


Figure 18. A and B: Sample 18 (19.6 mm in length), an emerald crystal developed in the form of a deep cup. B and C: Openings at one end are developed in the basal pinacoid but also in the largest  $p$  dipyrmaid (arrows); within the cup, a framework of irregularly shaped thin emerald walls is present. D: The crystal faces at the inner surface of the wall are oriented parallel to the outer prism faces. E: Growth steps on the surface of an  $m$  prism. Photos by K. Schmetzer; fields of view 11.5 mm (D, vertical) and 5.1 mm (E).

the hillocks or columns also end in faces parallel to the basal pinacoid. The  $m$  prism faces of the cups show growth steps (figure 17D).

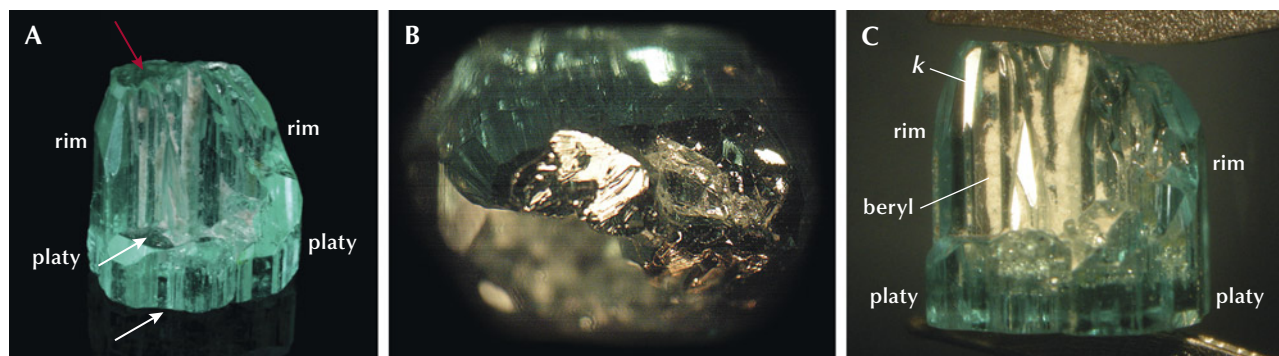
The three other emerald crystals are “common” columnar crystals with prismatic and basal faces (figure 17A), which also show growth steps on  $m$  prism faces and no etch features (figure 17E).

Sample 18 is the largest crystal, in the form of a deep open cup (figure 18, A and B). Morphologically, the columnar and somewhat distorted crystal shows several prism faces and hexagonal dipyrmaids (see figure 3, C and D). The main opening at one end is in

the basal pinacoid, but holes are also developed in the largest  $p$  dipyrmaid (figure 18C). The cup’s wall thickness ranges from 1.5 to 2.0 mm. Within the cup, a framework of irregularly shaped thin emerald walls is present (figure 18, B and C). The main walls of the inner surface of the rim are oriented parallel to prism faces (figure 18D). The outer  $m$  prism faces are covered by growth steps (figure 18E).

Sample 19 is considered to be a half cup. Formally, the sample is described as a crystal formed of two parts. The first part shows platy habit, with two basal  $c$  faces and  $m$ ,  $a$ , and  $i$  prism faces (figure 19A). On

Figure 19. A: Sample 19 (7.8 mm in length), an emerald crystal in the form of a half cup developed with two parts: as a platy part with lower and upper basal pinacoid (white arrows) and an upper curved rim surrounding about half of the area of the platy part; this rim is terminated by a small basal face (red arrow). B: Stepped surface of the basal face on top of the horizontal surface of the rim. C: View of the inner surface of the circular rim on top of the platy part, in this orientation with reflective steep  $k$  hexagonal dipyrmaids, the elongated cavities are filled with fine-grained white beryl. Photos by G. Martayan (A) and K. Schmetzer (B and C); field of view 14.5 mm (B).



the upper side of the first part of the crystal, a curved rim is formed that encircles about half of the area formed by the prism faces of the first part. This rim is considered to be the second part of the crystal. On top of this rim, we observe a small area with a stepped surface in an orientation parallel to the basal pinacoid (figure 19B). We can consider this to be the end of the second part of the crystal.

The other faces of the outer surface of the rim are the already mentioned prism faces *m*, *a*, and *i* in combination with *u*, *p*, *s*, *f*, and *k* dipyrramids. Not only are the *f* and *k* dipyramid faces rarely observed in Colombian emerald, but they are also rarely observed in the mineral beryl as a whole. These faces are steeper than the commonly observed *u*, *p*, and *s* dipyrramids and are inclined 18.2° and 18.5° to the *c*-axis. The open structure of the rim allows us to determine the faces at the inner surface of this rim, which are the common prism faces in combination with the two steep dipyrramids *f* and *k* (figure 19C). The open cavities formed at the inner surface of this rim, elongated parallel to the *c*-axis, are partially filled with a white fine-grained material, which was determined to consist mainly of beryl with small admixtures of quartz and albite (iden-

tified by a combination of X-ray diffraction, EDXRF, and Raman spectroscopy).

Samples 20 and 21 are also incomplete cups with only partially developed walls or rims. In both samples, the bottom of the internal cavity is filled with pyrite crystals, surrounded by an incomplete circle of walls (figure 20). In sample 20, the outer *m* prism faces show growth striations parallel to the *c*-axis, and the internal surface of the walls displays open channel structures, comparable to the open channels observed in sample 19. The outer and inner surfaces of the rim in sample 21 are completely flat.

*Emerald Crystal with an Internal Channel.* Sample 22 is an elongated tube that is open at both ends. From top to bottom, the external form of the tube is slightly conical, and the channel inside it is also wider at one end, following the external form of the tube (figure 21). The tube was cut at the thinner bottom of the sample, showing a hole with a small diameter (figure 21, left). This indicates that the original crystal might have been closed at its end. At the other end with the larger opening, the thickness of the tube walls ranges from about 0.2 to 0.6 mm, with an opening between 2.5 and

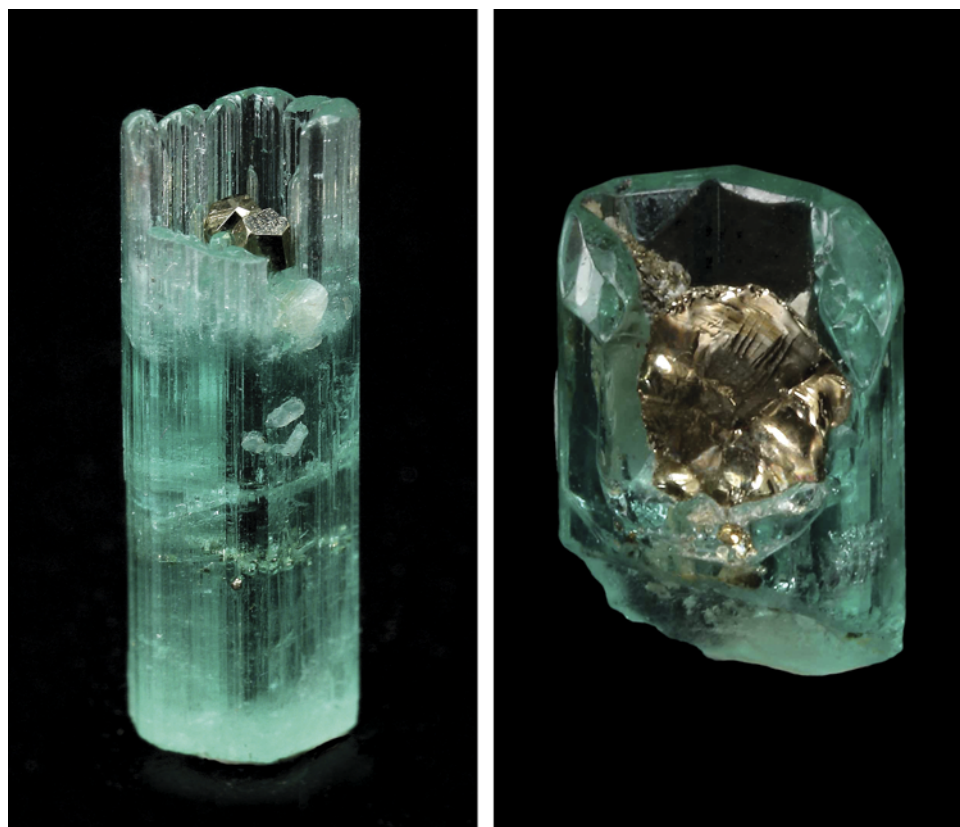


Figure 20. Emerald crystals in the form of incomplete cups with pyrite crystals at the bottom of the cavities, which are surrounded by incomplete rims. Sample 20 on the left is 13.0 mm in length, and sample 21 on the right is 9.0 mm in length. Photos by G. Martayan.





Figure 21. Emerald crystal (sample 22, 14.4 mm in length) in the form of a slightly conical hollow tube (left), with openings at both ends (right). The lower end of the crystal (right, inset) was cut artificially and shows a hole (arrow). Photos by K. Schmetzer.

3.5 mm in diameter. The diameter of the channel through the crystal at the other end is approximately 1.0 mm. Outside, the tube is terminated by *m* prism faces, which show etch features—i.e., the original surface of the tube is partially dissolved (figure 22). The horizontal part of the wall or rim oriented parallel to the basal pinacoid (see figure 21B) reveals small pits, most likely due to etching.

**Evaluation.** Samples 11–21, all originating from Chivor, show the same phenomenon: incomplete growth of the basal face, but with a different degree of development. In general, our Colombian samples display an upper rim surrounding indentations (see again figures 12 and 13) and somewhat deeper depressions (figures 14 and 15) or somewhat higher walls or rims surrounding deeper cavities (figures 16–20). In other words: The patterns observed in cups of various depths in samples 16–21 or in emeralds with deeper indentations of basal faces in samples 14 and 15 reflect deeper indentation patterns on basal planes than those observed in samples 11–13.

The rims or walls end with faces oriented perpendicular to the *c*-axis, and the outer surface of the rims are formed by various prismatic and pyramidal faces. The inner surface of the walls or rims are formed by the same faces, mainly first- and second-order prism faces and occasionally in combination with steep dipyrramids. This means that the outer and the inner outlines of the skeletal beryl walls are parallel to prismatic and steep dipyramid faces. Within these depressions or cavities, we observe irregular walls or columns, which end at different heights in the cavities with small basal faces. In samples 15 and 16, it is clearly indicated that the inner bottom of the cavities is confined to a zone of strong color zoning, which indicates a change of growth conditions at this stage of crystal growth (see again figures 15 and 16).

Considering the patterns described for beryl with skeletal and polygonal growth (box B), we conclude that the morphology seen in Colombian emerald samples 11–19 can be understood as a combination

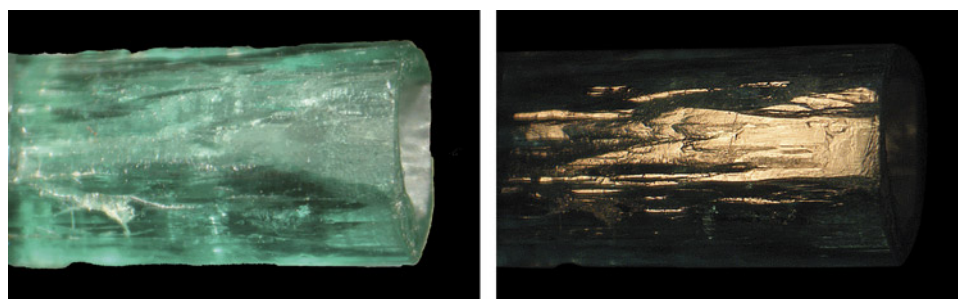


Figure 22. The surface of sample 22 is partially dissolved by corrosion—i.e., no clear reflective plane is seen. The same area of the crystal is shown in transmitted light (left) and in reflected light (right). Photos by K. Schmetzer; field of view 9.5 mm.

of both growth phenomena: skeletal growth of the walls and polygonal growth of columns and walls inside the cavities. Or we could describe the pattern observed as the growth of a dominant wall and the growth of small columns or pyramids within the area surrounded by the rim. Samples 20 and 21 clearly show inhibited growth of emerald (skeletal growth) due to pyrite obstacles, forming cavities with incomplete walls.

Sample 22, the elongated emerald tube, also originates from Chivor. Considering samples 11–21 and the heavily corroded samples 2–4, our understanding of etch patterns in beryl (summarized in box A), and our knowledge about the surface structure of non-corroded emerald crystals (sample 1, figure 4, and other examples in this paper), we interpret the growth history of this sample as skeletal growth followed by etching and partial dissolution of the outer and inner faces of the crystal, i.e. the outer and inner surfaces of the walls, but with no regrowth after etching.

Pignatelli et al. (2022) explained the growth of several Colombian emeralds developed as cups with conical or prismatic shape simply as etching processes, without taking skeletal growth into consideration. While we take into consideration a combination of skeletal growth and post-growth etching for one sample (see description and growth evaluation of sample 22), we cannot support the idea that all growth structures and morphological patterns of samples 11–22 are due to “simple” etching processes. We conclude that, for samples 11–21, they are not even partly related to etching processes.

To support our conclusions with further arguments, we observed several growth features in this group of samples that are not consistent with the idea of etching, starting at an as-grown basal plane. In other words:

- Etching would not create internal prism faces, which form the dominant pattern of inner surface of the circular rims.
- Etching would not stop and form the bottom of cavities just at the height of a strong color zoning along the *c*-axis of the crystals.
- Etching would form stepped surfaces and cavities, but in our samples we observe instead the presence of small basal faces at the end of pyramids or columns of different height within the cavities.
- The layered appearance of the surface of the rim and the *m* prism faces of the crystals does not reflect etching structures.

All these features indicate that the described morphology of this group of crystals cannot be explained simply by etching processes of the basal face. It cannot be assumed that the different morphological forms described are due to etching, starting at one planar basal face and leaving the rest of the crystal, especially all prism faces, without any clear sign of etching.

### Comparison with Properties Observed in Cut Stones.

It has already been mentioned in various studies that the heavily included areas between the transparent basal and prismatic growth sectors of Colombian trapiche emerald are intensely corroded (e.g., Bernauer, 1926; Nassau and Jackson, 1970; Pignatelli et al., 2015). In general, Colombian trapiche emeralds consist of a basal growth sector in the form of a tapered core and six prismatic growth sectors. The core and the six prismatic growth sectors and each of the prismatic sectors are separated from others by areas with high concentration of mineral inclusions and carbonaceous material. The basal growth sector mainly consists of basal and occasionally of pyramidal growth layers, but without any prismatic growth areas.

Corrosion, in general, commences at crystal defects that could be lattice defects or areas at trapped inclusions. Sample 9 described here might represent the final stage of such corrosion processes. The general appearance is reminiscent of the central tapered core of trapiche emerald (figure 23). Furthermore, we observed etch structures and residual dark gray carbonaceous material. This indicates that the tapered sample examined in this paper might be the core of a trapiche emerald that was separated from its prismatic growth zones by etching processes. If this interpretation is correct, the prismatic growth layers at the upper end of the crystal (see figure 10B) might be understood as later overgrowth of the tapered crystal.

The irregularly shaped hillocks, columns, or walls within the cavities of the samples with surface indentations on basal faces—i.e., the emerald cups described in samples 11–19—resemble the internal growth structure found in the so-called *gota de aceite* emeralds (figure 24; e.g., Bosshart, 1991; Ringsrud, 2008; Hainschwang, 2008; Schmetzer, 2009; Gao et al., 2017). An overgrowth of the polygonal patterns within such a crystal, especially in crystals with shallower indentations as seen in samples 11–13 (figures 12 and 13), in further growth steps would result in emerald crystals with the characteristic *gota de aceite* structural inclusion pattern. It is plausible



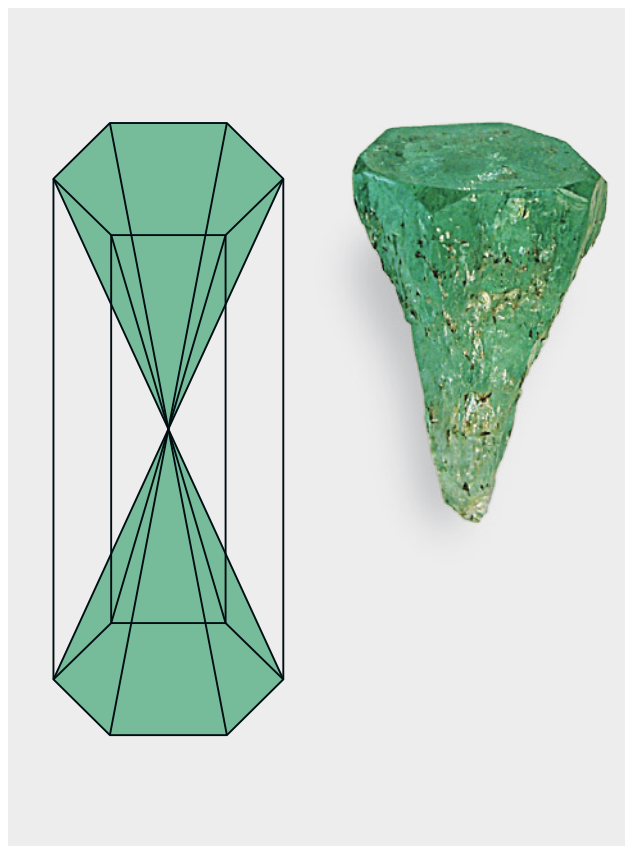


Figure 23. Left: Diagram of a trapiche emerald consisting of two tapered cores representing basal growth sectors (green) and six prismatic growth sectors (after Schmetzer, 2019). Right: The outline of sample 9 conforms to the shape of one of the basal growth sectors in trapiche emerald.

that, with changing environmental growth conditions, such further growth steps could take place. A general scenario with a multistep growth history has already been proposed by various authors (e.g., Gübelin and Koivula, 2008; Ringsrud, 2009; Schwarz and Curti, 2020; Sun and Goa, 2022).

## SUMMARY AND CONCLUSIONS

Most Colombian emeralds show a columnar to prismatic habit with growth steps or growth layers on prism faces, which can be seen occasionally even with the unaided eye. Several groups of samples with specific morphological patterns on the surface have been studied and described. However, some of the samples from our study theoretically could be grouped into several different categories, simply because they have undergone several subsequent growth stages and dissolution processes (e.g., sample 10). Because optical observation allows us to examine only the last result of such multistep growth processes, not all morphological features of the emerald crystals in the post-grown and post-dissolved state can be completely understood.

Heavily etched crystals show dissolved  $m$  prism sectors, whereas the  $a$  prism zones are less affected by the dissolution process. The deep cavities or grooves seen in the post-growth dissolved state have a stepped microstructure on  $m$  prism faces. The basal pinacoid, in some cases, reveals irregularly shaped openings to cavities below that face, but this face may also be dissolved in a way to show tiny pointed hillocks. Because the degree of etching varies within a single emerald crystal, it is concluded that such samples were partially shielded from contact with other minerals of the natural assemblage from the etching fluid.

Conically developed emerald crystals, in general, show only growth layers related to basal and dipyrarnidal growth faces, but no prismatic growth sectors were developed in such crystals. The morphology of such samples resembles the basal growth sectors of Colombian trapiche emerald.

Emerald cups showing a skeletal rim with prismatic or dipyrarnidal faces forming its outer and inner surface reveal more or less deep indentations on the basal face. In some cases, the walls or rims form deep

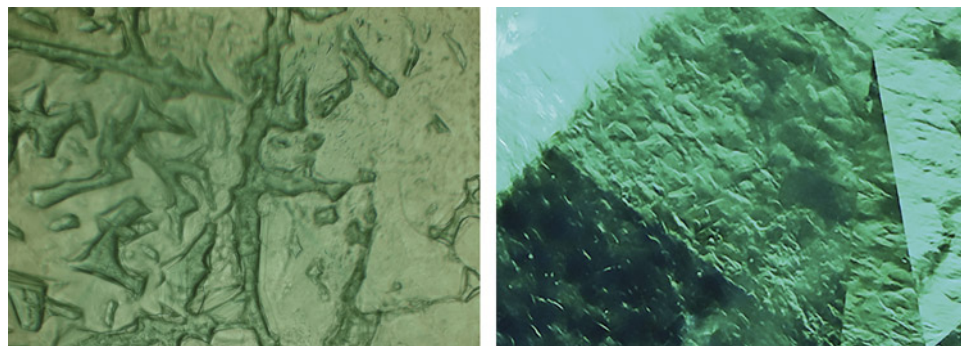


Figure 24. Patterns seen in faceted Colombian gota de aceite emeralds display numerous irregular hillocks, columns, or walls. The left image is viewed in immersion, parallel to the  $c$ -axis. Photomicrographs by K. Schmetzer (left) and M.P.H. Curti, Bellerophon Gemlab (right); fields of view 1.9 mm (left) and 1.6 mm (right).

cavities of prismatic or conical cups or even elongated central tubes within the crystal. Within the cavities of these cups, starting from a basal plane growth layer, we observe tiny columns or pyramidal crystallites, which frequently end in small basal faces. If such sur-

face structures are overgrown subsequently with new emerald, the final result would show a crystal with an internal growth structure containing an inclusion pattern resembling the pattern described as *gota de aceite* in Colombian emerald.

#### ABOUT THE AUTHORS

Dr. Karl Schmetzer is an independent researcher living in Petershausen, near Munich. Gérard Martayan is a senior geophysicist and longtime emerald aficionado residing in Paris.

#### ACKNOWLEDGMENTS

The authors are grateful to Professor H.A. Gilg and N. Preisinger for their help with X-ray diffraction, X-ray fluorescence, and Raman spectroscopy to identify the cavity fillings in one sample. We are also grateful for numerous helpful comments and suggestions of the three peer reviewers of this manuscript.

#### REFERENCES

- Arzruni A. (1894) Ein Beryllkrystall mit rhomboëdrischer Ausbildung. *Verhandlungen der Russisch-Kaiserlichen Mineralogischen Gesellschaft zu St. Petersburg*, Zweite Serie, Vol. 31, pp. 155–160.
- Bartoshinsky Z.V., Matkovsky O.I., Srebrodolsky B.I. (1969) Accessory beryl from chambered pegmatites of the Ukraine. *Mineralogical Sbornik (Mineralogicheskii Sbornik)*, Vol. 23, No. 4, pp. 382–397 [in Russian].
- Bernauer F. (1926) Die sog. Smaragddrillinge von Muzo und ihre optischen Anomalien. *Neues Jahrbuch für Mineralogie, Geologie und Paläontologie*, Supplemental Volume 54, pp. 205–242.
- Beus A.A. (1966) *Geochemistry of Beryllium and Genetic Types of Beryllium Deposits*. W.H. Freeman and Company, San Francisco.
- Bosshart G. (1991) Emeralds from Colombia (Part 2). *Journal of Gemmology*, Vol. 22, No. 7, pp. 409–425.
- Demianets L.N., Ivanov-Shitz A.K., Gainutdinov R.V. (2006) Hydrothermal growth of beryl single crystals and morphology of their singular faces. *Inorganic Materials*, Vol. 42, No. 9, pp. 989–995, <http://dx.doi.org/10.1134/S0020168506090111>
- Dem'yanets L.N., Ivanov-Schitz A.K. (2009) Beryl: Regeneration crystal growth and morphology of regeneration surfaces. *Journal of Surface Investigation. X-ray, Synchrotron and Neutron Techniques*, Vol. 3, No. 6, pp. 881–887, <http://dx.doi.org/10.1134/S1027451009060068>
- Feklichev V.G. (1963) Microcrystalline morphology and investigation of the phenomena of solution of beryllium crystals. *Trudi Institut Mineralogii, Geokhimii i Kristallochimii Redkich Elementov*, Akademija Nauk SSSR, Vol. 18, pp. 85–106 [in Russian].
- Ford W.E. (1906) Some interesting beryl crystals and their associations. *American Journal of Science*, Vol. 22, No. 129, pp. 217–223.
- Gao Y., Ng M., Carmona C., Lin Q. (2017) “Gota de aceite” effect in emerald: Observation and cause. *Gems & Technology Conference, Beijing*, pp. 95–97.
- Goldschmidt V. (1913) *Atlas der Krystallformen, Band I*. Carl Winters. Universitätsbuchhandlung, Heidelberg, Germany.
- Griffin L.J. (1951a) LXXXIX. Microscopic studies on beryl crystals. – I. Observation of uni-molecular steps. *The London, Edinburgh, and Dublin Philosophical Magazine and Journal of Science*, Vol. 42, No. 330, pp. 775–786, <http://dx.doi.org/10.1080/14786445108561306>
- (1951b) CXXXIII. Microscopic studies on beryl crystals. – II. Dislocations and the growth of {1010} prism faces. *London, Edinburgh, and Dublin Philosophical Magazine and Journal of Science*, Vol. 42, No. 335, pp. 1337–1352, <http://dx.doi.org/10.1080/14786445108560951>
- Grigor'ev D.P. (1965) *Ontogeny of Minerals*. Israel Program for Scientific Translations Ltd., Jerusalem.
- Gübelin E.J. (1944) Gemstone inclusions. *G&G*, Vol. 4, No. 12, pp. 174–179.
- Gübelin E.J., Koivula J.I. (2008) *Photoatlas of Inclusions in Gemstones*, Volume 3. Opinio Publishers, Basel, Switzerland.
- Hainschwang T. (2008) Extraordinary “gota de aceite” emerald submitted to the lab. *GEMLAB Research Newsletter*, Vol. 6.
- Hills R.C. (1890) Etched beryls from Mount Antero, Colorado. *Proceedings of the Colorado Scientific Society*, Vol. 3, No. 2, pp. 191–192.
- Himmel H., Schmidt-Zittel H. (1927) Wachstumsakzessorien am Beryll. *Zentralblatt für Mineralogie, Geologie und Paläontologie*, Abt. A., 1927, pp. 118–125.
- Honess A.P. (1917) On the etching figures of beryl. *American Journal of Science*, Vol. 43, No. 255, pp. 223–236.
- (1929) The theory of crystal etching and its significance in the classification of crystals. *Proceedings of the Pennsylvania Academy of Science*, Vol. 3, pp. 52–59.
- Hunt T.S. (1892) *Systematic Mineralogy Based on a Natural Classification*, 2nd ed. The Scientific Publishing Co., New York.
- Johnson P.W. (1961a) The Chivor emerald mine. *Journal of Gemmology*, Vol. 8, No. 4, pp. 126–152.
- (1961b) All about emeralds – natural or synthetic. *Lapidary Journal*, Vol. 15, No. 1, pp. 118–131.
- Johnston W.D. (1945) Beryl-tantalite pegmatites of Northeastern Brazil. *Bulletin of the Geological Society of America*, Vol. 56, No. 11, pp. 1015–1070, [http://dx.doi.org/10.1130/0016-7606\(1945\)56\[1015:BPONB\]2.0.CO;2](http://dx.doi.org/10.1130/0016-7606(1945)56[1015:BPONB]2.0.CO;2)
- Kiefert L., Schmetzer K. (1991) The microscopic determination of structural properties for the characterization of optical uniaxial natural and synthetic gemstones. Part 2: Examples for the applicability of structural features for the distinction of natural emerald from flux-grown and hydrothermally-grown synthetic emerald. *Journal of Gemmology*, Vol. 22, No. 7, pp. 427–438.
- Klein F. (1941) *Smaragde unter dem Urwald*. Oswald Arnold Verlag, Berlin.
- Kohlmann H. (1908) Beiträge zur Kenntnis des brasilianischen Berylls. *Neues Jahrbuch für Mineralogie, Geologie und Paläontologie*, Vol. 25 Supplement, pp. 135–181.
- Koivula J.I. (1981) Etch figures on beryl. *Journal of Gemmology*, Vol. 21, No. 3, pp. 142–143.
- von Kokscharow N. (Sohn) (1881) Beryll-Krystalle eines neuen Fundortes. *Bulletin de l'Académie Impériale des Sciences de*



- St-Petersbourg*, Vol. 27, No. 1-7, pp. 35–38.
- Kurumathoor R., Franz G. (2018) Etch pits on beryl as indicators of dissolution behaviour. *European Journal of Mineralogy*, Vol. 30, No. 1, pp. 107–124, <http://dx.doi.org/10.1127/ejm/2018/0030-2703>
- Lacroix A. (1896) *Minéralogie de la France et de ses colonies*. Vol. 2, Librairie Polytechnique, Paris, pp. 8–22.
- Lyckberg P., Chornousenko V., Wilson W.E. (2009) Famous mineral localities: Volodarsk-Volynski, Zhitomir Oblast, Ukraine. *Mineralogical Record*, Vol. 40, No. 6, pp. 473–506.
- Medina J.A., Morante M., Leguey S. (1983) Natural etch pits in beryl related with the structure. *Bulletin de Minéralogie*, Vol. 106, No. 3, pp. 293–297, <http://dx.doi.org/10.3406/bulmi.1983.7708>
- Moore T.P., Wilson W.E. (2016) The emerald mines of Colombia. *Mineralogical Record*, Vol. 47, No. 1, pp. 5–68.
- Nassau K., Jackson K.A. (1970) Trapiche emeralds from Chivor and Muzo, Colombia. *American Mineralogist*, Vol. 55, No. 3–4, pp. 416–427.
- Norton J.J., Page L.R., Brobst D.A. (1962) Geology of the Hugo pegmatite Keystone, South Dakota. U.S. Geological Survey Professional Paper 297-B, pp. 49–127.
- Oishi S., Mochizuki K., Hirano S. (1994) Growth of emerald crystals by the flux evaporation method in  $\text{MoO}_3\text{-B}_2\text{O}_3$  system. *Journal of the Ceramic Society of Japan*, Vol. 102, No. 1185, pp. 502–504, <http://dx.doi.org/10.2109/jcersj.102.502> [in Japanese]
- Penfield S.L. (1890) Some observations on the beryllium minerals from Mt. Antero, Colorado. *American Journal of Science*, Vol. 40, No. 240, pp. 488–491.
- Penfield S.L., Sperry E.S. (1888) Mineralogical Notes: Beryl. *American Journal of Science*, Vol. 36, No. 215, pp. 317–320.
- Petersson W. (1889) Om naturliga etsfigurer och andra lösningsfenomen på beryll från Mursinsk. *Bihang till Kongl. Svenska Vetenskaps-Akademiens Handlingar*, Afd. II, Vol. 15, No. 1, pp. 1–38.
- Pignatelli I., Giuliani G., Ohnenstetter D., Agrosi G., Mathieu S., Morlot C., Branquet Y. (2015) Colombian trapiche emeralds: Recent advances in understanding their formation. *G&G*, Vol. 51, No. 3, pp. 222–259, <http://dx.doi.org/10.5741/GEMS.51.3.222>
- Pignatelli I., Giuliani G., Morlot C., Salsi L., Martayan G. (2022) Colombian emerald oddities: Review and formation mechanisms. *Journal of Gemmology*, Vol. 38, No. 1, pp. 26–43.
- Ringsrud R. (2008) *Gota de aceite*: Nomenclature for the finest Colombian emeralds. *G&G*, Vol. 44, No. 3, pp. 242–245, <http://dx.doi.org/10.5741/GEMS.44.3.242>
- (2009) *Emeralds: A Passionate Guide*. Green View Press, Oxnard, California.
- Sahama T.G. (1966) Polygonal growth of beryl. *Bulletin of the Geological Society of Finland*, Vol. 38, pp. 31–45.
- Scandale E., Lucchesi S., Graziani G. (1990) Growth defects and growth marks in pegmatite beryls. *European Journal of Mineralogy*, Vol. 2, No. 3, pp. 305–312, <http://dx.doi.org/10.1127/ejm/2/3/0305>
- Schmetzer K. (2009) A rare ‘gota de aceite’ Colombian emerald which had been treated. *Gems & Jewellery*, Vol. 18, No. 1, pp. 3–4.
- (2019) Gem News International: Trapiche emerald from Colombia. *G&G*, Vol. 55, No. 1, pp. 156–158.
- Schwarz D., Curti M. (2020) *Emerald: Modern Gemmology*. Bellerophon Gemlab Ltd, Paris and Bangkok.
- Schwarz D., Giuliani G. (2002) South America: Colombia. In G. Giuliani et al., Eds., *Emeralds of the World*. extraLapis English No. 2. Lapis International, East Hampton, Connecticut, pp. 36–45.
- Seager A.F. (1953) The surface structure of crystals. *Mineralogical Magazine*, Vol. 30, No. 220, pp. 1–25, <http://dx.doi.org/10.1180/minmag.1953.030.220.02>
- Shaub B.M. (1937) Contemporaneous crystallization of beryl and albite vs. replacement. *American Mineralogist*, Vol. 22, No. 10, pp. 1045–1051.
- Sinkankas J. (1981) *Emerald and Other Beryls*. Chilton Book Company, Radnor, Pennsylvania.
- Smith J.S. (2021) From curio to designer gem... Rise of the trapiche. *Gems & Jewellery*, Vol. 30, No. 4, pp. 26–29.
- Sun X., Gao Y. (2022) Gem Notes: Hexagonal growth structures displaying *gota de aceite* effect in Colombian emerald. *Journal of Gemmology*, Vol. 38, No. 1, pp. 11–12.
- Sunagawa I. (1981) Characteristics of crystal growth in nature as seen from the morphology of mineral crystals. *Bulletin de Minéralogie*, Vol. 104, No. 2–3, pp. 81–87, <http://dx.doi.org/10.3406/bulmi.1981.7438>
- (1999) Growth and morphology of crystals. *Forma*, Vol. 14, pp. 147–166.
- (2003) Growth histories of mineral crystals as seen from their morphological features. In K. Byrappa and T. Ohachi, Eds., *Crystal Growth Technology*. Springer-Verlag, Berlin, Germany, pp. 1–23.
- (2005) Minerals formed by vapor growth. In *Crystals: Growth, Morphology, and Perfection*. Cambridge University Press, Cambridge, UK, pp. 236–250.
- Sunagawa I., Urano A. (1999) Beryl crystals from pegmatites: Morphology and mechanism of crystal growth. *Journal of Gemmology*, Vol. 26, No. 8, pp. 521–533.
- Taube H. (1895/1896) Ueber die Aetzfiguren einiger Minerale. *Neues Jahrbuch für Mineralogie, Geologie und Paläontologie*, Supplemental Volume 10, pp. 454–469.
- Tempesta G., Scandale E., Agrosi G. (2011) Striations and hollow channels in rounded beryl crystals. *Periodico di Mineralogia*, Vol. 79, No. 1, pp. 75–87, <http://dx.doi.org/10.2451/2011PM0006>
- Tschermak G. (1897) *Lehrbuch der Mineralogie*. 5th edition, Alfred Hölder, Vienna, p. 147.
- Vrba C. (1881) Smaragd von Sta Fé de Bogota. *Zeitschrift für Krystallographie und Mineralogie*, Vol. 5, No. 5, pp. 430–432.
- Vrba C. (1895) Beryll von Pisek. *Zeitschrift für Krystallographie und Mineralogie*, Vol. 24, No. 1–2, pp. 104–112.
- Weldon R., Ortiz J.G., Ottaway T. (2016) In Rainier’s footsteps: Journey to the Chivor emerald mine. *G&G*, Vol. 52, No. 2, pp. 168–187, <http://dx.doi.org/10.5741/GEMS.52.2.168>
- Zedlitz O. (1941) Goniometrische Untersuchungen der Lösungs- und Ätzerscheinungen an einem Beryllkristall von Minas Gerais, Brasilien. *Zentralblatt für Mineralogie, Geologie und Paläontologie, Abt. A.*, pp. 98–108.

For online access to all issues of GEMS & GEMOLOGY from 1934 to the present, visit:

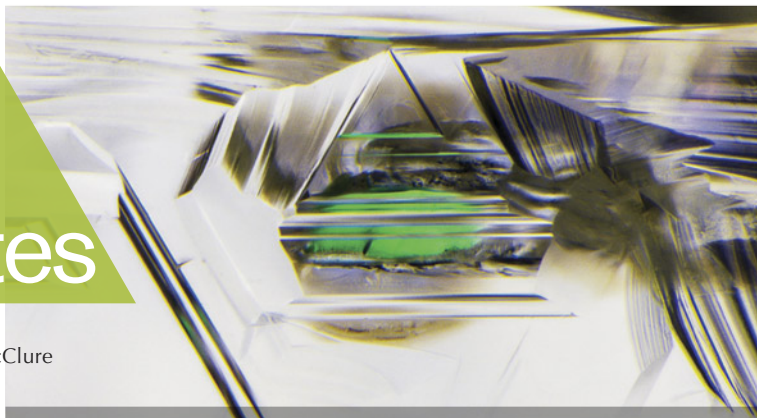
[gia.edu/gems-gemology](http://gia.edu/gems-gemology)



# Lab Notes

## Editors

Thomas M. Moses | Shane F. McClure



## Purple ANHYDRITE

Recently, the Carlsbad laboratory received a 2.13 ct transparent purple octagonal step cut, measuring  $7.32 \times 6.34 \times 6.01$  mm (figure 1), for a colored stone identification service. Microscopic observation showed twinning planes, cleavage cracks, needle-like inclusions, fluid fingerprints, and strong doubling of many internal features, confirming the stone was doubly refractive (figure 2).

Standard gemological testing revealed a specific gravity of 2.97 and a refractive index of 1.570–1.615 with a birefringence of 0.045. The refractive index measurement also indicated the stone was biaxial positive, and a biaxial interference figure was resolved using a conoscope and polarized light. Purple and light purple pleochroism was observed using a dichroscope. The specimen had no fluorescence reaction when exposed to long- and short-wave UV light. These characteristics were consistent with the rare collector gem anhydrite.

Raman spectroscopy confirmed that the stone was anhydrite. Using polarized ultraviolet/visible/near-infrared spectroscopy, we were able to determine that the purple color resulted from a prominent absorption band centered at around 550 nm. A sharp absorption feature was also observed at 307 nm.



*Figure 1. This 2.13 ct purple stone was identified as the rare collector gem anhydrite.*

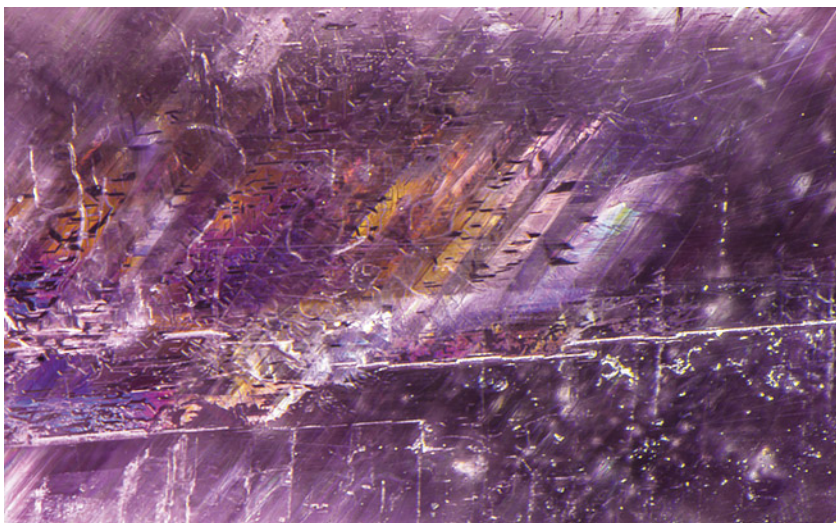
Anhydrite is a calcium sulfate with the chemical formula  $\text{CaSO}_4$ . It is not well suited for use in jewelry due to its low hardness of 3.5 on the Mohs scale and its perfect cleavage in one direction. This orthorhombic mineral is

commonly formed by the dehydration of gypsum, which has the chemical formula  $\text{CaSO}_4 \cdot 2\text{H}_2\text{O}$ , and can have multiple colors ranging from colorless to pale blue, light pink, and brown that is colored by impurities. Occurrences of purple anhydrite have been reported in Switzerland, Iran, and Sri Lanka (see, respectively, Spring 1998 Gem News, p. 60; Fall 2000 Gem News, p. 262; Fall 1988 Gem News, p. 179).

Faceted gem-quality and single-crystal anhydrite is rare, and while the Carlsbad laboratory has examined a couple of anhydrite gems, they were mostly aggregates bluish in color. This is the first example of a transparent purple faceted single crystal anhydrite examined at GIA's Carlsbad laboratory.

*Maria Estela Almeida and  
Nathan Renfro*

*Figure 2. Twinning planes and fluid fingerprints were observed throughout the faceted purple anhydrite. Field of view 3.89 mm.*



*Editors' note: All items were written by staff members of GIA laboratories.*

GEMS & GEMOLOGY, Vol. 59, No. 1, pp. 72–82.

© 2023 Gemological Institute of America





Figure 3. A 7.26 ct modified round brilliant identified as pink pyrope garnet. Courtesy of Bill Vance.

### Pink Pyrope GARNET

The Carlsbad laboratory received a 7.26 ct pink modified round brilliant (figure 3) for a colored stone identification report. Standard gemological testing revealed that the stone was singly refractive with a refractive index (RI) of 1.741 and a hydrostatic specific gravity (SG) of 3.77, properties consistent with garnet. Internally the stone was quite clean, with microscopic examination revealing scattered short needles.

The garnet group is composed of more than 20 species, all of them sharing the basic chemical formula  $X_3Y_2(SiO_4)_3$ . Five of these species are common within the jewelry industry: almandine, andradite, grossular, pyrope, and spessartine. Andradite and grossular are ugrandite garnets; they have calcium in the X site of their chemical formula. Almandine, pyrope, and spessartine are all pyral-spites garnets containing aluminum in the Y site. Isomorphous replacement, in which one chemical element substitutes for another in a mineral's crystal structure, makes it possible for garnets to be a chemical mixture of two or more garnet species. GIA gemologists use a garnet's gemological properties and chemistry to categorize the stone into its particular species.

Chemical analysis revealed that the 7.26 ct stone was a pyralspite garnet due to the high aluminum concentration (values expressed in wt. %: MgO 18.50%,  $Al_2O_3$  23.05%,  $SiO_2$  41.32%, CaO 1.89%,  $TiO_2$  0.05%,  $V_2O_5$  0.02%,  $Cr_2O_3$  0.04%, MnO 11.93%,  $Fe_2O_3$  3.17%). The composition of this garnet and its gemological properties were consistent with pyrope, which has an RI of 1.73–1.75, an SG of 3.78 (+0.009/–0.016), and magnesium dominating the X site and minor amounts of manganese and iron. Pyrope garnet, though, has a color range of red to reddish orange and colorless. Pink pyrope garnet is incredibly rare, especially in stones of this size.

Pyrope-spessartine can have a bodycolor similar to pyrope but has an RI range of 1.75 to over the limit and an SG of 3.78, both higher than the values documented for this pink garnet. The fact that garnet can be a mixture of species can make the identification of these stones challenging. This example is an important reminder to carefully analyze a garnet's gemological properties to accurately identify it and how the laboratory can use chemical analyses as validation.

Nicole Ahline

### Libyan Desert GLASS Bangle Bracelet

Libyan Desert glass is a light green or yellow natural glass which is composed of almost 98% silica. It is a type of tektite formed by meteorite impact in the desert and the fast quenching of the silica-rich melt produced. It was first reported by Clayton and Spencer in 1934 (F. Fröhlich et al., "Libyan Desert Glass: New field and Fourier transform infrared data," *Meteoritics and Planetary Science*, Vol. 48, No. 12, 2013, pp. 2517–2530) and is found in Egypt's Western Desert. Common inclusions are bubbles, cristobalite, dark brown streaks, and black iron oxides (J.A. Barrat et al., "Geochemistry and origin of Libyan Desert glasses," *Geochimica et Cosmochimica Acta*, Vol. 61, No. 9, 1997, pp. 1953–1959).

Recently, GIA's Hong Kong laboratory examined a transparent light yellow bangle bracelet measuring  $66.12 \times 13.10$  mm and weighing 144.67 ct (figure 4). It had a spot refractive index of 1.44 and revealed weak yellow fluorescence in short-wave UV. The chemical composition, determined by qualitative analysis using energy-dispersive X-ray fluorescence, was nearly pure silica with

Figure 4. A 144.67 ct Libyan Desert glass bangle measuring  $66.12 \times 13.10$  mm.





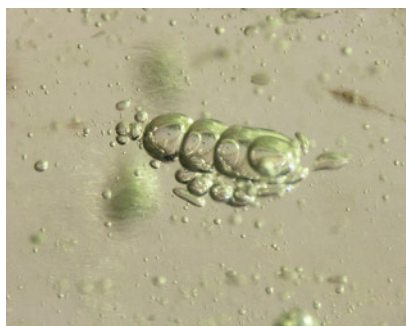
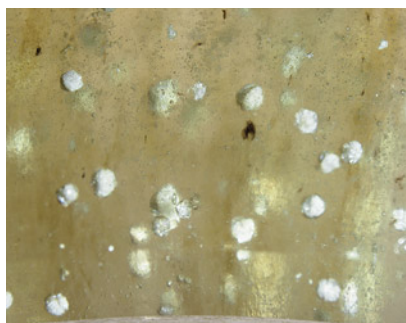


Figure 5. Various shapes of gas bubbles were dispersed individually and in clusters in the Libyan Desert glass bangle. The row of gas bubbles in this image resembles peas in a pod. Field of view 2.40 mm.

minor amounts of iron, strontium, potassium, titanium, and zirconium.

Based on the differences in molecular vibrations detected with Fourier-transform infrared (FTIR) analysis, it was determined that the molecular structure of Libyan Desert glass is significantly different from that of other pure silica glasses. It has a higher ratio of discontinuities and defects in the tetrahedral ( $\text{SiO}_4$ ) network (F. Fröhlich et al., 2013). Microscopic observation revealed common inclusions in glass such as numerous gas bubbles (figure 5) and flow structure. This bangle also presented abundant white spherulites identified by Raman spectroscopy as cristobalite (a polymorph of silica). These spherulites were small and individually dispersed throughout the glass (figure 6). The presence of this

Figure 6. White spherulites in the bangle were identified as cristobalite by Raman analysis. Field of view 5.98 mm.



high-temperature low-pressure silica phase indicates a natural high-temperature formation. From all the gemological, FTIR, and Raman data collected, this bangle was identified as Libyan Desert glass.

Most Libyan Desert glass is tubular in shape, and some are approximately spherical or rod-like (R.A. Weeks et al., "Libyan Desert glass: A review," *Journal of Non-Crystalline Solids*, Vol. 67, No. 1-3, 1984, pp. 593-619). Those fragments are usually 2 to 63 mm in size, so it is surprising to examine this material in the form of a bangle bracelet.

Ching Yin Sin

## PEARLS

### "Atypical Beads": Variations of Two Types of Nuclei

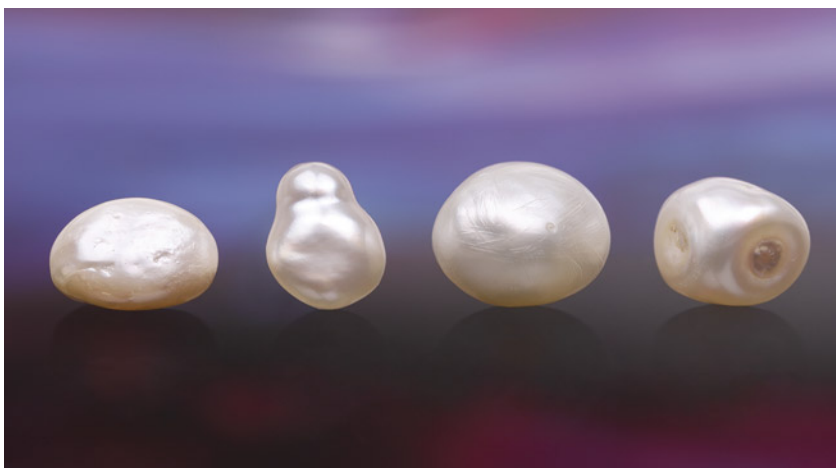
Atypical bead cultured pearls (aBCP) are occasionally encountered during laboratory testing. The nuclei used can take the form of various undrilled, partially drilled, or even drilled materials including natural pearls (abalone, scallop, turban species, *Pteria* species, and *Pinna* species), freshwater non-bead cultured pearls, coral, plastic, small shells, faceted sapphire beads of various colors, glass, quartz, and agate ("Atypical 'beading' in the production

of cultured pearls from Australian *Pinctada maxima*," *GIA Research News*, February 13, 2017). Four aBCPs (figure 7) were recently discovered in a group of 50 loose pearls submitted to GIA's Mumbai laboratory.

Externally, the four white to light cream-colored aBCPs looked similar to the other pearls submitted in the lot. When viewed under 40× magnification, their surfaces exhibited a typical nacreous surface of overlapping aragonite platelets. Energy-dispersive X-ray fluorescence spectrometry on all four revealed manganese levels between 13.30 ppm and 45.60 ppm and strontium levels between 1064 ppm and 1822 ppm, characteristic of a salt-water environment. Interestingly, optical X-ray fluorescence (XRF) of pearl 1 revealed a strong yellowish green reaction, while pearls 2, 3, and 4 were inert. The ultraviolet/visible reflectance spectra collected on the four pearls showed weak absorption features at around 320–420 nm. Raman analysis using 514 nm laser excitation showed the expected doublet at 702/705  $\text{cm}^{-1}$  and peak at 1085  $\text{cm}^{-1}$ , indicative of aragonite.

Real-time microradiography (RTX) and X-ray computed microtomography ( $\mu$ -CT) analysis revealed a variety of internal structures that required interpretation. RTX imaging of pearl 1 showed a thin irregular demarcation close to

Figure 7. Four loose atypical bead cultured pearls weighing 3.30 to 8.53 ct. Pearls 1–4 are shown from left to right.




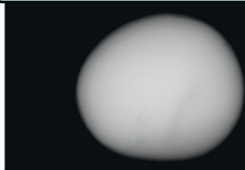
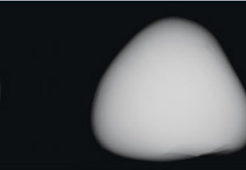
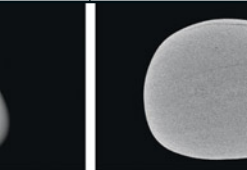

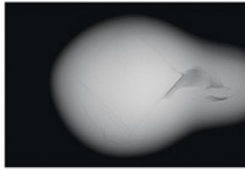

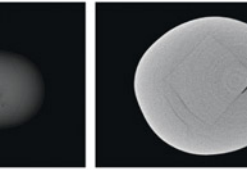

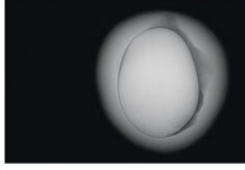
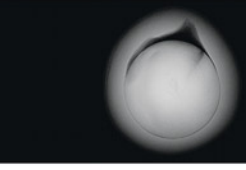

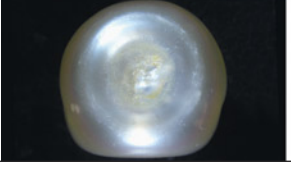

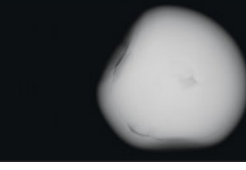
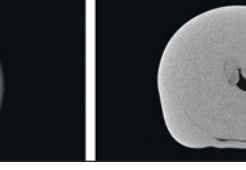
Sample details	Surface image	RTX image		μ-CT image
<b>Pearl 1</b> Button 5.50 ct				
<b>Pearl 2</b> Drop 3.30 ct				
<b>Pearl 3</b> Oval 8.53 ct				
<b>Pearl 4</b> Button 5.87 ct				

Figure 8. Surface appearance and internal structures of the four atypical bead cultured pearls. Fields of view 2 mm, 0.6 mm, 2.86 mm, and 16.3 mm.

the surface which was not continuous. On viewing the μ-CT, the demarcation was more discernible and followed the irregular outline of the pearl (figure 8, row 1). An irregularly shaped freshwater shell bead was clearly used as the nucleus, hence the strong yellowish green reaction observed in the optical X-ray fluorescence unit (figure 9, left). Under transmitted light, banding within the bead nucleus was also observed (figure 9, right); externally, the pearl had notable indentations on its surface.

Pearl 2 hosted the most interesting nucleus of the four. A rectangular “tissue-box” shaped bead, likely a piece of cut saltwater shell given the almost identical radio-opacity to that of its host, was evident in the RTX and μ-CT images (figure 8, row 2) (Fall 2022 Gem News International, pp. 378–380). Externally, the pearl was smooth, lustrous, and free of any surface blemishes.

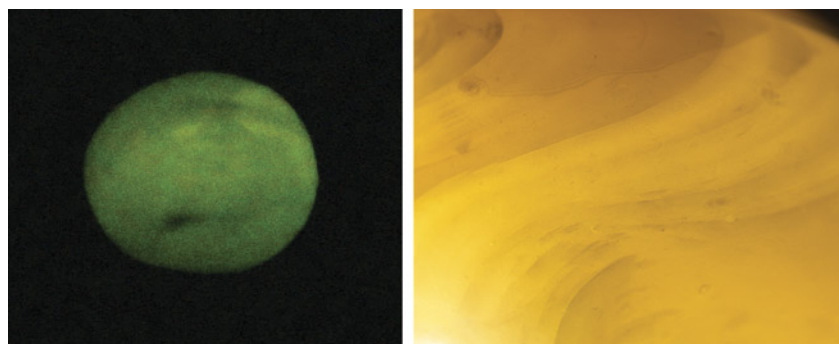
The RTX and μ-CT images of pearl 3 revealed an obvious demarcation with a linear structure at the

center of the nucleus and a small “organic tail-like feature” at one end within the boundary separating the bead from the overgrown cultured nacre (figure 8, row 3). All features were consistent with a saltwater non-bead cultured pearl being used as the bead nuclei. The lack of growth arcs around the demarcation was possibly due to rapid nacre deposition during

the culturing process (“Atypical ‘beading’ in the production of cultured pearls from Australian *Pinctada maxima*,” *GIA Research News*, February 13, 2017). This pearl exhibited distinct surface scratches that were visible without magnification.

Pearl 4 also showed a strong demarcation feature on the RTX and μ-CT images. However, the central area

Figure 9. Left: Pearl 1 revealed a strong yellowish green reaction under optical X-ray fluorescence. Right: Undulating shell banding visible within the sample’s shell bead nucleus using transmitted light; field of view 6.75 mm.



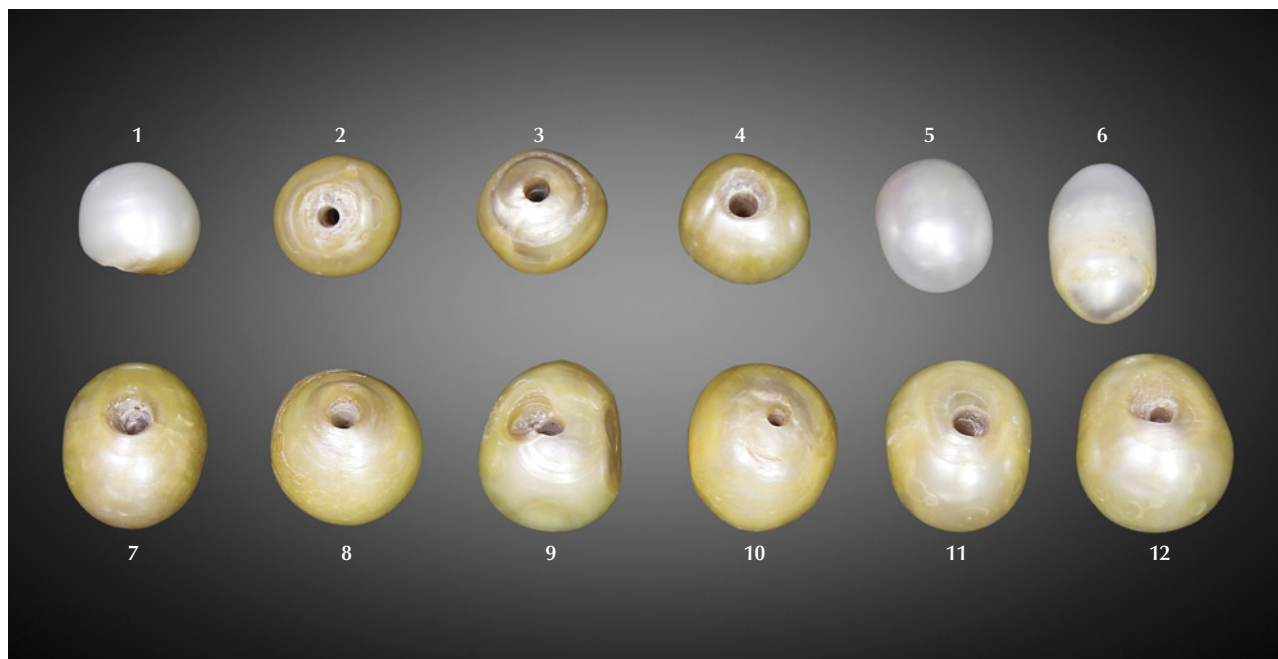


Figure 10. A group of 12 pearls ranging from  $7.38 \times 6.49 \times 6.05$  mm to  $10.61 \times 9.05 \times 8.05$  mm and weighing 44.37 carats total.

differed from the other three pearls, as it showed a void-like feature in the middle (figure 8, row 4). The bead nucleus used in the process was most likely a saltwater non-bead cultured pearl based on the fact that the pearl was inert to XRF, in keeping with pearl 3, despite the relatively thin nacre layers that would allow a freshwater bead to react. The pearl was also unusual because it possessed three nearly flat “bases” with concave features at the center of each. This raised questions about its identity even before X-ray examination, since the authors have rarely observed natural pearls with such features.

This is not the first time GIA has encountered aBCPs, but to receive four with variations on two types of nuclei—atypical shell (not typical round shell beads) and non-bead cultured pearls—in one lot was very interesting. This proves that such pearls are still circulating in the market and are being mixed with natural goods in an attempt at deception (Fall 2011 Lab Notes, pp. 229–230). Given the spectral data collected (S. Karampelas, “Spectral characteristics of natural-

color saltwater cultured pearls from *Pinctada maxima*,” Fall 2012 *G&G*, pp. 193–197) and the pearls’ internal structures and external appearance (A. Homkrajae et al., “Internal structures of known *Pinctada maxima* pearls: Cultured pearls from operated marine mollusks,” Fall 2021 *G&G*, pp. 186–205), it is apparent that all four of them formed within *Pinctada* species mollusks, most likely *Pinctada maxima*. Atypical bead cultured pearls have always been an interesting and sometimes challenging subject. With modern equipment and practical pearl testing experience, laboratories such as GIA aim to remain one step ahead of the possible experiments used by cultivators.

Rajesh S. Patel, Abeer Al-Alawi,  
Lubna Sahani, and Nicholas Sturman

#### Treated Freshwater Non-Bead Cultured Pearls with an Antique Appearance

GIA’s Mumbai laboratory recently received for identification a group of nine drilled and three undrilled pearls

weighing 44.37 carats total and ranging in size from  $7.38 \times 6.49 \times 6.05$  mm to  $10.61 \times 9.05 \times 8.05$  mm. The nine drilled pearls appeared to be old, while the three undrilled pearls looked whiter and much newer overall (figure 10). The shape of the samples varied, and the nine drilled pearls possessed a notable “aged” yellow coloration, which was also evident on some areas of the three undrilled whiter pearls.

The older-looking pearls possessed a dull luster, but the nacre condition was good. Microscopic examination at 70× magnification soon revealed that the color was concentrated on the outer layers and within surface-reaching features, proving that the color was not natural and a treatment had been used to alter their appearance (Summer 2017 Gem News International, pp. 255–256).

Although the color of pearls can change over time due to various causes (e.g., care factors such as storage conditions and contact with chemicals), these changes tend to be very gradual and develop over many years. This is partly due to their bio-



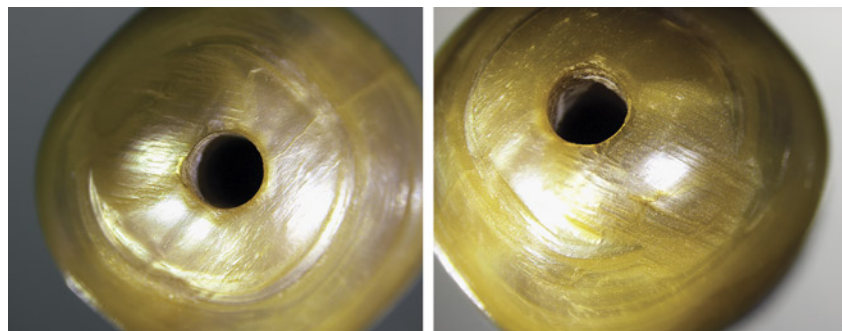


Figure 11. Two of the samples showing uneven surface coloration and color concentrations around the large drill holes. The worked surfaces around the drill holes are also clearly visible. Field of view 6.00 mm.

genic composition, which mainly consists of calcium carbonate with traces of organic substances, residual substances, and water. Dry environments are generally not advisable as they may result in surface alterations and, in rare cases, weight loss. The color can also change over time through wear and tear and the accumulation of external contaminants, so further analysis was required to prove whether these pearls naturally discolored over time or were treated to look antique, thereby inflating their value (M.S. Krzemnicki, "Fake historic provenance: 'Aged' cultured pearls," *Facette*, No. 25, 2019, p. 28).

Visually, it was readily apparent that the drill holes were very large in relation to the size of the pearls. When viewed with a 10× lens or under a gemological microscope at 70×, color concentrations were ob-

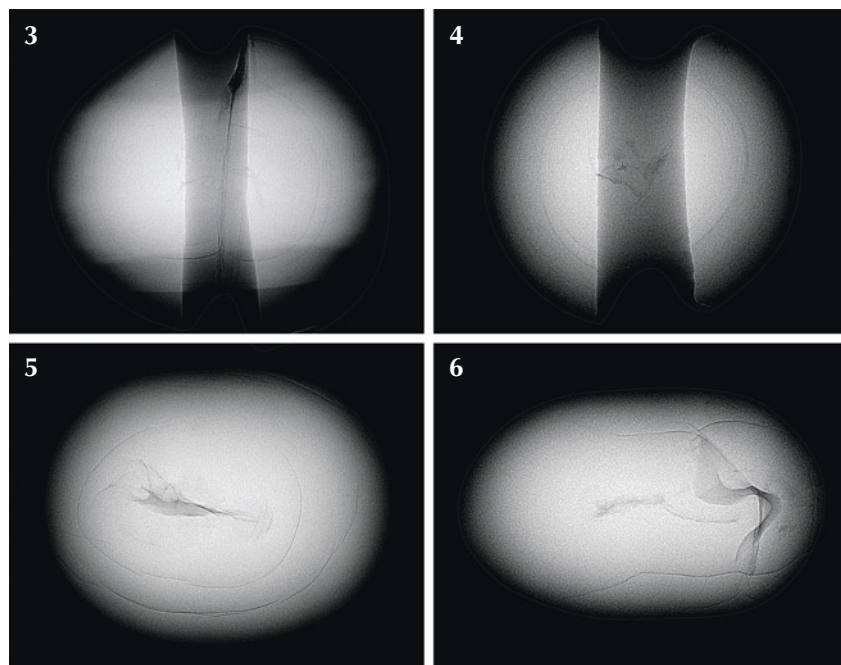
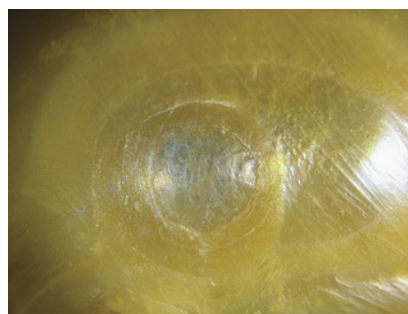
served around the drill holes of all nine drilled pearls. The surfaces were also heavily worked around the drill holes and did not resemble the wear and tear that might be expected on antique pearls. The surfaces of the nine drilled samples (2–4 and 7–12) were also slightly etched, indicating possible exposure to a mild acidic solution to create an "aging" effect.

Strikingly, the color was not typical of natural-color pearls (Summer 2017 Gem News International, pp. 255–256) and appeared to be restricted to the surface and around the drill holes (figure 11). Areas on some pearls also revealed the original underlying white color, further proof of treatment (figure 12).

Next, we needed to determine whether the pearls originated from a saltwater or freshwater environment, and whether they were natural or cultured. Real-time microradiography revealed small central twisting void-like features surrounded by fine growth lines typical of freshwater non-bead cultured pearls (figure 13), consistent with those produced by Chinese farms (K. Scarratt et al., "Characteristics of nuclei in Chinese freshwater cultured pearls," Spring 2000 *G&G*, pp. 98–109). The freshwater origin was confirmed when the pearls fluoresced a strong yellowish green color upon exposure to X-ray fluorescence, and further substanti-

Figure 13. The internal structures of four of the pearls showed twisted void-like features surrounded by fine growth arcs characteristic of non-bead cultured freshwater pearls. The two wide vertical gray features seen in pearls 3 and 4 are the drill holes.

Figure 12. An area of underlying white color below the treated surface of one of the samples. Field of view 5.00 mm.



ated by manganese values ranging from 500 to 1700 ppm and strontium values from 800 to 1000 ppm, obtained by energy-dispersive X-ray fluorescence spectroscopy.

Since Raman spectroscopy is also a valuable analytical tool for differentiating natural versus treated color in pearls, 514 nm ion-argon laser excitation was used on the surfaces. The results revealed a doublet at 702 and 705  $\text{cm}^{-1}$ , as well as a peak at 1085  $\text{cm}^{-1}$  indicative of aragonite, which is seen in the majority of pearls. High background fluorescence, often characteristic of treated-color pearls, was also noted in the drilled pearls. The photoluminescence spectra obtained displayed high fluorescence more typical of treated pearls, as well as the expected aragonite peaks. Other than the suspiciously high fluorescence, no other peaks characteristic of dyeing were observed.

All observations and results indicated that the nine drilled pearls had been treated to make them look antique. Pearls 1, 5, and 6 were predominantly white and showed only minimal evidence of any artificial aging attempts. These three showed a reaction to long-wave UV fluorescence more indicative of routine processing carried out on freshwater pearls. We concluded that these freshwater non-bead cultured pearls were also treated to make them appear aged. Hence, the report stated that these were freshwater non-bead cultured pearls from the Unionidae family and that pearls 2–4 and 7–12 had been color modified. Since the majority of the surfaces of pearls 1, 5, and 6 remained white and only showed insignificant areas of discoloration, the modified color description was not applied.

Andrew Aron, Abeer Al-Alawi, and  
Nicholas Sturman

### Heart-Shaped Golden South Sea Cultured Pearl

The heart shape has been a worldwide symbol of love and romance for centuries. GIA's New York laboratory recently received a golden-colored



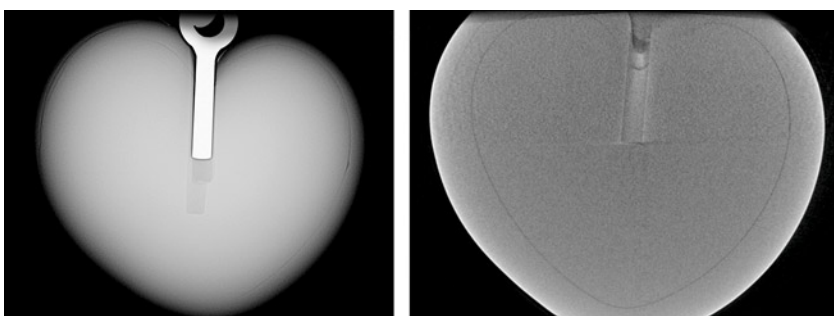
Figure 14. A heart-shaped golden South Sea pearl pendant measuring  $17.78 \times 11.65 \times 9.07$  mm and weighing 1.93 g (including the 18K yellow metal findings).

heart-shaped pearl pendant that drew our attention. The pearl was reportedly produced in the Philippines, which is a major source of golden South Sea cultured pearls. Upon routine gemological and advanced instrumental examination—including microradiography, ultraviolet/visible spectroscopy, manganese and strontium contents from energy-dispersive X-ray fluorescence, and reaction to long-wave UV—we concluded that it was an atypical bead cultured pearl from the *Pinctada maxima* species, commonly known in the trade as a South Sea cultured pearl (figure 14), and its heart shape and golden color were entirely natural.

Unlike the traditional bead cultured pearls typically nucleated with spherical shell bead nuclei, a heart-shaped bead nucleus was used in this pearl to achieve its unique shape. Hence, it was described as an “atypical bead” cultured pearl (aBCP) according to GIA's pearl identification terminology. Real-time microradiography (RTX) and X-ray computed microtomography (CT) clearly revealed the internal structure of a heart-shaped bead nucleus (figure 15). The nacre coverage, averaging 0.80 mm thick, was evenly distributed all around the nucleus, demonstrating that the heart shape of the pearl was consistent with the shape of the nucleus. Magnification revealed no signs of surface working or treatment, suggesting the pearl was in its original form after harvest. It displayed a strong orangy yellow color that is highly sought after among South Sea pearls. Ultraviolet/visible reflectance and photoluminescence spectroscopy further confirmed its natural color origin (C. Zhou et al., “Update on the identification of dye treatment in yellow or ‘golden’ cultured pearls,” Winter 2012 *G&G*, pp. 284–291).

Although this was not the first time a heart-shaped pearl has been examined in the lab, it is very rare to see a whole pearl with such a perfect non-round cultured shape. Previous submissions have either been identified as mabe pearls (assembled cultured blisters) or have had poorly defined heart shapes. Mabe pearls are not con-

Figure 15. X-ray images from RTX (left) and CT (right) show the demarcation of a heart-shaped bead nucleus with an average nacre thickness of 0.80 mm.





sidered whole pearls and often possess a thin nacre dome top (Fall 2021 Gem News International, pp. 277–279). Due to the thin nacre, their shape is easier to control. Therefore, fancy-shaped nuclei are commonly used in mabe pearls.

Many atypical bead cultured pearls have been studied and examined over the years at GIA (“Atypical ‘beading’ in the production of cultured pearls from Australian *Pinctada maxima*,” *GIA Research News*, February 13, 2017; Fall 2022 Gem News International, pp. 378–380). However, the majority of the end products are very different from the original shape of the nuclei. This remarkable use of an atypical bead nucleus to achieve a perfect shape in a cultured pearl suggests recent improvements in pearl culturing techniques.

Joyce Wing Yan Ho and  
Emiko Yazawa

### A Gastropod Shell in a Unique Shell Blister

Natural blister pearls and natural shell blisters have long been a subject of debate for gemologists and can be very challenging to definitively identify (see *G&G Lab Notes* from Fall 1992, Spring 1995, Winter 1996, Winter 2015, Summer 2016, and Spring 2018). According to the World Jewellery Confederation (CIBJO), a natural blister pearl forms when a natural pearl detaches itself from the pearl sac and attaches to the inner wall of the shell, while a natural shell blister is an internal protuberance that forms on a shell’s inner surface. It is usually caused by a foreign object accidentally finding its way into the space between the mantle and shell surface.

GIA’s Mumbai laboratory recently examined an interesting dark greenish brown baroque-shaped blister attached to a portion of shell weighing 2.60 g (13.00 ct) total and measuring approximately 25.54 × 18.11 × 7.79 mm (figure 16).

Examination under 40× magnification revealed a graduated hexagonal

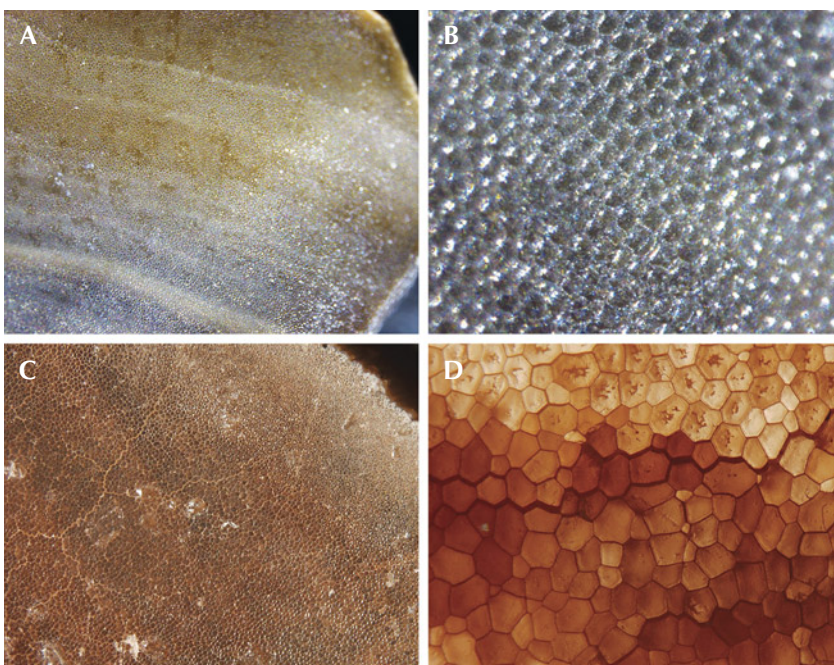


Figure 16. The natural shell blister attached to a portion of the shell on which it formed, weighing 2.60 g (13.00 ct) total and measuring 25.54 × 18.11 × 7.79 mm.

structure on the shell base (figure 17, A and B). The shell was cut and worked around the edges, and growth layers were visible when the cut surfaces were examined. Exposure to X-ray fluorescence yielded no reaction for the shell blister. Energy-dispersive

X-ray fluorescence spectrometry on two areas (top and base) revealed manganese levels below the detection limit, and strontium levels of 1470 ppm (top) and 2431 ppm (base) were consistent with those expected for saltwater pearls.

Figure 17. Photomicrographs show graduated cellular structures from the natural shell blister examined in the Mumbai laboratory (A and B; fields of view 4 mm and 3 mm, respectively) compared to those from a known *Pinnidae* shell from GIA’s Bangkok laboratory (C and D; fields of view 4 mm and 3 mm, respectively).





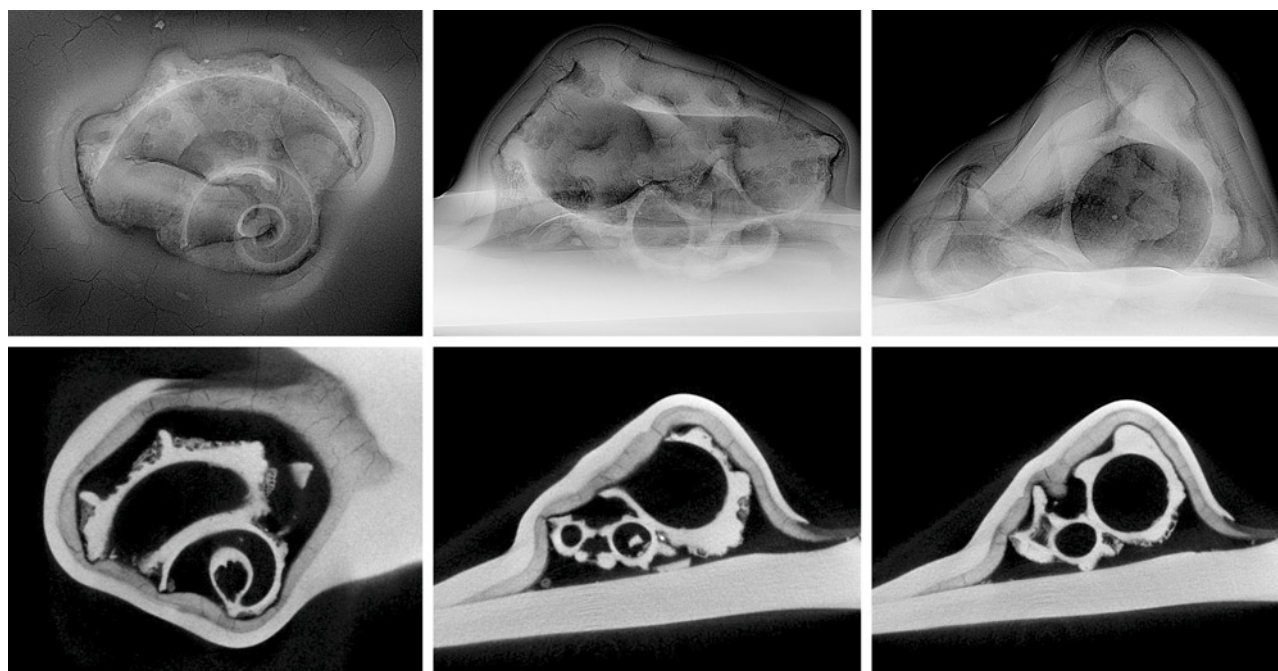


Figure 18. Top row, left to right: RTX images of the face, the right side, and the length or thickest direction reveal a prominent gastropod shell measuring approximately  $8.30 \times 5.75$  mm within the shell blister. Bottom row:  $\mu$ -CT images show the structures for the same three directions and provide even clearer details of the entombed gastropod.

Real-time microradiography (RTX), shown in the top row of figure 18, revealed a pleasant surprise. An obvious and intriguing gastropod shell was hidden beneath the overlying layers, which resulted in further study using X-ray computed microtomography ( $\mu$ -CT) (figure 18, bottom row). The minute details of a unique marine gastropod exoskeleton measuring approximately  $8.30 \times 5.75$  mm were observed within a void feature, and the overlying growth layers on the face side (the surface that grew within the mollusk it formed in) revealed minimal growth arcs. Marine gastropods are known to vary in size, and the class consists of many thousands of species (A. Nutzel, "Larval ecology and morphology in fossil gastropods," *Paleontology*, Vol. 57, No. 3, 2014, pp. 479–503). These observations provided enough evidence to make a clear distinction between a shell blister, such as this sample, and a shell blister pearl ("Natural shell blisters and blister pearls: What's the difference?" *GIA Research News*, August 26, 2019).

The ultraviolet/visible reflectance spectra showed a prominent feature at around 450 nm and weaker features at 320, 330, 450, and 460 nm proving that the sample's color was natural and lacked any treatment. Raman analysis using 514 nm laser excitation showed a series of peaks at 158, 186, 204, and 213  $\text{cm}^{-1}$ ; a weak peak at 280  $\text{cm}^{-1}$ ; a doublet peak around 701–704  $\text{cm}^{-1}$ ; and a strong peak at 1085  $\text{cm}^{-1}$ . These were indicative of aragonite. The photoluminescence spectra were also consistent with the Raman and displayed high fluorescence and aragonite-related peaks. These results were unexpected given the cellular-looking structure observed through the microscope, as this type of structure usually results in Raman spectra indicative of calcite.

While the lustrous dark color and the cellular-looking structure indicated the host shell was likely a species from the Pinnidae family, it was not clear given the spectral data collected (N. Sturman et al., "Observations on pearls reportedly from the Pinnidae family (pen pearls)," Fall 2014

*G&G*, pp. 202–215). When the surface structures were compared to photomicrographs of known *Pinna* species shell from GIA's Bangkok laboratory (figure 17, C and D), the results showed some similarity. However, Raman spectra indicative of calcite were obtained for the Bangkok research collection samples, which differed from the sample studied here. The *Atrina vexillum* species may have been responsible for producing the natural shell blister, and this would explain the aragonite-related Raman peaks since this mollusk is known to produce pearls with an aragonitic structure. However, since *Atrina* species pearls are often nacreous when aragonite is present and the sample in question was non-nacreous, the contradicting data still leaves some doubt as to the true identity of the host. Nevertheless, this example of a shell blister encompassing a gastropod shell represents a noteworthy phenomenon of nature that is rarely encountered.

Jayesh Surve, Abeer Al-Alawi, and  
Nicholas Sturman

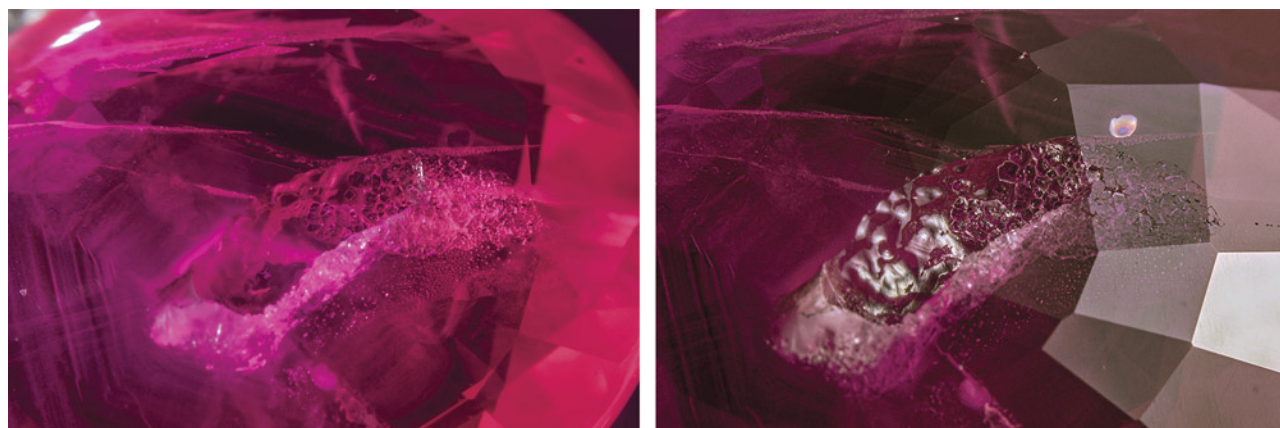


Figure 19. A large cavity partially filled with synthetic overgrowth on the pavilion of a heated Burmese ruby in darkfield lighting (left) and reflected lighting (right). Field of view 7.19 mm.

### RUBY with Interesting Synthetic Overgrowth

The Carlsbad laboratory received a 3.02 ct ruby for a colored stone identification and origin report. Standard gemological testing was consistent with ruby: a hydrostatic specific gravity of 3.96 and a ruby spectrum in a handheld spectroscope. Internally, the stone displayed white flakes in a hexagonal formation and roiled graining. Partially healed fissures with residue, which result from heating in the presence of a flux, were also documented. The inclusion scene, along with the stone's trace element chemistry collected using laser ablation-inductively coupled plasma-mass spectrometry (LA-ICP-MS), were consistent with Burmese ruby. This ruby was not treated by beryllium diffusion, as no beryllium was detected by LA-ICP-MS. The curious feature of this stone was a large cavity on the pavilion that was partially filled with synthetic overgrowth that was observed in the microscope (figure 19).

Synthetic overgrowth can be a by-product of heating a piece of corundum at high temperatures, with or without the presence of a flux. This creates an environment in the crucible that allows for the partial dissolution of corundum and can result in synthetic corundum overgrowth on the surface and in cavities of the heated stone. Synthetic overgrowth is typically an aggregated structure of hexa-

gonally shaped, platy crystals (Fall 2002 *G&G Lab Notes*, pp. 255–256). When viewed in reflective lighting, there is no luster difference between the host corundum and the synthetic overgrowth, as the two materials have the same refractive index. The gaps that could be observed between the crystals in this stone showed how they grew in different orientations.

Synthetic overgrowth is common enough that it should always be looked for in corundum that has undergone high-temperature heat treatment. There are cases where synthetic overgrowth can be observed

using polarized light, but careful analysis is required because the overgrowth can completely fill cavities and be inconspicuous.

Nicole Ahline

### Exceptionally Large SYNTHETIC RUTILE

The Carlsbad laboratory received three light yellow modified round brilliants weighing 11.13, 11.91, and 110.18 ct (figure 20) for identification reports. Standard gemological testing revealed the stones to be synthetic rutile based

Figure 20. Three large synthetic rutile brilliants weighing 11.13, 110.18, and 11.91 ct. Courtesy of Arya Akhavan.



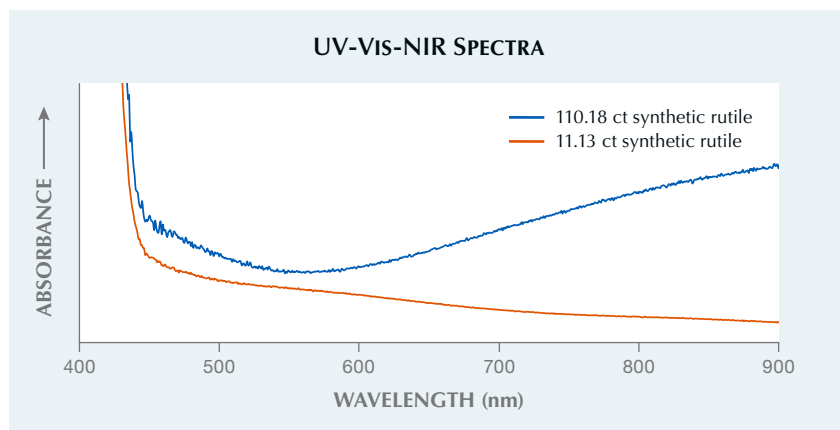


Figure 21. UV-Vis-NIR absorption spectra comparing the 110.18 ct and 11.13 ct synthetic rutile studied, here demonstrating the effect of aluminum doping in the smaller stone to produce a nearly colorless appearance.

on over-the-limit refractive index readings and extreme fire and doubling, an identification that was supported by Raman spectroscopy.

Of particular note was the astonishing size of these stones. The 110.18 ct synthetic rutile is the largest encountered in the GIA laboratory. Even the smaller 11.13 ct and 11.91 ct stones are much larger than normal for this material, which is usually seen in sizes up to several carats. The owner of the stones indicated that the manufacturer had to modify their fur-

nace to accommodate growth of the 110.18 ct crystal. Also notable were the novel facet pattern and precision cutting usually only seen in the high-end collector market.

Interestingly, the two smaller stones had a much lighter yellow color than the 110.18 ct stone, which was notable even considering the shorter light path length through the smaller stones. Chemical analysis using laser ablation-inductively coupled plasma-mass spectrometry showed a higher concentration of alu-

minum in these two samples (~80 ppm Al compared to ~3 ppm). The difference in color was also demonstrated in the ultraviolet/visible/near-infrared absorption spectra (figure 21). This finding aligns with the practice of growing rutile doped with small amounts of aluminum to bring the appearance of the material closer to nearly colorless (C.H. Moore, "Rutile boule and method of making the same," U.S. Patent 2,715,070, issued August 9, 1955). Additionally, the owner indicated that the two smaller rutile crystals were grown by National Lead Co. between 1961 and 1964, while the larger stone is from a modern producer.

Aaron Palke

#### PHOTO CREDITS

Adrianna Gudino—1; Nathan Renfro—2; Towfiq Ahmed—3; Johnny Leung—4; Sze Ling Wong—5, 6; Gaurav Bera—7, 16; Nishka Vaz—8, 9 (right); Jayesh Surve—10–12, 17 (A and B); Sood Oil (Judy) Chia—14; Nicholas Sturman—17 (C and D); Nicole Ahline—19; Robert Weldon—20





# The Dr. Edward J. Gübelin Most Valuable Article AWARD

## First Place

### METHODS AND CHALLENGES OF ESTABLISHING THE GEOGRAPHIC ORIGIN OF DIAMONDS

FALL 2022

*Evan M. Smith, Karen V. Smit, and Steven B. Shirey*

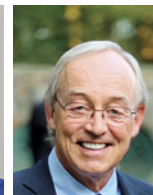
**Evan Smith** is a senior research scientist at GIA in New York. His primary research focuses on the geology of gemstones and serves to highlight diamonds as some of the most scientifically valuable materials on Earth. Dr. Smith holds bachelor's and master's degrees in geological engineering from Queen's University and a PhD in geology from the University of British Columbia. **Karen Smit** has been conducting research on the origin of natural diamonds and studying diamonds from mines worldwide for 15 years, publishing much of her work in scientific journals. She holds a PhD in geology from the University of Alberta and a master's in geochemistry from the University of Cape Town. Formerly a research scientist at GIA in New York, Dr. Smit is currently a senior lecturer in isotope geochemistry at the University of the Witwatersrand in Johannesburg. **Steven Shirey** is a senior staff member in the Earth and Planets Laboratory of the Carnegie Institution for Science. Dr. Shirey's main interests include diamonds as the deepest probe of plate tectonics, the igneous evolution of the earth, and the emergence of the continents. He holds a PhD from the State University of New York at Stony Brook and is a fellow of the American Geophysical Union, the Geochemical Society, the Geological Society of America, and the Mineralogical Society of America (of which he is a former president).



Evan Smith



Karen Smit



Steven Shirey

## Second Place

### GEMS ON CANVAS: PIGMENTS HISTORICALLY SOURCED FROM GEM MATERIALS

FALL 2022

*Britni LeCroy*

**Britni LeCroy** is a staff gemologist at GIA in Carlsbad, California. She obtained a bachelor's degree in geoscience from the University of Texas at Dallas before receiving gemology diplomas from GIA and the Gemological Association of Great Britain. A frequent contributor to *G&G*, her areas of interest include pearls, organic gem materials, and historical gemology.



Britni LeCroy

## Third Place

### A CANARY IN THE RUBY MINE: LOW-TEMPERATURE HEAT TREATMENT EXPERIMENTS ON BURMESE RUBY

WINTER 2022

*E. Billie Hughes and Wim Verriest*

**E. Billie Hughes** is a gemologist and cofounder of Lotus Gemology in Bangkok. An award-winning photomicrographer and sought-after lecturer, she has delivered talks on gemology around the world. She is a graduate of the University of California, Los Angeles. **Wim Verriest** is manager of field gemology at GIA in Bangkok, where he curates GIA's colored stone reference collection. He obtained a master's degree in geology (geodynamics and geofluids) from KU Leuven in Belgium.



E. Billie Hughes



Wim Verriest

*Many thanks to the members of G&G's Editorial Review Board for voting this year.*



G&G

# Micro-World

Editor: Nathan Renfro

Contributing Editors: Elise A. Skälwold and John I. Koivula

## Three-Phase Inclusion in Alexandrite

Natural gemstones form under very intense conditions that allow for a wide range of interesting phenomena and inclusions to occur within them. Environmental conditions within the earth's crust influence the types and amounts of inclusions that occur. Various categories of inclusions, such as crystals or structural defects, for example, are widespread among almost all gem species. On the other hand, there are less frequent types of inclusions that form only under specific geological conditions and are found only in certain gem species. Although less common, it is possible to observe up to three phases of matter within a single inclusion suite.

At conditions slightly above room temperature (i.e., in the well light of a gemological microscope), the largest jagged cavity pictured here contains multiple separate crystals and a transparent colorless fluid (figure 1). At a temperature below 31.2°C, the fluid separates into liquid and multiple bubbles of carbon dioxide gas are released (figure 2). Differences in environmental conditions during formation influence the amount of static pressure within the stone, which explains why some three-phase inclusions are visible at room temperature while others are only visible at lower temperatures (see J.I. Koivula, "Carbon dioxide fluid inclusions as proof of natural-colored corundum," Fall 1986 *G&G*, pp. 152–155). Despite the shape and the relief of the

*Figure 1. Top: Negative crystal in an alexandrite containing a fluid and crystals at room temperature. Bottom: Below 31.2°C, multiple gas bubbles appear. Photomicrographs by Jamie Price; field of view 1.99 mm.*



*About the banner: Acicular inclusions of the blue mineral dumortierite are present throughout this quartz crystal from Brazil. Photomicrograph by Nathan Renfro; field of view 5.68 mm.*

GEMS & GEMOLOGY, VOL. 59, NO. 1, PP. 84–91.

© 2023 Gemological Institute of America



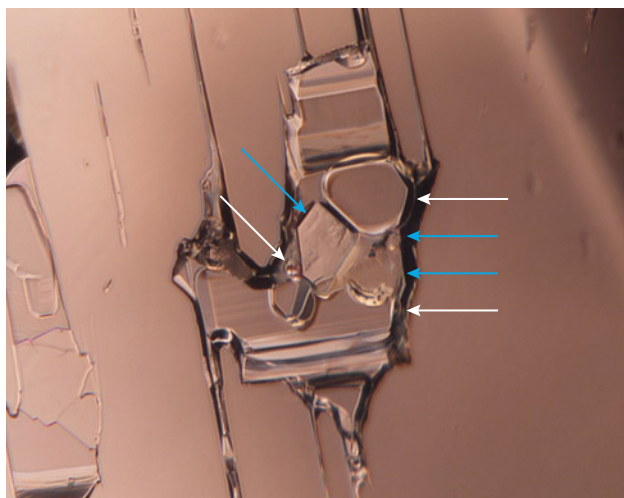


Figure 2. Close-up view distinctively pointing out the locations of the crystals (blue arrows) and gas bubbles (white arrows). Photomicrograph by Jamie Price.

crystals present, the overall appearance of this alexandrite's multiphase inclusion is comparable to the typical jagged three-phase inclusions that are distinctive for Colombian emerald.

Jamie Price  
GIA, Carlsbad

### Apatite in Hackmanite

Hackmanite,  $\text{Na}_8\text{Al}_6\text{Si}_6\text{O}_{24}(\text{Cl}_2, \text{S})$ , is a variety of sodalite notable for its tenebrescence. When kept in darkness, samples can fade to pale purple and even gray or translucent to opaque white. When exposed to long-wave ultraviolet illumination, they can display a strong orange fluorescence



Figure 3. A hackmanite with a faded purple color after storage in the dark (left), illuminated with long-wave UV light (center), and after removal from a few seconds of exposure to the long-wave UV light (right). The color has deepened after exposure to UV light. Photos by Ronnakorn Manorotkul.

reaction. After exposure to sunlight or artificial light with a UV component, samples can quickly develop a much stronger color. One hackmanite sample recently examined by the author (figure 3) showed this phenomenon.

Another hackmanite was submitted that displayed an interesting elongated white inclusion (figure 4, left) that was identified by micro-Raman as apatite. As we examined the sample in the microscope, we tried exposing it to a 6-watt long-wave UV light for approximately one second. Almost immediately, a change was observed. The hackmanite developed a more vibrant purple color that is clearly displayed in figure 4 (right).

E. Billie Hughes  
Lotus Gemology, Bangkok

Figure 4. Left: In darkfield illumination, a white apatite crystal is visible in the hackmanite. Right: After exposure to long-wave UV light for approximately one second, a dramatic change can be seen. The overall color of the hackmanite is now a more vivid shade of purple. Photomicrographs by E. Billie Hughes; field of view approximately 5 mm.







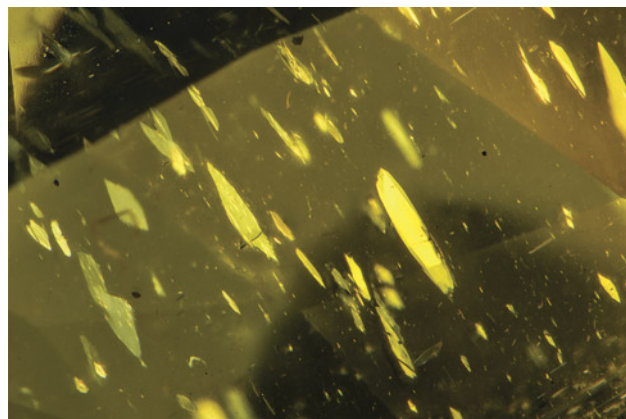
*Figure 5. This 4.63 ct chondrodite contained irregular multiphase and reflective iridescent platelets with a bright orangy yellow color. Photo by Adriana Gudino; courtesy of Bill Vance.*

### Inclusions in Chondrodite

The authors recently examined a 4.63 ct orangy yellow pear modified brilliant (figure 5). The gemological properties as well as infrared and Raman spectroscopy identified the stone as chondrodite.

Microscopic observation revealed a lively inclusion scene with colorless reflective and iridescent platy inclusions (figure 6). Dark, highly reflective platelets of graphite, which can be associated with low-relief colorless crystals of various minerals (figure 7), were also confirmed by Raman analysis.

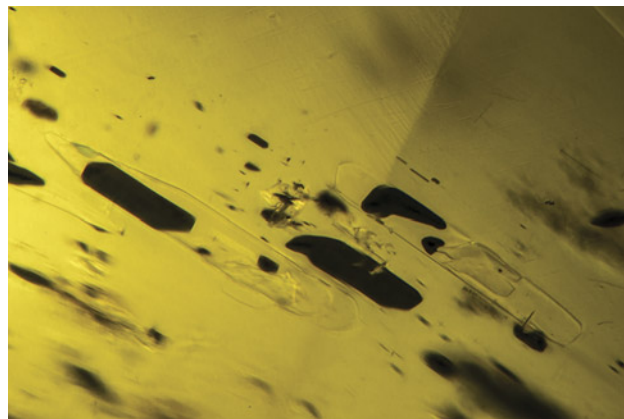
*Figure 6. Platy inclusions were observed throughout the chondrodite. Photomicrograph by Nathan Renfro; field of view 4.11 mm.*



Chondrodite,  $\text{Mg}_5(\text{SiO}_4)_2(\text{F},\text{OH})_2$  is a member of the humite group. This rare mineral occurs primarily in metamorphosed limestones and dolomites (W.L. Roberts et al., *Encyclopedia of Minerals*, 2nd ed., Van Nostrand Reinhold, New York, 1990, p. 170). If contact metamorphism occurs in an area with sufficient magnesium, chondrodite and other associated magnesium-bearing minerals such as spinel, phlogopite, and tremolite may form.

Chondrodite has been found to originate from Tanzanian localities at Mahenge (Winter 2011 Gem News Inter-

*Figure 7. Dark, highly reflective platelets of graphite as well as unidentified low-relief colorless inclusions of multiple minerals were also observed in the chondrodite. Photomicrograph by Nathan Renfro; field of view 0.91 mm.*



national, p. 316), Sumbawanga (Winter 2007 Gem News International, pp. 377–379), and Tanga (B. Clark, “Chondrodite reportedly from Tanga, Tanzania,” *Journal of Gemology*, Vol. 34, No. 8, p. 655). It has also been identified as an inclusion in a spinel from Mogok, Myanmar (Winter 2021 *G&G Micro-World*, p. 383). The gemological properties of this stone were consistent with material from Mahenge, but the origin could not be confirmed.

Chondrodite is an uncommon mineral and even more rare as a gemstone. This exceptional example of a bright orangy yellow color, faceted by Bill Vance of Vance Gems, showcases the types of inclusions that can be found in this gemstone.

Kendra Carty and Amy Cooper  
GIA, Carlsbad

### A “Flying Insect” in Diamond

The authors recently examined a 0.75 ct type IaA Fancy Light brownish yellow diamond. This diamond, with a clarity grade of I<sub>1</sub>, contained at least 10 orange inclusions, the largest one ~500 µm in its longest dimension. A partially exposed orange inclusion resembled a flying insect,

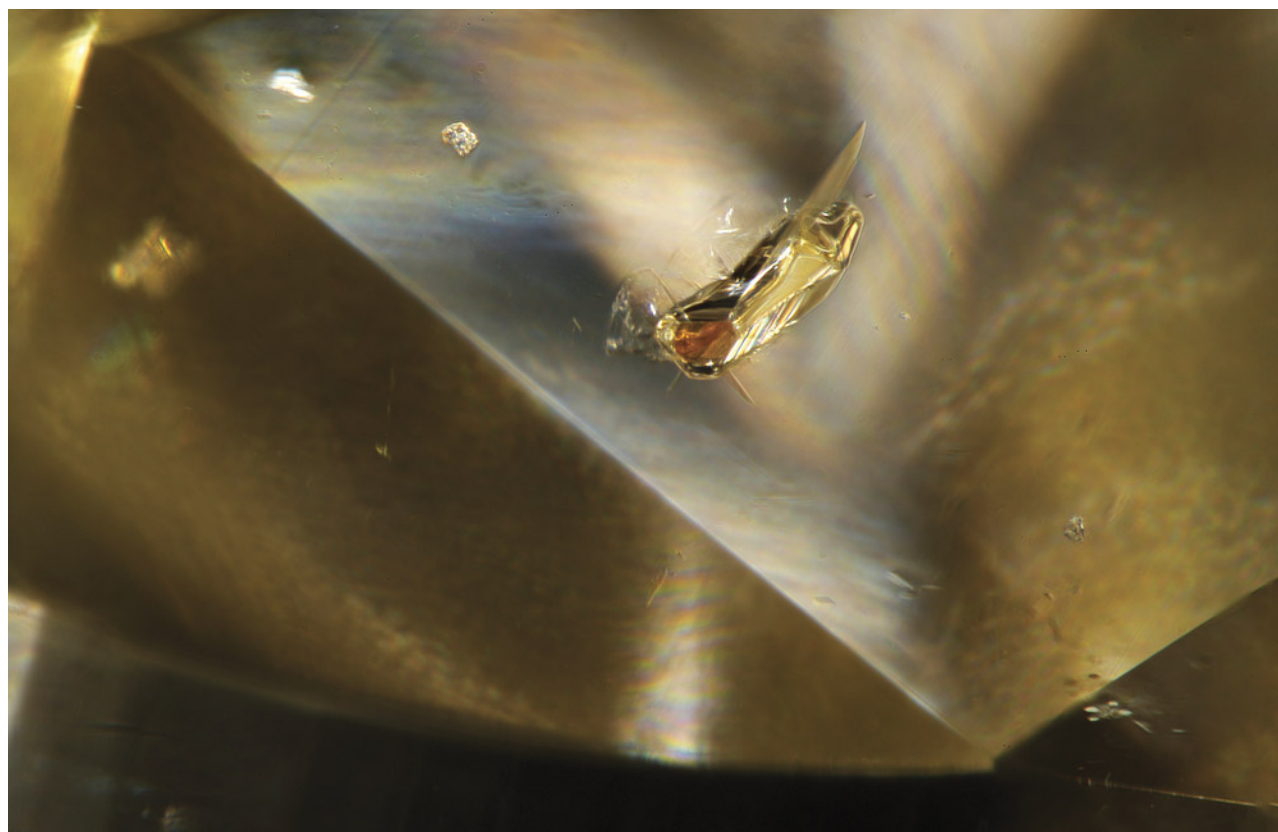
with “flapping wings” and “antennae” caused by fractures around the inclusion (figure 8). Raman spectroscopy revealed the inclusion to be pyrope-almandine-grossular garnet,  $(\text{Mg,Fe,Ca})_3\text{Al}_2(\text{SiO}_4)_3$ , a major constituent mineral of eclogite.

Eclogite and peridotite are the major diamond host rocks in the lithospheric mantle. Worldwide, the ratio of diamonds with eclogitic mineral inclusions to those with peridotitic inclusions is ~1:2 (T. Stachel and J.W. Harris, “The origin of cratonic diamonds – constraints from mineral inclusions,” *Ore Geology Reviews*, Vol. 34, No. 1-2, 2008, pp. 5–32).

Although the presence of inclusions generally reduces a diamond’s clarity grade, diamonds containing visually identifiable mineral inclusions are uncommon. Studies of some smaller diamonds (~2 mm) from South Africa and Botswana revealed a low abundance of inclusion-bearing diamonds (about 1% in a total of one million diamonds examined; Stachel and Harris, 2008). For a gem-quality diamond to contain more than 10 mineral inclusions is therefore notable.

Mei Yan Lai and Taryn Linzmeyer  
GIA, Carlsbad

Figure 8. This partially exposed orange garnet inclusion with surrounding fractures in a brownish yellow diamond resembled a flying insect. Photomicrograph by Mei Yan Lai; field of view 1.58 mm.



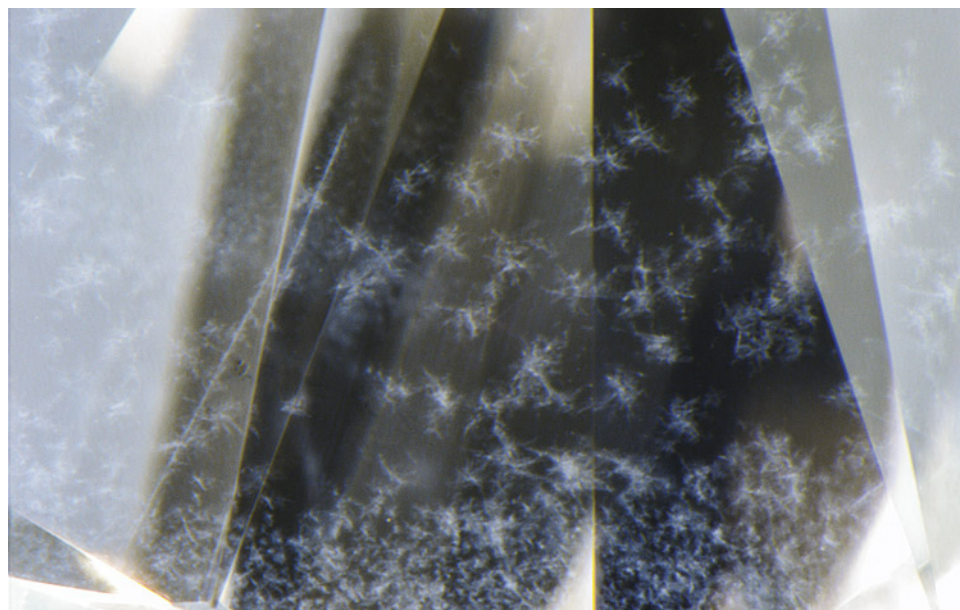


Figure 9. Rare cloud inclusions were observed in a 0.53 ct D-color diamond. Photomicrograph by Nathan Renfro; field of view 2.39 mm.

## Starry Night in Diamond

In astronomy, a star cloud is defined as a group of many stars. A diamond recently submitted to GIA's Surat lab contained cloud inclusions resembling a starry night (figure 9). This diamond was a 0.53 ct D-color natural round brilliant with SI<sub>2</sub> clarity. Fourier-transform infrared absorption spectroscopy indicated a type IaAB diamond with low nitrogen content of about 5 ppm. Each of the cloud inclusions had apparently randomly placed dendrites. The star field in this stone appeared comparable to a diamond described previously (Fall 2017 *G&G Micro-World*, p. 369); however, the individual clouds in that diamond resembled crosses of uniform orientation that corresponded with the cube face.

Photoluminescence (PL) mapping using 455, 532, and 633 nm excitations was used to determine whether optical features could be detected within the cloud inclusions, as that analysis method has proven useful with cloud features in other diamonds (Fall 2020 Lab Notes, pp. 416–419). However, the PL maps were inconclusive, as no distinctive features were detected within the star-shaped inclusions. In deep ultraviolet fluorescence imaging, they appeared to be contained within the same growth zone (figure 10).

The inclusion suite was an interesting collection of cloud formations and a delightful discovery in this unusual diamond.

*Sally Eaton-Magaña and Stephanie Shaw*  
GIA, Carlsbad

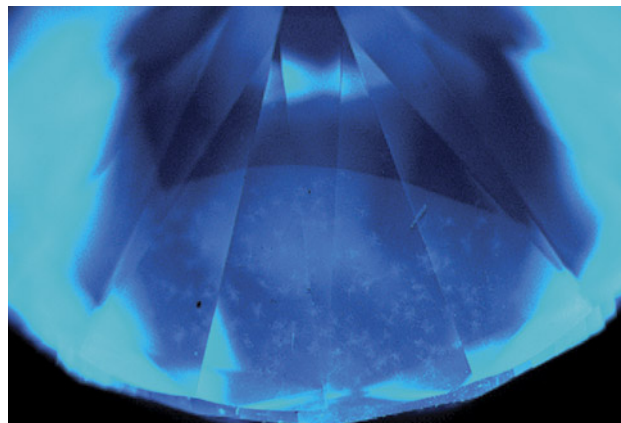
*Alpesh Vavadiya*  
GIA, Surat

## Xenomorphous Garnet in Diamond

Garnet is a nesosilicate mineral belonging to the cubic crystal system. The crystal habit most commonly assumed by this mineral is a dodecahedron. A garnet crystal with

rare octahedral morphology was recently encountered in the form of a xenomorphous inclusion within diamond. Xenomorphism is the process by which a growing mineral forces a syngenetic mineral inclusion to adopt a crystal habit familiar to the host (J.I. Koivula, *The MicroWorld of Diamonds*, Gemworld International, Northbrook, Illinois, 2000). Xenomorphous crystals may also be referred to as “anhedral” since they lack their own characteristic crystal shape in favor of the host’s. However, it should be noted that not all anhedral included mineral crystals are xenomorphous. As an octahedron is the most common diamond habit, the garnet inclusion grew into this form, complete with triangular growth marks visible on one of the octahedral faces (figure 11). Xenomorphism in diamond can also occur with mineral inclusions that do not belong to the

Figure 10. This deep ultraviolet fluorescence DiamondView image shows that the cloud inclusion features appear to be contained within a single growth zone. Image by Sally Eaton-Magaña.







*Figure 11. A purplish pink xenomorphic octahedral garnet crystal seen in a diamond. Note the trigons on the upper right octahedral face and stress fractures around the intersections of the crystal faces. Photomicrograph by Britni LeCroy; field of view 1.26 mm.*

cubic crystal system, and these can be forced into other diamond habits. For example, a monoclinic crystal of diopside may be forced into a cuboctahedral habit. Xenomorphic crystals are just one of many unique inclusion types possible within diamond.

*Britni LeCroy and Virginia Schwartz  
GIA, Carlsbad*

### **Arrow-Patterned Negative Crystals in Sapphire**

Negative crystals are a common inclusion in corundum and often rupture upon exposure to moderate heat treatment. The author recently analyzed a sapphire containing a series of negative crystals arranged in an arrow-like pattern.

tern (figure 12). Careful examination revealed a partially healed fissure intersecting one of the negative crystals, indicating the stone had been subjected to heat treatment.

Fortunately, this spectacular pattern of negative crystals endured the heat treatment process, decorating the internal micro-world of this sapphire.

*Piradee Siritheerakul and Tao Shiu Hei  
GIA, Bangkok*

### **Unusual Solid Inclusions in Flame-Fusion Ruby**

The author recently examined unusual dark red solid inclusions in a flame-fusion laboratory-grown ruby. Standard gemological testing yielded a refractive index of 1.760–



*Figure 12. Negative crystals arrayed in an arrow-like pattern. Photomicrograph by Suwasan Wongchacree; field of view 1.07 mm.*



Figure 13. Numerous natural-looking dark red solid inclusions were observed in a flame-fusion laboratory-grown ruby. Photomicrograph by Ezgi Kiyak; field of view 2.9 mm.



Figure 14. Strong curved growth lines and numerous gas bubbles and dark solid inclusions were present in the flame-fusion ruby. Photomicrograph by Ezgi Kiyak; field of view 2.9 mm.

1.768, a chromium emission line in red using a handheld spectroscope, medium red fluorescence under long-wave UV, and weak red fluorescence under short-wave UV. These properties were consistent with ruby. Microscopic examination using brightfield illumination revealed numerous dark red inclusions (figure 13) that resembled crystals commonly seen within natural corundum.

Furthermore, magnification showed characteristic internal features of flame-fusion ruby such as curved striae and gas bubbles. The strong curved growth lines and numerous gas bubbles (figure 14) suggested that this was an early type of flame-fusion ruby. Although flame-fusion corundum is widely available in the marketplace, it is unusual to encounter a specimen containing natural-looking dark red solid inclusions. These inclusions are possibly unmelted alumina powder, and the fact that Raman was unable to identify something other than alumina supports this (E.J. Gübelin and J.I. Koivula, *Photoatlas of Inclusions in Gemstones*, Volume 3, Opinio Publishers, Basel, Switzerland, 2008).

Identification of the natural or laboratory-grown origin of a stone with this type of natural-looking inclusion can be difficult. Careful observation is needed to correctly identify such a specimen's origin.

Ezgi Kiyak  
GIA, New York

### Quarterly Crystal: Columbite(?) in Beryl

Those in the gem and mineral community can appreciate the near-perfection of a beautifully crystallized mineral specimen or a well-cut gemstone. But these surfaces are only the exterior, covering a complex, multilayered story within. These internal contents often remain unknown unless we choose to explore below the surface. Somewhat like trees and their rings, minerals and gems form as concentric, typically crystallized layers, recording the developmental details within each layer through changes in

temperature, pressure, and chemistry. While some of these growth details are submicroscopic and remain hidden during microscopic observation, other features such as mineral inclusions and encapsulated fluids are waiting to be discovered. In a very real sense, inclusions and their developmental sequencing in their host gems and minerals are descriptions of mineralogical genetics.

Researchers focused specifically on inclusions usually cannot outbid serious gem and mineral collectors for crystals and fashioned gems with interesting internal targets. As a result, many such “gems” end up in private collections, and their inclusions are rarely, if ever, fully documented. This is a tremendous missed opportunity, because inclusions contain geological information that tells a story about themselves and their host.

For this issue's Quarterly Crystal, we recently had the opportunity to document a well-formed gem-quality, transparent, very light greenish blue terminated hexagonal crystal of aquamarine, with a small amount of light brown matrix at the base and a clearly visible inclusion cluster at the near center (figure 15). The aquamarine was obtained from Muntazir Mehdi of Shad Fine Minerals International in Gilgit-Baltistan, Pakistan. The geographic source was reportedly the Kharguluk mine in Baltistan Province.

At 56.00 ct with corresponding measurements of 26.36 × 16.09 × 15.02 mm, this aquamarine played host to an easily eye-visible tight cluster of randomly arranged dark reddish brown to black bladed crystals (figure 16) that resembled the mineral columbite-(Mn),  $\text{Mn}^{2+}\text{Nb}_2\text{O}_6$ , as shown by E.J. Gübelin and J.I. Koivula (*Photoatlas of Inclusions in Gemstones*, Volume 2, Opinio Verlag, Basel, Switzerland, 2005, pp. 263, 319).

Micro-Raman has significantly reduced the time required to instrumentally identify many inclusions. Some inclusion identifications that once took hours can now be made in a matter of minutes using this technique. The Raman instrument can also analyze some subsurface inclusions at depths of more than a millimeter in certain fa-



*Figure 15. Measuring 26.36 mm in length and weighing 56.00 ct, this Pakistani aquamarine crystal is host to an eye-visible 7.20 mm mineral inclusion cluster. Photo by Annie Haynes.*

vorable instances, which means inclusions do not need to be exposed to the surface.

After several Raman attempts from different directions, we realized that destructive analysis would be needed to clearly identify the inclusion cluster deep within this

stone. Due to the value of this inclusion specimen, we opted to forgo destructive analysis and keep the beryl crystal intact for future gemological exploration.

*John I. Koivula and Nathan Renfro  
GIA, Carlsbad*



*Figure 16. None of the analytical techniques at our disposal were able to conclusively identify the mineral making up the 7.20 mm inclusion cluster. The distinctive morphology shown by these inclusions strongly suggests that the cluster is composed of columbite-(Mn) crystals. Photomicrograph by Nathan Renfro; field of view 10.28 mm.*





# GEMS & GEMOLOGY®

Take the 2023

# CHALLENGE



The following 25 questions are from the four 2022 issues of *G&G*. Please refer to the feature articles in those issues to find the single best answer for each question.

Visit [gia.edu/gems-gemology](http://gia.edu/gems-gemology) to take the Challenge online. Entries must be received no later than **September 1, 2023**. All entries will be acknowledged with an email.

Score 75% or better, and you will receive a certificate of completion (PDF file). Earn a perfect score, and your name also will be listed in the Fall 2023 issue of *Gems & Gemology*.

- Nearly half of the diamonds from Guyana
  - have green spotting or skins.
  - are found as aggregates.
  - reach 10 carats in size.
  - possess D color.
- Heating ruby to 600°C may
  - significantly alter the Raman spectra of any spinel inclusions.
  - cause fissures to begin forming around solid inclusions.
  - affect sphene and apatite inclusions the most.
  - alter the appearance of any mica inclusions.
- Geographic origin determination of diamonds
  - is reliant upon identification of inclusions.
  - is reliant upon trace element analysis.
  - is reliant upon carbon dating.
  - is not currently possible.
- Only the most important paintings were allowed to use this natural pigment during its prime.
  - Ultramarine
  - Red ochre
  - Cinnabar
  - Azurite
- Amber from Phu Quoc, Vietnam
  - is mostly opaque.
  - is almost exclusively pale yellow in color.
  - commonly contains fauna.
  - commonly contains gas bubbles and spangles.
- Schneckenstein topaz
  - is currently an important commercial gemstone.
  - likely formed at low temperatures.
  - has high levels of trace impurities.
  - rivals Imperial topaz in color.
- The higher the silica content detected in turquoise, the more likely
  - it will command a higher per-carat price.
  - it will have a higher specific gravity.
  - its bodycolor will be sky blue.
  - it has been porcelain treated.
- Chinese sapphire from Muling
  - is mostly yellow, green, and blue in color.
  - is always heavily weathered in its rough form.
  - shows remarkable optical homogeneity.
  - can be blue and yellow bicolor.
- Today, the Habachtal emerald mine
  - produces emeralds similar to those from Colombia.

- B. produces a small amount of mineral specimens and facetable rough.  
C. is one of several Austrian emerald mines.  
D. is no longer in operation.
10. Which gem is considered too radioactive for daily wear?  
A. Green diamond  
B. Nephrite jade  
C. Ekanite  
D. Amber
11. A gem bead cultured pearl  
A. is of the highest quality if produced using a freshwater “Edison” pearl.  
B. must use a bead with a thermal expansion coefficient similar to that of nacre.  
C. involves incorporating a diamond in a pearl.  
D. is always under 8 mm in diameter.
12. How do the optical data plots for Schneckenstein topaz differ using a wavenumber versus a wavelength scale?  
A. Wavenumber data is directly proportional to photon energy.  
B. Wavelength data is directly proportional to photon energy.  
C. At lower energies, wavelength data is compressed.  
D. There is no difference.
13. What happens to pink spinel after heating to 1000°C?  
A. The full width half maximum (FWHM) of its R- and N-lines decrease.  
B. Its R-line becomes less dominant than its N-lines in a PL spectrum.  
C. The saturation of its pink bodycolor decreases significantly.  
D. Its Cr<sup>3+</sup> ions transition from non-ideal to ideal classes.
14. The red color in plagioclase feldspars  
A. increases in saturation with increasing Cu<sup>+</sup> concentration.  
B. is only seen in copper-diffused material.  
C. cannot be fully explained today.  
D. is due to Cu<sup>2+</sup> in the lattice.
15. Geographic origin determination of diamonds versus colored stones is complicated by the fact that diamonds  
A. form in a much less chemically diverse environment.  
B. can only contain three possible mineral inclusions.  
C. do not contain incompatible elements.  
D. have too high a refractive index.
16. “Natural porcelain” turquoise is separated from “porcelain-treated” turquoise by  
A. infrared and UV-Vis spectroscopy.  
B. infrared, UV-Vis, and Raman spectroscopy.  
C. color, refractive index, and surface luster.  
D. specific gravity, silica content, and Raman spectroscopy.
17. A possible origin discriminator for nephrite may be its  
A. ratio of thorium to uranium.  
B. degree of compactness.  
C. concentration of iron.  
D. depth of green color.
18. Blue sapphires from Muling  
A. are mined exclusively from source rocks.  
B. all show angular color zoning.  
C. are not all formed by the same geological process.  
D. are clearly metamorphic in origin.
19. Copper diffusion treatment of near-colorless plagioclase feldspars  
A. increases the fluorescence intensity at around 400 nm.  
B. reduces the concentration of Cu<sup>+</sup>-Cu<sup>+</sup> dimers.  
C. imparts a red color only to labradorite.  
D. imparts a red color only to andesine.
20. Why are diamonds from Guyana commonly green?  
A. They were damaged by radioactivity.  
B. Their color comes from inclusions.  
C. They contain high levels of nickel.  
D. They are generally type IIb or Ib.
21. Low-temperature heat treatment of ruby  
A. covers the range of temperatures from 600–1500°C.  
B. involves the dissolution of secondary-phase microcrystals.  
C. does not always produce the same reactions for inclusions of the same type.  
D. reliably produces telltale visual features.
22. Heat treatment of ekanite to improve color  
A. is performed on virtually all commercially sold material.  
B. results in a green similar to peridot.  
C. has not been successful.  
D. removes yellow tints.
23. In ancient times, white pigment was created by  
A. heating bone in the absence of oxygen.  
B. heating bone in the presence of oxygen.  
C. heating ivory in a closed crucible.  
D. finely grinding hematite.
24. Jewelry that incorporates near field communication (NFC) microchips  
A. requires the NFC microchip to be placed in a Faraday cage.  
B. must be larger to accommodate a battery.  
C. can easily be found with an app on your smartphone.  
D. cannot be subjected to temperatures greater than 700°F (370°C).
25. The emeralds from the coronation crown of Napoleon III  
A. came from the Habachtal emerald mine.  
B. contain the *gota de aceite* optical effect in many cases.  
C. were all cut specifically for this crown.  
D. were clarity enhanced.

To take the Challenge online,  
please scan the QR code.



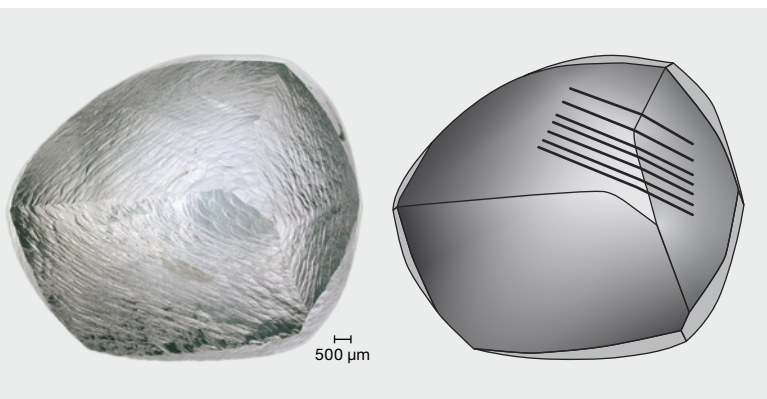


Editor: Evan M. Smith

## Plastic Deformation: How and Why Are Most Diamonds Slightly Distorted?

Extreme hardness is one of the most well-known physical properties of diamond. It is difficult to imagine this same material bending or squishing like putty, but many natural diamonds have evidence of plastic deformation (figure 1). This process is even responsible for creating the value behind the most expensive diamonds sold at auction to date, by both per-carat price and total price. Specifically, the 11.15 ct Williamson Pink Star that sold for \$57.7 million and the 59.6 ct Pink Star that sold for \$71.2 million owe their Fancy Vivid pink colors to plastic deformation.

*Figure 1. A 4.56 ct rough diamond with plastic deformation lines, highlighted in the sketch on the right. Deformation has occurred along a set of parallel internal slip planes. The planes appear as thin ridges on the diamond's surface, exposed by natural dissolution of the surface by fluids (i.e., resorption). In fact, the whole surface has been resorbed into this overall dodecahedroid shape, decorated by elongate hillocks and plastic deformation lines, both fine features representing slight interruptions and imperfections in the diamond crystal lattice. Images by Evan M. Smith.*



Plastic deformation does not always lead to pink color, though. More commonly the result is brown color. Our understanding of brown color in diamond has improved in the last 20 years, in part due to the need to screen for decolorizing high-pressure, high-temperature (HPHT) treatment. Most mined diamonds have at least some amount of brown color due to plastic deformation, varying from dark to barely noticeable (Harris et al., 1979; Fisher, 2009; Dobrinets et al., 2013). In other instances, where the deformation is less intense, there may be no color imparted. Plastic deformation is one of the most prevalent features in natural diamond (Urusovskaya and Orlov, 1964; Harris et al., 1979). It is a natural phenomenon thought to occur sometime after a diamond crystallizes, during its residence deep in Earth's mantle and/or during its volcanic journey up to the surface.

### What Is Plastic Deformation?

When stresses act on a solid, they can cause it to deform, or change shape, in one of three ways. There is elastic deformation, the kind of deformation that springs are designed for. When you remove the stress, it “springs” right back into its original shape. Brittle deformation is the kind of deformation at play when a water glass falls to the floor and shatters. The material fractures and breaks apart. Finally, there is plastic deformation, the kind of deformation associated with putty. The material deforms into a new shape but the change is lasting, even after removing the stress.

*Editor's note: Questions or topics of interest should be directed to Evan Smith (evan.smith@gia.edu).*

GEMS & GEMOLOGY, VOL. 59, No. 1, pp. 94–100.

© 2023 Gemological Institute of America



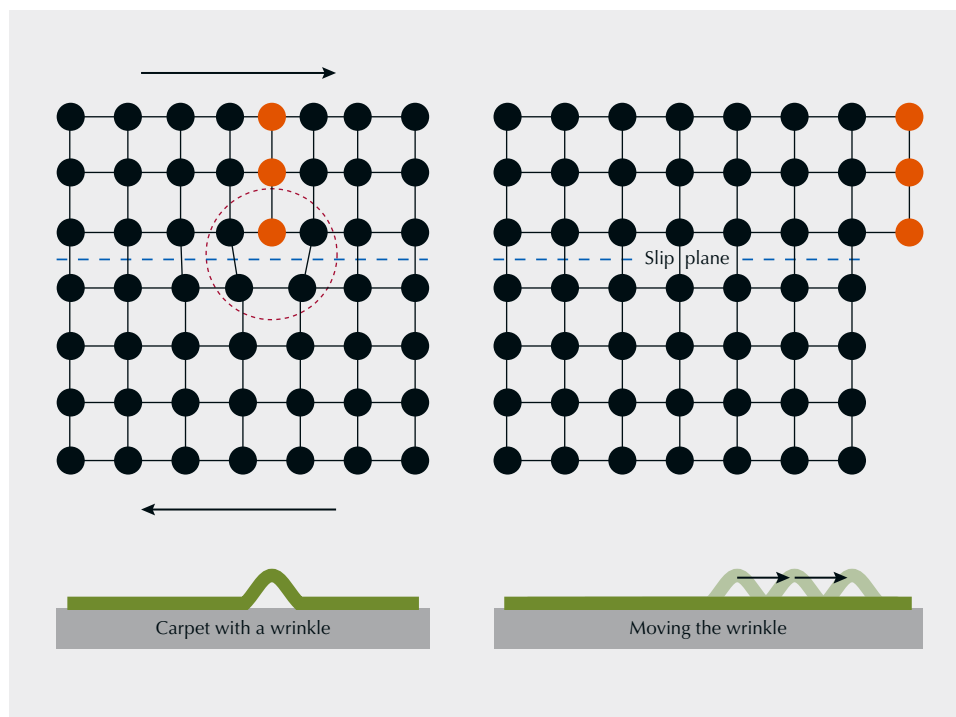


Figure 2. Left: Simplified drawing of a diamond lattice with a dislocation. The red dotted circle shows the dislocation where a break in the regular order of the bonding structure results in an extra half-plane of carbon atoms, shown in orange. Stress on the crystal, indicated by black arrows, allows stepwise breaking and reforming of bonds that causes the dislocation and half-plane to move to the right along a slip plane (blue dashed line). Right: The dislocation has moved all the way to the right and out of the crystal so that it no longer exists. The dislocation and its movement can be thought of as a carpet with a wrinkle.

A familiar wire paper clip can serve to demonstrate deformation. If you bend it just slightly, it will deform elastically and return to its unbent shape. The elastic behavior is what allows a paper clip to hold on to a few sheets of paper. If you bend it beyond a certain point, the bend becomes permanent. This is plastic deformation. If you bend it back and forth a few times in one spot, the paper clip will break.

Often we see just one of these three mechanisms dominate, whether it is elastic, brittle, or plastic. Deformation behavior depends on many factors, such as the temperature, how much stress is applied, and, of course, what kind of material it is. For diamond, temperature is a key factor. If you tried to squeeze, twist, or stretch a diamond at room temperature, the elastic deformation would be minimal. It is among the most rigid of all known materials. If it is subjected to high stresses, diamond tends to exhibit brittle deformation by cracking or chipping. But at higher temperatures, diamond begins to exhibit plastic deformation. Experiments show that significant plastic deformation requires temperatures above approximately 900°C (DeVries, 1975; Weidner et al., 1994).

### How Does Diamond Deform Plastically?

Many metal objects, including paper clips, deform plastically under conditions we can easily create and deform to a degree that is obvious. Our understanding of how crystalline solids deform is underpinned by engineering studies of metals, such as steel used for car frames and bridges. Aluminum foil is an example of a metal whose plastic deformation behavior can be felt as we shape and conform it

in the kitchen. Although we cannot feel and observe diamond deformation in the same way, it involves the same basic principles at the atomic scale. During plastic deformation, atomic bonds are breaking and re-forming along imperfections called *dislocations*. Plastic deformation in all crystalline solids, including diamond, is accomplished by the creation and movement of dislocations (Nesse, 2017).

A dislocation is a linear (one-dimensional) disruption in the regular, repeating atomic structure. Figure 2 shows a simplified illustration of a dislocation in a crystal lattice. The dislocation is shown end-on, and the crystal lattice appears to have an extra half-plane of atoms, shown in orange (figure 2), which resembles a half sheet of paper inserted into an otherwise orderly paper stack. This is an edge dislocation, one of two major dislocation types. The second type is a screw dislocation, which has a different geometry.

Dislocations allow a crystal to deform plastically little by little as bonds break and re-form. The crystal as a whole remains fully intact, as only a small number of its bonds are broken at any given time. A dislocation is much like a wrinkle in a carpet (figure 2, bottom). A carpet could be moved by introducing a wrinkle and working it across the carpet. Most of the carpet remains in contact with the floor, but moving the wrinkle shifts the carpet slightly by breaking and reestablishing contact with the floor. Similarly, as dislocations move through a crystal, they can allow atomic layers to move with respect to one another. Systematic movement of many dislocations can allow the whole crystal to deform plastically when subjected to stress.

Given that crystals are orderly structures, it should come as no surprise that dislocation movement is not ran-

dom. The crystal structure constrains the dislocation movement into certain configurations and directions. In figure 2, dislocation movement or “slip” occurs along a plane (shown as a blue dashed line) that is parallel to the atomic layering. In diamond, slip occurs along octahedral or {111} planes, with the direction of slip within those planes being described by  $\langle 110 \rangle$ , together giving a “slip system” described as {111}  $\langle 110 \rangle$  (Evans and Wild, 1965). In other words, when diamond deforms, the deformation takes place along internal {111} planes, which is the same orientation as the faces of an octahedron-shaped diamond crystal. And the three lines defining the edges of that triangular octahedral face have a  $\langle 110 \rangle$  orientation, which illustrates the three possible directions of slip within that octahedral plane. Slip planes will contain many dislocations, not just one, and deformation can be spread across multiple dislocations and multiple slip planes simultaneously.

### What Does It Look Like?

Plastic deformation involves the creation and movement of dislocations through the diamond crystal lattice. Even though this is something that happens at the atomic scale, it does leave some visible signs. Figure 1 shows plastic deformation lines as a series of fine parallel ridges on a diamond’s surface. These lines trace out where the internal {111} slip planes meet the outer surface of the diamond. They stand out because the diamond surface is resorbed, meaning it has been partially dissolved or etched by natural fluid or magma (Smit and Shirey, 2020). The slip planes do not etch at the same rate as neighboring regions of the crystal, resulting in surface relief and lines visible to the unaided eye.

Plastic deformation lines (figure 1) are the archetypal feature of plastically deformed diamonds (Harris et al., 2022). They are frequently but variably observed within some diamonds from most diamond deposits (Harris et al., 1979). However, only diamonds with resorbed surfaces can show deformation lines (Gurney, 1989). On primary octahedral crystal faces, evidence of plastic deformation can occasion-

ally be observed as rows of trigons (figure 3). These negative trigons are small pits where the diamond has been etched away preferentially due to the presence of dislocations. Each row of trigons marks a separate {111} plane.

In addition to dislocation movement on {111} planes, a related plastic deformation mechanism can lead to the crystal lattice being distorted into a totally new orientation. This abrupt and localized change in crystal lattice orientation is called *mechanical twinning* or *deformation twinning*. Unlike twins arising from growth, such as macles (Harris et al., 2022), mechanical twins in diamond are strictly from deformation (Titkov et al., 2012; Yu et al., 2012). This process is sometimes called *glide*, and the resulting mechanical twin planes are called *glide planes* (Nesse, 2017). In fact, the rows of trigons in figure 3 technically reveal glide planes, which in this case are associated with a pink color. The close-up (figure 3, right) shows that the trigons are connected by thin pink lines, actually pink lamellae viewed end-on, that correspond to glide planes. Pink lamellae like these are typically about 1 micrometer thick and may consist of multiple closely spaced mechanical twins (Gaillou et al., 2010).

A more dramatic example of mechanical twinning is shown in figure 4. A sharp step in surface topography runs all the way around this large rough diamond like a belt and perfectly traces out a {111} plane. This is a ~0.5 mm thick mechanical twin zone, where the diamond has been distorted and the lattice reoriented as a result of applied stress. Again, the new lattice orientation is not random, but rather a symmetrical mirror image so that the different lattice orientations match up neatly at the interface between the twinned region and the rest of the diamond on either side. Natural broken cleavage surfaces intersecting the mechanical twin (figure 4, left) demonstrate the change in crystal orientation by a corresponding change in the cleavage direction within the ~0.5 mm thick twinned zone.

Rough diamonds and their naturally sculpted surfaces can reveal a lot about their deformation history. Thankfully, since plastic deformation happens internally, it is still possible to observe it once a diamond is cut and polished.

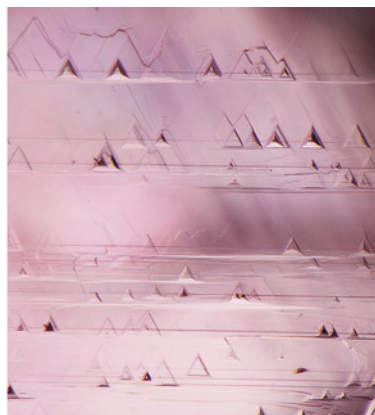
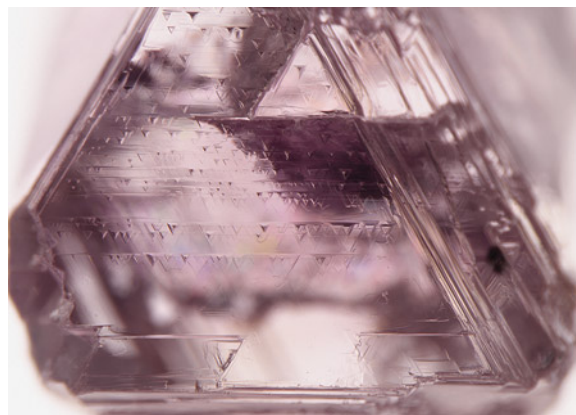


Figure 3. Left: A 0.31 ct pink octahedral diamond crystal with rows of negative trigons indicating that plastic deformation has taken place. Right: This close-up shows the horizontal rows of trigons marking the location of pink {111} glide planes approximately 1  $\mu\text{m}$  thick. Photomicrographs by Evan M. Smith; fields of view 3.57 mm (left) and 0.71 mm (right).



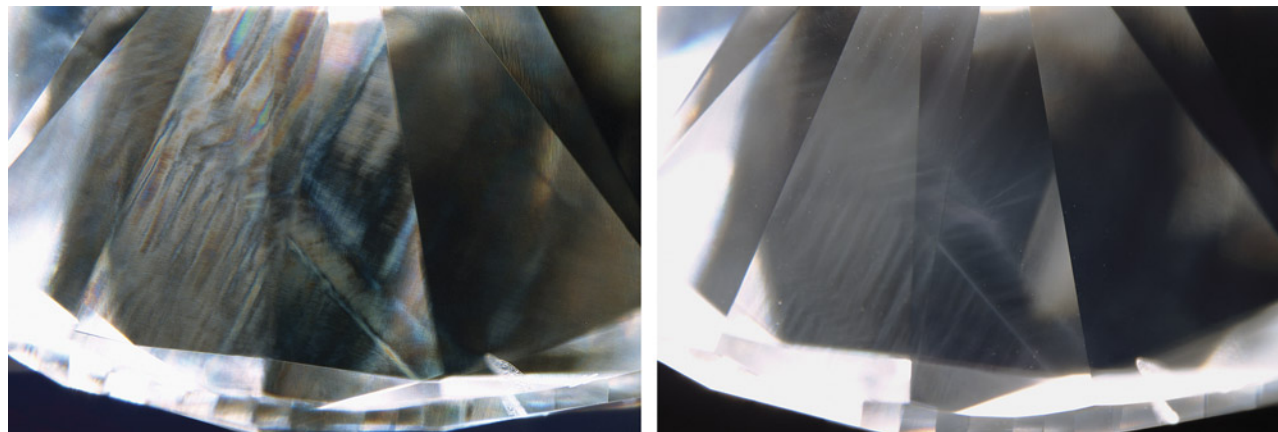
Figure 4. Two views of a large rough diamond with a pronounced mechanical twin plane. This 812 ct diamond, named the Constellation, has both freshly cleaved surfaces (left) and natural resorbed surfaces (right). Both views show a kink that wraps around the entire surface and defines an internal {111} twin plane where the crystal orientation is reversed with respect to the rest of the diamond. The diamond is 6.6 cm in its longest dimension. Photos by Jian Xin (Jae) Liao.

Polarizing filters are a simple yet powerful tool for this application, whether using a polariscope or a gem microscope (Renfro, 2015). Viewing a diamond using crossed polarizing filters is an easy way to see anomalous birefringence, which in natural diamond is typically the result of plastic deformation (figure 5). With this technique, a perfect, unstrained diamond should appear uniformly dark inside. Bending and twisting of the light as it passes through deformed (strained) regions of the diamond will result in a

pattern of anomalous birefringence, such as banding, mottling, or cross-hatching.

Plastic deformation can also be observed using cathodoluminescence imaging or deep UV fluorescence imaging (e.g., DiamondView). These techniques are especially useful for examining polished diamond surfaces, where slip planes can appear as bright or dark lines (figure 6, left). Another deformation-related pattern sometimes revealed with these methods is dislocation networks (figure 6,

Figure 5. A natural type IIa diamond with evidence of plastic deformation. Examination with a microscope using crossed polarizing filters (left) reveals internal banding of dark/light and interference colors due to strain-related anomalous birefringence. In this diamond, the geometry of the banding correlates with the appearance of unusual whitish graining (right). The hazy whitish graining may be caused by plastic deformation. Photomicrographs by Evan M. Smith; field of view 4.79 mm.





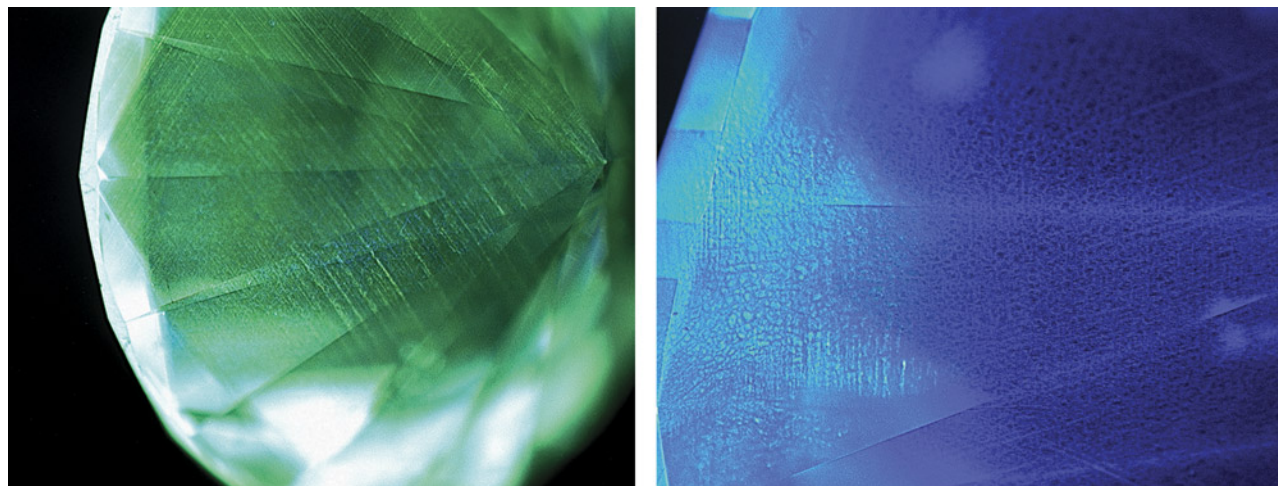


Figure 6. Deep UV fluorescence images of deformation features. Left: Deformation lines in the pavilion of a round brilliant diamond, with two distinct sets of parallel lines that trace out octahedral or {111} slip planes. Right: A dislocation network pattern, appearing as a dark mesh against a bright background in the left portion of the diamond but as a bright mesh against a dark background toward the right. Images by Evan M. Smith; field of view is 4.66 mm.

right), which have a cellular appearance resembling mud cracks or a fine mesh (De Corte et al., 2006). Dislocation networks are thought to be the result of not just plastic deformation, but also a period of recovery at high temperatures that allows the dislocations to reorganize into a more stable configuration (Hanley et al., 1977). This process may be similar to hammering or working metals and then heating them up to relax and reconfigure the tangled dislocations that have been introduced. Sublithospheric or superdeep diamonds often have dislocation network patterns, and it has been suggested that their formation is promoted by low nitrogen content and/or high temperatures (Smith et al., 2019).

### How Does Plastic Deformation Cause Color?

In 1999, General Electric and Lazare Kaplan International announced that HPHT processing could be applied as a commercial treatment to decolorize brown diamonds (Vagarali et al., 2004). This spurred research into the cause of brown color, which up until that point had been poorly understood. Visual indications of deformation had long been recognized to correlate with the presence of brown and to a lesser extent pink colors in diamond (Urusovskaya and Orlov, 1964; Harris et al., 1979). Internally, these colors often concentrate along slip planes, glide planes, or less distinctly along “graining,” all of which are deformation features. Theoretical modeling and experiments played important roles in linking brown color to dislocation movement and the creation of vacancies in the crystal structure (Avalos and Dannefaer, 2003; Hounscome et al., 2006; Barnes et al., 2007).

A vacancy is a missing atom in the crystal lattice. Vacancies can be created during plastic deformation when

multiple dislocations interact or jogged dislocations move through the crystal (Leipner et al., 2000, 2003). At the high temperatures necessary for plastic behavior, these vacancies are mobile and tend to cluster into groups. These small groups of vacancies can absorb visible light and cause color. Vacancy clusters made up of about 40–60 vacancies are thought to be responsible for the common brown color in diamond (Avalos and Dannefaer, 2003; Hounscome et al., 2006; Barnes et al., 2007).

The cause of deformation-related pink is believed to be similar but involves a broad absorption band centered near 550 nm that is not fully understood (Gaillou et al., 2010). To be fair, not all brown and pink color is attributable to plastic deformation, but it is the leading cause (Harris et al., 1979; Fisher, 2009). An excellent review of brown and pink color in diamond was presented in Eaton-Magaña et al. (2018).

### What Causes the Deformation?

It is plain to see that many natural diamonds bear evidence of plastic deformation, but it is not intuitively obvious why this should be the case. There must be some geological processes that lead to compression or shearing forces that occasionally deform diamonds. The geological process should be neither too gentle, because the relatively soft silicate host rocks should simply flow around the diamonds, nor too violent, which would break diamonds rather than plastically deform them. Several theories have been proposed.

Kimberlites and related eruptions that bring diamonds from the mantle up to the surface could have the power to deform diamonds. The magmatic journey is thought to be relatively violent, however, and it is clear that diamonds

can break as they ascend within a kimberlite (Harris et al., 2022). This may mean that the conditions are too forceful and chaotic to develop significant plastic deformation. The early stages leading up to an eruption could also provide opportunities for diamond deformation.

Another possibility is that diamond deformation is related to the movements at the lithosphere-asthenosphere boundary, where the base of a rigid continental tectonic plate meets underlying weak, mobile rocks at a depth of approximately 200 km (Stachel et al., 2018). This would involve shearing between the lithosphere, the rigid host rock where most diamonds form, and the asthenosphere, the underlying warm flowing rock that is the topmost part of the convecting mantle.

Yet another theory suggests that deformation in some settings might be related to the movement of tectonic plates, specifically oceanic lithosphere sinking into the mantle by the process of subduction (Bulanova et al., 2018). Subduction and the motion of tectonic plates could also play a role in the deformation of super-deep diamonds. The formation of these diamonds has been linked to deep-focus earthquakes (Shirey et al., 2021), which could involve localized shearing and faulting, potentially favorable conditions for plastic deformation of diamonds.

The deformation histories recorded within natural diamonds are valuable for studying Earth's interior. In the future, it may be possible to constrain the temperature, pressure, and strain rate (i.e., the speed of deformation) required to produce the various features we observe. This information about deep mantle processes would help paint a clearer picture of how and why rocks deep inside the earth move around over geologic time.

## Diamonds Bear Witness to Our Active Planet

The fact that natural diamonds frequently contain evidence of deformation reminds us that Earth is not a static ball of rock. As far as we know, Earth is the only planet with active plate tectonics, meaning its outer layer is made up of multiple moving plates (Condie and Pease, 2008). The processes of mantle convection and subduction mean Earth's interior is on the move as well. Measurable effects of these mechanisms exist in the chemical and isotopic composition of diamonds and their inclusions. But what makes a diamond's plastic deformation features special is that they are a visible, tangible testament to rock and magma churning, shearing, and moving about inside our active planet.

## ACKNOWLEDGMENT

Many thanks to Dr. Steven B. Shirey for discussion and suggestions that helped to improve this column.

## REFERENCES

- Avalos V., Dannefaer S. (2003) Vacancy-type defects in brown diamonds investigated by positron annihilation. *Physica B: Condensed Matter*, Vol. 340-342, pp. 76–79, <http://dx.doi.org/10.1016/j.physb.2003.09.006>
- Barnes R., Bangert U., Scott A. (2007) Investigating large vacancy clusters in type IIa diamond with electron energy loss spectroscopy (EELS). *Physica Status Solidi (a)*, Vol. 204, No. 9, pp. 3065–3071, <http://dx.doi.org/10.1002/pssa.200776323>
- Bulanova G.P., Speich L., Smith C.B., Gaillou E., Kohn S.C., Wiberley E., Chapman J.G., Howell D., Davy A.T. (2018) The unique nature of Argyle fancy diamonds: Internal structure, paragenesis, and reasons for color. In A.T. Davy et al., Eds., *Geoscience and Exploration of the Argyle, Bundar, Diavik, and Murowa Diamond Deposits*, Volume 20. Society of Economic Geologists, Littleton, Colorado, pp. 169–190, <http://dx.doi.org/10.5382/SP.20.07>
- Condie K.C., Pease V., Eds. (2008) When Did Plate Tectonics Begin on Planet Earth? Geological Society of America, Special Paper 440, 294 pp.
- De Corte K., Anthonis A., Van Royen J., Blanchaert M., Barjon J., Willems B. (2006) Overview of dislocation networks in natural type IIa diamonds. *G&G*, Vol. 42, No. 3, pp. 122–123.
- DeVries R.C. (1975) Plastic deformation and “work-hardening” of diamond. *Materials Research Bulletin*, Vol. 10, No. 11, pp. 1193–1199, [http://dx.doi.org/10.1016/0025-5408\(75\)90026-4](http://dx.doi.org/10.1016/0025-5408(75)90026-4)
- Dobrinets I.A., Vins V.G., Zaitsev A.M. (2013) *HPHT-Treated Diamonds: Diamonds Forever*. Springer Series in Materials Science, Springer Berlin, Heidelberg, <http://dx.doi.org/10.1007/978-3-642-37490-6>
- Eaton-Magaña S., Ardon T., Smit K.V., Breeding C.M., Shigley J.E. (2018) Natural-color pink, purple, red, and brown diamonds: Band of many colors. *G&G*, Vol. 54, No. 4, pp. 352–377, <http://dx.doi.org/10.5741/GEMS.54.2.352>
- Evans T., Wild R.K. (1965) Plastic bending of diamond plates. *Philosophical Magazine: A Journal of Theoretical Experimental and Applied Physics*, Vol. 12, No. 117, pp. 479–489, <http://dx.doi.org/10.1080/14786436508218894>
- Fisher D. (2009) Brown diamonds and high pressure high temperature treatment. *Lithos*, Vol. 112, pp. 619–624, <http://dx.doi.org/10.1016/j.lithos.2009.03.005>

- Gaillou E., Post J.E., Bassim N.D., Zaitsev A.M., Rose T., Fries M.D., Stroud R.M., Steele A., Butler J.E. (2010) Spectroscopic and microscopic characterizations of color lamellae in natural pink diamonds. *Diamond and Related Materials*, Vol. 19, No. 10, pp. 1207–1220, <http://dx.doi.org/https://doi.org/10.1016/j.diamond.2010.06.015>
- Gurney J.J. (1989) Diamonds. In J. Ross, Ed., *Kimberlites and Related Rocks: Proceedings of the Fourth International Kimberlite Conference*, Volume 2. Geological Society of Australia, Sydney, Australia, pp. 935–965.
- Hanley P.L., Kiflawi I., Lang A.R. (1977) On topographically identifiable sources of cathodoluminescence in natural diamonds. *Philosophical Transactions of the Royal Society of London. Series A, Mathematical and Physical Sciences*, Vol. 284, No. 1324, pp. 329–368, <http://dx.doi.org/10.1098/rsta.1977.0012>
- Harris J.W., Hawthorne J.B., Oosterveld M.M. (1979) Regional and local variations in the characteristics of diamonds from some southern African kimberlites. In H.O.A. Meyer and F.R. Boyd, Eds., *Kimberlites, Diatremes, and Diamonds: Their Geology, Petrology, and Geochemistry*, Vol. 15, American Geophysical Union, Washington, DC, pp. 27–41, <http://dx.doi.org/10.1029/SP015p0027>
- Harris J.W., Smit K.V., Fedortchouk Y., Moore M. (2022) Morphology of monocrystalline diamond and its inclusions. *Reviews in Mineralogy and Geochemistry*, Vol. 88, No. 1, pp. 119–166, <http://dx.doi.org/10.2138/rmg.2022.88.02>
- Hounscome L.S., Jones R., Martineau P.M., Fisher D., Shaw M.J., Briddon P.R., Öberg S. (2006) Origin of brown coloration in diamond. *Physical Review B*, Vol. 73, No. 12, article no. 125203, <http://dx.doi.org/10.1103/PhysRevB.73.125203>
- Leipner H.S., Hübner C.G., Staab T.E.M., Haugk M., Sieck A., Krause-Rehberg R., Frauenheim T. (2000) Vacancy clusters in plastically deformed semiconductors. *Journal of Physics: Condensed Matter*, Vol. 12, No. 49, pp. 10071–10078, <http://dx.doi.org/10.1088/0953-8984/12/49/307>
- Leipner H.S., Mikhnovich Jr. V.V., Bondarenko. V., Wang Z., Gu H., Krause-Rehberg R., Demenet J.L., Rabier J. (2003) Positron annihilation of defects in silicon deformed at different temperatures. *Physica B: Condensed Matter*, Vol. 340–342, pp. 617–621, <http://dx.doi.org/10.1016/j.physb.2003.09.119>
- Nesse W.D. (2017) *Introduction to Mineralogy*. Oxford University Press, New York.
- Renfro N. (2015) Digital photomicrography for gemologists. *G&G*, Vol. 51, No. 2, <http://dx.doi.org/10.5741/GEMS.51.2.144>
- Shirey S.B., Wagner L.S., Walter M.J., Pearson D.G., van Keken P.E. (2021) Slab transport of fluids to deep focus earthquake depths—Thermal modeling constraints and evidence from diamonds. *AGU Advances*, Vol. 2, No. 2, <http://dx.doi.org/10.1029/2020AV000304>
- Smit K.V., Shirey S.B. (2020) Diamonds are not forever! Diamond dissolution. *G&G*, Vol. 56, No. 1, pp. 148–155.
- Smith E.M., Shirey S.B., Richardson S.H., Nestola F., Bullock E.S., Wang J., Wang W. (2019) Reply to: Evidence for two blue (type IIb) diamond populations. *Nature*, Vol. 570, No. 7760, pp. E28–E29, <http://dx.doi.org/10.1038/s41586-019-1246-8>
- Stachel T., Harris J.W., Hunt L., Muehlenbachs K., Kobussen A.F., Edinburgh Ion Micro-Probe Facility (2018) Argyle diamonds: How subduction along the Kimberley Craton Edge generated the world's biggest diamond deposit. In A.T. Davy, et al., Eds. *Geoscience and Exploration of the Argyle, Bunder, Diavik, and Murowa Diamond Deposits*, Volume 20. Society of Economic Geologists, Littleton, Colorado, pp. 145–168, <http://dx.doi.org/10.5382/SP.20.06>
- Titkov S.V., Krivovichev S.V., Organova N.I. (2012) Plastic deformation of natural diamonds by twinning: Evidence from X-ray diffraction studies. *Mineralogical Magazine*, Vol. 76, No. 1, pp. 143–149, <http://dx.doi.org/10.1180/minmag.2012.076.1.143>
- Urusovskaya A.A., Orlov Y.L. (1964) Nature of plastic deformation of diamond crystals. *Doklady Akad. Nauk. SSSR*, Vol. 154, pp. 112–115.
- Vagarali S., Webb S., Jackson W., Banholzer W., Anthony T., Kaplan G. (2004) High pressure/high temperature production of colorless and fancy-colored diamonds. United States Patent 6692714.
- Weidner D.J., Wang Y., Vaughan M.T. (1994) Strength of diamond. *Science*, Vol. 266, No. 5184, pp. 419–422, <http://dx.doi.org/10.1126/science.266.5184.419>
- Yu X., Raterron P., Zhang J., Lin Z., Wang L., Zhao Y. (2012) Constitutive law and flow mechanism in diamond deformation. *Scientific Reports*, Vol. 2, article no. 876, <http://dx.doi.org/10.1038/srep00876>

For online access to all issues of GEMS & GEMOLOGY from 1934 to the present, visit:

[gia.edu/gems-gemology](http://gia.edu/gems-gemology)





# Knowledge and Skills for Today's Hot Topics



## Online and In-Person Seminars Designed for Gem and Jewelry Professionals

- Natural and Laboratory-Grown Diamonds
- Jewelry Design
- Colored Stones
- Pearls
- Bench Skills



Visit [collective.gia.edu/seminars](https://collective.gia.edu/seminars) for schedules and more information.

**GIA Alumni receive a 10% discount.**  
**Seminars are open to all.**

CONTINUING EDUCATION BY

**GIA** Alumni  
*Collective*™

These seminars are avocational and are not intended to prepare individuals for entry-level employment. They are non-credit bearing and do not lead to a GIA academic credential. They do not fall under the approval of the Accrediting Commission of Career Schools and Colleges (ACCSC) or the Distance Education Accrediting Commission (DEAC).  
© 2023 Gemological Institute of America, Inc. All trademarks owned by Gemological Institute of America, Inc. and used under license.



### Contributing Editors

Gagan Choudhary, *IIGJ-Research & Laboratories Centre, Jaipur, India* (gagan.choudhary@iigjrlc.org)

Christopher M. Breeding, *GIA, Carlsbad* (christopher.breeding@gia.edu)

Guanghai Shi, *School of Gemmology, China University of Geosciences, Beijing* (shigh@cugb.edu.cn)

## TUCSON 2023

This year's Tucson shows were well attended, and many vendors were relieved by the strong sales. In fact, the only "complaint" from vendors this year was that for many it was too busy to take even a short break away from their booths. Some vendors reported selling less than in 2022, but still more than in pre-COVID years.

Supply chain issues resulting from lack of output during the pandemic are still being felt. For many sellers demand often exceeded supply, especially for fine-quality colored stones, and prices are increasing to reflect that. With this increase expected to continue, the heavy booth traffic could be due to consumers buying as much as possible at these price points. This corresponds with comments from Nathan Renfro on the GIA show services laboratory, which received a near-record number of submissions this year. As for the trends in materials submitted to the lab, he indicated a typical mix of the major stones: mainly ruby, sapphire, emerald, Paraíba tourmaline, and alexandrite.

At the AGTA GemFair and Gem & Jewelry Exchange (GJX) shows, sapphire, large freshwater pearls from China, and Ethiopian opal were among the eye-catching gems. Sapphire was once again a top seller, with blue and untreated colors doing especially well. Many fancy-color sapphires, including ones in saturated hues such as magenta, were available (Pantone's Color of the Year for 2023 is Viva Magenta) (figure 1). There were multiple sellers of akoya,

Tahitian, and "Edison" pearls in both venues. Most notably, "Edison" pearls were available in much larger sizes and with more saturated colors than in years past (figure 2). Non-nacreous pearls were also featured more prominently. Ethiopian opal, first introduced in Tucson in 2009, was very popular this year. It has climbed from a novelty to a gemstone found in top designer luxury jewels, such as the Zoltan David necklace shown on the cover of this issue and the pin featuring both Ethiopian opal and conch pearls

*Figure 1. This ring from Graff features a 3.95 ct pink sapphire and 7.5 carats of diamond in a spiral design. Photo by Robert Weldon; courtesy of Jewelerette Co.*



*Editors' note: Interested contributors should send information and illustrations to Stuart Overlin at soverlin@gia.edu.*

*Banner photo of Afghan kunzite by Robert Weldon; courtesy of Dudley Blauwet, Mountain Minerals International.*

GEMS & GEMOLOGY, VOL. 59, NO. 1, pp. 102–162.

© 2023 Gemological Institute of America



Figure 2. Left: “Edison” pearls were available in large sizes and attractive colors. Photo by Si Athena Chen; courtesy of A&B Jewelry. Right: A strand of “Edison” pearls of various colors, in sizes from 14 to 16 mm. Photo by Mimi Travis; courtesy of Yen’s Jewelry & Accessories.

in figure 3. Tourmaline from newly discovered pockets in San Diego County’s Pala District was also on display.

Figure 3. This pin features a 63.92 ct Ethiopian opal with 23.85 carats of conch pearl, 5.88 carats of natural pearl, and 15.85 carats of diamond, set in platinum. Photo by Robert Weldon; courtesy of Pioneer Gems of New York.



The demand for one-of-a-kind gems was apparent in all aspects—cut, color, and even inclusions. Nontraditional cuts such as slices, fantasy cuts, rose cuts, kites, and tablets were readily found in gems ranging from rutiled quartz to diamond (figure 4). Beyond nonstandard cuts, stones

Figure 4. Earrings featuring diamond slices and rose-cut rubies. Photo by Mimi Travis.







Figure 5. “Salt and pepper” diamonds containing eye-visible inclusions. Photo by Jennifer Stone-Sundberg; courtesy of Misfit Diamonds.

with obvious inclusions were very popular. The appeal of these stones centers on their uniqueness. “Salt and pepper” diamonds with multiple eye-visible white, gray, and black inclusions were available loose (figure 5) and in jewelry items throughout the shows. Similarly, nontraditional colors for particular varieties, including color-change stones, pastel colors (such as “mint” tourmaline), teal, and bicolor stones, were trending (figure 6). Strong demand for these nontraditional or one-of-a-kind stones comes from small-scale individual designers with the ability to promote to a wide audience via social media.

In 2020, we reported on the first Ethical Gem Fair in Tucson. This year, suppliers at the fair were pleasantly surprised by the number of large jewelry manufacturers who attended for the first time. The trend toward responsible sourcing, traceability, transparency in practices, and social

awareness, which has long been a key differentiator for some jewelers, is clearly becoming more mainstream as customers increasingly demand to know more about the origin and impact of the stones they are purchasing. This year, jewelers at AGTA and GJX also emphasized the importance of providing an environmentally conscious product and the increasing demand from clients for full chain-of-custody information on stones. Similarly, many small-scale designers and buyers were seeking out gems mined in the United States, such as Montana sapphire, Oregon sunstone, and amethyst from the Four Peaks mine in Arizona. They noted high demand for these gems, which seem to satisfy consumer sustainability concerns. In many cases, the younger generation of jewelers has brought a focus on ethical and environmentally sound practices to multigenerational businesses.

We hope you enjoy our coverage of the 2023 Tucson gem shows, where you’ll find striking pieces we saw, the latest trends, mining updates, and more.

The following contributed to this report: Lisa Neely, Mimi Travis, Nathan Renfro, Albert Salvato, and Wim Verriest.

Jennifer Stone-Sundberg, Si Athena Chen, Lisa Kennedy, Robert Weldon, and Erin Hogarth

## COLORED STONES AND ORGANIC MATERIALS

**Enormous cat’s-eye aquamarine.** On the AGTA show’s opening day, we were on hand as Gary Bowersox and Kathleen Kolt-Bowersox donated an extraordinary cat’s-eye aquamarine to Dr. Jeffrey Post, mineralogist and curator-in-charge of gems and minerals at the Smithsonian National Museum of Natural History (figure 7).

The 586.43 ct untreated transparent light greenish blue aquamarine with a sharp cat’s-eye is from the Pech Valley pegmatite mine in Afghanistan. The rough (figure 8, left) weighed approximately 7,700 ct and was kept for 15 years

Figure 6. An unusual 6.95 ct cushion-cut bicolor alexandrite from Madagascar displaying a color change from yellowish green and reddish brown in daylight (left) to yellowish orange and orangy brown in incandescent illumination (right). Photos by Robert Weldon; courtesy of Bryan Lichtenstein, 3090 Gems, LLC.





Figure 7. Left: A 586.43 ct cat's-eye aquamarine donated by Gary Bowersox and Kathleen Kolt-Bowersox to the Smithsonian National Museum of Natural History gem collection. Photo by Robert Weldon; courtesy of the Smithsonian National Museum of Natural History. Right: Dr. Jeffrey Post (left) and Gary Bowersox with the cat's-eye aquamarine. Photo by Kathleen Kolt-Bowersox.

before it was finally cut in 2017 by Rohitha Perera in Sri Lanka (figure 8, right). The Bowersoxes have several other cut gems from this find, with the next largest weighing in at 541.96 ct.

*Jennifer Stone-Sundberg and Si Athena Chen  
GIA, Carlsbad*

**New violet orbicular chalcedony from Ethiopia.** At the GJX show, the author encountered a relatively new find of violet chalcedony reportedly discovered in Ethiopia in 2019 (figure

9). Processed and brought to market as tumble-polished freeforms, the chalcedony was offered by Orbit Ethiopia Plc. According to managing director Tewodros Sintayehu, the mine is located in the Gamo Zone region, approximately 600 km from Addis Ababa. The material was first discovered in the Gerese District and has since been found in the adjacent districts of Kamba and Garda Marta. Sintayehu noted that he had a very large quantity of the material stockpiled.

The notable features of this material were its fairly vivid violet color as well as the multitude of white orbicular struc-



Figure 8. Left: Kathleen Kolt-Bowersox holding the 7,700 ct aquamarine rough before it was cut. Right: The rough aquamarine was cut and polished in Sri Lanka by Rohitha Perera. Photos by Gary Bowersox.





Figure 9. This relatively new type of violet chalcedony from Ethiopia (here, 75–198 ct) displays a wonderful pattern of white orbs. Photo by Annie Haynes; courtesy of Orbit Ethiopia Plc.

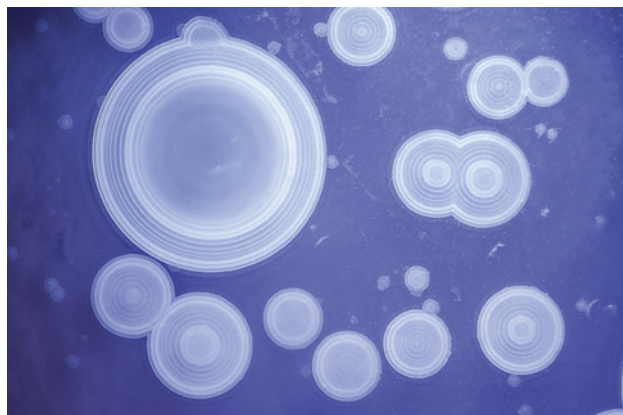


Figure 10. White orb-like structures were confined to a shallow surface layer in the violet chalcedony from Ethiopia. Photomicrograph by Nathan Renfro; field of view 15.16 mm.

tures distributed across the surface of the gems (figure 10). Microscopic examination revealed that the white color was related to a distinct botryoidal structure where a shallow outer layer of the gems contained all of the white areas. Because the white orbs are confined to a shallow surface layer, this explains why the material was sold as tumble-polished nuggets: Cutting the material into cabochons would likely result in the loss of the white orbicular pattern. A few unidentified mineral inclusions were also observed with the microscope, but the cause of the outer layer's white orb pattern remains unclear.

This new material is quite remarkable for its beautiful pattern. Even if it is only made available as freeform tumble-polished stones, it will be a welcome addition to the chalcedony market.

Nathan Renfro  
GIA, Carlsbad

**Italian precious coral.** Coral from the Mediterranean Sea has been harvested and used for adornments for thousands of years. More than 7,000 species are categorized as precious, common, or reef coral. Precious coral is defined by the World Jewellery Confederation (CIBJO) Coral Commission as “those that are used in jewelry and decoration, specifically red, pink, and white varieties with porcelain-like luster after polishing.” Italian coral harvested from the *Corallium rubrum* species is considered precious.

At the GfX show, the authors spoke with Sergio Di Gennaro of Fulvio Di Gennaro Srl. (Torre del Greco, Naples) about the Italian coral market. The Mediterranean has been precious coral's major source since it was first collected for ornamentation over 3,000 years ago, followed by Taiwan and Japan with smaller quantities. Beginning in the late 1970s, Mediterranean coral was threatened by over-harvesting. Di Gennaro explained that many strict regula-

tions for harvesting coral are in place today. Harvesting is limited to coral with trunks having a basal diameter of at least 7 mm recovered from 50 meters or deeper by licensed scuba divers.

Precious coral is the exoskeleton of very tiny marine invertebrates, known as coral polyps. When a colony of polyps arrives in a particular area, they start to create the exoskeletons on rocks, growing upward in a branch-like or fan formation. Di Gennaro mentioned that divers do not harvest coral with active colonies as these will continue to grow and the future, larger coral will be more valuable. Divers therefore tend to harvest the coral where the colony has already left. Unlike other types of corals, such as common and reef, these Mediterranean “deep sea” precious corals are not a natural habitat for other marine species. Reef coral species, which are a natural environment to many different marine species, are in many cases endangered and must be preserved.

Di Gennaro explained that the quality of the coral depends on the locality. He showed us a piece of dark red coral (figure 11, left), which is the typical color of coral harvested from northern Sardinia. It is a darker red due to cooler water temperatures from strong currents in the area. Coral from the southern portion of Sardinia (figure 11, center) tends to be lighter in color. Di Gennaro described this as a more “classic” color of Mediterranean coral. He also showed us a piece of reddish orange coral called “Sciacca,” named for a town in southern Sicily where the coral is harvested (figure 11, right). Di Gennaro said that volcanic activity below the surface results in warmer water temperatures, which in turn causes a more orangy color.

Di Gennaro emphasized the importance of sustainability in the coral industry, noting the heritage of the city of Torre del Greco, which was built on the art of processing coral. While current restrictions have reduced the amount of coral





Figure 11. Mediterranean coral from different regions. Left: Dark red fine coral from the northern coast of Sardinia. Center two pieces: “Classic” coral from the southern coast of Sardinia. Right: Orangi coral, termed “Sicacca,” from the coast of southern Sicily. Photo by Lisa Kennedy; courtesy of Fulvio Di Gennaro Srl.

being harvested compared to decades past, sustainable production will guarantee that we continue to see stunning Mediterranean precious coral for decades to come.

*Lisa Kennedy and Cristiano Brigida  
GIA, New York*

**Exceptional gemstone acquisitions by the Kreis family.** Kreis Jewellery (Niederwörresbach, Germany) is known for master cutting expertise and distinctive jewelry design (see Spring 2022 GNI, pp. 86–87). At the GJX show, Stefan and Alexander Kreis showed us three recent gemstone acquisitions.

First was a 155 g aquamarine crystal containing a two-phase liquid and gas inclusion measuring 4.3 cm long (figure 12; see video at [www.gia.edu/gems-gemology/spring-2023-gemnews-kreis-family-gemstones](http://www.gia.edu/gems-gemology/spring-2023-gemnews-kreis-family-gemstones)). The crystal was found in the 1960s in Marambaia, Minas Gerais, Brazil, and had been part of a private collection before the Kreises obtained it in 2022.

“It would even be a cuttable crystal,” Alexander said. “Of course we would never touch it because of the specialty of the huge liquid inclusion. A liquid chamber that size in quartz would already be amazing,” he continued. “But having it in an aquamarine, which is totally intact—you have the complete termination. And look at the sheer size of that crystal.”

Marambaia was known for large quantities of aquamarine by 1900 and produced the 110.5 kg (244 lb), 552,500 ct Papamel, discovered in 1910, the largest known gem-quality aquamarine crystal. The crystal that was the basis for the Dom Pedro, the largest cut aquamarine, weighed around 45 kg (100 lb) and was also from Marambaia.

Stefan said they had received a 35.05 ct cat’s-eye alexandrite (figure 13) that morning. He noted the size, exceptionally sharp eye, and superb color change for Sri Lankan alexandrite, which typically has a weaker color change than material from Russia and Brazil. Alexander pointed out that cat’s-eyes are less common in alexandrite than in other chrysoberyl. “A cat’s-eye alexandrite with a strong color

change like this one is extraordinary,” he said. “A size of 35 carats is what makes it outstanding.”

Figure 12. A 155 g aquamarine crystal containing a liquid and gas bubble inclusion. The crystal measures 11.9 cm long and the inclusion 4.3 cm long. Photo by Robert Weldon; courtesy of Kreis Jewellery GmbH.





Figure 13. A 35.05 ct Sri Lankan cat's-eye alexandrite in daylight (left) and incandescent light (right). Photo by Robert Weldon; courtesy of Kreis Jewellery GmbH.

The Kreises also showed us a 7.08 ct padparadscha sapphire (figure 14). "The color mixture of this stone is a real padparadscha color," Stefan said. Alexander added that a range of colors fall into the padparadscha category, but "this is the perfect color."

The cat's-eye alexandrite and padparadscha sapphire will undoubtedly inspire exquisite jewelry designs from Sonja and Vanessa Kreis. Sonja noted, "It is a very intuitive process in which we try to bring out a gem's natural beauty in such a way that it blurs the boundaries between jewelry and art."

*Erin Hogarth  
GIA, Carlsbad*

**Rare double pseudomorph ikaite-calcite-opal.** At the Pueblo Gem & Mineral Show, Graeme Dowton of Red Earth Opal (White Cliffs, Australia) exhibited rare double pseudomorph ikaite-calcite-opal gem specimens mined from the Naatji Nest mine at White Cliffs in New South Wales, Australia. Ikaite was initially substituted with calcite and then opalized, therefore making these double pseudomorph opals. Also called "pineapple opal" in the market due to the form of their clusters, they are found

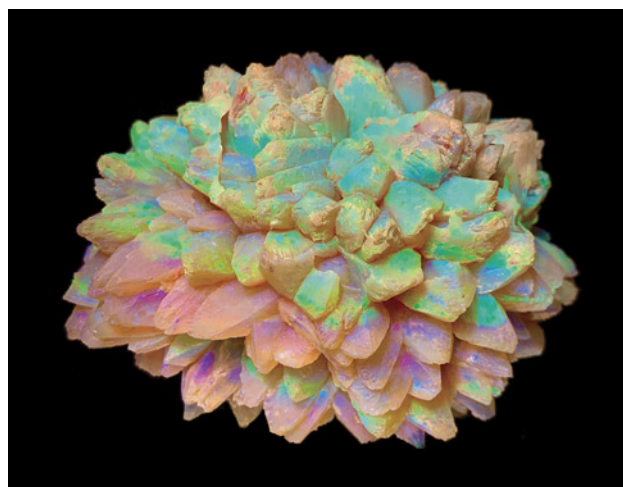
exclusively in White Cliffs and typically occur within weathering-bleached siltstones and claystones. According to Dowton, no other type of gem-quality opal was found in the same layer where the pineapple opals were mined. During mining, it was noticed that two opals had formed within a few feet of each other but with distinctly different coloration: One displayed a rich spectrum of play-of-color, while the other showed almost no coloration. The 3,510 ct Heart of Australia (figure 15) shows rich play-of-color and is considered one of the finest specimens of this type ever unearthed. In some of Dowton's samples, the precursor calcite was not fully substituted by silica gel, and white calcite crystals can be observed (figure 16).

Ikaite,  $\text{CaCO}_3 \cdot 6\text{H}_2\text{O}$ , is a rare and metastable hydrated carbonate in sedimentary rocks that has only been identified in environments ranging from  $-2^\circ$  to  $7^\circ\text{C}$  in nature (M.L. Vickers et al., "The ikaite to calcite transformation: Implications for paleoclimate studies," *Geochimica et Cosmochimica Acta*, Vol. 334, 2022, pp. 201–216). The occurrence of ikaite suggests a period of very cold to near-freezing paleoclimate conditions in White Cliffs. At ambient

Figure 14. A 7.08 ct padparadscha sapphire. Photo by Robert Weldon; courtesy of Kreis Jewellery GmbH.



Figure 15. The Heart of Australia, a 3,510 ct double pseudomorph ikaite-calcite-opal gem specimen, is considered one of the finest ever unearthed. Courtesy of Graeme Dowton.



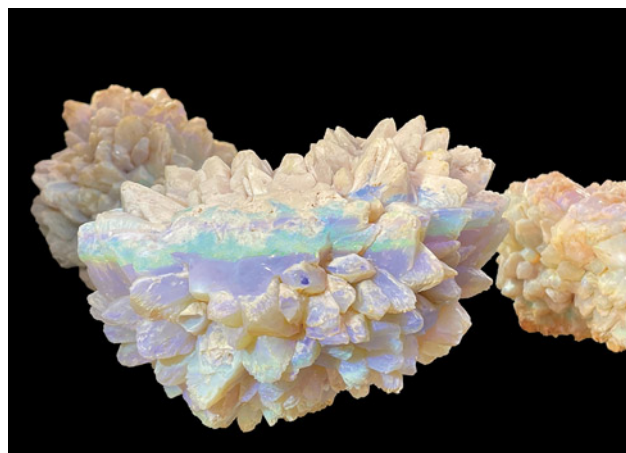


Figure 16. The intergrowth of opal and its precursor calcite in pineapple opal. This specimen is 12 × 10 × 8 cm and weighs 690 g. Photo by Si Athena Chen; courtesy of Graeme Dowton.

temperatures (10°–30°C), ikaite transforms to more stable carbonate polymorphs such as calcite, aragonite, and/or vaterite. The ikaite and its following pseudomorphs act as paleothermometers (D. Shearman and A. Smith, “Ikaite, the parent mineral of jarroviite-type pseudomorphs,” *Proceedings of the Geologists Association*, Vol. 96, No. 4, 1985, pp. 305–314). When the host sedimentary rocks were weathered, they released silica into groundwater. This silica-bearing groundwater contacted with calcite, which gradually dissolved and reprecipitated to opal over time (B. Pewkling et al., “The formation of precious opal: Clues from the opalization of bone,” *Canadian Mineralogist*, Vol. 46, No. 1, 2008, pp. 139–149). However, the detailed formation mechanism of ikaite-calcite-opal in White Cliffs requires future investigation.

Si Athena Chen and Jennifer Stone-Sundberg

**Cultured pearl market update.** At the AGTA show, we spoke with several pearl dealers to acquire some insight into the current cultured pearl market. With demand for pearls trending upward in the secondary market, as reported by The Real Real in its Luxury Consignment Report in January 2023, it was easy to spot similar trends in other areas of the pearl market as well.

Bead cultured (BC) pearls are the result of the deliberate insertion of a bead nucleus along with a small piece of mantle tissue into the gonad of a living host mollusk to start the growth of the cultured pearl, a process known as nucleation or grafting. Non-bead cultured (NBC) pearls need only a piece of tissue implanted into the gonad or mantle of a host mollusk to form. A technique originally developed and successfully operated in Japan before adoption by other global operations including Australia, the Philippines, Indonesia, French Polynesia, and China, the nucleation process is intricate and requires expertly trained technicians.

The pearl industry, like others, was adversely affected by the COVID-19 pandemic. Many dealers noted a supply shortage of the main types of cultured pearls: South Sea, Tahitian, akoya, and freshwater. According to dealers, many pearl farms, especially Tahitian, use Chinese and Japanese technicians to perform the critical nucleation step. Due to travel restrictions and border closures during the pandemic, many experts were unable to travel to these locations, resulting in smaller harvests since 2020. In some farming areas, there were not enough employees on-site to keep the mollusks in good health, and thus the mortality rate was high. Assuming grafting returned to normal levels by 2022, a greater influx of supply is expected in 2024, given the typical 24-month growth periods. Some dealers added that strong demand for cultured pearls from Chinese and other Asian consumers is contributing to the current global shortage.

Small freshwater BC pearls from China (approximately 2–4 mm) were more widely available at the show than in past years, in near-round to round shapes and in various colors including white, pink, purple, and orange (figure 17). Freshwater cultured pearls of this particular size are typically NBC, normally oval (a potato-like shape), and can look similar to white saltwater Japanese akoya BC pearls of the same size. However, Gina Latendresse of American Pearl Company Inc. (Nashville, Tennessee) demonstrated

Figure 17. Near-round to round small freshwater bead cultured pearls (approximately 2–4 mm) were widely available at the AGTA show in various colors including white, pink, purple, and orange. Photo by Artitaya Homkrajae; courtesy of Betty Sue King, King’s Ransom.







Figure 18. Left: Small round freshwater bead cultured (BC) pearls (top group of strands) and small round Japanese akoya BC pearls (bottom strands) appear very similar at first glance. Right: Upon closer inspection, the freshwater pearls more often show a rounded flat surface feature. Photos by Artitaya Homkrajae and Lisa Kennedy; courtesy of American Pearl Company Inc.

that upon closer inspection, the freshwater pearls more often show a rounded flat surface feature on an otherwise spherical pearl, a feature usually too small to affect basic shape (figure 18). This feature is also occasionally observed in other types of freshwater cultured pearls.

Eliko Pearl Company (New York City) displayed numerous strands of Vietnamese akoya BC pearls with bodycolors ranging from silver to light gray and light bluish gray with exceptional orient (figure 19). These provide a greater selec-

Figure 19. Vietnamese akoya bead cultured pearls in various colors ranging from silver to light gray to light bluish gray. The pearls were said to be unprocessed and untreated. Photo by Lisa Kennedy; courtesy of Eliko Pearl Company.



tion of colors compared to traditional akoya BC pearls. Some white, light cream, and cream pearls were also presented as unprocessed and untreated—steps normally used to improve appearance and alter color. However, many akoya BC pearls in the market have been processed to generate a classic white appearance. Vietnam has produced saltwater cultured pearls commercially since the 1990s and is expected to produce approximately 2,000 kg per annum (N. Sturman et al., “Vietnam: Shell nuclei, pearl hatcheries, and pearl farming,” Fall 2020 *G&G*, pp. 402–415), which is significantly smaller than Japan’s anticipated annual production of approximately 20 tons (roughly 18,000 kg) (T. Matsuyama et al., “Mass mortality of pearl oyster (*Pinctada fucata* (Gould)) in Japan in 2019 and 2020 is caused by an unidentified infectious agent,” *PeerJ*, Vol. 9, 2021, article no. 12180).

Eric Yen of Yen’s Jewelry & Accessories Inc. (San Francisco) and Alan Hakimian of Yoko London presented strands that combined multicolor pearls from different pearl types, offering variety and high fashion all at once (figures 20 and 21). Both pointed out that making mixed and graduated color strands is an efficient use of all the pearls produced from a harvest, just one example of economic sustainability in the pearl industry. Producing only perfectly matched color stands would lead to more waste.

Overall, pearl dealers are looking forward to the return of the gem, jewelry, and pearl shows in Hong Kong in 2023, as these are some of the largest shows for cultured pearls. Many have not been able to attend since 2019 due to lockdown restrictions in Hong Kong.

Lisa Kennedy  
Artitaya Homkrajae  
GIA, Carlsbad

**“Edison” pearls: Increasing market presence.** Several vendors at both the AGTA and GJX shows carried large and attractively colored “Edison” pearls from China (see C. Zhou

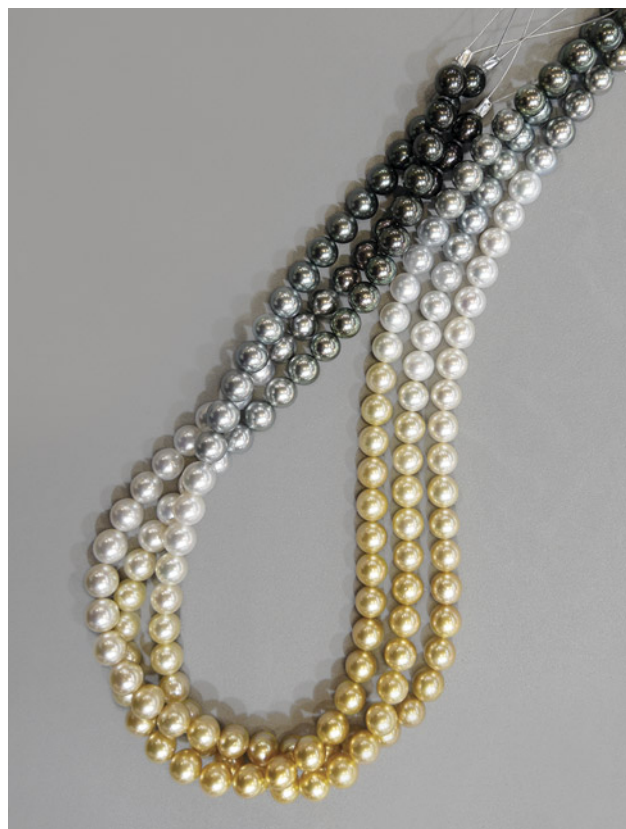


Figure 20. This set of ombré pearl strands, made up of round Tahitian pearls with silver and gold South Sea pearls ranging from 10 to 10.4 mm, is also known as shikisai, which means “colors of four seasons” in Japanese. Photo by Mimi Travis; courtesy of Yen’s Jewelry & Accessories Inc.

et al., “Detection of color treatment and optical brightening in Chinese freshwater ‘Edison’ pearls,” Summer 2021 *G&G*, pp. 124–134). These round freshwater bead cultured pearls generally ranged in size from 9 to 14 mm. Some baroque pearls were also offered. This year we saw deeper hues and more purple, bronze, copper, peach, and orangy pink colors than in the past; lighter colors such as white, cream, and light pink were more scarce. Popular trends included “rainbow” strands of pearls featuring a mix of colors, strands with alternating blocks of color, and strands with metallic colors (figure 22). At GJX, we spoke with Amy Hansen of A&B Jewelry (Honolulu, Hawaii) to learn about current purchasing trends and the latest developments at the pearl farms.

Hansen indicated that “Edison” pearls are still finding their place in the market. Her designer clients are seeking larger pearls, and those in the 12–14 mm size range are doing particularly well, with pearls larger than 13 mm in highest demand. She explained the limits in producing larger pearls: Larger sizes (particularly greater than 14 mm in diameter) take much more time to culture, which greatly limits the yield of top-grade product with respect to shape, nacre, surface, and luster. As a result, the highest-quality



Figure 21. Mixed strand of 79 pearls ranging from 11.8 to 14.8 mm, consisting of pink Chinese freshwater, black Tahitian, golden Indonesian, and white Australian bead cultured pearls. Also pictured is an exceptionally large 20.4 mm South Sea bead cultured pearl, weighing 12 g. Photo by Robert Weldon; courtesy of Yoko London.

“Edison” pearls in sizes over 14 mm are rare and considerably more costly. That said, she noted that “Edison” pearls are still a good value, available in an appealing variety of colors and sizes with a price point substantially below akoya and Tahitian saltwater cultured pearls.

Hansen explained that the cultivation of “Edison” pearls in terms of bead size and culturing times is similar to that for saltwater Tahitian pearls. She described improvements in the process, including Chinese freshwater pearl farmers moving inland to access cleaner rivers and lakes and using more sound environmental practices. The move to these newer locations has resulted in more colors being achieved, broadening the offerings of these pearls. Chinese freshwater cultured pearl production has also decreased over the past five years as the focus has shifted





Figure 22. A graduated strand of “Edison” pearls in copper and bronze metallic colors, ranging from 9 to 12 mm. Also shown are three loose pearls: 10 mm peach, 11 mm purple, and 11 mm copper. Photo by Robert Weldon.

more to quality over quantity. The wholesale price of fine-quality “Edison” pearls is still considerably below that of similarly sized Tahitian and akoya pearls, but we expect the price gap to narrow somewhat as the quality and popularity of these beautiful freshwater cultured pearls continues to increase.

*Jennifer Stone-Sundberg and Si Athena Chen*

**Spotlight on natural nacreous pearls.** A natural pearl forms in the interior of a mollusk within a naturally formed pearl sac without human intervention. The use of natural pearls goes back thousands of years, and these biogenic gem materials have been treasured in jewelry and adornment throughout human history. In general, pearls can be separated into two varieties based on surface structure: nacreous and non-nacreous. The nacreous pearls are more common in the market. These are formed by a layered structure of aragonite platelets together with organic substances as well as water, and they normally display a pearly luster.

At the AGTA show, Alex Vock of ProVockative Gems Inc. (New York City) shared some of his expertise in natural saltwater nacreous pearls. With more than 30 years in the business, he is considered an industry leader specializing in signed collectible jewelry, natural gemstones, and natural pearls. He had several pieces on display, including an attractive pair of natural pearl earrings set with unheated Burmese rubies and unoled emeralds (figure 23).

Vock discussed the global market for natural nacreous pearls, noting that it was greatly diminished by the 1980s due to the prevalence of cultured pearls. However, regions such as many of the Gulf countries and India did not feel pressure from the cultured pearl market. These countries have led a resurgence of natural pearl’s popularity, specifically with Basra pearls. These originate in the Arabian (Persian) Gulf, and their namesake is the city of Basra in Iraq. Historically, Basra was the center of natural pearl commerce, with the greatest selection of natural pearls and the most informed dealers.

Vock mentioned that the most prized natural nacreous pearls today are from either the Gulf region or Australia. Currently, both regions produce what dealers describe as “new material,” which are freshly harvested natural pearls. Natural pearls form in the mantle of the pearl mollusk shells, whereas cultured saltwater pearls grow inside the gonad of the mollusks. Many natural pearls have a large flat surface, similar to a button shape, because they grow against the mantle. For that reason, round, oval, and drop-shaped pearls are rarest and most valuable.

Figure 23. A pair of earrings with unoled emeralds weighing about 8 ct total, natural pearls measuring 9.5–10.0 mm, unheated Burmese rubies weighing just under 5 ct total, and diamonds set in yellow gold. Photo courtesy of ProVockative Gems Inc.







Figure 24. Left: The mother shell (*Mercenaria mercenaria*) and an 18K gold ring featuring a  $14.43 \times 14.63$  mm lilac quahog pearl. Right: A rare collection of round quahog pearls ranging from 5.65 to 12.33 mm in diameter and in colors from white and beige to deep purple and tan. Photos by Robert Weldon; courtesy of ECIJA.

When comparing pearls from the two regions, Vock explained, there are some differences. Basra pearls usually have a warmer bodycolor, while Australian pearls tend to be whiter. Also, Basra pearls are often rounder than their Australian counterparts. In fact, the Gulf region has the highest percentage of round natural nacreous pearls of any producing area. He credited this to the smaller shell of the Gulf region mollusks.

To see Alex Vock explain these common appearances with examples from his current collection, go to [www.gia.edu/gems-gemology/spring-2023-gemnews-natural-nacreous-pearls](http://www.gia.edu/gems-gemology/spring-2023-gemnews-natural-nacreous-pearls).

Lisa Kennedy and Artitaya Homkrajae

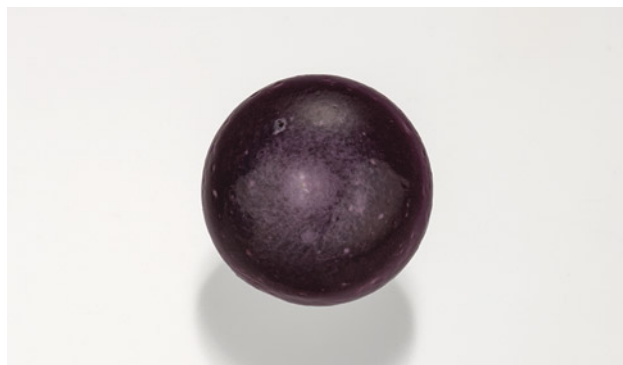
**Exceptionally rare pearls from ECIJA.** At the GJX show, ECIJA (Santa Barbara, California) displayed a variety of natural, wild, nacreous, and non-nacreous pearls, including conch, oyster, scallop, abalone, and quahog pearls. Only 0.2% of all pearls in the current market are natural (S. Karamelas et al., "Raman spectroscopy of natural and cultured pearls and pearl producing mollusc shells," *Journal of Raman Spectroscopy*, Vol. 51, No. 9, 2019, pp. 1813–1821), and the authors found the non-nacreous collection especially notable.

ECIJA owner Aylene Norris and her husband, Jeremy Norris (Oasis Pearl), have been sourcing for 34 years and specialize in natural pearls. For the first time in Tucson, ECIJA displayed a collection of round quahog pearls (figure 24). Quahog pearls are produced in the bivalve mollusk *Mercenaria mercenaria* (figure 24, left), a type of saltwater clam native to the Atlantic Ocean. These non-nacreous pearls consist mainly of fibrous aragonite and organic matter. They are often not perfectly spherical but form irregular shapes such as button or baroque, making this set of round quahog pearls extremely rare (figure 24, right). Moreover, they exhibited an attractive and strong porcelaneous surface with

sizes ranging from 5.65 to 12.33 mm in diameter. Quahog pearls are known for their unique range of colors, including white, beige, pink, lavender, purple, brown, and black. These 21 quahog pearls showed a wide color range, from white and beige to deep purple and tan (figure 24, right). According to Jeremy, lilac and deep purple are the most desirable and command the highest price. The color of a quahog pearl is determined by various factors, including the clam species and environmental and geochemical conditions.

Another rarity on display was a large (16.44 ct,  $14.50 \times 14.36 \times 11.95$  mm) deep purple, button-shaped non-nacreous pearl showing an obvious flame structure at its surface (figure 25). This pearl formed from one of the many *Spondylus* species, also known as "thorny" or "spiny" oysters, which are harvested on the western coast of the Americas as *Spondylus princeps* and *Spondylus calcifer/limbatus*.

Figure 25. This non-nacreous pearl weighing 16.44 ct and measuring  $14.50 \times 14.36 \times 11.95$  mm is reportedly from a *Spondylus calcifer/limbatus* mollusk from the Sea of Cortez in Baja California. Photo by Robert Weldon; courtesy of ECIJA.



Reportedly from *calcifer/limbatus* from the Sea of Cortez in Baja California, the pearl's large size, attractive purple color, and strong flame structure set its value. Previously, GIA has reported that flame structure is usually caused by subsurface to surface-reaching acicular inclusions (Fall 2016 Lab Notes, pp 303–304). Although several *Spondylus* pearls have been reported in *G&G* (Summer 2016 Micro-World, pp. 202–203; Fall 2016 Lab Notes, pp. 303–304), this is one of the largest and finest examples.

ECIJA also featured other nacreous and non-nacreous pearls for designers and buyers, including conch, scallop, and abalone pearls. Each of these species exhibits unique shapes and colors. Conch pearls are typically oval in shape and exhibit white, beige, brown, yellow, orange, pink, and red colors. They range in size from 1 mm to over 20 mm. Scallop pearls from *Nodipecten nodosus*, also known as "Lion's Paw" or "Mano de Leon," form button, oval, and baroque shapes that range from white and brown to rare purple or maroon colors. These exhibit beautiful reflective mosaic-like patterns on their surface. Abalone typically produce conical or baroque-shaped pearls exhibiting a combination of vibrant colors and a mirror-like luster. Symmetrical abalone pearls, especially in large sizes, are very rare.

While GIA has developed seven value factors to evaluate the quality of nacreous pearls (size, shape, color, luster, surface, nacre, and matching; see J.W.Y. Ho and S.C. Shih, "Pearl classification: The GIA 7 Pearl Value Factors," Summer 2021 *G&G*, pp. 135–137 and accompanying wall chart), it is difficult to set the value for non-nacreous pearls due to their rarity and individual characteristics. In addition, demand dictates the value and price of rare pearls. An increasing demand for conch pearls has attracted buyers from all around the world. Jeremy indicated that conch pearls are especially popular in the European, U.S., and Asian markets. Deep pink to red pearls exhibiting a strong flame pattern are the most desirable and have doubled in value over the last

10 years, whereas pastel colors continue to be a more affordable solution for designers and collectors alike.

Si Athena Chen

Chunhui Zhou

GIA, New York

#### New find of petroleum-included quartz from Madagascar.

At the Tucson Gem and Mineral Show (TGMS), a new find of quartz with petroleum inclusions was offered for sale by Hidden Gem Gallery (Portland, Oregon). According to owner G. Moses Samora, the material is from the Andranotokana Massif in the Alaotra-Mangoro region of eastern Madagascar. Petroleum inclusions in quartz have been seen for a number of years from many deposits, most notably from Baluchistan, Pakistan (Spring 2004 Gem News International, pp. 79–80). The petroleum in these quartz crystals from Madagascar appeared brownish yellow and, as with many other petroleum inclusions in quartz, reacted to long-wave UV light with yellow to blue fluorescence (figure 26).

Microscopic examination revealed numerous complex fluid inclusions containing obvious brownish yellow petroleum, a gas bubble presumed to be methane, dark solids of what was likely asphaltite, and a colorless immiscible liquid that was probably water (figure 27). Interestingly, in some fluid inclusions the methane bubble was mobile provided there was enough available space within the petroleum-filled cavities. These components are consistent with petroleum fluid inclusions in quartz from other deposits. When exposed to long-wave UV light, the petroleum component strongly fluoresced light yellow (which appeared blue in the photomicrographs), as has been previously observed in similar material. The two crystals from this new deposit displayed a scepter morphology, which seems unusual, though it remains unclear whether this is diagnostic for the locality or just unique to these specific examples.

Figure 26. These two quartz crystal scepters containing a multitude of complex petroleum fluid inclusions (left) that fluoresce yellow to blue to long-wave UV light (right) are from a new deposit in Madagascar. The larger crystal weighs 11.05 ct and measures 22.81 mm in length. Photos by Annie Haynes; courtesy of Hidden Gem Gallery.



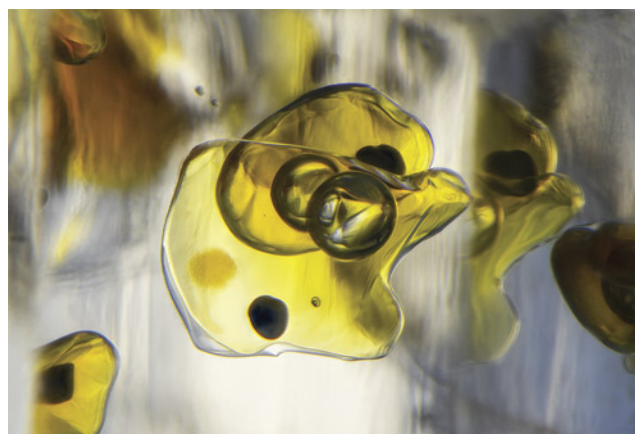


Figure 27. The new find of quartz from Madagascar contained complex fluid inclusions consisting primarily of petroleum, methane, asphaltite, and water (left). When exposed to long-wave UV light, the petroleum appeared to fluoresce a strong yellow. However, the digital camera used to capture the image registered the fluorescence as a blue color (right). Photomicrographs by Nathan Renfro; field of view 2.81 mm.

Microscopic inclusions in quartz are enjoyable to examine, and petroleum inclusions are of particular interest to the collector due to their spectacular UV reaction. The introduction of this new quartz find at the Tucson show is an exciting addition to the gem and mineral trade.

Nathan Renfro and John I. Koivula  
GIA, Carlsbad

**Bright orange sapphire from Greenland.** The Aappaluttoq mine in Greenland is home to the oldest known ruby-bearing rocks on Earth. These host rocks are nearly three billion years old (A. Polat et al., "New age (ca. 2970 Ma), mantle source composition and geodynamic constraints on the Archean Fiskensæset anorthosite complex, SW Greenland," *Chemical Geology*, Vol. 277, No. 1-2, 2010, pp. 1–20). This deposit was initially known for producing translucent to opaque ruby and pink sapphire, much of it

cut into cabochon form. However, transparent material has always been found in this mine and makes up about 5–10% of the production.

At the AGTA show, Greenland Ruby displayed many examples of attractive transparent ruby and pink to orangy pink sapphire, including several fancy-color sapphires in sizes greater than one carat (figure 28; see also pp. 145–149 of this issue). These fancy colors are achieved by heat treating nearly colorless to slightly pink transparent material. A transparent bright orange sapphire weighing 0.89 ct and measuring  $6.41 \times 5.02$  mm (figure 29) immediately caught our eye. Martin Viala, product manager for Greenland Ruby, shared with us a video of the original 1.07 g sapphire rough (visit [www.gia.edu/gems-gemology/spring-2023-gemnews-bright-orange-sapphire-greenland](http://www.gia.edu/gems-gemology/spring-2023-gemnews-bright-orange-sapphire-greenland)). This unusual stone was mined in late 2019 and heated in May 2022. Viala noted that it was a textbook example of a chromium trapped-hole ( $h^+-Cr^{3+}$ ) chromophore (E.V. Dubinsky et al.,

Figure 28. A 1.28 ct heated pink round brilliant sapphire. Photo by Robert Weldon; courtesy of Greenland Ruby.



Figure 29. A 0.89 ct heated orange oval brilliant sapphire. Photo by Robert Weldon; courtesy of Greenland Ruby.







Figure 30. A 7.94 ct rectangular step-cut rhodochrosite from the Sweet Home mine in Colorado's Alma Mining District. Photo by Robert Weldon; courtesy of Barker & Co.

"A quantitative description of the causes of color in corundum," Spring 2020 *G&G*, pp. 2–28].

Jennifer Stone-Sundberg and Si Athena Chen

**Sweet Home mine rhodochrosite from 1888.** At AGTA, Ann Barker and Tori Lopez of Barker & Co. (Scottsdale, Arizona) exhibited a 7.94 ct rectangular step-cut rhodochrosite (figure 30) with a provenance dating back more than a hundred years. The stone is from the Sweet Home mine in Colorado's Alma Mining District, at an elevation of about 3,300 m in the Rocky Mountains.

Sweet Home was established as a silver mine in 1872. Miners initially discarded most of the rhodochrosite found in association with the silver ore because it interfered with the amalgamation process used then in silver mining. But the large, highly saturated, and nearly perfectly formed crystals later discovered there are some of the world's finest rhodochrosite specimens.

Rhodochrosite was first described in the mineralogical literature in 1813 based on specimens from what is now Romania. In 1887, George F. Kunz wrote of gem-quality rhodochrosite in Colorado, noting it was the first source with such large and transparent crystals. Most of the rhodochrosite available worldwide was light pink, opaque, and often banded—typically used for beads, cabochons, and carvings. This source introduced pink to red gem-quality single-crystal rhodochrosite, which is rare. The gemstone became more widely known in the late 1930s, after a German gemologist found large volumes in Argentina's Catamarca Province high in the Andes. (In Argentina, the use of rhodochrosite dates back to the ancient Incas, who are said to have believed it was the solidified blood of their fallen rulers.)

The step-cut stone's traceable history began in 1888, when a shaft collapse resulted in a 32.61 ct cleavage fragment. Miner Edward Abbott kept it and in 1925 gave it to Denver businessman Edwin Spray, who later owned the mine. The same year, Sweet Home miners found large spec-

imens on quartz matrix, many of which were sold to museums in the U.S. and Europe. In 1968, the fragment made its way from Spray's widow, Eleanor, through a friend of the family to geologist and mineral collector Charles Trantham in California. In 1981, Glenn Vargas, a gem and mineral dealer and university instructor, expertly cut the stone. Rhodochrosite often presents challenges for cutting due to its low hardness (3.5–4.0 on the Mohs scale) and perfect rhombohedral cleavage.

Rhodochrosite mining at Sweet Home expanded significantly in 1991—long after silver production ended in the 1960s—when Eleanor Spray's nephew, F. Leonard Beach, leased the property to a group of investors led by Collector's Edge Minerals. The group found several new pockets and in 1992 uncovered the Alma King, a 14.2 × 16.5 cm deep cherry red rhombohedron, the world's largest known fine rhodochrosite crystal.

The Sweet Home mine closed in 2004, but the group went on to develop the associated Detroit City mine, which has produced some fine specimens since 2019.

Erin Hogarth

**New tourmaline pockets in San Diego County's Pala District.** At the AGTA show, Bill and Carl Larson (Pala International, Fallbrook, California) shared details about new pockets uncovered at the Tourmaline King mine. The first was discovered in January 2022—the first major find at the mine in more than a hundred years, and the first in Southern California since the "Big Kahuna" pocket at the Oceanview mine in 2010. "We've hit off and on three or four pockets, some of which are very good," Bill said.

The Larsons showed us several stones, including a 16.96 ct emerald-cut green tourmaline (figure 31) from rough found near the first pocket in 2022. Bill said the green tourmaline is relatively uncommon for the Pala District. "The green has actually been transparent enough to

Figure 31. A 16.96 ct emerald-cut green tourmaline from rough found near a new pocket at the Tourmaline King mine. Photo by Robert Weldon; courtesy of Pala International.

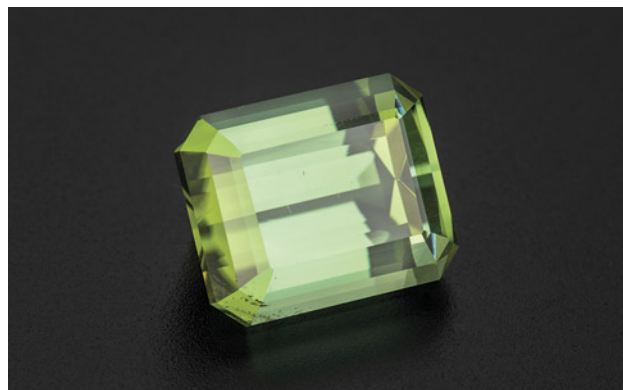




Figure 32. Rubellite tourmaline rough (440 g) from one of the Tourmaline King mine's new pockets. Photo by Robert Weldon; courtesy of Pala International.

facet," Carl added. "That's been the best material so far." The new pockets have also produced about 3 kg of fine-color rubellite rough (figure 32).

The Tourmaline King mine's main tunnel produced eight tons during San Diego County's massive output of tourmaline in the early nineteenth century, which also involved the Pala District's Tourmaline Queen, Pala Chief, and Stewart mines, as well as Mesa Grande's Himalaya mine. (There was a resurgence of mining at Pala in the 1970s.)

Around 1920, mine owner R.M. Wilke and his crew installed a new tunnel below the main one. "They hit this very dangerous zone right before they hit the pegmatite," Bill said. Here they encountered a shear zone that caused a roof collapse. Wilke abandoned mining efforts around 1922.

Pala International's mining partner, San Diego Mining Company, reclaimed the tunnel several years ago and began extending it in 2019. "They got to the dangerous area, and then they backed up about 10 meters and went around and hit the pegmatite," Bill said. "Now they're in from the front to the back, where we're hitting tourmaline."

Carl recalled his initial look at the first new pocket. "Kiel Snyder stopped me and said, 'Everyone else gave up here,'" he said. "He just believed in it and kept going. Then they hit a small pocket—nothing of note, but something that said, 'There are stones here.' I think they called that the 'Never Give Up' pocket. Within 10, 15 feet, they hit that first pocket."

The crystals were large and well formed, and the miners uncovered a very large terminated quartz crystal, a collector specimen. Carl said the crystals in this pocket lack the rubellite color and are not typical of the mine, making

them inadequate for cutting and cabbing. But in January of 2023, they discovered a pocket of beautifully colored red rubellite, too included for faceting but suitable for cabbing and carving. "We're hoping that we'll hit some more gemmy transparent material," he said.

"It's really exciting to have an active mine in Southern California because of its rich history," Carl said. "At the turn of the century we were hitting a lot, and then it was vacant for so long. So to have some energy coming in with new material is exciting."

Erin Hogarth

**Vibrant green grossular garnet "Transvaal jade."** At the Pueblo show, Tom Schneider of TMS Gems (San Diego, California) offered "Transvaal jade" rough displaying an exceptionally vivid green color. Also known as "African jade" or "South African jade," this is not a true jade (jadeite or nephrite). The stone is instead a grossular garnet whose trade name is derived from its massive habit and green color, and the type locality. Specimens of this material are typically more translucent and lighter in color (J. Frankel, "Uvarovite garnet and South African jade (hydrogrossular) from the Bushveld Complex, Transvaal," *American Mineralogist*, Vol. 44, No. 5-6, 1959, pp. 565–591). Nested in a fine-grained chromite matrix, the opaque green portion of the stone in figure 33 had a refractive index of 1.731 and was inert to both long-wave and short-wave ultraviolet radiation.

The sample was identified as grossular garnet using Raman spectroscopy and further classified as a grossular-andradite garnet using X-ray fluorescence chemical analysis and the naming convention proposed in 1995 (M.L. Johnson et al., "Gem-quality grossular-andradite: A new garnet from Mali," Fall 1995 *G&G*, pp. 152–166). The chemical

Figure 33. This 110.4 g partially polished rough grossular garnet "Transvaal jade" and three polished cabochons (41.95–92.87 ct) display unusually vibrant green colors between seams of dark chromite matrix. Photo by Diego Sanchez; courtesy of TMS Gems.







Figure 34. Alex Skachkov of Misfit Diamonds. Photo by Jennifer Stone-Sundberg.

data show 80.83 mol.% grossular ( $\text{Ca}_3\text{Al}_2\text{Si}_3\text{O}_{12}$ ), 10.50 mol.% uvarovite ( $\text{Ca}_3\text{Cr}_2\text{Si}_3\text{O}_{12}$ ), 7.11 mol.% andradite ( $\text{Ca}_3\text{Fe}_2\text{Si}_3\text{O}_{12}$ ), and trace amounts of other garnet. Garnets in the grossular to andradite range can show 4.64–20.91 wt.%  $\text{Fe}_2\text{O}_3$  (Johnson et al., 1995) and typically have low chromium values ( $\leq 0.23$  wt.%  $\text{Cr}_2\text{O}_3$ ) (C.M. Stockton and D.V. Manson, “A proposed new classification for gem-quality garnets,” Winter 1985 *G&G*, pp. 205–218). Increased iron content will impart a yellow, orange, or brown color component, while the most intensely green stones owe their color to chromium and possibly vanadium (Johnson et al., 1995). The low iron content (2.49 wt.%  $\text{Fe}_2\text{O}_3$ ) and elevated chromium content (3.50 wt.%  $\text{Cr}_2\text{O}_3$ ) of this sample likely resulted in its remarkable coloration.

The chromium-rich nature of this particular specimen produced a beautiful vibrant green with a high-polish luster, making it an outstanding example of this material.

Kendra Carty and Amy Cooper  
GIA, Carlsbad

## DIAMONDS

**Misfit Diamonds: Beauty in the imperfect.** At the AGTA show, we spoke with Alex Skachkov of Misfit Diamonds (Vancouver, Canada) about some of their unusual diamonds (figure 34). When asked what was popular, he showed us their aptly named “salt and pepper” diamonds (see also figure 5 of the Tucson 2023 overview), which contained eye-visible black and white inclusions. These had a very distinct look and were cut into various nonstandard shapes (figure 35).

Skachkov described the appeal of these unique and beautiful “imperfect” diamonds, particularly to younger



Figure 35. “Salt and pepper” diamonds. Left to right: a 4.30 ct hexagonal step cut, a 5.56 ct octagonal step cut, a 3.58 natural-color orange cushion cut, and a 3.39 ct pear cut. Photo by Robert Weldon; courtesy of Misfit Diamonds.

designers and consumers. In his words, younger customers are not necessarily interested in absolutely flawless gems. Rather, many are looking for gems that charm in their distinctive and rare “perfect imperfection.” He noted that these diamonds are also a more budget-friendly option. In addition to the “salt and pepper” diamonds, we got a close look at diamonds and sapphires cut into nontraditional shapes, including slices (figure 36).

Skachkov mentioned that many of their customers now look for full disclosure of the entire mine-to-market custody chain. Misfit Diamonds provides this information whenever possible, though at times their diamonds arrive in mixed-origin parcels, with stones from a variety of global locations. Moving forward, they aim to meet the challenge of reporting full chain of custody, as they predict increasing demand for this feature.

Jennifer Stone-Sundberg and Si Athena Chen

Figure 36. Nontraditional diamond cuts and slices in a range of sizes. Photo by Jennifer Stone-Sundberg; courtesy of Misfit Diamonds.





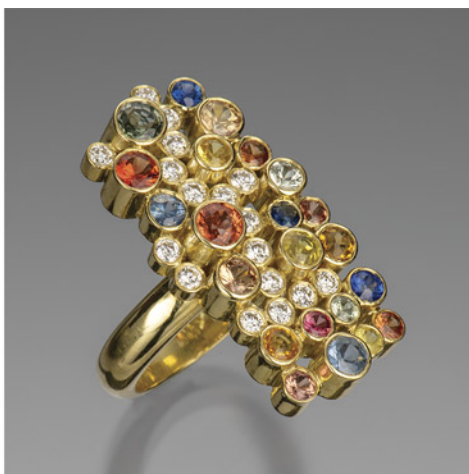
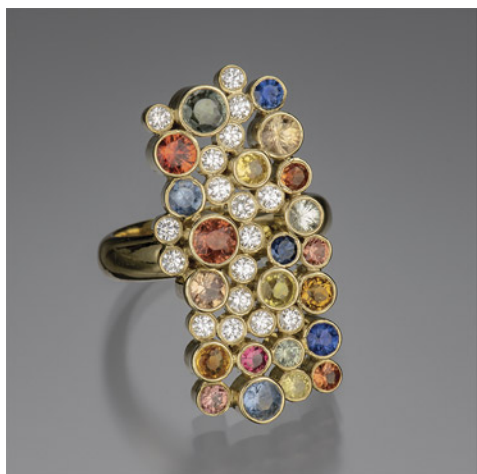


Figure 37. The “Seven Sisters” ring in 18K gold with 17 bezel-set diamonds (0.55 carats total) and 22 sapphires ranging in size from 2.5 to 4.0 mm in blue, orange, mandarin, pink, and green (3.15 carats total). Photo by Robert Weldon; courtesy of Sean Hill Designs.

## JEWELRY DESIGN

**Sean Hill: Exquisite jewelry designs.** At the GJX show, Sean Hill of Tucson presented some striking jewelry designs with masterful control of shape and line. A gold ring set with diamond, blue sapphire, and fancy-color sapphire (figure 37) drew us into his booth. Dr. Hill, a self-taught jeweler, has been active designing and handcrafting jewelry since 1998, after a previous career as a university professor in literature and philosophy. His academic and philosophical nature is immediately evident when discussing design, and his meticulous attention to space and volume becomes more apparent the longer one studies his pieces. The “Seven Sisters” ring in figure 37 raises each stone to a unique height above the flat base, filling the rectangle with an appealing placement of 17 colorless diamonds interspersed among 22 sapphires.

A stunning pair of 18K white gold earrings featuring both diamond slices and faceted diamonds (figure 38) is a case study in filling a plain geometric shape to bring it to life. As Dr. Hill said in describing the piece, “A rectangle is a basic shape, a self-imposed constraint. It is how you choose to fill it that makes it interesting.” Adding to the design quality, the rectangles are not actually flat but gently curved so that the earrings fit seamlessly on the ear.

A pair of 18K gold earrings with brilliant-cut diamonds and sapphires (figure 39) illustrates a modern and considered take on the classic chandelier earring, with squares and rectangles outlining floating round gems on delicate strings of gold. Dr. Hill explained some of his jewelry philosophy: “You can always take a stone for its beauty, color, and cut, set it into a finding, and it is all about the stone. But how do you make it into art?”

*Jennifer Stone-Sundberg and Si Athena Chen*

Figure 38. “Rose Cut” 18K white gold and diamond earrings. The faceted diamonds are 1.5–2.0 mm in diameter. Photo by Robert Weldon; courtesy of Sean Hill Designs.



Figure 39. “Event Horizon” earrings in 18K gold, diamond (0.07 carats total), and orange, mandarin, pink, green, and blue sapphire (5.2 carats total). Photo by Robert Weldon; courtesy of Sean Hill Designs.





Figure 40. These handcrafted jewelry pens are created with silver, embellished with 24K gold, and inlaid with diamond, sapphire, and crushed emerald. Left: The peacock design is a miniature painting coated in clear enamel. Right: A pen with fine metal engraving and dimming just below the 24K gold nib. Photo by Robert Weldon; courtesy of Zeki Karaca.

**Zeki Karaca Jewelry: Luxury pens.** Some of the most original work we saw at the GJX show included bejeweled pens made by Turkish designer Zeki Karaca (figure 40). These intricate pens feature exquisite details and fine craftsmanship in metalworking, enameling, engraving, inlay, and stone setting. In addition to pens, Karaca also creates other desk items such as letter openers and magnifying glasses (figure 41).

Born in Istanbul, Karaca has 41 years of jewelry-making experience, originally designing jewelry to sell in the Grand Bazaar. To apply his experience and creativity to different

designs and styles, he began making luxury pens and products three years ago. He first ventured into these new products by crafting silver gemstone handles for Damascus steel knives. After finding success there, he expanded to meet the demand for luxury pens, letter openers, and magnifying glasses.

Each pen takes about six months to design and craft. All production steps are done by hand, making each item one of a kind. After designing an item, Karaca creates a silver body using fold forming, with the folds created using emery sheets. Engraving is executed by a master engraver using different nibbed steel pens, and dimming is used to emphasize the engraving. Karaca incorporates diamond, sapphire, emerald, and ruby into the designs and uses 24K gold for design highlights. Miniature paintings, such as the peacock on the pen cap in figure 40 (left), are created by hand with a small brush and then coated with a transparent enamel for protection. For micro-mosaics, gemstones such as emerald are crushed and added to the pen body, as seen in both pens in figure 40. The pen parts are welded together with a laser, and then the 24K gold nibs are added.

With high demand for his products from collectors, Karaca continues to explore additional high-end objects as well as custom designs for some clients.

*Jennifer Stone-Sundberg and Mimi Travis  
GIA, Carlsbad*

Figure 41. Silver magnifying glass with 24K gold embellishments, inlay, carvings, and diamonds. Photo by Robert Weldon; courtesy of Zeki Karaca.



**Brenda Smith Jewelry designs.** Brenda Smith Jewelry has earned four AGTA Spectrum Awards to date for design excellence. At this year's AGTA designer showroom, Smith presented three masterpieces to the authors: two award-winning rings featuring pearl and blackened gold lace and an opulent pair of earrings featuring *millefiori* faces.

Smith's most prized creation is her Lace Ring design. She shared her white Lace Ring featuring a large cultured pearl accented with gold lace, sapphires, and diamonds (figure 42A), followed by a black Tahitian pearl Lace Ring with



Figure 42. A: This Lace Ring is crafted in 18K rose gold with blackened gold lace, featuring a cultured freshwater pearl measuring 16.5 mm in diameter, enclosed by natural-color pink and lavender sapphire round brilliants weighing 2.86 carats total. The shank of the ring is embellished with 0.06 carats of diamonds. B: This Tahitian pearl Lace Ring is created in 18K white gold with sandblasted and blackened gold lace. The cultured Tahitian pearl measures 16.0 mm and is surrounded by round brilliant diamonds, 1.35 carats total. The rubies in the shank weigh a total of 0.08 carats. C: A handmade doily crocheted by Smith's grandmother. Photos courtesy of Brenda Smith.

blackened gold lace, rubies, and diamonds (figure 42B). Inspired by her grandmother's handmade crocheted doily featuring a pineapple motif (figure 42C), the rings were created as a tribute to her memory. In 2021, the white freshwater pearl ring won Best Use of Pearls in the AGTA Spectrum competition and the Tahitian pearl ring won the InDesign Award in the category of Pearl Jewelry Over \$5,000.

Figure 43. These "Gibson Girl" millefiori earrings in 18K white gold contain Paraíba tourmalines (1.11 carats total), pink tourmalines (1.54 carats total), and 0.56 carats of aquamarine. Photo courtesy of Brenda Smith.



Smith's one-of-a-kind "Gibson Girl" earrings (figure 43) are inspired by the Austrian symbolist painter Gustav Klimt. Klimt's paintings combined realistic faces with geometric clothing, and Smith mirrored this style to create this high-end piece of jewelry. The technique used to create the girl faces is *millefiori*, which means "thousand flowers" in Italian and produces slices from canes with concentric and colorful patterns. *Millefiori* techniques can be used to make jewelry, decorative objects, candy, and art pieces. Creating these objects requires a skilled artisan who possesses a deep understanding of material properties, considerable experience, and patience. American artist Barbara McGuire handcrafted the complex face canes for the earrings by arranging and embellishing polymer clays to create a lifelike image. Though *millefiori* objects are commonly used in decorative pieces, Smith's design incorporates a harmonious blend of colored gemstones expertly paired and crafted to create a lively figure with a unique personality and color scheme, making it an extravagant and elegant piece of jewelry.

Si Athena Chen and Jennifer Stone-Sundberg

**YNY Jewels: Designer Surbhi Pandya.** A dazzling pair of carved tanzanite earrings (figure 44) caught our attention at the GJX show. Designer Surbhi Pandya of YNY Jewels (New York), who goes by the single name Surbhi, described the significance of the carving featured on each of the large unheated tanzanite crystals. Depicted in violet and green is the lotus blossom, a flower with ancient cultural significance in India, rising with its deep roots from the mud without stains, symbolizing purity and strength. As the blossoms close up at night and reopen the next day, they also symbolize rebirth. Each carving is immediately surrounded by a ring of blue Kashmir sapphires and emeralds, followed by colorless diamonds and bright green tsavorite garnets. Each





Figure 44. Surbhi's "Orient" earrings with tanzanite carvings surrounded by blue sapphires, emeralds, white diamonds, and tsavorite garnets with an upper flower-shaped dangle composed of faceted tanzanites, emeralds, and pink sapphires, all set in 18K white gold. The total diamond weight for the pair is 1.60 carats, and the total colored stone weight is 62.23 carats, 48.32 carats of which are from the two tanzanite carvings. Photo by Robert Weldon; courtesy of YNY Jewels Inc. and Karats Inc.

upper dangle contains faceted slices of tanzanite and emerald with a central hot pink sapphire. She also shared a pendant with a paisley-shaped unheated tanzanite similarly

Figure 45. An 18K white gold pendant containing a paisley-shaped unheated tanzanite with a lotus blossom carving, surrounded by pavé-set black diamonds and pink and purple princess-cut Sri Lankan sapphires. The total weight of the diamonds is 1.00 carats, and the colored stones total 23.40 carats. Photo by Robert Weldon; courtesy of YNY Jewels Inc.



Figure 46. Designer Surbhi. Photo by Jennifer Stone-Sundberg.

containing a lotus carving (figure 45). She explained that the paisley shape represents continuity and life.

Surbhi (figure 46) has been making jewelry for 20 years and was trained by her father, Yogendra Sethi, a renowned artist in India. She described designing jewelry as a journey filled with energy. She does not make jewelry to please herself, but out of a drive to create things that speak to others. Surbhi shared stories of customers' deeply personal connections with her jewelry, a profoundly rewarding experience for her as an artist.

Jennifer Stone-Sundberg and Si Athena Chen

## RESPONSIBLE PRACTICES

### Ethical supply chain practices in Africa with Virtu Gem.

This year marked Tucson's fourth Ethical Gem Fair, a market cooperative of ten responsibly sourced gemstone suppliers (see Spring 2020 GNI, pp. 177–179). The fair was held January 28–31 at the Scottish Rite Cathedral. Virtu Gem sells gemstones directly from artisanal mining communities in Kenya, Malawi, and Zambia (figure 47) and debuted at the fair in 2022. We spoke with cofounder Susan Wheeler and Percy Maleta, Virtu Gem's country exporter and ambassador in Malawi, about its beginnings, programs, and impacts.

Wheeler said more new customers come to the Ethical Gem Fair each year. "All the large companies come by, too," she said. "There were a lot this year that everybody was surprised by. I think that the awareness of what artisanal mining is and what it can be is spreading."



*Figure 47. Some of Virtu Gem's larger gemstones from Kenya, Malawi, and Zambia at the Ethical Gem Fair. Clockwise from top: 45.00 ct citrine, 32.33 ct rutilated quartz, 9.80 ct aquamarine, 21.65 ct citrine, 9.99 ct aquamarine, 12.32 ct aquamarine, 17.20 ct aquamarine, and 20.15 ct citrine (center). Photo by Robert Weldon; courtesy of Virtu Gem.*

Virtu Gem gives artisanal miners, cutters, and traders formal access to international markets and began as a project of Wheeler's nonprofit Responsible Jewelry Transformative (RJT). Virtu Gem's programs also offer training in cutting and basic gemology and help miners improve

safety, labor, and environmental conditions at the mines, all with a focus on women. Their gemstone prices include a 10% premium that goes toward fulfilling the mining communities' various needs. During the height of the COVID-19 pandemic, the premium was used for food drives in all three countries and personal protective equipment for Kenyan women miners; currently it goes to the purchase of safety equipment (figure 48).

Wheeler and cofounders Jessica Hudson and Monica Gichuhi (figure 49) began selling gemstones from Zambia online in 2020, after the pandemic forced the cancellation of a conference they had planned there that would have provided a market for traders. "There was a call to action from the Organisation for Economic and Co-operative Development (OECD) to support all the artisanal miners because no one was coming to the country to buy their stones," Wheeler said. The OECD's Call to Action for Responsible Mineral Supply Chains cited COVID-19's disproportionate impact on artisanal and small-scale miners, who make up more than 80% of the global mining workforce and already face inequities in the supply chain. Wheeler and Hudson are both jewelry designers; Gichuhi is a founding member of the Association for Women in Extractives in Kenya (AWEIK). Her connections with mining associations in Zambia were a starting point.

Beginning in 2021, Virtu Gem received two grants through RJT from the World Bank's Extractives Global Programmatic Support fund. The fund's purpose is to promote sustainable and inclusive mining in developing countries and thereby reduce poverty. The grants allowed them to expand into Kenya and Malawi, hold virtual cutting workshops, and implement CRAFT Code in eight mines. ("CRAFT" stands for Code of Risk mitigation for Artisanal and small-scale miners engaging in Formal Trade.) Virtu Gem also hired experienced international consultants.



*Figure 48. Artisanal emerald miners in Zambia celebrate a donation by Virtu Gem of safety equipment and a jackhammer. Photo courtesy of Virtu Gem.*





*Figure 49. Left: Virtu Gem cofounders Jessica Hudson, Monica Gichuhi, and Susan Wheeler on a recent visit to Malawi. Right: Percy Maleta, the organization's country exporter and ambassador in Malawi, examines a rough gemstone. Photos courtesy of Virtu Gem.*

"There's been a huge amount of progress over the past two years," Wheeler said. The funding helped Virtu Gem develop a strong foundation, she said, and grow enough to be able to pass any chain of custody standard for large-capacity buyers.

While Virtu Gem has had success in all three countries, Wheeler said Kenya has seen the most because some in the trade already had Ultra Tec cutting machines and were selling to the international market. "After the first few purchases we did, word spread," she said. "People were showing up with 50 gems at a time to process." Miners can also bring gems to the country coordinators for cutting.

Virtu Gem's gemstones are cut in each country and tracked with Provenance Proof Blockchain. They include amethyst, aquamarine, citrine, moonstone, rhodolite and other garnets, in all three countries; emeralds in Zambia; tsavorite in Kenya (figure 50); and color-change garnet in Malawi. The three countries also produce tourmaline in various colors, including pinkish orange ("sunset") in Malawi and Zambia and golden in Kenya and Malawi. Production of morganite from newly discovered deposits in northern Malawi recently began.

Virtu Gem has helped miners implement CRAFT Code at four mines in Zambia, two in Malawi, and two in Kenya. CRAFT Code is designed to improve safety, labor, and pay conditions through education at the mines. Its components include mine site certification, safety standards and equipment, and environmental planning, including carbon data tracking and reduction.

CRAFT Code has an emphasis on protecting women, and Wheeler said they focused on women for the associated training. Focusing on woman-owned mines was more difficult, however. "It's a big challenge for women to own any

land at all, especially in Zambia, Kenya, and Malawi," Maleta said. In Zambia, two of the mines—one emerald and one amethyst—were woman-owned, and in Kenya they worked with a young woman whose family owned a mine.

One of Virtu Gem's benefits is helping artisanal miners formalize their mining process. In Malawi, country coordinator Chiko Manda wanted to focus on rhodolite. Maleta said women account for roughly 80% of rhodolite production there (figure 51). Rhodolite is alluvial and best mined

*Figure 50. Rough tsavorite mined from a site in Kenya. Photo courtesy of Virtu Gem.*







Figure 51. Artisanal rhodolite miners in Malawi. Photo courtesy of Virtu Gem.

during the rainy season in Malawi, when the women are busy tending their gardens. Virtu Gem worked with a young couple, Ben and Tamara, who did not have a mining certificate.

"The chief of the Chewa people didn't want the women mining," Wheeler recalled. "Ben had to go and prove himself to the chief, that he wasn't going to take advantage, and that the women could still do their agriculture." Ben joined Virtu Gem's calls with miners in Kenya and Zambia who shared advice. "He ended up getting permission to mine on the land and the blessing of the chief," she said. "He sent me on WhatsApp a picture that he had gotten his certificate. He was so happy." Maleta said that Ben recently received another land permit and is applying for a second mining certificate. "That was a way we could still work with the women," Wheeler said.

Wheeler mentioned the danger of holding a large amount of gemstones in an informal market, which Ben and Tamara encountered with a quantity of rhodolite. "You have the paradox of the women's safety," she said. "Everybody hears about it, and you get all these other dealers and traders coming in. How are they going to get a fair price? Yet they can't hold on to it." She said Ben called his friends and pleaded with them to purchase some of the rhodolite. She would like to see a formal system to address this type of scenario.

Maleta said the past four or five years have seen an influx of Kenyans and Zambians to Malawi to buy gems, some of whom export them back home and misrepresent the source country. By exporting directly from Malawi, Virtu Gem has improved supply chain transparency.

Maleta said Virtu Gem pays more than the informal market, but convincing people to participate can be a challenge. "To have someone leave a stone with you and wait—for maybe two months, three months—it hasn't

been easy," he said. "But we have people who understand the process, who know that the stone they are leaving with Virtu will be sold, but also understand that if it's not sold, it will be returned. That is trust."

"I was surprised by the lack of trust at the beginning," Wheeler said. "We have to work hard to earn the trust from everybody in the gemstone community. We couldn't have done this without our partner, Monica Gichuhi, working within the communities, and our country coordinators." She mentioned Caroline Muchira in Kenya, who is also a cutter and a GIA Graduate Gemologist; Manda in Malawi; and Pauline Mundia in Zambia, a respected woman leader whom everyone calls "Mama Pauline."

"Living up to expectations is hard every single day," Wheeler said. "Tucson is hard because we don't own anything on display. Those are people sending us their stones that they've invested in. Before, they would have just sold them and not invested in separating parcels and cutting. That's a lot of pressure. We've earned some of that trust, and we really have worked hard to earn that."

"It's a dream come true for many to have their stones sold at this level," Maleta said. "For us, for the country, for the people who are trading, the future is bright."

*Erin Hogarth*

## SYNTHETICS AND SIMULANTS

**Luminescent synthetic garnet-like crystals.** At the 22nd Street show, the author spoke with Tim Challener of Turtle's Hoard (Raleigh, North Carolina), who was selling some unique rough and faceted luminescent synthetic garnet-like crystals, which he referred to as "lumogarnets." After 12 years in the gem business, Turtle's Hoard began selling only laboratory-made materials in March 2022. Challener noted

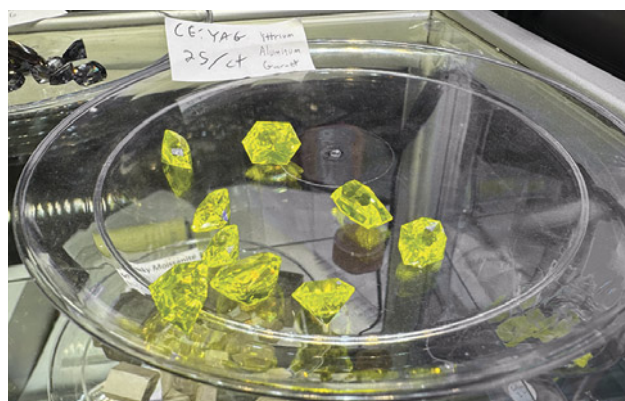


Figure 52. Yellow to greenish yellow faceted cerium-doped YAG “lumogarnets” ranging from 4 to 12 ct apiece. Photo by Lisa Kennedy; courtesy of Turtle’s Hoard.

that their best-selling gemstone is Ce:LuAG, lutetium aluminum garnet ( $\text{Lu}_3\text{Al}_5\text{O}_{12}$ ) doped with cerium. This material was introduced to the optics industry in the late 1990s and acts as a scintillator, a fluorescent crystal that absorbs high-energy radiation such as X-rays or gamma rays and reemits them as lower-energy visible light that is much easier to detect. LuAG is closely related to YAG electronically and both have the same garnet structure, yielding a gem with similarly excellent optical and gem properties (see figure 52).

Yttrium aluminum garnet, known as YAG ( $\text{Y}_3\text{Al}_5\text{O}_{12}$ ), a lab-grown crystal that crystallizes in the cubic garnet structure, was one of the most popular diamond simulants from the 1960s to the mid-1970s due to its relatively good hardness (about 8.25 on the Mohs scale) and brilliance. Cartier’s replica of the 69.42 ct Taylor-Burton diamond famously used YAG. Gadolinium gallium garnet, known as GGG ( $\text{Gd}_3\text{Ga}_5\text{O}_{12}$ ), was the next garnet-like material to be used as a diamond simulant. GGG is slightly more brilliant and dispersive than YAG but scratches fairly easily due to its lower hardness (about 6.5 to 7.5 on the Mohs scale).

Most of these garnet-like crystals are doped with various rare earth elements such as neodymium, erbium, cerium, and ytterbium. These dopants not only increase the materials’ value in the optics industry but also yield the variously colored synthetic garnet-like crystals seen in the gem and jewelry industry today.

These synthetic garnet-like crystals are most commonly produced by the Czochralski method, also known as the pulling method. In this melt process, the boule (a cylindrical synthetic crystal produced by a melt process) grows from a thin cylindrical seed crystal that is dipped into a melt of the desired garnet composition. The seed is rotated and then lifted very slowly at a controlled rate, allowing the melt to crystallize onto it. The material produced is extremely pure, with few inclusions or none at all. However, the material is not actually made for the gem and jewelry industry; rather, those in the industry can only purchase some of the less-perfect material and off-cuts of the boules to facet and sell (figure 53).

Challenger explained, “They are lab-created, but each one has its own history beyond its use as a gem. And while there have been conflicting messages about whether some lab-grown stones, particularly lab-grown diamonds, are truly eco-friendly, the materials we work with are an inevitable byproduct of necessary crystal growth. Our modern lives rely on these materials being grown—we can’t have cell phones without lithium niobate or modern PET scanners without scintillators—so there isn’t really any additional waste associated with them.”

Turtle’s Hoard offered a variety of “lumogarnets,” including rough and faceted luminescent yellow and yellowish green cerium-doped GAGG (gadolinium aluminum gallium garnet,  $\text{Gd}_3\text{Al}_2\text{Ga}_3\text{O}_{12}$ ), cerium-doped LuAG, and cerium-doped YAG (see again figure 52). In addition, they displayed rough grayish purple neodymium-doped YAG, rough and cut greenish blue ytterbium-doped YAG (figure 54), rough pinkish orange erbium-doped YAG, and rough and faceted green chromium-doped YAG, a green stone with strong red fluo-

Figure 53. The top of a YAG boule doped with cerium and neodymium and produced by the Czochralski method, measuring approximately 36 mm in diameter and 45 mm tall. Parts of the boule that cannot be used for scientific purposes can be sold to the gem and jewelry trade for faceting. Photo by Lisa Kennedy; courtesy of Turtle’s Hoard.





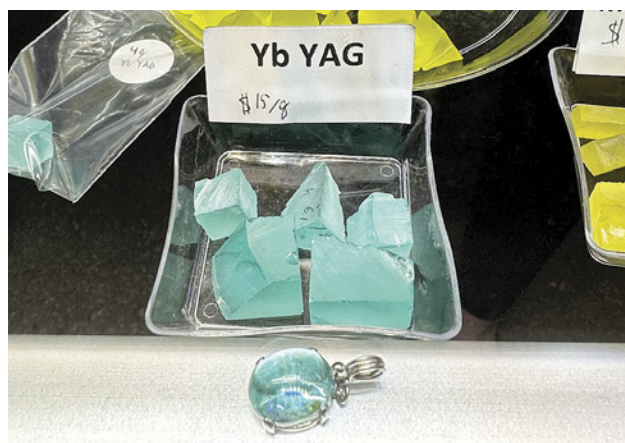


Figure 54. Greenish blue rough and cut ytterbium-doped YAG. The cabochon in front is 14 x 10 mm. Photo by Lisa Kennedy; courtesy of Turtle's Hoard.

rescence showing simultaneous flashes of green and red based on lighting, dubbed "Christmas garnet." Although synthetic and possessing a garnet-like structure, YAG, GGG, LuAG, and GAGG are not synthetic garnet, since they lack the chemistry of any garnets known in nature.

Lisa Kennedy

## EXHIBITS

**GIA Museum's "Paint the Town Ruby Red" exhibit at TGMS.** At the Tucson Gem and Mineral Show, the GIA Museum exhibited a Burmese ruby and diamond necklace and earrings against a backdrop of the necklace fluorescing in ultraviolet light (figure 55). The necklace contains 39 untreated rubies from Mogok totaling 83.73 carats and 302 diamonds totaling 42.62 carats. The largest ruby is 5.00 ct.

The exhibit highlighted the "magic ingredient"—chromium—that gives ruby not only its color but also its fluorescence. Mogok rubies are renowned for their high concentration of chromium and low concentration of iron. The latter element, if present in a high enough concentration, quenches all or part of the red fluorescence produced by the chromium. This fluorescence is an important factor in the high value of Mogok rubies.

TGMS began in 1955 and is one of the longest-running gem and mineral shows in the world. GIA Museum curator Terri Ottaway said she was thrilled at the opportunity to showcase such a gorgeous necklace and include a bit of chemistry and geology for the gem and mineral enthusiasts.

Erin Hogarth

**GIA Library wins exhibit award at TGMS.** GIA's Richard T. Liddicoat Gemological Library and Information Center was awarded the Betty Clayton Gibson Memorial Trophy for Best Museum Exhibit for 2023 at the Tucson Gem and Mineral Show. The winning exhibit illustrated the importance of mercury-free gold mining (figure 56). Historically, mercury has been used in artisanal and small-scale gold mining because of its ability to bond with gold to form an amalgam, but its high toxicity and negative effects on humans and wildlife have led to increased emphasis on mercury-free options for mining gold.

The exhibit featured a traditional wooden bowl used for gold panning, along with many of the library's books on ecological jewelry and responsible and sustainable mining and jewelry practices.

"This exhibit illustrates how mercury-free gold mining can have positive long-term implications for both gold miners and the environment," said library director Robert Weldon. He noted that among all the deserving exhibits displayed at TGMS, the GIA Library's stood out due to the



Figure 55. The GIA Museum's "Paint the Town Ruby Red" exhibit at TGMS featured a Burmese ruby and diamond necklace and earrings, courtesy of Mona Lee Nesseth (Custom Estate Jewels) and a private collector. Photo by Terri Ottaway.





Figure 56. The GIA Library's award-winning exhibit on mercury-free mining at the Tucson Gem and Mineral Show. Photo by Chris Rogers.

importance of responsible mining and sustainability in the industry.

In 2021, GIA provided a grant to Mercury Free Mining (MFM) and the Alliance for Responsible Mining (ARM). New methods for concentrating gold continue to be explored and tested with the goal of significantly reducing, or even eliminating, the use of mercury in gold mining.

*Erica Zaidman  
GIA, Carlsbad*

## ANNOUNCEMENTS

**Sixth annual Gianmaria Buccellati Foundation Award winner.** Sara Guergova, a graduate of GIA's Jewelry Design program in London, received the sixth annual Gianmaria Buccellati Foundation Award for Excellence in Jewelry Design. The 12 finalists and winner were announced at the GIA Alumni Collective's "Night at the Museum" event held

during the AGTA GemFair in Tucson. Guergova, the first student from the London campus to win the award, designed a stunning bracelet featuring swans to represent togetherness and loyalty (figure 57).

Created in partnership with the Gianmaria Buccellati Foundation in 2018, the award recognizes outstanding talent in design among GIA students worldwide. Larry French, chief officer for North America strategies at the foundation, said, "On behalf of the Gianmaria Buccellati Foundation, we want to congratulate Ms. Sara Guergova, this year's winner, plus all the other finalists whose work so enriched this year's competition. We also want to recognize the talented GIA design instructors who helped guide the students on their way to the final judging in Tucson."

The 2023 Gianmaria Buccellati Foundation Award for Excellence in Jewelry Design competition is underway and open to students in GIA's Jewelry Design courses who meet the eligibility requirements. Visit [www.gia.edu/buccellati-foundation-award-jewelry-design](http://www.gia.edu/buccellati-foundation-award-jewelry-design) for more information.



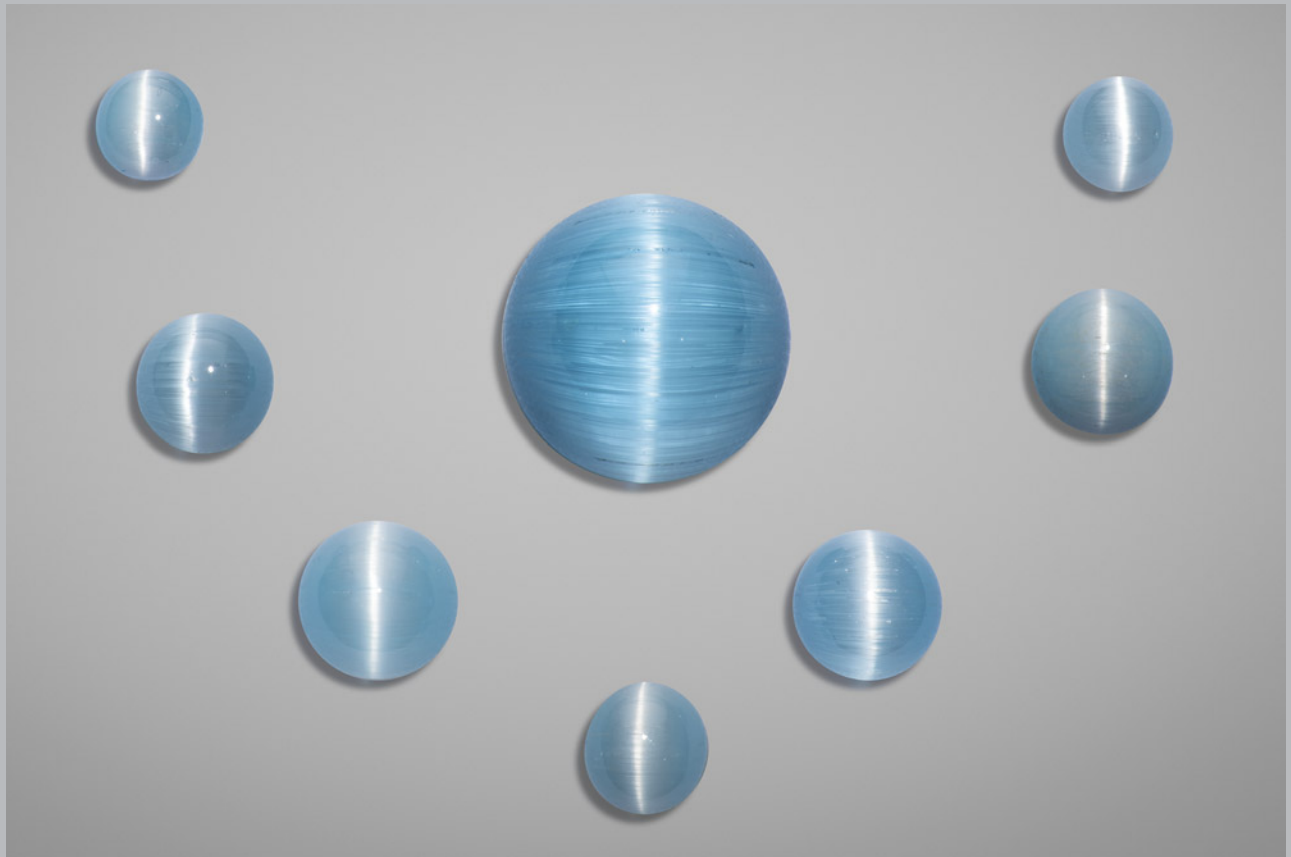
Figure 57. Sara Guergova's winning design sketch for the 2022 Gianmaria Buccellati Foundation Award for Excellence in Jewelry Design, featuring gold, black onyx, ruby, diamond, tourmaline, and blue sapphire.

## 2023 Tucson Photo Gallery

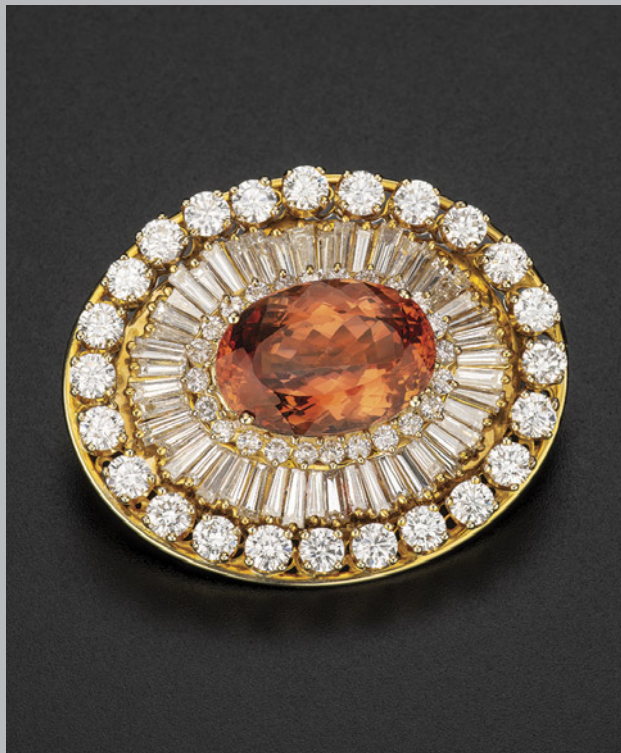


*The pendant on the right is a miniature recreation of the “Bahia,” a massive rutilated quartz fashioned by Glenn Lehrer and Lawrence Stoller. Each pendant in the collection is carved from leftover raw material. The photo on the left is by Harold and Erica Van Pelt; courtesy of Glenn Lehrer. The photo on the right and the rest of the photos in this gallery are by Robert Weldon.*





*This suite of cat's-eye topaz cabochons of unknown origin features a 135.80 ct center stone. Courtesy of Mayer & Watt.*



*This brooch features a 13.27 ct Imperial topaz surrounded by 8.50 carats of diamonds, mounted in 18K yellow gold. Courtesy of Jewelerette & Co.*



*In this beautifully matched pair of natural pearl earrings, each 10 ct round pearl sits atop an astonishingly large 32 ct pearl drop. Courtesy of Sima G. Ltd.*





*A spray of “mango” quartz measuring  $92 \times 103$  mm from the Boyacá Province in Colombia. The yellow coloration is believed to be due to the mineral halloysite. Courtesy of Cornerstone Minerals.*



*This naturally formed azurite disc on kaolinite matrix, accompanied by a cluster of malachite, hails from the Malbunka copper mine in Northern Territory, Australia. It measures 123 × 140 mm. Courtesy of Fine Art Minerals and Ghulam Mustafa.*



*A stunning pair of Alexandre Reza 18K gold earrings. In this design, 112 diamonds (totaling 7.86 carats) dangle from two emeralds (totaling 2.12 carats). Courtesy of Jardin Jewels.*



*Rough and carved hemimorphite, weighing 173.35 ct and 112.26 ct, respectively. Courtesy of Evan Caplan.*



*A vintage Fred of Paris demi-parure of earrings and a bangle, set with diamonds, rubies, emeralds, and sapphires. Courtesy of Jardin Jewels.*





*This aquamarine spray cluster from Skardu, Pakistan, measures 160 × 102 mm. Courtesy of Fine Art Minerals and Ghulam Mustafa.*

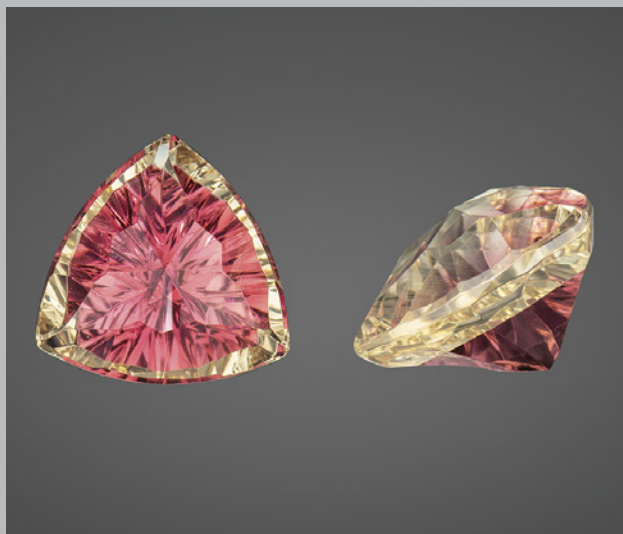




*Indicolite from Afghanistan. The 116.7 ct crystal is from Nuristan Province, and the 9.39 ct cut gem is from Kunav Province. Courtesy of Dudley Bauwet Gems and Mountain Minerals International.*



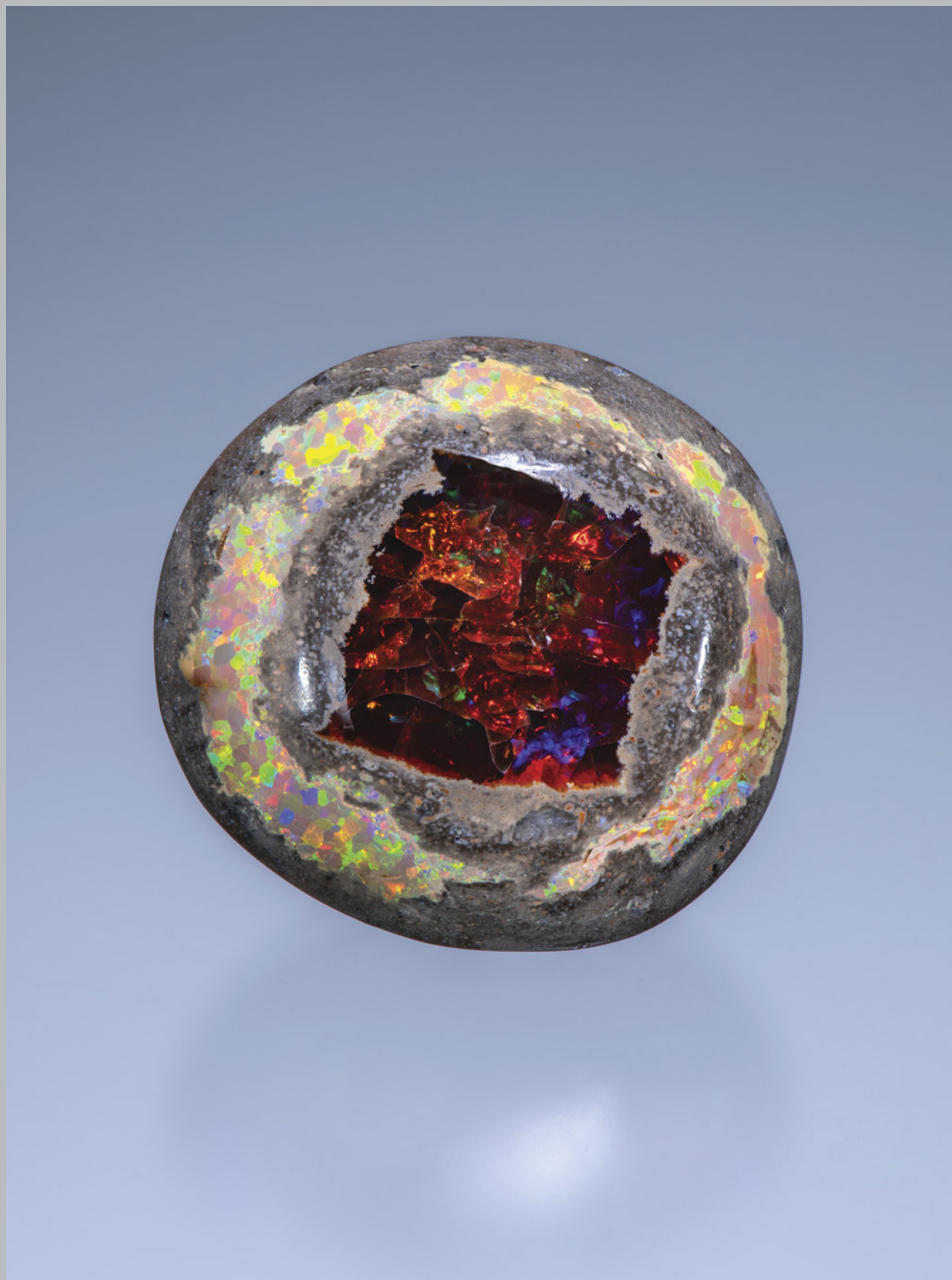
*Earrings and necklace in a jellyfish motif, set in 14K yellow gold. The mabe pearls are from the Sea of Cortez. Courtesy of Columbia Gem House.*



*Master cutter Mark Gronlund combines natural Oregon sunstone with unheated Nigerian pink tourmaline in this 7.35 ct doublet, shown in table and profile views. Courtesy of Desert Sun Mining and Gems.*



*A Cartier Les Oiseaux Libérés diamond, emerald, and sapphire ring crafted in 18K white gold. Courtesy of Jardin Jewels.*



*Aptly named the “Ring of Fire,” this Ethiopian opal in matrix displays a square of dark opal surrounded by a ring of white opal. Courtesy of Ellie Gem Arts.*





*This bicolored spodumene is from Nuristan Province, Afghanistan. Terminations of the crystal appear to mimic the mountain range from which it was mined. Courtesy of Dudley Blauwet Gems and Mountain Minerals International.*



*Vintage diamond and carved emerald bracelet designed by Alexandre Reza. Courtesy of Jardin Jewels.*



*An art nouveau enameled necklace in a floral motif incorporating 20 seed pearls, four natural freshwater pearls, and a freshwater Mississippi dogtooth pearl. Courtesy of Bernard Nacht & Co./Under the Crown.*



*This horn-shaped boulder opal measures 75.5 × 15.9 × 4 mm and weighs 74.20 ct. Courtesy of Dufty Weis Opals Inc.*



## REGULAR FEATURES

### COLORED STONES AND ORGANIC MATERIALS

***Pinctada radiata* atypical bead cultured pearls from the UAE.** Pearling is embedded in the culture and traditions of everyday life in the United Arab Emirates (UAE), especially in the trading center of Julfar. Abdulla Al Suwaidi, grandson of one of the last traditional pearl divers in the UAE, took on the challenge of reviving the country's pearling industry. He succeeded in establishing the Suwaidi Pearl Farm in Al Rams, Ras Al Khaimah (RAK), in 2005. Suwaidi's cultured pearl farm is recognized as the first of its kind in the Arabian (Persian) Gulf region.

GIA's Mumbai laboratory recently examined a quantity of cultured pearls obtained from the farm. The parcel contained variously shaped white to cream-colored pearls. Examination by real-time microradiography (RTX) showed a variety of different internal structures including bead and non-bead cultured pearls, but two pearls in particular (figure 58) revealed very interesting structures and were confirmed to be samples from atypical "bead" culturing experiments conducted by the farm. Pearl A was light cream and near-round, weighing 0.87 ct and measuring  $5.13 \times 4.93$  mm, while pearl B was cream and button shaped, weighing 0.94 ct and measuring  $5.42 \times 5.12 \times 4.93$  mm. When viewed under  $40\times$  magnification, both pearls exhibited a smooth surface and possessed typical nacreous overlapping aragonite platelets.

Additional RTX and X-ray computed microtomography ( $\mu$ -CT) analyses were conducted to further study the internal structures. RTX imaging of pearl A revealed a non-bead cultured pearl used as a "bead" nucleus (figure 59). A light gray core surrounded by organic-rich concentric growth structures followed by finer growth arcs was visible. An obvious demarcation with a small organic tail-like feature just below the surface overgrown with cultured nacre was also apparent. The lack of growth arcs in the nacreous layers was due to rapid growth during the culturing process ("Atypical 'beading' in the production of cultured pearls from Australian *Pinctada maxima*," *GIA Research News*, February 13, 2017). Similarly, pearl B revealed a natural pearl used as a "bead" nucleus (figure 60), with a very small but clearly visible dark gray core surrounded by faint growth arcs. As with pearl A, a distinct demarcation with organic-rich areas and a small organic tail-like feature were evident just below the surface overgrown with cultured nacre. X-ray computed microtomography analysis of both samples revealed clearer images of the demarcation between the "bead" pearls used as nuclei and the cultured nacre overgrowths.

Optical X-ray fluorescence examination did not show any fluorescence in either sample. Energy-dispersive X-ray fluorescence spectrometry revealed manganese levels below detection limits and strontium levels of 1130 ppm for pearl A and 1446 ppm for pearl B. The results from both testing methods were consistent with a saltwater growth environment. The ultraviolet/visible reflectance spectra collected for both pearls showed features around 435 and 460 nm and an additional weak band at 495 nm. These fea-



Figure 58. Two atypical bead cultured pearls recovered from *Pinctada radiata* mollusks from Abdulla Al Suwaidi's farm in the UAE. Pearl A (left) weighs 0.87 ct, and pearl B (right) weighs 0.94 ct. Photo by Gaurav Bera.

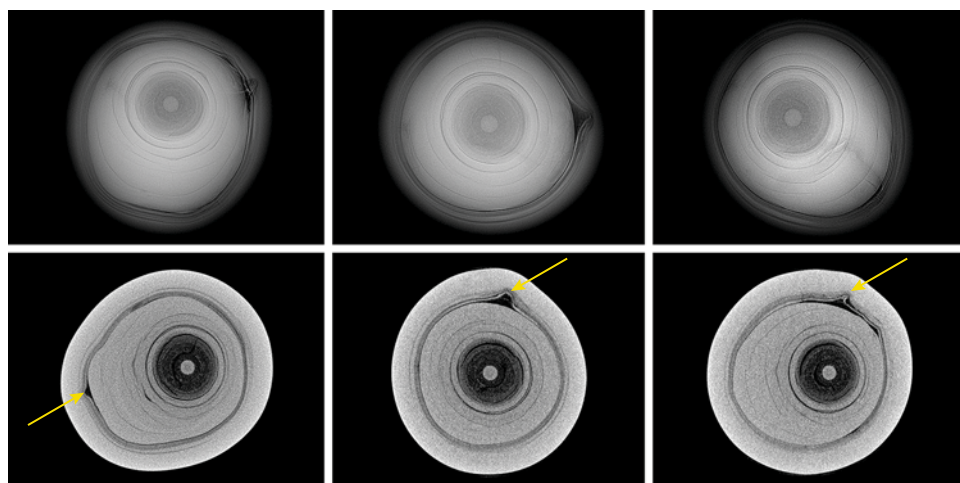


Figure 59. Top: RTX images in three directions of the non-bead cultured pearl used as a “bead” with a distinct demarcation and an organic tail-like feature in pearl A. Bottom:  $\mu$ -CT scans of pearl A. The tail feature is indicated by a yellow arrow.

tures are similar to spectral observations previously recorded for natural *Pinctada radiata* pearls (A. Al-Alawi et al., “Saltwater cultured pearls from *Pinctada radiata* in Abu Dhabi [United Arab Emirates],” *Journal of Gemmology*, Vol. 37, No. 2, 2020, pp. 164–179). Raman analysis using 514 nm laser excitation was carried out on the surfaces of both pearls, and a doublet at 704/705  $\text{cm}^{-1}$  as well as a peak at 1085  $\text{cm}^{-1}$ , indicative of aragonite, were observed. Weak polyenic pigment-related peaks at 1130 and 1540  $\text{cm}^{-1}$  were only observed for pearl B and were associated with its cream coloration. The photoluminescence spectra were also consistent with the Raman results and displayed high fluorescence together with the aragonite peaks, typical of most nacreous pearls.

Using lower-quality pearls (both nacreous and non-nacreous), gemstones, and other materials as “bead” nuclei has been a known practice for the last decade (“Chasing cultured pearls at SSEF: Cultured pearls using a natural pearl as a bead,” 2020, <https://www.ssef.ch/chasing-cultured-pearls-at-ssef-cultured-pearls-using-a-natural-pearl-as-a-bead/>). Although not seen on a regular basis, atypical “bead” cultured pearls (aBCPs) are encountered in laboratories from time to time and can be very challenging to

separate from some natural pearls. This would be especially true of the two samples featured in this report: If either of them were drilled and mixed in strands with natural Gulf pearls, an experienced gemologist would find it difficult to separate them from the other pearls. The authors have encountered natural pearls with similar distinct boundaries. It should also be noted that the aBCPs produced at the Suwaidi farm are the result of successful experiments, and they are not commercially available at the time of this writing. The farm continues to conduct various experiments and aims to restore the UAE’s place in the global market by producing the finest *Pinctada radiata* cultured pearls available.

Abeer Al-Alawi  
GIA, Global

Lubna Sahani  
GIA, Mumbai

Nicholas Sturman  
Bangkok

Chunhui Zhou  
GIA, New York

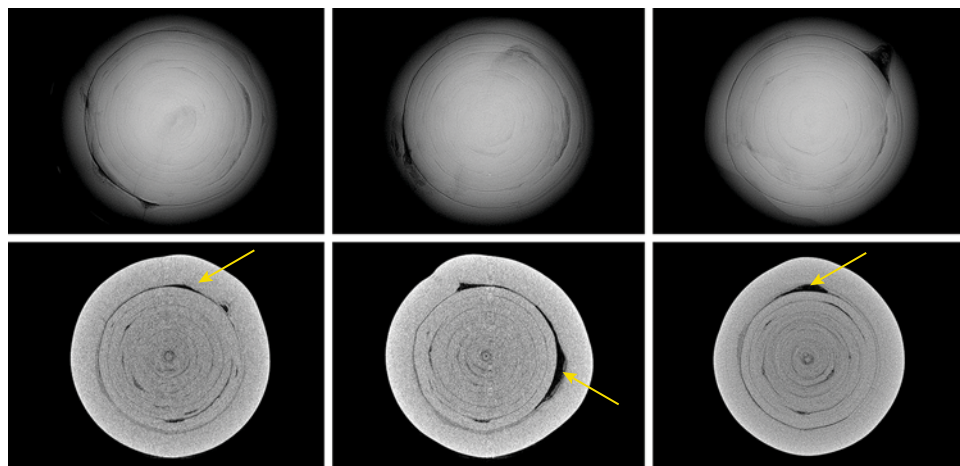


Figure 60. Top: RTX images in three directions of a natural pearl used as a “bead” with a clear demarcation and an organic tail-like feature in pearl B. Bottom:  $\mu$ -CT scans of pearl B. The tail feature is indicated by a yellow arrow.





Figure 61. Twelve Chilean abalone cultured pearls and two red abalone (*Haliotis rufescens*) shells with attached cultured shell blisters, as well as three 7 mm traditional freshwater shell bead nuclei used to culture the pearls. Photo by Emily Lane.

**Bead cultured abalone pearls from Chile.** Abalone is the common name of the marine mollusk species that belongs to the *Haliotis* genus. Various abalone species are distributed worldwide along cold coastal waters. They live in rocky habitats, attaching firmly with their muscular foot. Abalone is highly prized for its meat, shell, and pearls. Due to a marked decrease of abalone populations, harvesting wild-caught abalone is heavily regulated. Thus, approximately 95% of the global abalone supply comes from farms around the world, in countries such as China, South Korea, South Africa, Chile, Australia, Taiwan, Japan, the United States, and New Zealand (P.A. Cook, "Worldwide abalone production statistics," *Journal of Shellfish Research*, Vol. 38, No. 2, 2019, pp. 401–404).

Abalone's ear-shaped shells and pearls are known for their unique, vibrant iridescent nacre, which is sought after in jewelry and decorative items. The iridescence phenomenon is also known as "orient," and it is attributed to interference and diffraction of light in the multilayered aragonite platelet microstructure and organic components. Due to the rarity of natural abalone pearls, most abalone products used in jewelry today are either abalone shells or assembled cultured shell blisters (also known as "mabe pearls").

The culturing of whole pearls in abalone mollusks started around the same time as shell blister culturing for producing mabe pearl (assembled cultured shell blister),

and various methods have been attempted over the years (C.Y. Wentzell, "Cultured abalone blister pearls from New Zealand," Fall 1998 *G&G*, pp. 184–200; M. Monteforte and H. Bervera, "Abalone pearl culture on the west coast of the Baja California peninsula, Mexico," *World Aquaculture*, 2010, pp. 12–17). However, due to abalone's hemophilia and poor tolerance for chemicals and handling, any significant cut could cause major bleeding, and the nucleation and implantation procedures could induce infection that prohibits the mollusk from producing nacre. Therefore, the success rate of bead cultured (BC) abalone pearls was always low and the pearls were of unmarketable quality.

After 10 years of experimenting, scientists from the University of Antofagasta, Chile, have successfully created abalone BC pearls using a patented method for producing free pearls in abalone. Twelve of their cultured pearls and two abalone shells with a cultured shell blister attached (figure 61) were submitted to GIA for study in May 2022. They were the pilot crop of a new pearl culturing technique using traditional freshwater shell bead nuclei (5 to 8 mm) inserted into grafting channels in the visceral mass of *Haliotis rufescens* (red abalone) imported into Chile from Mexico in the 1990s (figure 62, left) for abalone farming. The BC pearl cultivation takes place during the last 24–28 months of the abalone culture process that usually takes 48–52 months, allowing the abalone meat and the pearl to be harvested at



Figure 62. Abalone mollusks were grown in an aquaculture recirculation system in eight raceways of 5000 liters. A local kelp species (shown on the right) was used to feed the mollusks twice per week. Photos courtesy of Jorge Donoso Mena.

the same time. The facilities include an aquaculture recirculation system in eight raceways of 5000 liters, with continuous aeration by blowers and a culture water flow of 5000 liters per hour (figure 62, right). The local kelp species *Lessonia trabeculata* obtained from natural, sustainably managed sources is used to feed the mollusks twice a week. Despite a high rate of bead nucleus rejection, the survival rate of the mollusks after grafting has been 99% and is currently at 15,000 grafted mollusks per trial, according to the farm.

The cultured abalone pearls produced using this method displayed multicolored nacreous surfaces due to

strong iridescence, along with patches and stripes of dark brown organic materials. They exhibited a variety of baroque forms, and four samples possessed horn or tooth shapes often found in natural abalone pearls. A characteristic underlying botryoidal-like surface structure, usually observed on natural abalone pearls and shells, was also present (Fall 2015 Lab Notes, pp. 319–320). Real-time micro-radiography (RTX) revealed a round bead nucleus in the majority of samples, and the nacre layer thickness surrounding the bead nuclei ranged from 0.10 to 1.20 mm (figure 63). One sample lacked a bead nucleus and was

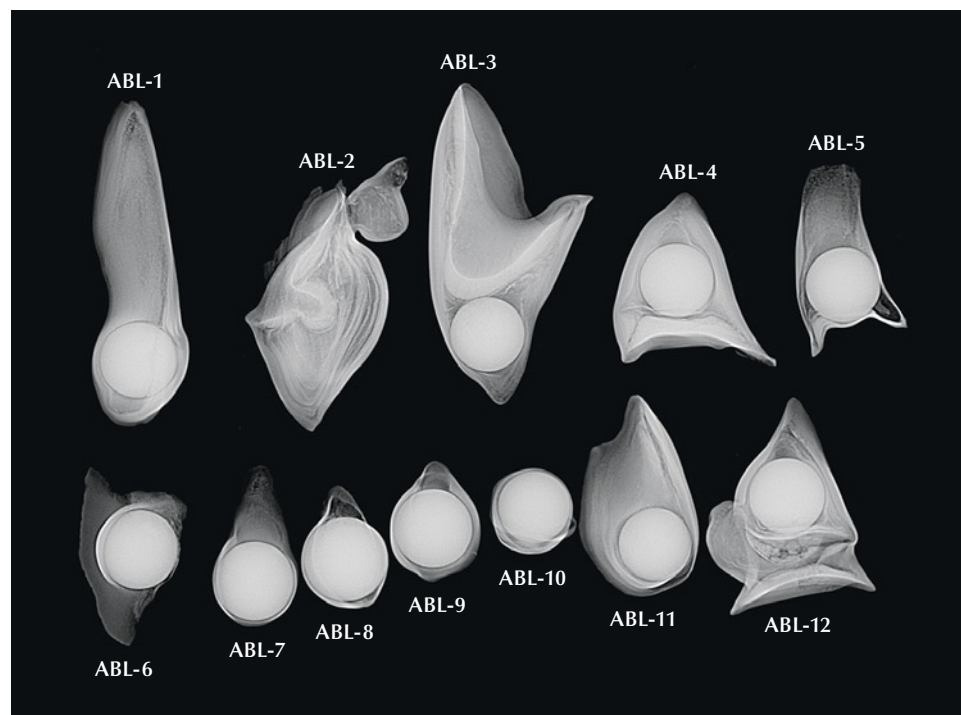


Figure 63. RTX images reveal 5–8 mm round shell bead nuclei in a majority of the abalone samples (ABL), with the nacre layer thickness surrounding the bead nuclei ranging from 0.10 to 1.20 mm. A bead nucleus was absent in sample 2, only showing layered growth with void-related features. While it is considered a non-bead cultured pearl, its internal structure resembled the internal structure commonly found in natural abalone baroque pearls. Image by Amiroh Steen.



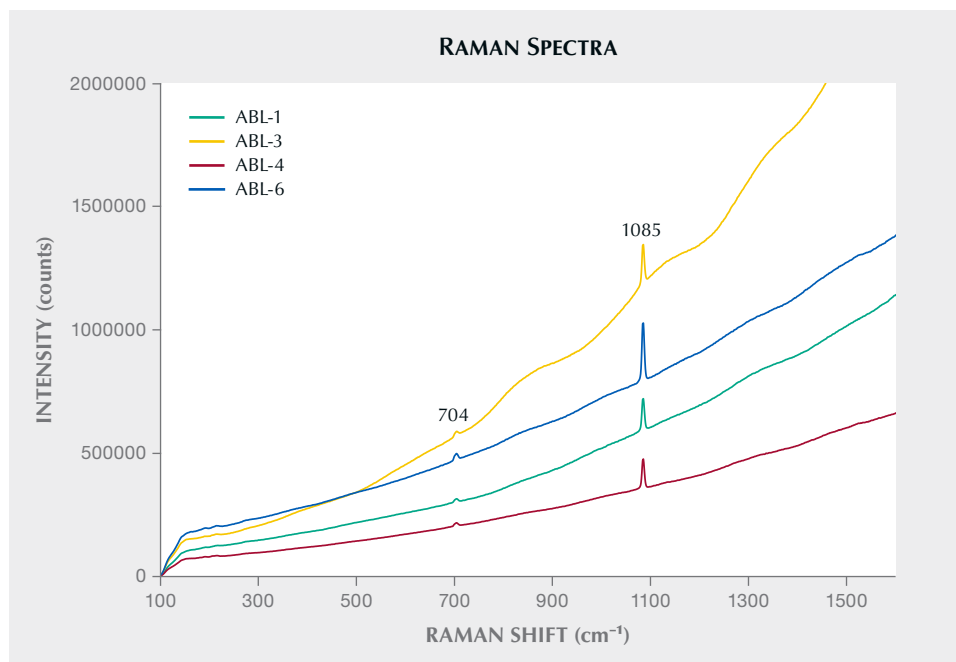


Figure 64. Raman spectra using 514 nm laser excitation showed high fluorescence background and weak peaks of aragonite displayed at 704 and 1085  $\text{cm}^{-1}$ . These results are consistent with 10 natural abalone samples selected for preliminary comparison study.

identified as a non-bead cultured (NBC) pearl. Its layered growth with void-related features resembled the internal structure commonly found in natural abalone baroque pearls.

Ten natural abalone pearls were selected for spectroscopic and chemical comparison with the cultured pearl samples, and both types of samples showed similar results. No specific patterns were observed in ultraviolet/visible

reflectance and photoluminescence spectra, and Raman spectra showed high fluorescence background and weak peaks of aragonite at 704 and 1085  $\text{cm}^{-1}$  (figure 64). Energy-dispersive X-ray fluorescence analysis revealed all the samples had very low or below detection limit manganese content and high levels of strontium ranging from 1100 to 5000 ppm. High iodine levels were also detected in most samples, which is common in abalone. Trace element concentrations determined by laser ablation-inductively coupled plasma-mass spectrometry (LA-ICP-MS) were compositionally similar in both sample types. However, the cultured samples contained lower boron and higher potassium contents. All four tested spots of the NBC samples could be clearly separated from natural samples in the plot of boron vs. potassium contents (figure 65). Since the one NBC pearl showed an internal structure similar to that of natural abalone pearls, the plot can potentially be used to differentiate NBC pearls from natural samples. However, further study on both sample types is required. Additionally, all abalone samples showed higher strontium concentrations than *Pinctada* species previously studied.

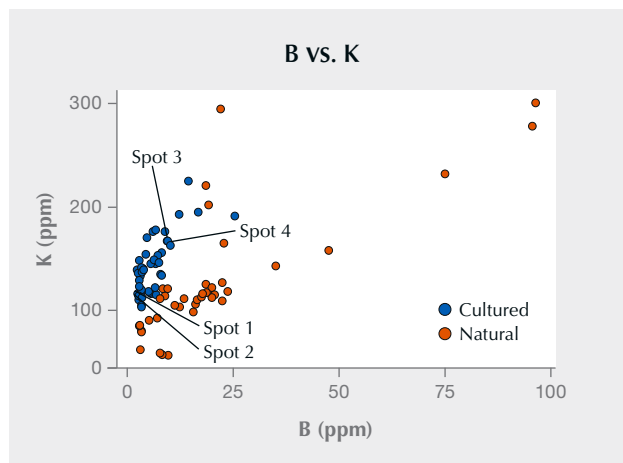
The success of abalone BC pearl production could be a promising addition to the gem and jewelry industry, and this study provided useful information for future reference.

Artitaya Homkrajae, Amiroh Steen,  
Matthew Hardman, and Ziyin Sun  
GIA, Carlsbad

Rubén Araya Valencia  
Alexander von Humboldt Institute of Natural Sciences,  
University of Antofagasta

Jaime Pablo Maturana Zuñiga  
Abalone Pearl Technology (APT SpA)  
Antofagasta, Chile

Figure 65. The cultured and natural abalone pearl samples were compositionally similar in trace element concentrations determined by LA-ICP-MS. However, the cultured samples contained lower boron and higher potassium than the natural pearls. All four tested spots of the NBC samples are clearly separated from natural samples in this plot.



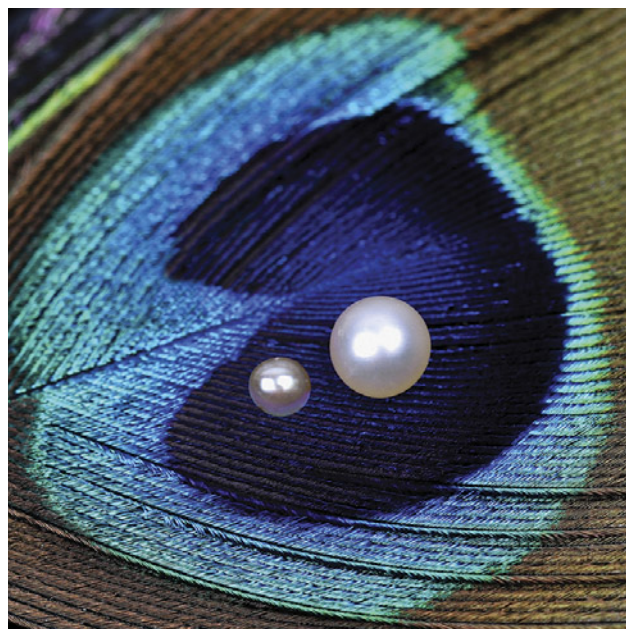


Figure 66. Two natural pearls recovered from *Pinctada radiata* mollusks by Bahraini divers, weighing 0.06 ct (pearl A, left) and 0.25 ct (pearl B, right). Photo by Gaurav Bera.

#### Microscopic shells in natural pearls from *Pinctada radiata*.

For centuries, natural pearl diving was Bahrain's main industry. The vast majority of natural pearls fished around the islands of Bahrain are found in the *Pinctada radiata* bivalve (known in Arabic as *mahar*). These pearl beds have been known to produce the finest-quality natural pearls in the Arabian (Persian) Gulf region. Given the Gulf's strategic trading location and the richness of its pearling industry, the pearls from this region are coveted by traders and collectors alike (R. Carter, "The history and prehistory of pearling in the Persian Gulf," *Journal of the Economic and Social History of the Orient*, Vol. 48, No. 2, 2005, pp. 139–209). GIA's Mumbai laboratory recently examined a quantity of these pearls obtained from two local Bahraini divers who claimed they were recovered from wild mollusks living in the nutrient-rich shallow waters off the coast of Sitra, one of Bahrain's 33 islands.

Natural pearls from *Pinctada radiata* fished from Bahrain and the Gulf region in general have a wide range of shapes and colors. While most of the pearls examined showed a variety of interesting internal structures, two of them had a noteworthy feature: a minute shell contained within. Natural pearls are very rare and form inside mollusk shells, and a shell within a pearl within a shell is like nature's version of a nesting doll. Such structures have been encountered by GIA on rare occasion (see Winter 2015 Lab Notes, pp. 434–436).

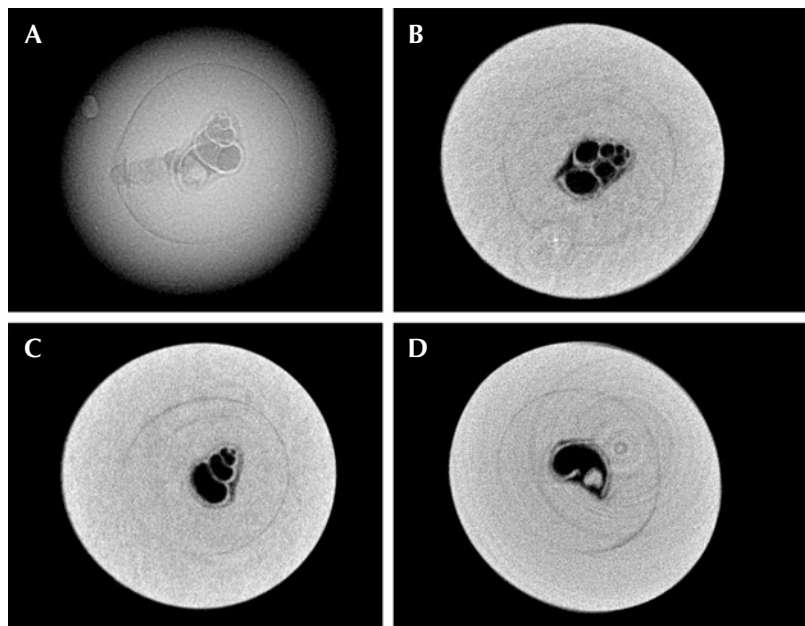
Both pearls were very small (figure 66). The smaller one (A) had a strong yellow bodycolor and an oval shape, weighing 0.06 ct and measuring  $2.07 \times 1.93$  mm. The larger round one (B) had a light cream color, weighing 0.25 ct and meas-

uring 3.30 mm in diameter. When viewed under 40× magnification, both exhibited typical nacreous overlapping aragonite platelets. Real-time microradiography (RTX) and X-ray computed microtomography ( $\mu$ -CT) analyses were carried out to examine the internal structures in greater detail.

A minute gastropod shell measuring approximately  $0.50 \times 0.30$  mm was observed in pearl A. The shell walls were very thin, and minimal growth arcs were present in the nacre surrounding it (figure 67). Marine gastropods are known to range in size from a few millimeters to more than a meter, so the size of the shell inside this pearl suggests it was from a juvenile gastropod just beginning to form its shell. The juvenile shell later forms the protoconch or first whorls of an adult gastropod (A. Nutzel, "Larval ecology and morphology in fossil gastropods," *Paleontology*, Vol. 57, Part 3, 2014, pp. 479–503).

RTX imaging of pearl B revealed a minute shell that appeared to be a foraminifera test (shell), measuring approximately  $0.45 \times 0.35$  mm. Foraminifera are small unicellular marine organisms found on the sea floor. A thin layer of organic matter that appeared darker in the RTX and  $\mu$ -CT images seemed to envelop the foraminifera test, and a few growth arcs were observed within the surrounding nacre (figure 68). The  $\mu$ -CT scan was also rendered using specialized software (C. Zhou et al., "New 3-D software expands GIA's pearl identification capabilities," *GIA Research News*, May 13, 2016) to create a three-dimensional image that

Figure 67. The gastropod shell, measuring approximately  $0.50 \times 0.30$  mm, observed in pearl A. A: RTX image of the shell. B–D:  $\mu$ -CT scans of the shell in the X, Y, and Z directions, respectively. (The weak white rings on the lower right image are artifacts and not pearl-related structures.)





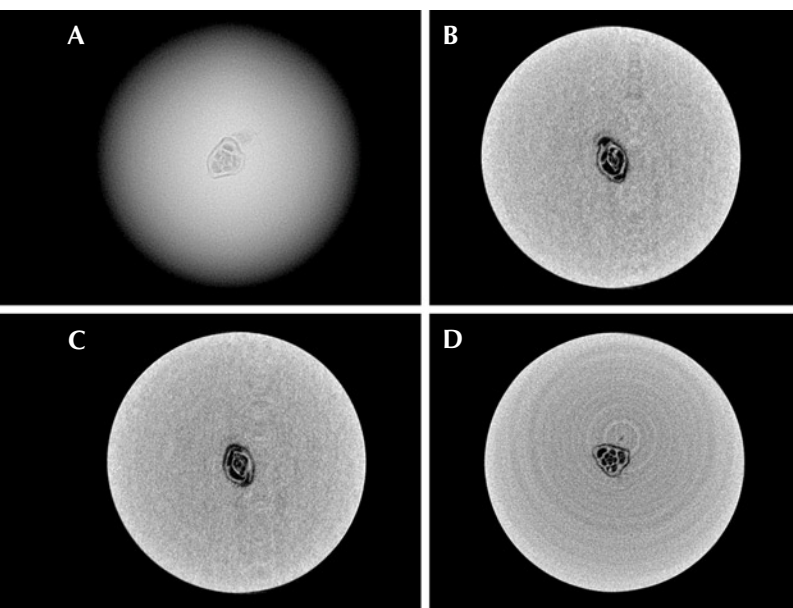


Figure 68. The foraminifera test, measuring approximately  $0.45 \times 0.35$  mm, observed in pearl B. A: RTX image of the foraminifera test. B–D:  $\mu$ -CT scans of the foraminifera test in the X, Y, and Z directions, respectively. (Again, the weak white rings on the lower right image are artifacts.)

made it easier to see the external morphology of the shell within the pearl (figure 69). The foraminifera test appeared

multilocular, or multichambered, with tubular chambers arranged around a growth axis to form a beautiful milioline arrangement of chambers (A.R. Loeblich and H. Tappan, *Foraminiferal Genera and Their Classification*, Springer, New York, 1988). The minute size of the shells within these tiny pearls is a good indicator of their natural origin.

Energy-dispersive X-ray fluorescence spectrometry on pearls A and B revealed low manganese levels of 39.0 ppm and 17.8 ppm and high strontium levels of 1768 ppm and 1497 ppm, respectively, which is characteristic of formation in a saltwater environment. Raman analysis was also carried out using 514 nm laser excitation on the surface of each pearl. A doublet at  $702$  and  $705\text{ cm}^{-1}$  as well as a peak at  $1085\text{ cm}^{-1}$  indicative of aragonite were observed, along with minor polyenic pigment peaks at  $1130$  and  $1530\text{ cm}^{-1}$ . Photoluminescence (PL) spectra were also collected on both pearls. Pearl A revealed three broad peaks at 620, 650, and 680 nm, characteristic of many naturally colored pearls, while pearl B showed clear aragonite peaks and low fluorescence. An ultraviolet/visible reflectance spectrum was collected only for pearl B within the 220–850 nm range, as pearl A's size prevented the detector from obtaining a clear result. Faint features at 420 and 495 nm were, like the PL results, consistent with natural coloration. Similar spectral observations have previously been documented in natural *Pinctada radiata* pearls (A. Al-Alawi et al., "Saltwater cultured pearls from *Pinctada radiata* in Abu Dhabi (United Arab Emirates)," *Journal of Gemmology*, Vol. 37, No. 2, 2020, pp. 164–179).

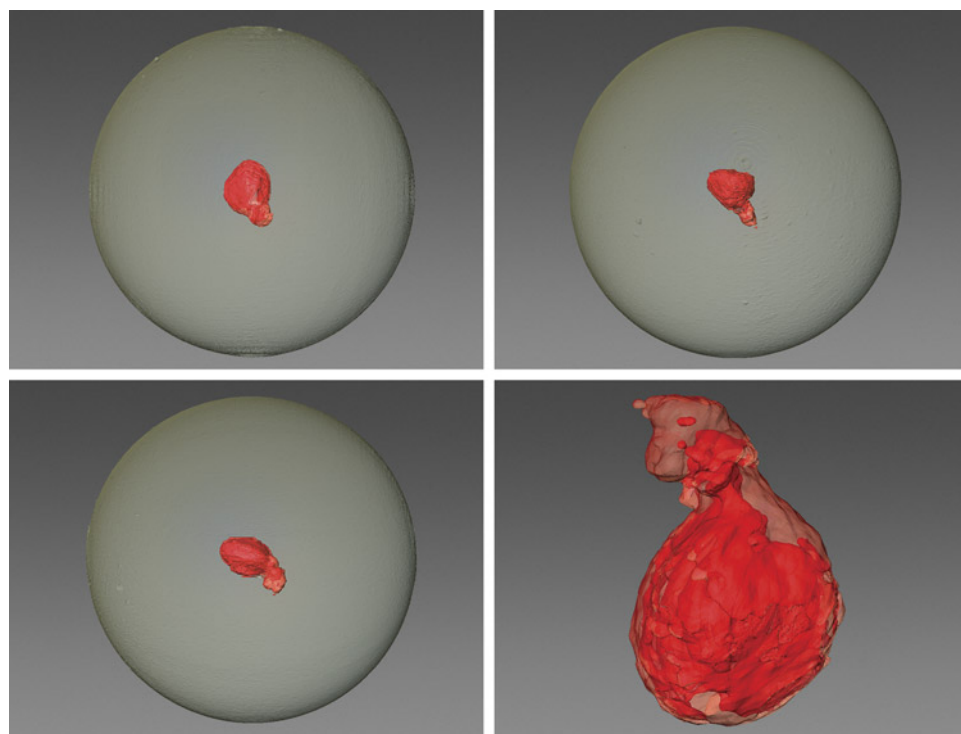


Figure 69. 3D images constructed from  $\mu$ -CT scans of pearl B illustrate the morphology of the foraminifera test. Images by Emiko Yazawa.

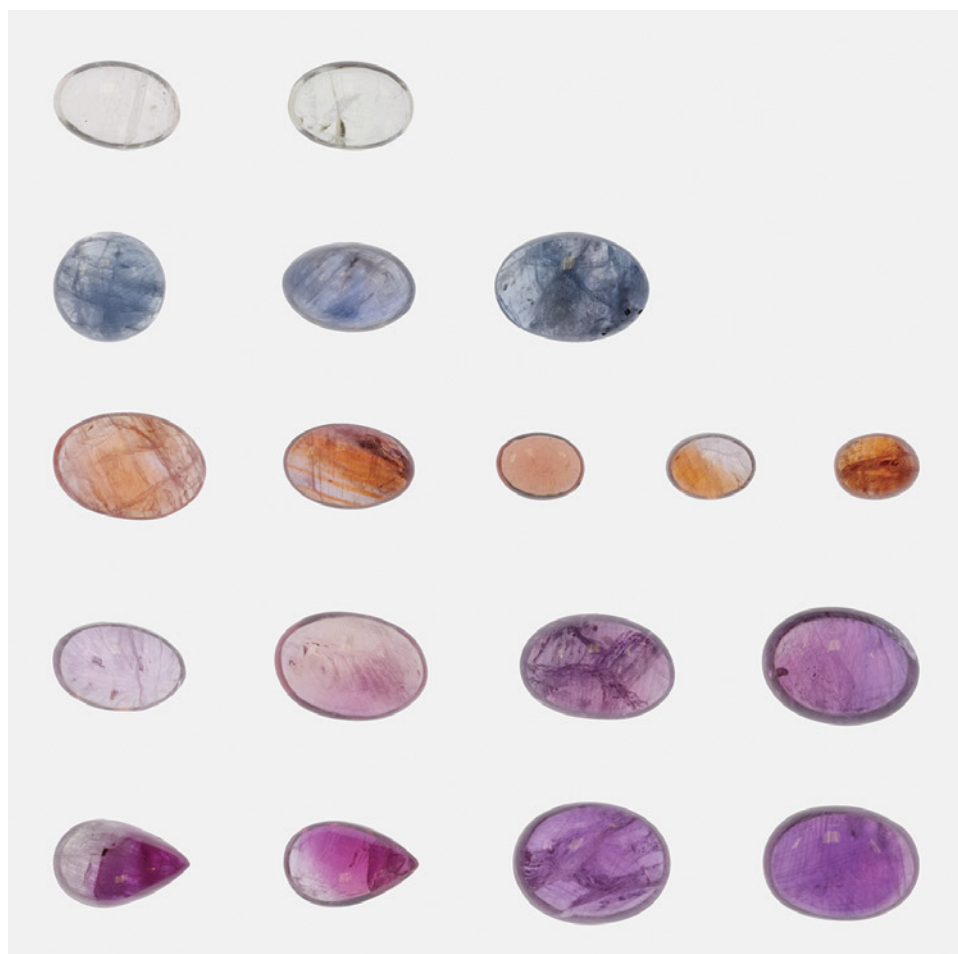


Figure 70. Part of the suite of sapphires studied for this project (weighing 0.23–1.41 ct). Photo by Sasithorn Engniwat; courtesy of Greenland Ruby.

The gemological examination of these *Pinctada radiata* pearls proved very rewarding, especially with regard to their internal structures. Research into what causes the formation of a pearl in the wild is ongoing. Hence, finding these minute shells that may be the initiation of growth in these two natural pearls is a truly rare circumstance.

Nishka Vaz  
GIA, Mumbai  
Nicholas Sturman  
Bangkok  
Abeer Al-Alawi  
GIA, Global

**Color study of fancy sapphire from Greenland.** Over the past 70 years, several ruby and pink sapphire localities have been documented in the region of Greenland's capital city, Nuuk (P.W.U. Appel and M. Ghisler, "Ruby- and saphirine-bearing mineral occurrences in the Fiskenaeset, Nuuk and Maniitsoq regions, West Greenland," GEUS, Geological Survey of Denmark and Greenland, 2014). Several of these localities are currently exploited on a small scale by the local communities. In 2017, Greenland Ruby A/S started a large-scale mining operation at the Aappalut-

toq ruby and pink sapphire deposit, located 160 km south of Nuuk.

The corundum extracted at Aappaluttoq is heated in air at temperatures over 1500°C for several hours, with some flux added. In rare cases, the heating significantly alters the color of light pink and near-colorless sapphire, resulting in fancy-color sapphire. GIA recently studied a parcel of 22 of these fancy-color sapphires mined and treated by Greenland Ruby (figure 70).

A combination of ultraviolet/visible/near-infrared (UV-Vis-NIR) spectra and trace element chemistry using laser ablation–inductively coupled plasma–mass spectrometry (LA-ICP-MS) were collected at GIA in Bangkok to identify the causes of color. For full quantification of the chromophores, it is necessary to do this analysis in oriented, clean samples with a known path length. Since most of the Greenland material is polished as cabochons and contains some inclusions, it is very challenging to calculate or even estimate the absorption coefficients. We limited ourselves to a rough interpretation of the chromophores based on the shape of the spectra. Orientation of the samples was estimated based on the pleochroism.

Additionally, we could not precisely identify which area of the stone was analyzed during the spectroscopy, and



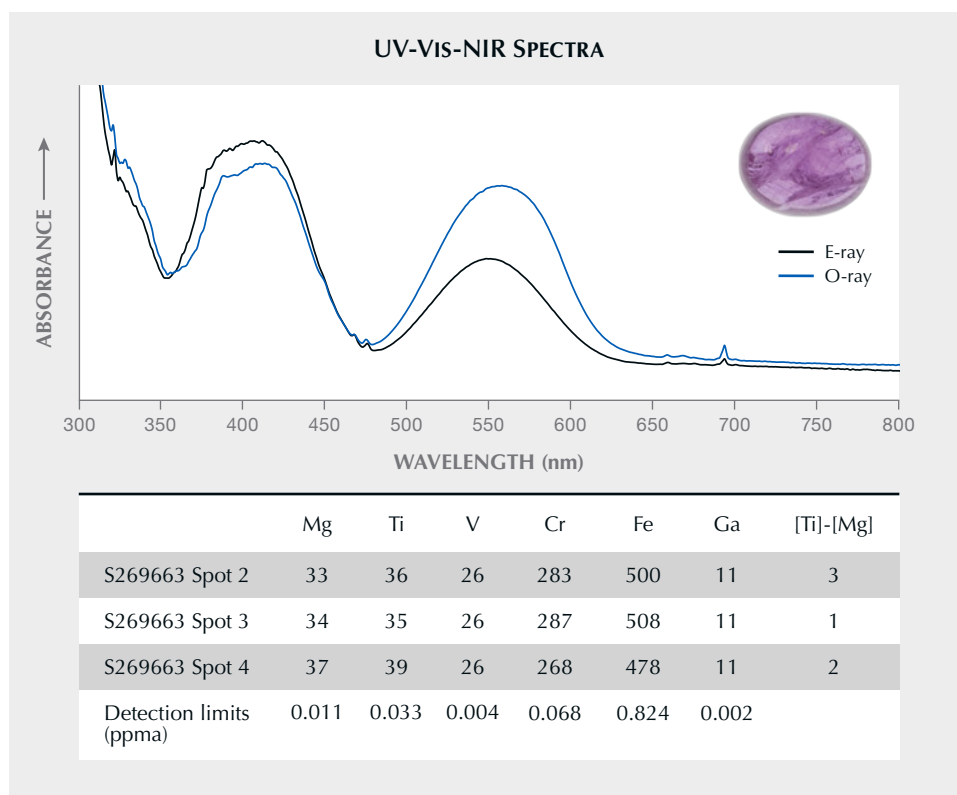


Figure 71. A UV-Vis-NIR spectrum dominated by  $\text{Cr}^{3+}$  features often results in a pink to red stone, depending on the concentration of  $\text{Cr}^{3+}$  (in ppma). When the sample is oriented down the c-axis, the color often trends toward reddish purple (i.e., fancy sapphire).

thus all UV-Vis spectra were bulk measurements and combined the color of different zones. In contrast, the LA-ICP-MS analysis was performed at very specific spots, allowing the analysis of specific zones.

The literature describes six chromophores responsible for color in natural corundum (E.V. Dubinsky et al., “A quantitative description of the causes of color in corundum,” Spring 2020 *G&G*, pp. 2–28). Four of the chromophores from that study are responsible for the colors in this suite.

Most stones from the Aappaluttoq deposit are colored by the  $\text{Cr}^{3+}$  chromophore, giving them their typical pink to red color (figure 71). The intensity of the color is directly linked to the concentration of  $\text{Cr}^{3+}$ , which can go up to several 1000 ppma, and in exceptional cases even to 15,000 ppma. Most of the lighter-colored material has a concentration of a few 100 ppma, resulting in a pink color.

Depending on the orientation, it can appear more purple (when viewed through the c-axis). In some cases, this is so strong that the face-up color of the stone is modified to an extent that it cannot be defined as ruby or pink sapphire and falls into the fancy reddish purple range. Some of the stones develop a more orangy tone after treatment. (A bright orange oval brilliant seen at the 2023 Tucson shows is highlighted on pp. 115–116 of this issue.) This color can be attributed to the creation of trapped holes in combination with  $\text{Cr}^{3+}$  (figure 72).

To create trapped holes, the chemical balance in the stone needs to be correct. Only when a stone is acceptor dominated will trapped holes be present. In the case of

Greenland ruby, this comes down to the balance between  $\text{Mg}^{2+}$  vs.  $\text{Ti}^{4+}$ ,  $\text{Si}^{4+}$ , and  $\text{H}^+$ . Since the stones have all been treated in air (oxidizing atmosphere), we can assume that  $\text{H}^+$  has diffused out of them. With the method used to measure trace elements (LA-ICP-MS with a quadrupole MS), we cannot correctly quantify the  $\text{Si}^{4+}$  content in these stones. The possibility that  $\text{Si}^{4+}$  plays a role in the color cannot be excluded. Regardless, there is no indication here that  $\text{Si}^{4+}$  is required to tilt the balance of chromophores when comparing trace elements vs. observed color. Since we do not aim to quantitatively analyze the color, we ignore any potential presence of  $\text{Si}^{4+}$ . This means that the concentrations of  $\text{Mg}^{2+}$  and  $\text{Ti}^{4+}$  are the determining factors: Only if the amount of  $\text{Mg}^{2+}$  is larger than the  $\text{Ti}^{4+}$  concentration can trapped holes develop in sapphire from Greenland.

Two ions in sapphire can pair with trapped holes:  $\text{Fe}^{3+}$  and  $\text{Cr}^{3+}$ . Since the trapped hole preferentially pairs with  $\text{Cr}^{3+}$ , this is the chromophore observed in these stones. The quantity of trapped holes that can form in corundum is very low, and as such, not all the  $\text{Cr}^{3+}$  couples with a trapped hole. The final color will be a combination of the trapped hole color and the pure  $\text{Cr}^{3+}$  chromophore, resulting in a combination of pink to red and orange colors. Trapped holes are very strong coloring agents that can have a major impact even when their concentration is very low.

The  $\text{Fe}^{3+}$  chromophore is the weakest one encountered in natural corundum. Very high concentrations of  $\text{Fe}^{3+}$  are required to create a yellow color, often exceeding several thousand ppma. Since the Greenland rubies have a maximum iron concentration under 1500 ppma, this chro-

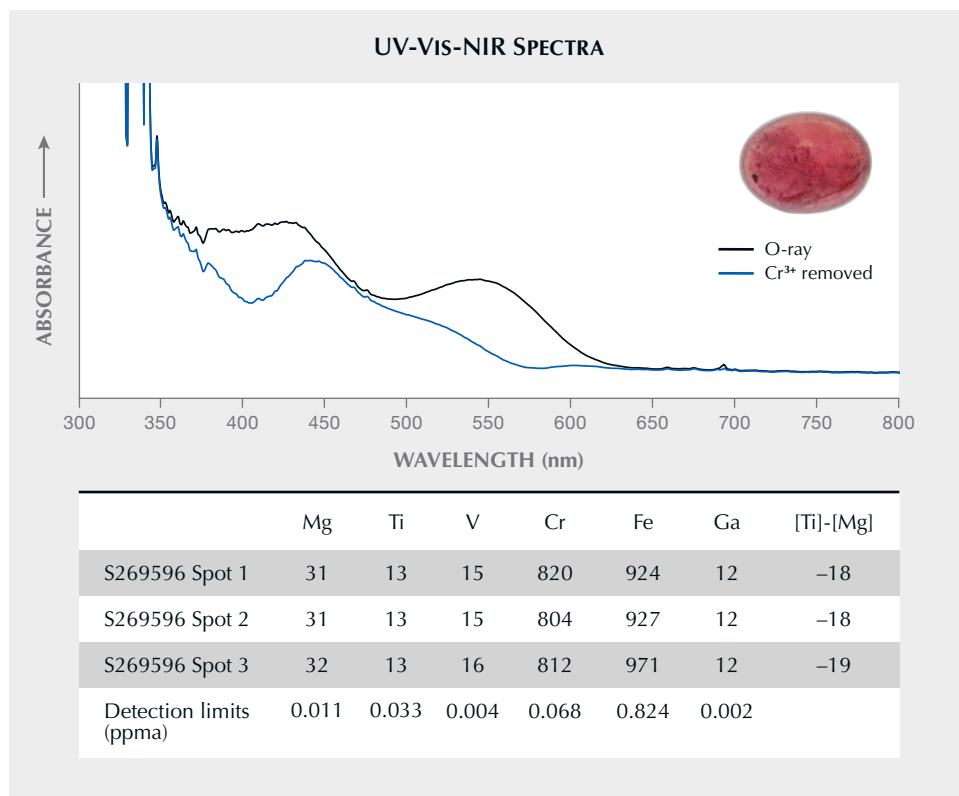


Figure 72. The peaks at 550 and 430 nm in the o-ray spectrum (black) suggest the presence of  $\text{Cr}^{3+}$ , causing pink to red in the stone. The trace element analysis (in ppma) shows a clear excess of  $\text{Mg}^{2+}$  compared to the Ti concentration, highlighting that trapped hole creation is very likely. When we remove the absorbance spectrum of  $\text{Cr}^{3+}$  from the stone's absorption spectrum (blue), it is obvious that the combination of  $\text{Cr}^{3+}$  with the trapped hole is the cause of the remaining color and the strong orange tint observed in the stone.

mophore creates only a very weak yellow color (figure 73). Other common chromophores are much stronger and more

common, which makes it very difficult to notice any color contribution by  $\text{Fe}^{3+}$ . Only when the  $\text{Cr}^{3+}$  concentration is

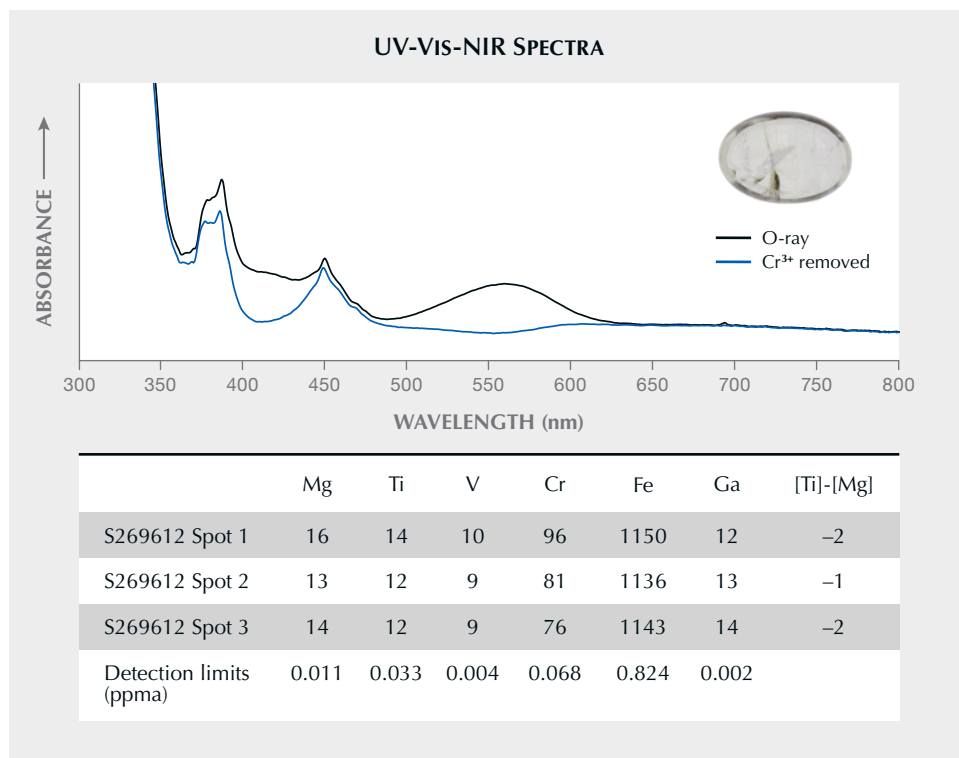


Figure 73. This plot shows the o-ray spectrum of a pale yellow sample (black) and a modified o-ray spectrum where some contribution by  $\text{Cr}^{3+}$  is subtracted (blue). When the  $\text{Cr}^{3+}$  spectrum is removed, a pure  $\text{Fe}^{3+}$  spectrum remains. This spectrum is characterized by the double peak at 377–388 nm and one at 450 nm. The ratio of the 388 to 377 nm band suggests a relatively low  $\text{Fe}^{3+}$  chromophore concentration, which matches the observed color and analyzed chemistry (in ppma).

extremely low can we detect the pale yellow color from the  $\text{Fe}^{3+}$  chromophore.

The  $\text{Fe}^{2+}\text{-Ti}^{4+}$  chromophore creates a blue color in corundum and is relatively strong (figure 74). When observed in ruby from Greenland, its effect is usually limited to a slightly increased purplish hue in the chromium-rich corundum, occasionally modifying the color to a dominant purple hue. Only when the  $\text{Cr}^{3+}$  concentrations are extremely low is there a chance for the corundum to have a blue color. We still observe some cloudiness after the treatment in the blue zones.

We assume that this type of rough corundum had a milky appearance caused by a high concentration of fine rutile particles before treatment. During treatment at temperatures over  $1200^{\circ}\text{C}$ , some of the particles dissolved into the lattice, becoming available to pair with  $\text{Fe}^{2+}$  that was already present and creating a blue bodycolor. Due to the large amounts of  $\text{Ti}^{4+}$  that diffused into the crystal lattice, the iron was forced to remain in a reduced state ( $\text{Fe}^{2+}$ ).

The nature of the treated corundum from Greenland makes high-quality spectroscopy a challenge. Nevertheless, we were able to isolate and identify the chromophores responsible for the fancy colors observed in these sapphires.

It is important to note that many of these fancy colors developed as a result of heat treatment. The trapped hole-related chromophores only become visible after  $\text{H}^{+}$  diffused out of the stone under oxidizing conditions. These same conditions also allow the iron to oxidize and create the pale yellow color by  $\text{Fe}^{3+}$  chromophores. The high temperatures were also required to dissolve rutile particles into the corundum lattice and form Fe-Ti pairs.

While these fancy-color stones remain a curiosity, they make for a welcome addition from a mine that is known for its ruby and pink sapphires.

Wim Vertriest, Charuwan Khawpong,  
and Polthep Sakpanish  
GIA, Bangkok

Martin Viala  
Greenland Ruby

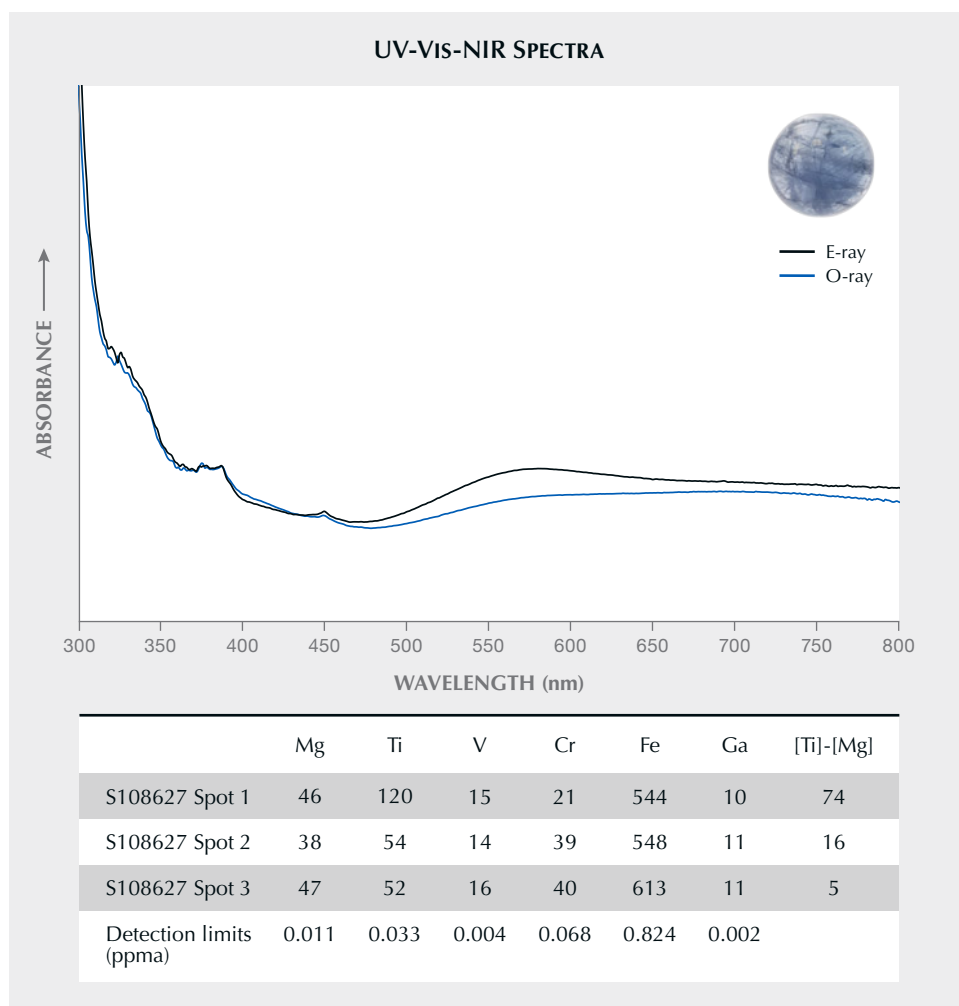


Figure 74. The extremely low  $\text{Cr}^{3+}$  contents allow other features to be dominant. In this case,  $\text{Fe}^{2+}\text{-Ti}^{4+}$  charge transfers with a large peak at 580–620 nm are responsible for a blue color. The absorption spectrum of the stone also shows some features related to  $\text{Fe}^{3+}$ , which is a very weak chromophore and does not influence the color.





Figure 75. A handful of gem gravel collected from the Lofa River in Weasua, Liberia, showing the high concentration of ruby material. Photo courtesy of Diamonds for Peace.

**Liberian ruby.** A gemological education can often prove useful in the most unusual of circumstances. On a recent trip to rural Liberia with the Japan-based NGO Diamonds for Peace (DfP), the author discovered a previously unacknowledged source of ruby. The original purpose of the visit was to deliver a rough diamond grading and valuation workshop to the miners working and living in 17 communities across Liberia. During the trip, the author stayed in the town of Weasua, one of the larger mining communities, to experience the standard of living and the general working conditions of the miners. The poverty is extreme. Most homes are without electricity, facilities, or running water, and only three functional water pumps exist for a population of 5,000, all of which place the health and the well-being of this community at risk. DfP has been working with this community since 2018 and has made significant inroads in supporting and improving the lives of these miners, but there is a long way to go, and strategies to aid their mission are continually being developed.

It was therefore fortuitous that during the visit, the author learned that there were other promising gem-quality minerals in the alluvial gravels the miners were collecting in their pursuit of diamond (figure 75). Upon initial inspection while on-site, the author noted material resembling corundum (primarily ruby), garnet, topaz, rock crystal

quartz, and possible spinel. Samples were purchased from the miners for analysis, which came as a welcome surprise since they were unaware that these colored stones could carry any value (figure 76, left).

The author subsequently analyzed all the samples at the Gemmological Certification Services (GCS) laboratory in London. Using advanced and standard gemological testing, the identity of all the presumed gem-quality minerals of the collected specimens was confirmed. Particular focus was placed on the rubies due to their apparent abundance at the mine site, with the hope of providing another means of income for this community.

All ten samples tested were identified as corundum. Due to the nature of the rough material, standard testing was limited, beyond measuring specific gravity—which, averaging 4.0 across all samples, supported corundum. The ultraviolet/visible/infrared absorption spectrum, with its chromium-associated features, was also consistent with ruby. X-ray fluorescence analysis of the trace element chemistry revealed 1029–2377 ppm iron and 721–2915 ppm chromium, with low levels of gallium (54 ppm) and vanadium (53 ppm).

Generally, the color of the alluvial material collected ranged from pinkish gray to a deep purplish red, with sizes varying from 6 to 14 mm (1.45–15.90 ct), although the au-





Figure 76. Left: One of the Liberian diamond miners displays some of the rubies she found while digging. Right: A ring mounted with a Liberian ruby. Photos by Diamonds for Peace (left) and Alex Herbert (right).

thor was shown larger pieces on-site. All of the material showed a moderate to weak red fluorescence response in long-wave UV and inert to weak red in short-wave UV, consistent with high-iron ruby due to the quenching of  $\text{Cr}^{3+}$ -associated fluorescence by iron. The majority of the samples showed lamellar twinning, surface-reaching fractures, and iron staining. The material was translucent to opaque, meaning that clear observation of any other inclusions was limited.

Although the material is not considered high-quality ruby, some of the better pieces have been polished to create attractive cabochons (figure 76, right). Diamonds for Peace is currently developing a business plan to monetize this material for the benefit of the community. The GCS laboratory will continue to support Diamonds for Peace as that organization explores this new potential avenue of income for the miners of Weasua.

*Beth West*  
*Gemmological Certification Services, London*

**Forsterite in a purple Tanzanian spinel.** Purple/violet spinel from Tanzania is popular in the gem market today. Recently, author JW encountered an oval-shaped purple

gemstone reportedly from Tanzania (figure 77). Its refractive index of 1.714 and hydrostatic specific gravity of 3.59

Figure 77. This faceted purple spinel, weighing 0.51 ct and measuring  $5.20 \times 4.17 \times 3.10$  mm, was reportedly from Tanzania. Photo by Jinlin Wu.



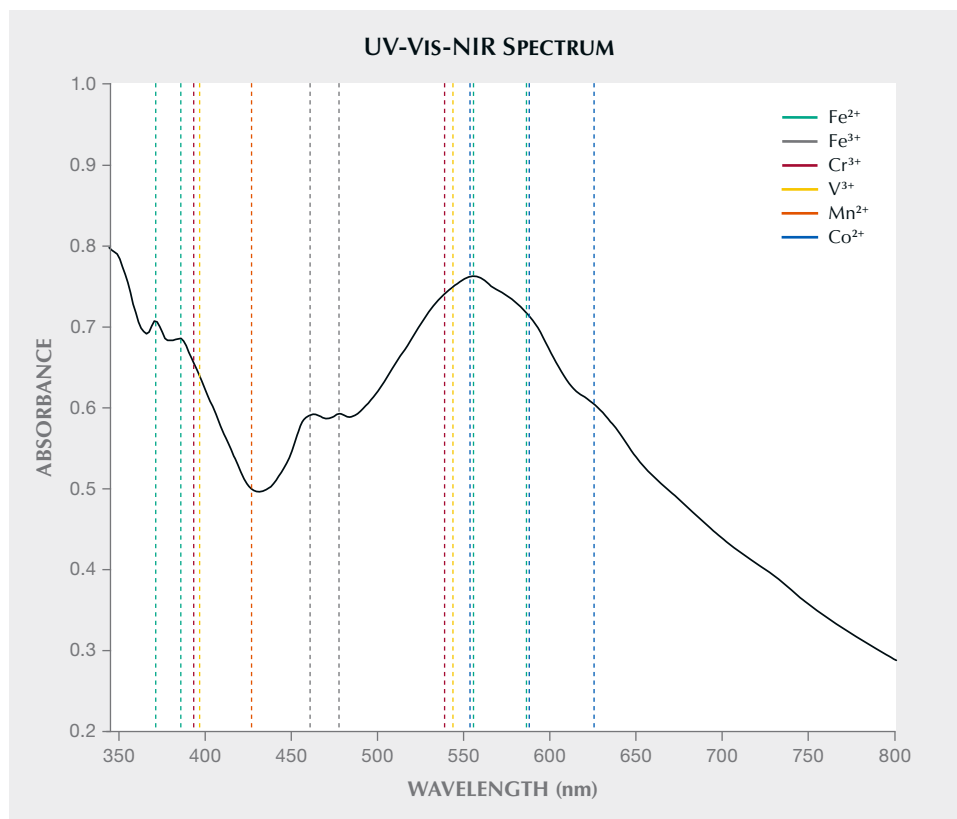


Figure 78. The UV-Vis-NIR spectrum of the spinel sample shows absorption peaks mainly related to  $\text{Fe}^{2+}$  and  $\text{Fe}^{3+}$ .

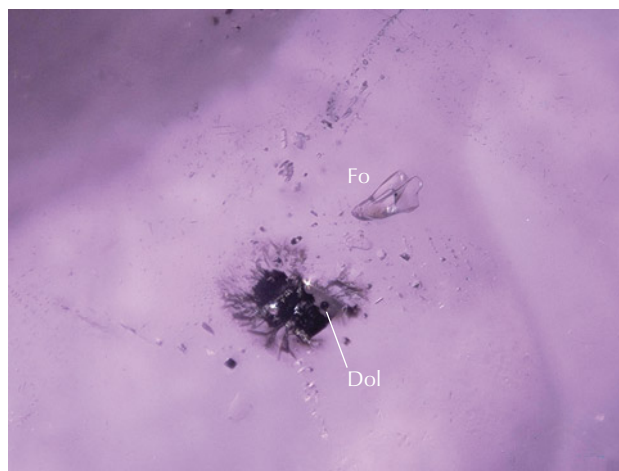
indicated spinel. Its ultraviolet/visible/near-infrared (UV-Vis-NIR) absorption spectrum was characterized by a series of absorption bands centered at 555 nm and several iron-related small bands centered at around 371, 385, 461, and 478 nm, as well as an extremely weak band at ~625 nm for  $\text{Co}^{2+}$  (figure 78). This absorption profile revealed that iron ( $\text{Fe}^{2+}$  and  $\text{Fe}^{3+}$ ) was the main coloring element (P.M. Belley and A.C. Palke, "Purple gem spinel from Vietnam and Afghanistan: Comparison of trace element chemistry, cause of color, and inclusions," Fall 2021 *G&G*, pp. 228–238).

Energy-dispersive X-ray fluorescence analysis was performed to determine the sample's trace element concentration, which showed 10950 ppmw iron, 963 ppmw zinc, 52 ppmw chromium, 94 ppmw vanadium, and 9 ppmw cobalt. These results were similar to the chemical features of representative purple Tanzanian spinel: extremely high iron content, medium zinc content, and low chromium and vanadium contents (G. Giuliani et al., "Pink and red spinels in marble: Trace elements, oxygen isotopes, and sources," *Canadian Mineralogist*, Vol. 55, No. 4, 2017, pp. 743–761).

Microscopic observation revealed a colorless subhedral mineral, a dolomite with an unknown dark material attached (figure 79), and oriented short needles (figure 80). Raman spectroscopy identified the colorless mineral as forsterite. According to the RRUFF database (B. Lafuente et al., <https://rruff.info/about/downloads/HMC1-30.pdf>), peaks at 822, 855, 918, and 963  $\text{cm}^{-1}$  were consistent with the main peaks of forsterite (figure 81).

As a rock-forming mineral, forsterite ( $\text{Mg}_2\text{SiO}_4$ ) itself is common, especially in marble-hosted spinel. However, it is rarely observed in Tanzanian spinel and has been reported only once to our knowledge (E. Gübelin and J.I. Koivula, *Photoatlas of Inclusions in Gemstones*, Vol. 2, Opinio Publishers, Basel, Switzerland, 2005, 829 pp.).

Figure 79. A colorless subhedral forsterite (Fo) inclusion and a dolomite (Dol) inclusion with an unknown dark material attached. Photomicrograph by Jinlin Wu; field of view 0.66 mm.





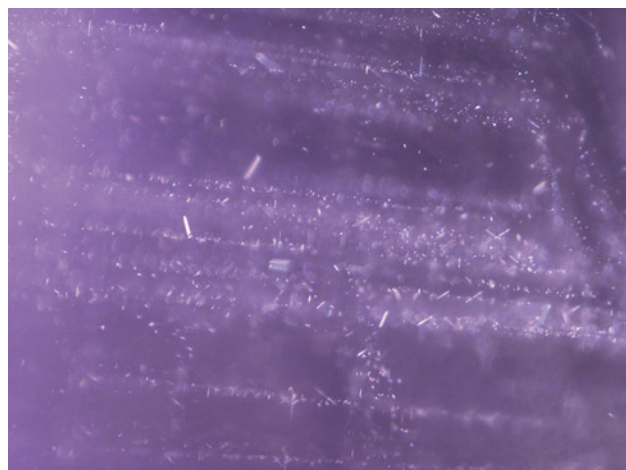


Figure 80. Oriented short needles in the spinel. Photomicrograph by Jinlin Wu; field of view 1.10 mm.

In Tanzania, the primary deposits of spinel occur in marbles and calc-silicate rocks that belong to the Neoproterozoic metamorphic Mozambique Belt (G. Giuliani et al., "Les gisements de rubis et de spinelle rouge de la Ceinture Métamorphique Néoprotérozoïque Mozambicaine," *Revue de Gemmologie*, Vol. 192, 2015, pp. 11–18).

Under high-temperature conditions, spinel and forsterite are both stable mineral phases in marbles (Giuliani et al., 2017). Spinel is found in marble or impure marble associated with calcite, dolomite, forsterite, clinohumite, and phlogopite in deposits in Myanmar and Vietnam. Thus, forsterite is commonly seen as an inclusion in spinel from these sources (G. Giuliani et al., "Pink and red gem spinels in marble and placers," *InColor*, No. 43, 2019, pp. 14–28).

It was noteworthy to see forsterite in the Tanzanian sample. This finding could indicate a similar formation environment between spinel in Tanzanian deposits and those in Myanmar and Vietnam.

Jinlin Wu (wujl@ngtc.com.cn), Hong Ma,  
and Huihuang Li  
National Gemstone Testing Center Shenzhen Lab  
Shenzhen, China

## DIAMONDS

**Grayish blue CVD diamond colored by GR1 and SiV<sup>-</sup>.** Silicon is a common impurity in chemical vapor deposition (CVD) laboratory-grown diamond. The silicon-related SiV<sup>-</sup> center, which has zero-phonon lines at 736.6 and 736.9 nm

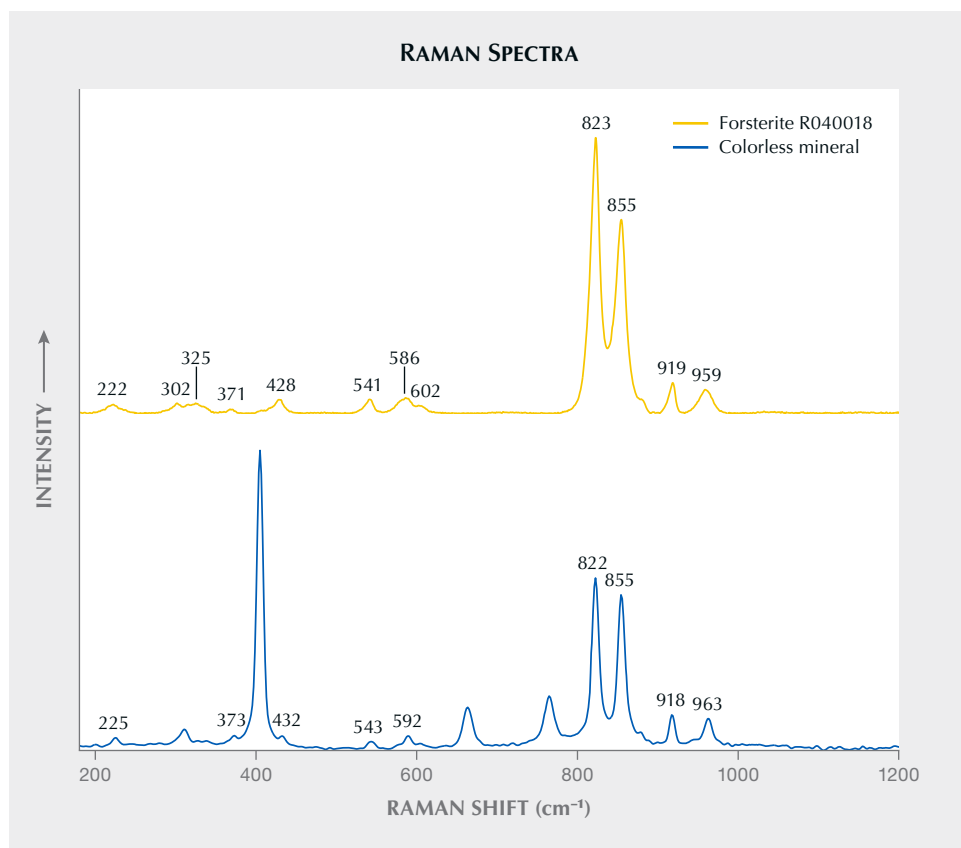


Figure 81. Comparison of Raman spectra of the colorless mineral and forsterite in the RRUFF database. Peaks in the inclusion spectrum at 312, 405, 664, and 766  $\text{cm}^{-1}$  are from the host spinel. Spectra are offset vertically for clarity.

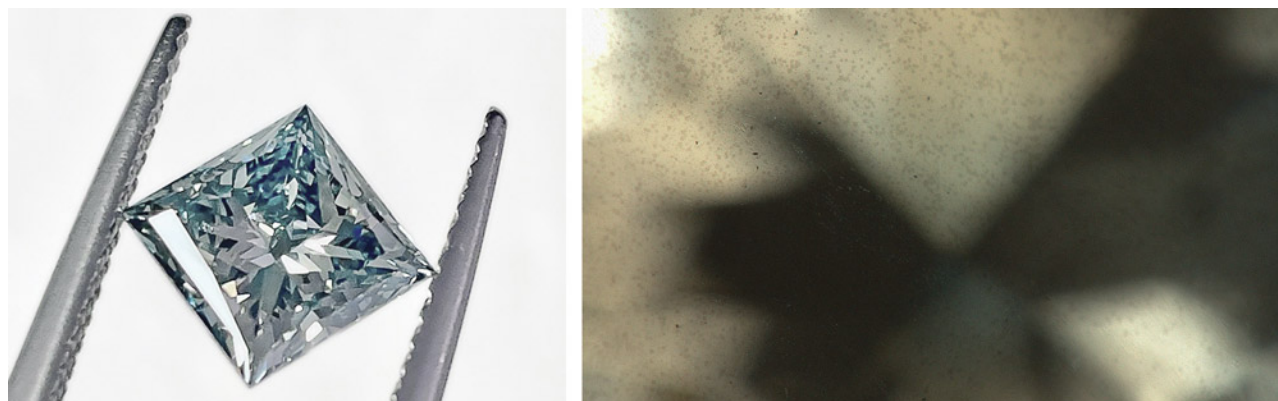


Figure 82. Left: This 1.63 ct grayish blue diamond was identified as a CVD synthetic, with its color caused by both the GR1 and SiV<sup>-</sup> centers. Photo by Xiaoyu Zhang. Right: Dark cloud-like non-diamond carbon inclusions. Photomicrograph by Meng Li; field of view 0.25 mm.

and is active in absorption and luminescence, is widely considered an identifying feature of CVD diamond. Generally, the SiV<sup>-</sup> center is detected by photoluminescence spectroscopy and is not observed using absorption spectroscopy for most CVD synthetics due to the low silicon content. The absorption spectra may reveal the presence of the SiV<sup>-</sup> center in the case of a relatively high silicon content, but rarely in amounts significant enough to affect the color. When the silicon content becomes particularly high, the absorption of SiV<sup>-</sup> is in sufficient concentration to influence the bodycolor of a diamond. It has been reported that the color of silicon-doped blue CVD diamonds produced by the PDC Company is attributed to strong absorption of the rather intense SiV<sup>-</sup> center (A. Peretti et al., "New generation of synthetic diamonds reaches the market (Part A): Identification of CVD-grown blue diamonds," *Contributions to Gemology*, No. 14, 2013, pp. 3–20).

National Gemstone Testing Center's (NGTC) Beijing laboratory recently received a 1.63 ct grayish blue princess cut (figure 82, left) for identification. Standard testing identified it as a CVD synthetic diamond. The sample showed an even color distribution. Microscopic investigation revealed abundant non-diamond carbon inclusions in the form of both crystals and clouds, with the clouds distributed along the growth layer (figure 82, right). The visible/near-infrared (Vis-NIR) spectrum (figure 83), recorded at liquid nitrogen temperature, included a strong broad SiV<sup>-</sup> center defect at 737 nm next to an equally strong GR1 center. The diamond's grayish blue bodycolor was attributed to both the strong GR1 center and the high intensity of the SiV<sup>-</sup> center, which produced preferential absorption in the red part of the spectrum. In addition, weak absorptions at 830, 856, and 946 nm (the SiV<sup>0</sup> center) were observed, which were also reported in CVD synthetic

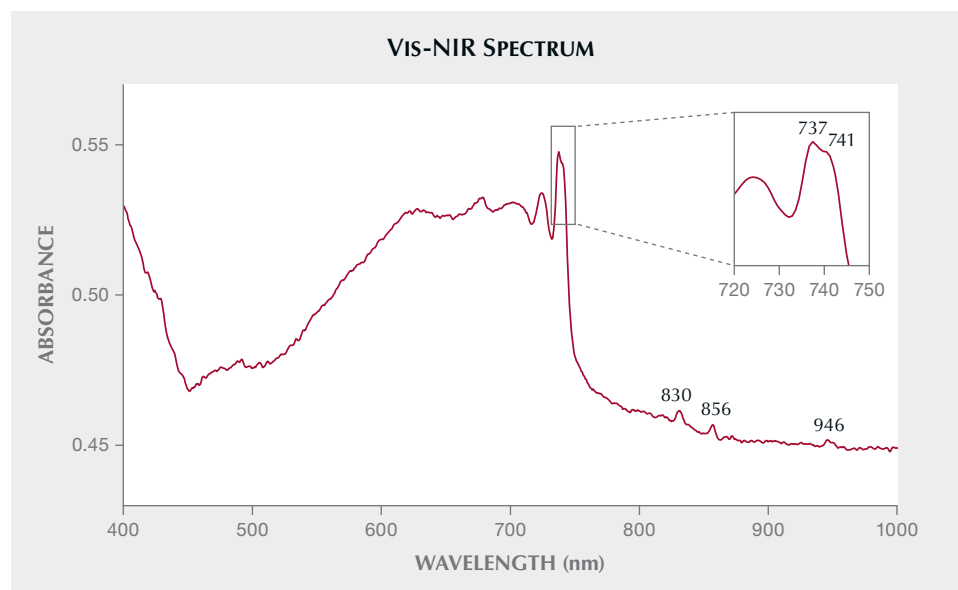


Figure 83. In the Vis-NIR region, in addition to very strong absorptions at 737 nm (SiV<sup>-</sup>) and 741 nm (GR1), weak absorptions at 830, 856, and 946 nm (SiV<sup>0</sup>) were observed.

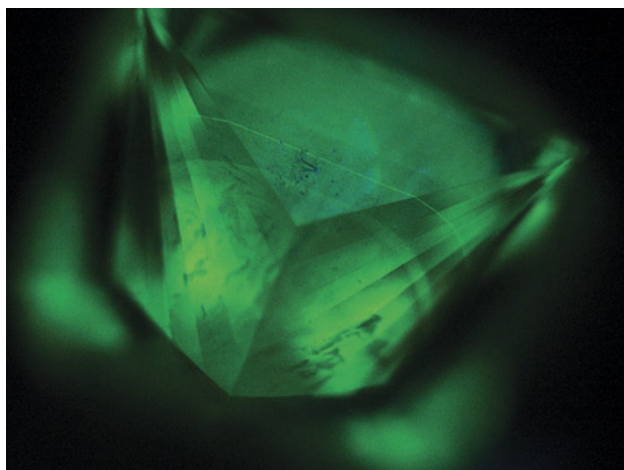


Figure 84. DiamondView imaging showed green fluorescence with blue dislocations. The diamond also revealed a layered growth structure, indicating a start-stop cycling growth process typical of CVD diamond, as CVD diamond growth takes place layer by layer on the top surface of the growing crystal. Image by Xiaoyu Zhang.

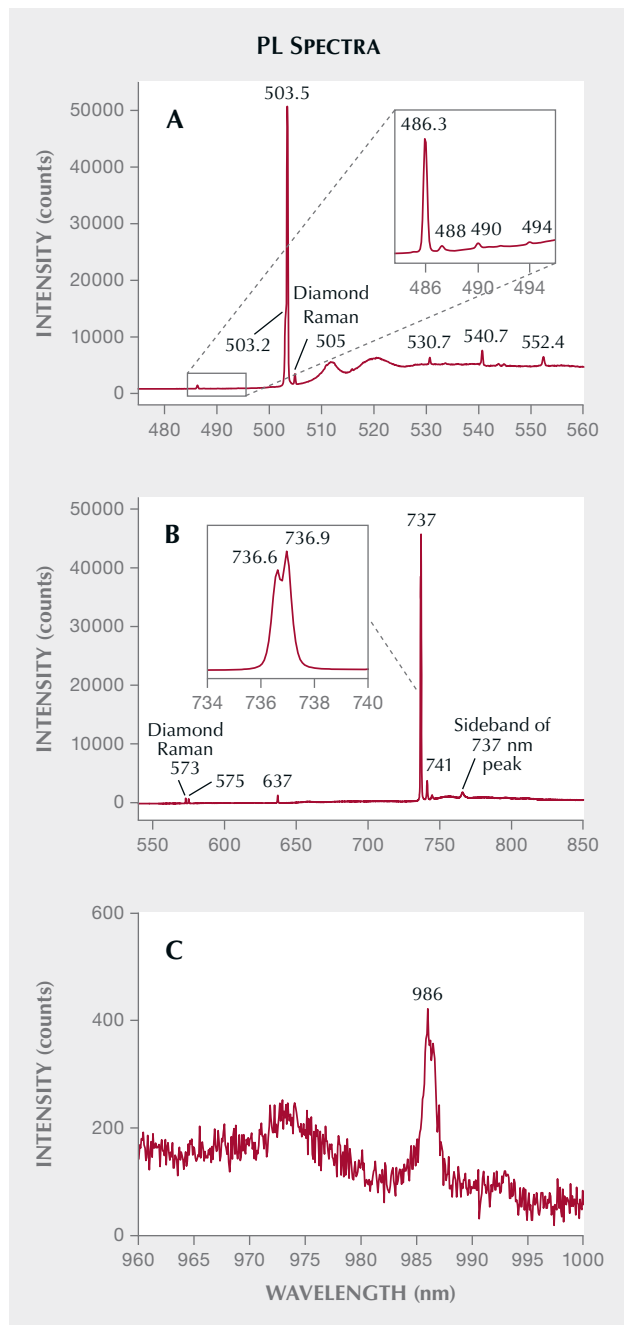
diamonds with high silicon content (Peretti et al., 2013; Z. Song et al., "Silicon-doped CVD synthetic diamond with photochromic effect," *Journal of Gems and Gemmology*, Vol. 18, No. 1, 2016, pp. 1–5).

Infrared spectroscopy showed features typical for type IIa diamond (i.e., no defect-related absorptions were detected). The diamond was inert to short-wave and long-wave ultraviolet illumination. Under the ultra-short-wave UV radiation of the DiamondView, the sample fluoresced green, with minor areas showing some blue dislocations. It also showed subtle growth striations and two parallel planes fluorescing stronger than the bulk of the crystal (figure 84). The sample did not phosphoresce. Photoluminescence (PL) spectra taken with various laser excitation wavelengths and at liquid nitrogen temperature (figure 85) showed the presence of radiation-related features including very strong 3H at 503.5 nm, strong GR1 at 741 nm, and weak 486.3 nm. The PL spectra also indicated strong nitrogen-vacancy centers at 575 NV<sup>0</sup> and 637 NV<sup>-</sup> nm and multi-nitrogen defects such as H3 and H2, combined with the absence of the unassigned 596/597 nm doublet that is normally seen in as-grown CVD syn-

Figure 85. The PL spectrum of the grayish blue CVD synthetic diamond obtained with 473 nm excitation (A) showed that the H3 center (503.2 nm) and radiation-related features included very strong 3H at 503.5 nm and weak 486.3 nm. B: 532 nm excitation revealed the NV centers and silicon-vacancy center that are typically observed in CVD-grown diamonds, along with strong GR1. C: 785 nm excitation showed the H2 center at 986 nm.

thetics, suggesting that it had undergone post-growth high-temperature annealing before irradiation.

The PL spectrum with 532 nm laser excitation also exhibited a rather large silicon doublet peak at 736.6/736.9 nm that dwarfs all other PL peaks, including the GR1 in the spectrum. The intensity ratio between the 736.6/736.9 nm PL peak and the diamond Raman peak was about 52. The PL spectrum reaffirmed that the 737 nm absorption peak of the ultraviolet/visible spectrum was the SiV<sup>-</sup> defect, and the





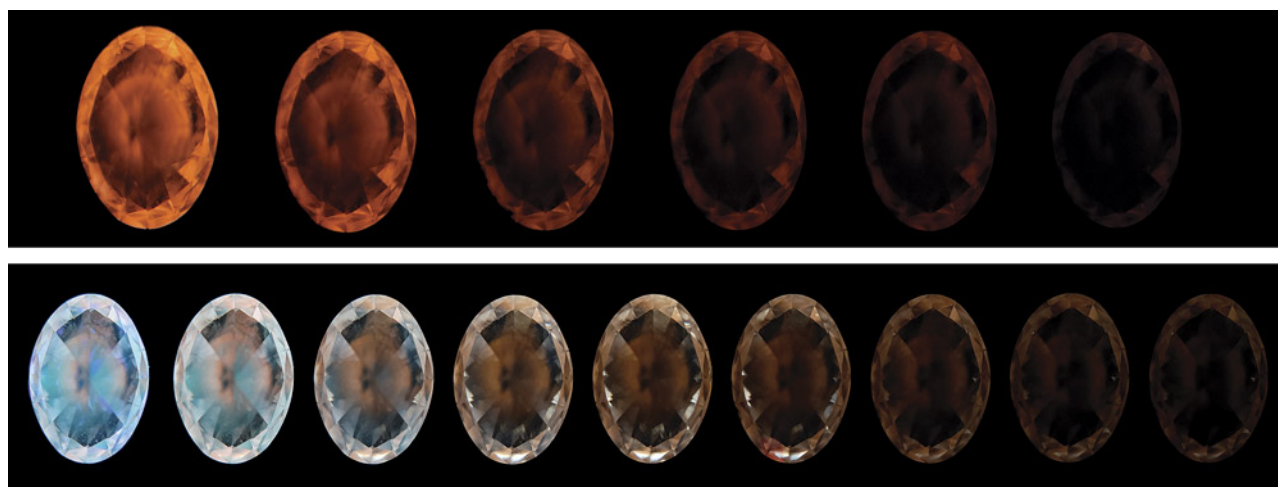


Figure 86. Top: A series of images showing the gradual change (left to right) in the phosphorescence of the 0.71 ct HPHT-grown colorless diamond after removing it from the LWUV source (left image) in increments of 30 seconds for 150 seconds (right image). Bottom: The gradual change in phosphorescence after exposure to a SWUV source (left image) in increments of 30 seconds. The greenish blue and orange emissions decay differently, with the blue fading faster (~90 seconds, fourth image from left) than the orange (~240 seconds, right image). Images by Guy Borenstein.

silicon content of this diamond was so high that it produced strong absorption in the red range of visible light and affected the color of the diamond together with the GR1 center.

Wang Yang (wangyang@ngtc.com.cn), Xiaoyu Zhang, and Zhonghua Song  
NGTC, Guangzhou and Beijing

**HPHT-grown colorless diamond displaying unusual phosphorescence effects.** Phosphorescence longer than 10 seconds in reaction to ultraviolet radiation is regularly observed in colorless and blue-colored diamonds grown by a high-pressure, high-temperature (HPHT) technique. The gemological laboratory of Stuller Inc. recently tested an HPHT-grown colorless (approximately E color grade with a blue-gray overtone) oval brilliant diamond weighing 0.71 ct that showed unusual fluorescence and phosphorescence reactions.

When exposed to a long-wave ultraviolet (LWUV, 365 nm) source for 60 seconds using a standard UV viewing cabinet, the stone emitted a gradually increasing strong orange fluorescence, followed by a long-lasting noticeable phosphorescence (~150 seconds, figure 86, top). The fluorescence and phosphorescence reactions demonstrated a nonuniform color distribution. Similar results were observed using other light sources, including 395 nm UV LED, 405 nm blue laser, a tungsten incandescent flashlight, and a fiber-optic halogen unit.

Given that orange phosphorescence can also be generated by low- and non-UV light sources, further analysis was performed using a series of spectral bandpass filters to identify other wavelengths that stimulate the orange phosphorescence. Testing demonstrated that medium- to strong-intensity light centered at around 430 nm produces the excitation.

Under short-wave ultraviolet (SWUV, 254 nm) radiation using a standard viewing UV cabinet and a De Beers PhosView instrument, the stone displayed a mix of strong greenish blue and medium orange zoned fluorescence and phosphorescence (figure 86, bottom). The colored phosphorescing areas decayed at different rates, with the greenish blue fading faster than the orange (~90 seconds vs. ~240 seconds, with a half-life of about 25 and 35 seconds, respectively).

Deep-UV (<225 nm) imaging demonstrated a strong greenish blue fluorescence with a clear cuboctahedral structure associated with HPHT growth (figure 87). After removal

Figure 87. Deep-UV imaging of the 0.71 ct colorless diamond showing a cuboctahedral-structured luminescence associated with HPHT growth. Image by Guy Borenstein.



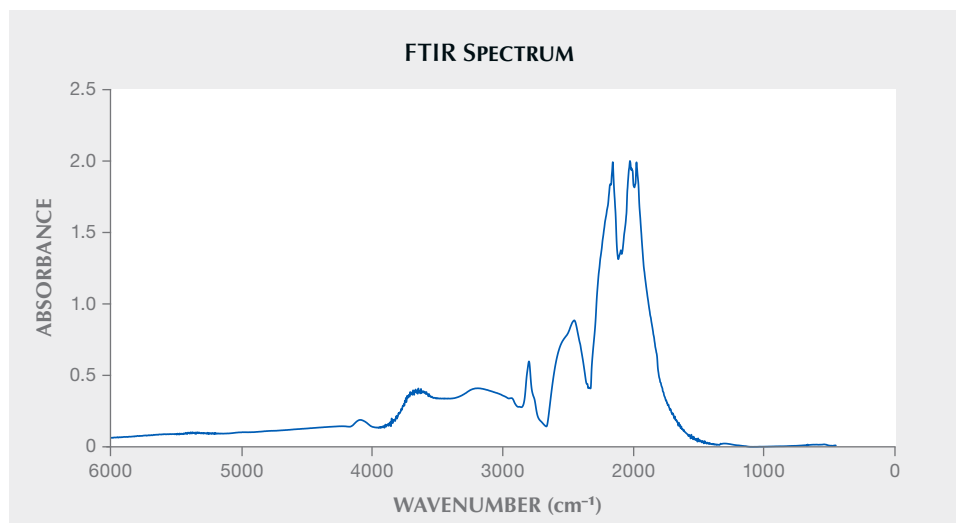


Figure 88. The infrared spectrum of the 0.71 ct HPHT-grown diamond revealed it was type IIb with relatively high levels of uncompensated boron (for a colorless diamond) at 4089, 2929, 2800, and 2455  $\text{cm}^{-1}$ .

from the excitation source, the stone displayed a phosphorescence reaction similar to the reaction under SWUV.

Infrared spectroscopy revealed a type IIb diamond with relatively high levels of electrically uncompensated boron at 4089, 2929, 2800, and 2455  $\text{cm}^{-1}$  (figure 88). Photoluminescence spectroscopy with 532 nm laser excitation at liquid nitrogen temperature (77K) showed no results, except for the diamond's first- and second-order Raman spectrum peaks, a common tendency in HPHT-grown colorless diamonds (S. Eaton-Magaña et al., "Observations on HPHT-grown synthetic diamonds: A review," Fall 2017 *G&G*, pp. 262–284).

The two phosphorescence colors emitted and their relatively long duration are well-known properties of HPHT-grown diamonds (S. Eaton-Magaña and R. Lu, "Phosphorescence in type IIb diamonds," *Diamond and Related Materials*, Vol. 20, No. 7, 2011, pp. 983–989; Eaton-Magaña et al., 2017), and a blue-orange luminescence combination in one gem was also previously reported (Eaton-Magaña and Lu., 2011; B. Deljanin et al., "NDT breaking the 10 carat barrier: World record faceted and gem-quality synthetic diamonds investigated," *Contributions to Gemology*, Vol. 15, No. 1, 2015) but of weaker intensity. The laboratory-grown diamond's property of bicolor, decay-varying phosphorescence has been previously reported as well (K. Watanabe et al., "Phosphorescence in high-pressure synthetic diamond," *Diamond and Related Materials*, Vol. 6, No. 1, 1997, pp. 99–106; Eaton-Magaña and Lu, 2011; Ulrika F.S. D'Haenens-Johansson et al., "Large colorless HPHT-grown synthetic gem diamonds from New Diamond Technology, Russia," Fall 2015 *G&G*, pp. 260–279).

Considering the HPHT growth method, the long-lasting greenish blue phosphorescence produced by exposure to SWUV and deep UV was expected. It was previously suggested to be related to nitrogen-boron donor-acceptor pair recombination (Watanabe et al., 1997). However, the orange phosphorescence demonstrated a new stimulation source. Its combination with the greenish blue phosphorescence and the identified visible-light excitation wave-

length reinforces the theory that the recorded orange phosphorescence is of a different donor-acceptor pairing.

Light of 430 nm wavelength can be found in most fluorescent and all incandescent indoor light sources, as well as the desk lamps and color grading cabinets found in gemological laboratories. Therefore, considering the possibility of more diamonds with this property in the market, their phosphorescence produced from visible light makes it challenging to assign a color in the colorless to near-colorless range for these diamonds during grading. Even under standard non- or low-UV output 6500K fluorescent bulbs, the orange luminescence generated by the source becomes noticeable, adding a yellowish overtone to the blue-gray bodycolor and changing its apparent color grade to approximately F to G. Such a change may impair the diamond grader's ability to accurately assess the stone's bodycolor.

Guy Borenstein and Sean O'Neal  
Stuller Inc.  
Lafayette, Louisiana

## SYNTHETICS AND SIMULANTS

**Synthetic color-change wakefieldite.** Author AA, a gemstone cutter and collector of rare synthetic gems, recently submitted one rough and one faceted stone to GIA for scientific examination. The material, sourced from RG Crystals in Bangkok, was stated to be Czochralski-pulled, neodymium-doped yttrium orthovanadate, which is commonly used in laser applications. It can also form naturally as the mineral wakefieldite-(Y), with an ideal chemical formula of  $\text{YVO}_4$ . His first observation was a striking color change from pink or purple to a blue or even green color under various lighting conditions and viewing angles. The finished gemstone (figures 89 and 90) displayed strong fire due to the material's very high dispersion.

Wakefieldite is a rare tetragonal mineral belonging to the xenotime mineral family with an ideal general formula of  $[\text{REE}]\text{VO}_4$ , where REE = Y, La, Ce, and Nd among other



Figure 89. Faceted and rough synthetic wakefieldite in LED lighting with 6400K color temperature. The faceted stone is 5.04 ct. Photo by Adriana Gudino; courtesy of Arya Akhavan.

rare earth elements. Its general physical and optical properties include a hardness of 5, specific gravity of 4.25, uniaxial + optic sign with refractive indices of  $n_o = 2.000$  and  $n_e = 2.140$ , birefringence of 0.140, and dispersion of 0.084. With prominent, perfect cleavage and relatively low hardness, the material is difficult to polish. Natural wakefieldite occurs as very small, non-gem crystals unsuitable for faceting; Czochralski-pulled materials represent the only

examples of faceted wakefieldite. In fact, this was the first faceted synthetic wakefieldite seen in a GIA laboratory. Chemistry and visible absorption spectra were collected to quantitatively study the striking color-change behavior.

A polished wafer with 10.6 mm thickness was analyzed. Laser ablation-inductively coupled plasma-mass spectrometry revealed the material was composed of mostly yttrium and vanadium, with 2.2% neodymium by weight (0.03 per

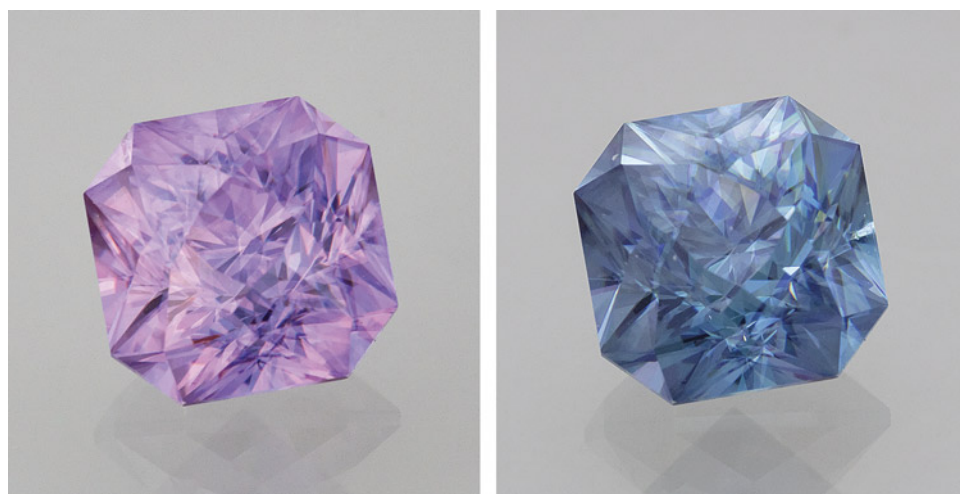


Figure 90. The color change of the faceted synthetic wakefieldite, observed between daylight (left) and cool fluorescent light F10 (right). Photos by Aaron Palke; courtesy of Arya Akhavan.



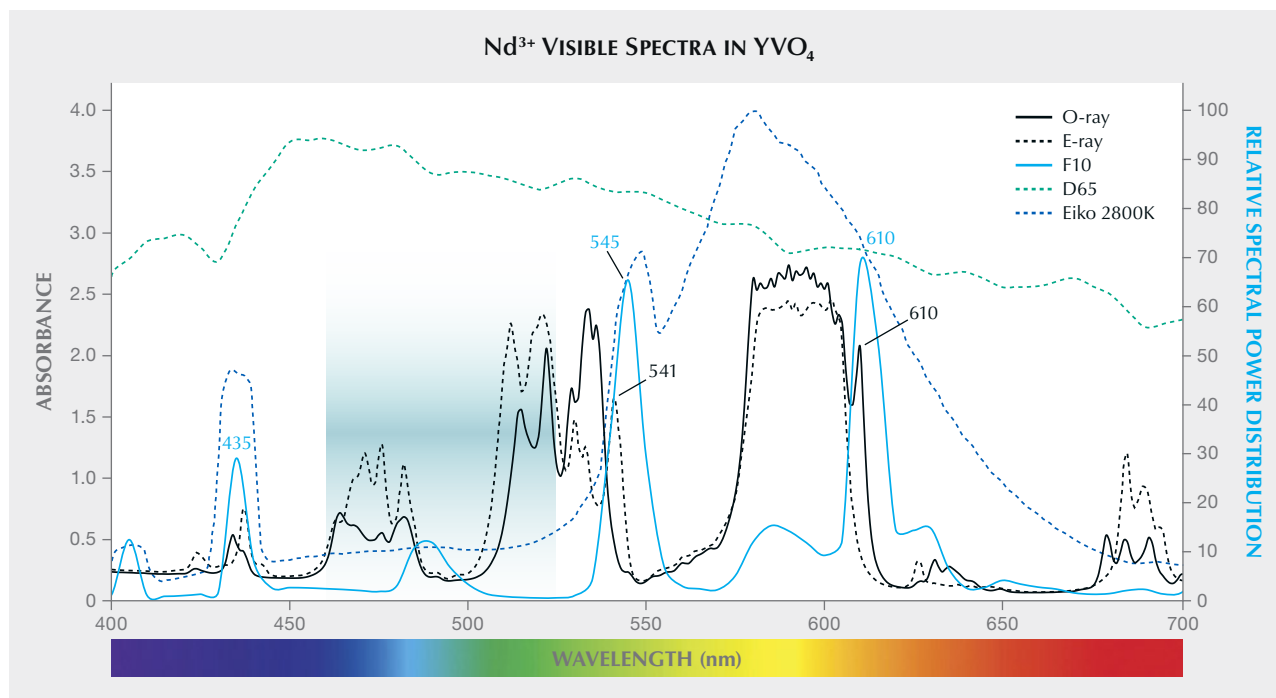


Figure 91. The visible absorption spectra of neodymium-doped  $\text{YVO}_4$  are shown with the relative power distribution curves of CIE illuminants F10 and D65 and an Eiko warm white fluorescent bulb with color temperature of 2800K.

formula unit). Since  $\text{Y}^{3+}$  does not produce color on its own, the color must be derived from the addition of  $\text{Nd}^{3+}$  ions substituting for  $\text{Y}^{3+}$  ions in the crystal lattice. Figure 91 shows polarized absorption spectra in the visible range collected with an ultraviolet/visible/near-infrared spectrometer for both the ordinary ray (o-ray) and extraordinary ray (e-ray). The expected color was calculated from the absorption spectra based on the formula described by Z. Sun et al. ("Quantitative definition of strength of chromophores in gemstones and the impact on color change in pyrospite garnets," *Color Research and Application*, Vol. 47, No. 5, 2022, pp. 1134–1154).

As shown in figure 92, the material exhibited a general pink to purple to violet color in most illuminants except the Eiko warm fluorescent light and the o-ray of CIE standard illuminant F10, which represents a typical cool fluorescent light. In fact, the color-change behavior noticed by author AA could be replicated when comparing illuminant F10 to any of the other illuminants such as daylight or incandescent light. Switching between warm incandescent light and actual cool daylight did not produce a dramatic change of color. The emission spectrum of F10 fluorescent light is mainly composed of sharp peaks at 435, 545, and 610 nm (figure 91). Therefore, the color of the synthetic wakefieldite crystal under illuminant F10 is only determined by the small absorption features at ~435, 541, and 610 nm of the  $\text{Nd}^{3+}$  ions. Broadband emitters such as incandescent light and actual daylight (D65 in figure 91), on the other hand, do not have these sharp emission features, so

the color was determined by the transmission windows in the spectrum (440–460, 490–500, 550–570, and 620–670 nm), which remain constant when switching between these illuminants. This was confirmed by observation of the stone in outdoor conditions, which produced the same pinkish purple color seen in incandescent light. The use of warm fluorescent light (Eiko fluorescent light in figures 91 and 92) with color temperature of 2800K also reproduced the greenish blue to blue color seen in cool fluorescent light (F10). It is also worth noting that the absorption features of  $\text{Nd}^{3+}$  ions at 541 and 610 nm were strongly dependent on the polarization of the light, resulting in a strong pleochroism (grayish purple for the o-ray and green-blue for the e-ray), only observed under F10 illuminant (figure 92).

The color panels under two LED illuminants in GIA's standard viewing box were also calculated in figure 92. The two LED lights, warm and cool, closely imitate the CIE standard illuminants A and D65. The two sets of color panels (A = LED warm pair and D65 = LED cool pair) are extremely close to each other based on their L, C, and H (lightness, chroma, and hue) color coordinates. This study also illustrates the consistent results of GIA's standard viewing box in grading gemstone color.

Ziyin Sun, Shiyun Jin, Adriana Gudino, and  
Aaron C. Palke  
Carlsbad, California  
Arya A. Akhavan  
Surgical Precision Gems, Toronto

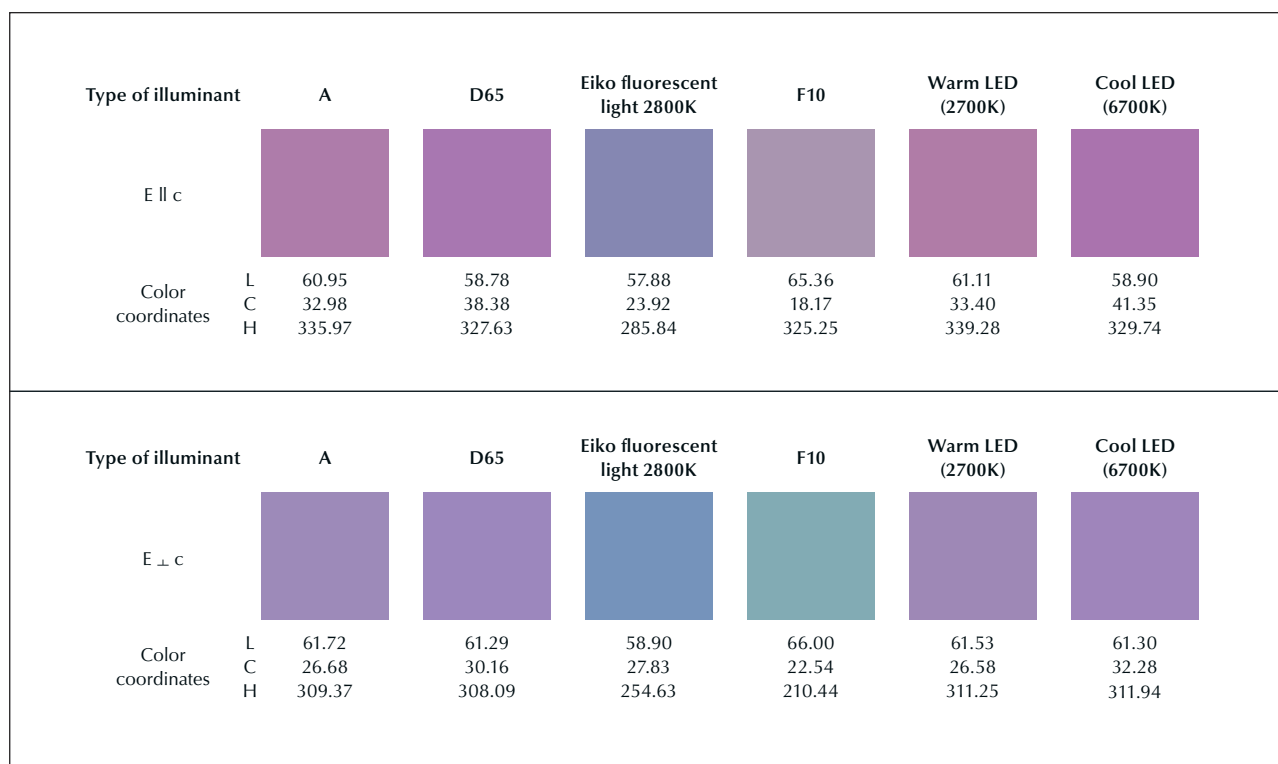


Figure 92. Color panels of the 10.59 mm wafer in six different lighting conditions were calculated for both the o-ray and e-ray. In the top row, A and D65 are CIE standard illuminants for incandescent light and daylight. Eiko is a fluorescent bulb with color temperature of 2800K, while F10 is a CIE standard narrowband fluorescent illuminant. Warm (2700K) and cool (6700K) LEDs represent the illuminants in the GIA standard viewing box.

## TREATMENTS

**Heated purplish pink sapphire from Ilakaka (Madagascar) with colored monazite inclusions.** The Laboratoire Français de Gemmologie (LFG) received a 3.02 ct purplish pink sapphire (figure 93) for identification. Under the microscope, zircon and monazite inclusions (figure 94) along with tubes (figure 95) were observed. This inclusion scene was characteristic of similarly colored sapphires from Ilakaka, Madagascar (W. Wang et al., “The effects of heat treatment on zircon inclusions in Madagascar sapphires,” Summer 2006 *G&G*, pp. 134–150; S. Saeseaw et al., “Low-temperature heat treatment of pink sapphires from Ilakaka, Madagascar,” Winter 2020 *G&G*, pp. 448–457). No indication of heating was observed. Moreover, the monazite inclusions were orange-brown. It was previously observed that monazite inclusions in pink sapphires turn colorless when heated above 600°C (see again Saeseaw et al., 2020).

Using Raman spectroscopy, the full width at half maximum (FWHM) of the band around 1010 cm<sup>-1</sup> due to anti-symmetric stretching vibration SiO<sub>4</sub> in the zircon structure and the band around 975 cm<sup>-1</sup> due to PO<sub>4</sub> stretching vibration in the monazite structure can decrease during heating of pink sapphires from Ilakaka (Wang et al., 2006; Saeseaw et al., 2020). The zircon and monazite inclusions were analyzed using a Raman Renishaw inVia spectrometer, with a

514 nm diode-pumped solid-state (DPSS) laser, with about 10 mW laser power on the sample, 50× long working distance objective lens, confocal mode (100 microns entrance slit), 1800 lines/mm grating, and about 1.5 cm<sup>-1</sup> spectral res-

Figure 93. A 3.02 ct heated purplish pink sapphire measuring 9.57 × 7.74 × 4.55 mm. Photo by Ugo Hennebois.





Figure 94. A series of colorless zircon inclusions and orange-brown monazite inclusions in the heated purplish pink sapphire. Photomicrograph by Ugo Hennebois; field of view 1.5 mm.

olution. The FWHM of the most intense band of seven monazite inclusions at around  $975\text{ cm}^{-1}$  ranged from  $12.7$  to  $14.2\text{ cm}^{-1}$ , and those of 10 zircon inclusions at around  $1010\text{ cm}^{-1}$  ranged from  $6.4$  to  $7.8\text{ cm}^{-1}$ . Both appeared to be sharper and less variable compared to FWHM in unheated pink sapphires, which present zircon inclusions with FWHM of the

Figure 95. Unaltered tubes in the heated purplish pink sapphire. Photomicrograph by Ugo Hennebois; field of view 2 mm.



main band from  $7.1$  to  $21.7\text{ cm}^{-1}$  and monazite inclusions with FWHM of the main band from  $14.2$  to  $18.4\text{ cm}^{-1}$  (Saeseaw et al., 2020; M. Krzemnicki et al., "Zircon inclusions in unheated pink sapphires from Ilakaka, Madagascar: A Raman spectroscopic study," *Proceedings of the Online International Gemmological Conference*, 2021, pp. 21–23; S. Karampelas et al., "Détection du traitement thermique à basse température des corindons," *Revue de Gemmologie a.f.g.*, No. 217, 2022, pp. 4–5).

Unpolarized Fourier-transform infrared spectra in different directions were collected using a Thermo Fisher Magna-IR560 with  $4\text{ cm}^{-1}$  spectral resolution and 500 scans using a diffuse reflectance accessory as beam condenser. The sample presented a band at  $3309\text{ cm}^{-1}$  and a less intense band at  $3232\text{ cm}^{-1}$ , which in pink sapphire is considered an indication of heating (Saeseaw et al., 2020). These bands are linked to different forms of titanium associated with hydroxyl defects in corundum (E. Balan, "Theoretical infrared spectra of OH defects in corundum ( $\alpha\text{-Al}_2\text{O}_3$ )," *European Journal of Mineralogy*, Vol. 32, No. 5, 2020, pp. 457–467).

In line with previous experiments showing that monazite inclusions can keep their color after heating to  $600^\circ\text{C}$  (Saeseaw et al., 2020), the presence of colored monazite inclusions alone cannot serve as evidence that a pink sapphire from Ilakaka is unheated. On the other hand, the presence of colorless monazite inclusions in pink sapphires from Ilakaka could be considered an indication of heat treatment.

Ugo Hennebois, Aurélien Delaunay, and  
Stefanos Karampelas (s.karampelas@lfg.paris)  
LFG, Paris

**Chromophore behaviors (including the 880 nm absorption band) in an irradiated pink sapphire.** Irradiation is a known process for enhancing color in corundum, particularly yellow and pink sapphire. Recently, some rubies and pink sapphires with bluish tint were reportedly treated with radiation ("LMHC makes progress on laboratory report harmonisation, discussed current challenges in detection of corundum treatments," LMHC press release, March 14, 2023). However, chromophore behaviors in irradiated ruby/pink sapphire have not been fully investigated. This report shows preliminary results of an experiment involving irradiated pink sapphire. An untreated Madagascar pink sapphire with a blue modifier (figure 96) was fabricated as an optical wafer with two polished faces perpendicular to the  $c$ -axis for ultraviolet/visible/near-infrared (UV-Vis-NIR) spectroscopic study. Trace element chemistry was analyzed in the UV-Vis-NIR measurement area using laser ablation–inductively coupled plasma–mass spectrometry. This information can be used to link the visual color and the color-causing trace elements listed in figure 96.

The spectrum of the untreated sample displayed broad absorption bands at  $\sim 400$  and  $\sim 560\text{ nm}$  together with weak peaks at  $\sim 470$  and at  $693\text{ nm}$ , demonstrating that the  $\text{Cr}^{3+}$  chromophore was responsible for the pink color (blue line in figure 97; see E.V. Dubinsky et al., "A quantitative de-



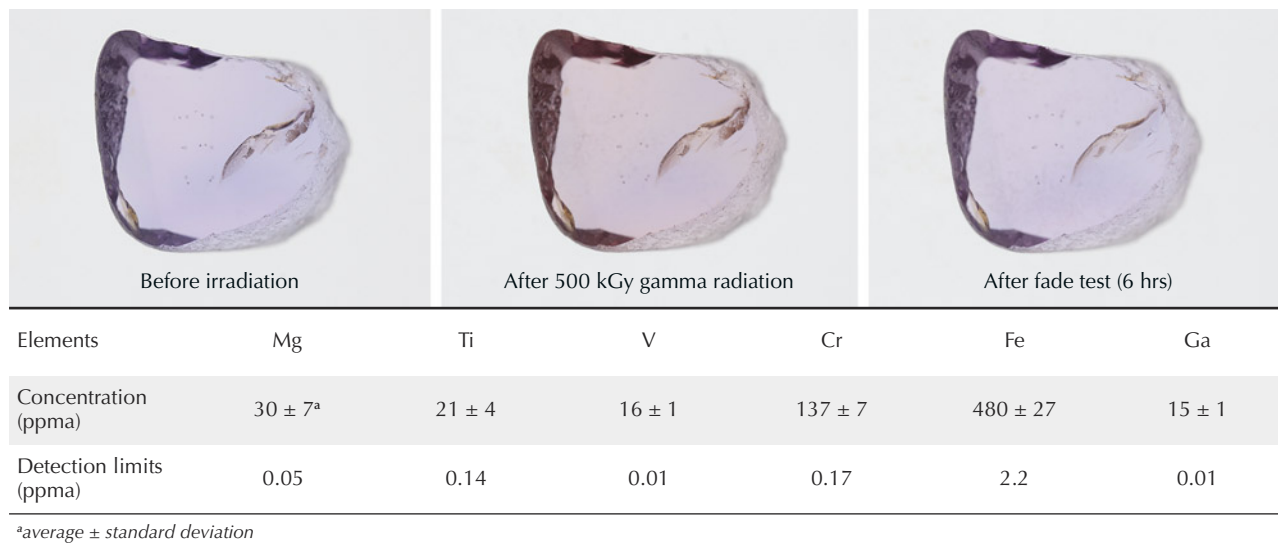


Figure 96. Color-calibrated photo of a 0.664 ct pink sapphire from Madagascar before and after irradiation, and after fade test using fiber-optic light for 6 hours. Path length/thickness: 1.514 mm. Photos by Sasithorn Engniwat.

scription of the causes of color in corundum,” Spring 2020 *GeG*, pp. 2–28). This sample also showed a weak broad band at around 580 nm related to Fe<sup>2+</sup>-Ti<sup>4+</sup> pairs, which produced a blue color, modifying the pink color from Cr<sup>3+</sup> to purple-pink. Weak Fe<sup>3+</sup>-related absorption features were also observed, represented by a broad band at ~330 nm and narrow peaks at 377, 388, and 450 nm. The iron-related chromophore only causes significant yellow color at relatively high iron concentrations (greater than ~1000 ppma) due to Fe<sup>3+</sup> chromophores’ weak color strength.

For our radiation experiment, the sample was treated with a gamma irradiation dose of 500 kGy at the Irradiation Center at the Thailand Institute of Nuclear Technology (public organization). After irradiation, the pink sapphire changed to a padparadscha-like coloration in which the subtle blue color was partially removed (figure 96). The UV-Vis-NIR spectrum after irradiation showed a significant increase in absorption intensities at wavelengths shorter than ~560 nm or longer than ~660 nm (red line in figure 97). To observe changes in chromophore be-

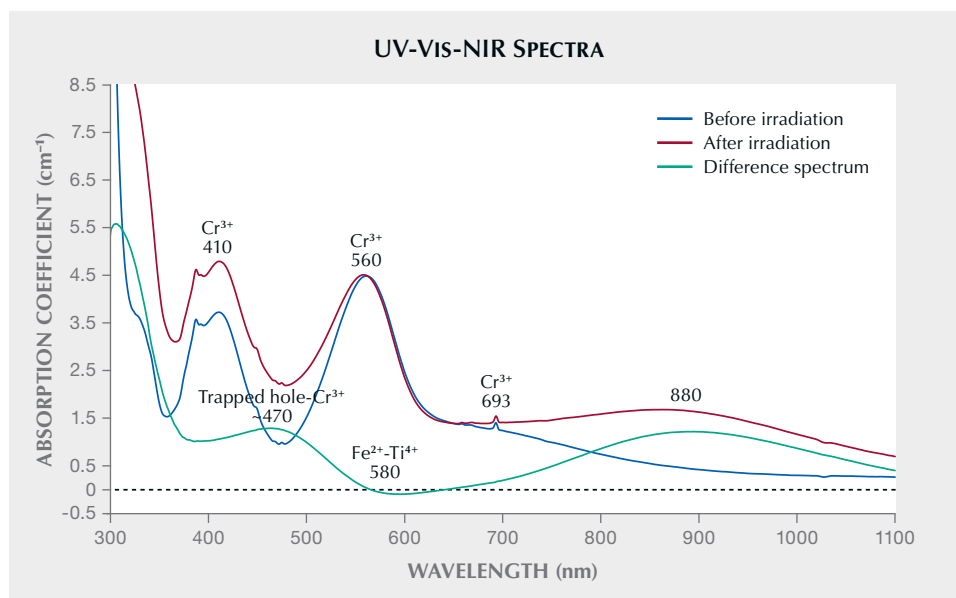


Figure 97. Polarized UV-Vis-NIR spectra comparisons of the pink sapphire before and after irradiation with a gamma irradiation dose of 500 kGy. The difference spectrum revealed a significant increase in trapped hole paired with Cr<sup>3+</sup> and the 880 nm band in the irradiated pink sapphire.

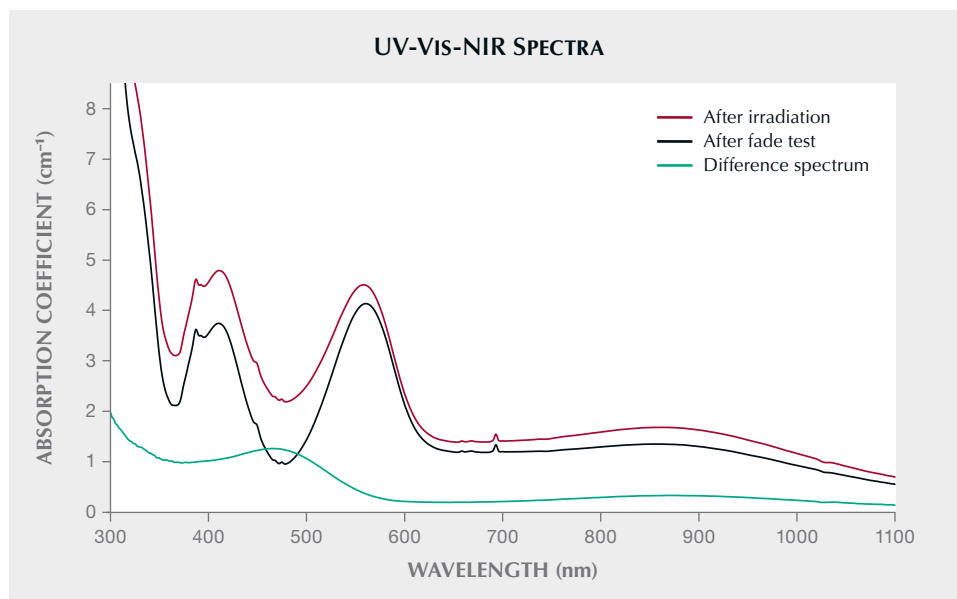


Figure 98. Polarized UV-Vis-NIR spectra comparisons of the pink sapphire after irradiation with a gamma irradiation dose of 500 kGy and after the fade test. The difference spectrum between after irradiation and after fade test obviously shows the reduction in the trapped hole paired with  $\text{Cr}^{3+}$  chromophore when exposed to intense light for several hours.

havior caused by irradiation, the spectrum after irradiation was subtracted from the pretreatment spectrum. The difference spectrum (green line in figure 97) revealed that this acceptor-dominated corundum with an atomic concentration of magnesium greater than the sum of titanium and silicon concentrations created a strong absorption feature below  $\sim 560$  nm to the UV region, which matches well with the trapped hole associated with the  $\text{Cr}^{3+}$  spectrum for causing orange coloration (Dubinsky et al., 2020). Using the absorption cross section information provided in Dubinsky et al. (2020), the concentration of trapped hole- $\text{Cr}^{3+}$  chromophores induced by irradiation was approximately 0.8 ppma in the sample. This chromophore had very high color strength, and therefore a noticeable color change could be observed with only a tiny concentration of the trapped hole paired with  $\text{Cr}^{3+}$  created after treatment. The  $\text{Fe}^{2+}$ - $\text{Ti}^{4+}$  chromophore also reduced by approximately 0.7 ppma in the treated sample, resulting in less blue color modification. This slight lightening in blue color after irradiation is possibly due to the change in oxidation state of iron (which would reduce the number of  $\text{Fe}^{2+}$ - $\text{Ti}^{4+}$  pairs). In addition, the creation of orange color (trapped hole- $\text{Cr}^{3+}$ ) masked a certain portion of remaining blue color after treatment, as blue and orange are complementary colors. The change in UV-Vis-NIR spectrum corresponded with the change in color appearance caused by irradiation.

When studying absorption features in the UV-Vis-NIR spectrum of corundum, a broad band centered at around 880 nm in the red to near-infrared region is typically associated with basalt-related blue sapphire (e.g., A.C. Palke et al., "Geographic origin determination of blue sapphire," Winter 2019 *G&G*, pp. 536–579). This band has little or no impact on color. In addition to basalt-related blue sapphires that are exposed to heat naturally, the 880 nm band can be induced in the spectrum of a metamorphic-type sapphire

that has been heat treated, such as heated Madagascar sapphire (E.B. Hughes and R. Perkins, "Madagascar sapphire: Low-temperature heat treatment experiments," Summer 2019 *G&G*, pp. 184–197) or heated Rock Creek sapphire (J.L. Emmett and T.R. Douthit, "Heat treating the sapphires of Rock Creek, Montana," Winter 1993 *G&G*, pp. 250–272). This feature can also be found in Mozambican ruby after heat treatment (S. Saeseaw et al., "Update on "low-temperature" heat treatment of Mozambican ruby: A focus on inclusions and FTIR spectroscopy," *GIA Research News*, April 30, 2018). The origin of this band is not fully understood but may be related to iron clusters.

The 880 nm band was absent in the UV-Vis-NIR spectrum of this sample before treatment. Interestingly, this pink sapphire developed the 880 nm band after irradiation, with a significant intensity around  $1.2 \text{ cm}^{-1}$ . Color stability testing is usually performed in gem laboratories for yellow to padparadscha sapphires that may contain unstable color centers (e.g., A.C. Palke et al., "An update on sapphires with unstable color," *GIA Research News*, December 12, 2022; Summer 2022 GNI, pp. 259–260). After the color stability test (figures 96 and 98), the orange coloration introduced by irradiation faded away after exposure to intense incandescent light due to the dissociation of the trapped hole paired with  $\text{Cr}^{3+}$ , whereas the 880 nm band remained. This preliminary observation suggests that the 880 nm band can be produced by an irradiation process, and this feature could provide some interesting evidence of treatment, either heat or irradiation, in pink sapphires and rubies. However, further studies would be needed to understand the development of the 880 nm absorption band.

Wasura Soonthorntantikul and Wim Vertriest  
GIA, Bangkok  
Aaron Palke  
GIA, Carlsbad